

UNIVERSIDAD COMPLUTENSE DE MADRID

FACULTAD DE CIENCIAS QUÍMICAS

Departamento de Química Física



TESIS DOCTORAL

**Nuevos avances en nanoestructuras poliméricas polimerización in-situ
e infiltración de polímeros en plantillas AAO**

**Advances in patterned polymer nanostructures in-situ polymerization
and polymer infiltration in AAO templates**

MEMORIA PARA OPTAR AL GRADO DE DOCTOR

PRESENTADA POR

Belén Sanz Sanz

Directora

Carmen Mijangos Ugarte

Madrid, 2017

UNIVERSIDAD COMPLUTENSE DE MADRID
FACULTAD DE CIENCIA QUÍMICAS
Departamento de Química-Física



**NUEVOS AVANCES EN NANOESTRUCTURAS POLIMÉRICAS.
POLIMERIZACIÓN IN-SITU E INFILTRACION DE POLIMEROS
EN PLANTILLAS AAO.**

**ADVANCES IN PATTERNED POLYMER NANOSTRUCTURES.
IN-SITU POLYMERIZATION AND POLYMER INFILTRATION IN
AAO TEMPLATES.**

Trabajo de investigación que presenta
BELÉN SANZ SANZ
para la obtención del Grado de Doctor

Bajo la dirección de la Profesora Carmen Mijangos Ugarte

INSTITUTO DE CIENCIA Y TECNOLOGÍA DE POLÍMEROS
Departamento de Nanomateriales Poliméricos y Biomateriales



MADRID, 2017

Agradecimientos

En primer lugar me gustaría agradecer a mi directora, Carmen Mijangos, por darme su confianza para realizar esta tesis doctoral dentro de su grupo. También le agradezco las muestras de apoyo y reconocimiento que ha tenido conmigo cuando las circunstancias no han sido las mejores y aun así, hemos conseguido superar.

En la parte profesional también me gustaría agradecer a los grupos que han colaborado con nosotros durante estos años. Empezando por cercanía al grupo del Prof. Manuel Vázquez que fue mi primera colaboración y subiendo para tierras del norte al Prof. J.M. Asua y a su grupo donde realicé una estancia de tres meses. Agradecer especialmente a Nick por trabajar con él, ayudarme desde el principio y estar tan dispuesto siempre a responder a todas mis dudas. Gracias al Prof. Alejandro Müller por su ayuda e interés mostrado en todo lo que hacía y a su grupo, en especial a Jordana, que me acogió durante mi estancia desarrollada en San Sebastián. Terminando con Alemania, me gustaría agradecer a la Prof. Arancha del Campo y a su grupo por el apoyo mostrado durante mi estancia en el Max Planck en Mainz. A Longjian por enseñarme tantas cosas y por su paciencia conmigo a pesar de que las cosas no salieron tan fáciles como pensábamos en un principio.

De estas estancias quería agradecer también a todos los compañeros encontrados y conocidos como a Lucía, Sheila, Guiomar o la familia Seijas, especialmente a Ana, por ayudarme desde el minuto uno en mi llegada a Donostia. Y a los descubiertos en Alemania como Rubén, Oya, Aleeza, Xuân-Anh, Noemí y a mi maruja Noelia, una argentina más, pero que como amiga me llevo para siempre.

También quería hacer una mención especial a mi grupo en el ICTP. Empezando por los que ya se fueron Jon, Vanesa y Aurora, los que pasaron Juan, Talitha, Merari, Rose Mary, Vincent, Miki, Jose...de todos ellos me llevo un gran recuerdo y muchas fotos para un gran álbum; y los que quedan Iwona, Rebeca, Laia y Diana, gracias por dar en este grupo un buen ambiente de trabajo. Una especial mención quería dedicar a mis chicas Sótano: Miryam y Nicoletta. Gracias por estar ahí, por los miles y sabios consejos de Nicoletta y por las miles de horas compartidas en el despacho con Miryam donde hemos compartido historias para escribir otro libro.

El grupo del taper y el café también debe de tener un apartado en los agradecimientos ya que es el momento en el que se desconecta y se habla de cualquier tipo de tema. Buenos ratos

con Ansel, Susana, Iván, Mario, Valentina, Marta Palacios, Marta Álvarez, Alberto, Lautaro, Virginia, Rodri...y alguno más que me olvidaré.

Un pequeño apartado quería destacar a mi primer año en este instituto donde empecé el máster de plásticos y caucho y donde tuve la oportunidad de conocer mucha de la gente que compone este instituto y me he seguido encontrando durante la tesis. A mis compañeros del máster, en especial a Antonio que ha sido mi oráculo para todas mis dudas de cualquier tipo, Isabel Raman una gran amiga con consultorio incluido donde hablar desde un punto de vista siempre positivo y Alejandra por su nervios convertidos en mi tranquilidad. Agradecer también a la parte de caracterización, con David SEM, Carolina, Esperanza y Álvaro (te meto como técnico/compañero de DSC y otras muchas técnicas que sabes como el que más) y a los chicos del taller Manuel, Alberto y Carlos por su enorme paciencia arreglando las celdas de anodización. Gracias también a todo el personal investigador que forma parte del centro que me ayudó en algún momento de esta tesis (Juan Rodríguez, Charo Benavente, Ángel Marcos, Juan Valentín, Alberto Caucho...) No quisiera olvidar en esta sección a toda la gente de administración, limpieza y portería.

Saliendo del entorno laboral me gustaría agradecer a mis amigos, tanto mi gente de Navas como mis amigas en Madrid. La lista de nombres es bastante larga, pero todos ellos han sido parte fundamente durante muchos años en mi vida y lo siguen siendo.

Por último, quería dejar los agradecimientos más importantes a mi familia. En especial a aquellas personas principales en mi vida y que ya no están entre nosotros, ya que sin ellos no podría haber llegado hasta aquí. Especialmente a mi padre, que justo se marchó en el momento en el que empecé la beca, esta tesis te la dedico a tí. Gracias por todo y os echo de menos. A mi madre que es mi referente como luchadora, a pesar de todos los problemas que la vida le ha dado siempre está ahí para apoyarnos y aunque no entienda nada de lo que hago se preocupa cada día por cómo va la tesis. A mis hermanos Antonio, Lucía y Gema por estar ahí, en los buenos y malos momentos, y seguir siendo los cuatro fantásticos. Y por último y no menos importante a Carlos. Gracias por acompañarme durante todo este tiempo y aguantar todo tipo de estado de ánimo que conlleva esta tesis. Me siento muy afortunada de tenerte a mi lado y por empezar esta nueva etapa que nos toca vivir juntos.

La inteligencia consiste no sólo en el conocimiento, sino también en la destreza de aplicar los conocimientos a la práctica.

Aristóteles

Table of Contents

Table of contents

<i>Resumen</i>	<i>ix</i>
<i>Summary</i>	<i>xiii</i>
1. GENERAL INTRODUCTION AND OBJECTIVES	1
2. STATE OF THE ART	11
2.1 Porous Anodic Aluminium Oxide Porous Template (AAO)	13
2.2 Polymerization in confinement	18
2.2.1 Polymerization reaction in porous materials	22
Mesoporous silicas	22
Metal-Organic Framework (MOF)	24
Controlled Pore Glasses (GPC)	28
2.2.2 Polymerization in Anodic Aluminium Oxide (AAO)	32
Polymerization kinetics in AAO confinement	36
2.3 Polymer infiltration process	37
2.3.1 Classification of templates synthesis methods	38
2.3.2 Polymer nanostructures from infiltration method	41
2.4 References	45
3. PREPARATION AND CHARACTERIZATION OF AAO TEMPLATES	57
3.1 Introduction	59
3.1.1 Anodization process	60
3.1.2 Wettability	65
3.2 Experimental part	68
3.2.1 Fabrication of AAO template	68
Description of equipment	68
First and second anodization	70
Pore widening	71
Thin alumina template	69
3.2.2 Characterizacion techniques	72
3.3 Results and discussion	74
3.3.1 Ordered AAO templates	74
3.3.2 Pore widening	78
3.3.3 Porosity and volume	77
3.3.4 Wettability	82
3.4 Conclusions	85
3.5 References	86
4. RADICAL POLYMERIZATION OF MMA IN AAO NANOREACTORS	89
4.1 Introduction	91
4.2 Experimental part	94

4.2.1	Materials and AAO templates	94
4.2.2	In-situ polymerization of MMA in AAO	94
4.2.3	Bulk polymerization of MMA	95
4.2.4	Infiltration of PMMA in AAO	95
4.2.5	Infiltration of AIBN in AAO	96
4.2.6	Characterization techniques	96
4.3	Radical polymerization kinetic model	100
4.4	Results and discussion	104
4.4.1	Free radical polymerization of MMA in confinement and bulk	104
	Morphological characterization	104
	Monitoring by Raman spectroscopy	105
	Monitoring by DSC	106
	Molecular weight by GPC	109
	Catalytic effect of the pore alumina walls	110
	Induction time and gel effect	112
4.4.2	Modeling of polymerization in bulk and in confinement	114
	Implementation of the model and model fit	114
	Modeling of polymerization in bulk	116
	Modeling of polymerization in confinement	118
4.4.3	Properties of synthesized PMMA nanostructures	120
	Thermal properties and polymer aging	120
	Wettability	123
4.5	Conclusions	127
4.6	References	128
5.	<i>POLYMERIZATION OF HYDROPHOBIC FLUORINATED MONOMER IN AAO NANOREACTOR</i>	<i>133</i>
5.1	Introduction	135
5.2	Experimental part	137
5.2.1	Materials and AAO templates	137
5.2.2	Bulk polymerization of FA	137
5.2.3	In-situ polymerization of FA in AAO	138
5.2.4	Infiltration of PFA in AAO	138
5.2.5	Characterizations techniques	139
5.3	Results and discussion	140
5.3.1	Free radical polymerization of FA in confinement and bulk	140
	Morphological characterization	140
	Monitoring by DSC	140
	Monitoring by Raman spectroscopy	140
5.3.2	Modelling of polymerization in bulk and confinement	144
5.3.3	Nanostructured PFA surface and applications	150
5.4	Conclusions	154
5.5	References	155

6. STEP-GROWTH POLYMERIZATION OF DIOL AND DIISOCIANATE IN AAO NANOREACTOR	159
6.1 Introduction	161
6.2 Experimental part	163
6.2.1 Materials and AAO templates	163
6.2.2 Bulk polymerization of Polyurethane	163
6.2.3 In-situ polymerization of Polyurethane in AAO	164
6.2.4 Infiltration of Polyurethane in AAO	165
6.2.5 Characterizations techniques	165
6.3 Polymerization model inside nanopores	167
6.4 Results and discussion	171
6.4.1 Monitoring polyurethane polymerization	171
6.4.2 Modelling results	178
6.4.3 Polymer morphology and surface properties	181
6.5 Conclusions	184
6.6 References	185
7. POLYMER INFILTRATION PROCESS. DEVELOPMENT OF NOVEL NANOSTRUCTURES	189
7.1 Core-Shell PCL-PS nanocylinders	191
7.1.1 Introduction	191
7.1.2 Experimental part	192
7.1.3 Results and discussion	194
7.2 Core-shell Ni-PS nanowires	202
7.2.1 Introduction	202
7.2.2 Experimental part	203
7.2.3 Results and discussion	204
7.3 PCL-PDMS Micropatterning to mimic the frog toe pad	208
7.3.1 Introduction	208
7.3.2 Experimental part	209
7.3.3 Results and discussion	214
7.4 Conclusions	223
7.5 References	225
8. GENERAL CONCLUSION AND PERSPECTIVES	229
ANNEX	235
A.1 Introduction	237
A.2 Experimental part	238
A.3 Results and discussion	238
A.4 Conclusion	243
A.5 References	244
i. Abbreviations	245
ii. List of publications	251

Resumen/Summary

Resumen

Las plantillas porosas de alúmina (AAO) son sistemas ordenados, formados por una matriz de poros cilíndricos uniformemente dimensionados. Estas plantillas han sido ampliamente empleadas en nuestro grupo para la obtención de nanoestructuras poliméricas como nanorods, nanofibras y nanotubos mediante el proceso infiltración de polímeros (nanomoldeo). Asimismo, numerosos trabajos han demostrado que las propiedades del polímero en confinamiento dentro de los nanoporos cambian con respecto a las propiedades del mismo polímero en masa. Sin embargo, cuando se trata de infiltrar polímeros termoestables o el proceso de infiltración debe llevarse a cabo a alta temperatura y/o durante un tiempo relativamente largo, de horas a días, el polímero se puede degradar y es conveniente buscar otro método. Esta tesis doctoral plantea la polimerización in situ de un monómero dentro de los poros de la plantilla AAO (nanoreactor) como método alternativo para producir nanoestructuras poliméricas. Una vez polimerizado el polímero puede extraerse para el estudio de sus propiedades y para su uso en distintas aplicaciones.

Esta tesis está basada en el empleo de plantillas AAO y comprende dos aspectos importantes, su empleo como nanoreactores y nanomoldes. Los objetivos de esta tesis son: el estudio de las reacciones de polimerización de diferentes monómeros en las nanocavidades y la preparación de nuevas nanoestructuras poliméricas nunca reportadas en la literatura, mediante la infiltración de polímeros en AAO. El primer objetivo además plantea la modelización de la polimerización en confinamiento estudiando las diferencias respecto al bulk.

Para alcanzar estos objetivos se prepararon plantillas de alúmina mediante el proceso de doble anodización. El empleo de distintas condiciones de anodización (temperatura, naturaleza y concentración del electrolito, voltaje y tiempo) permitió la elaboración de plantillas de distintos tamaños de diámetro y longitud de poro, entre 15-400 nanómetros y 0.7-100 micras, respectivamente.

El primer estudio sobre la polimerización en confinamiento en plantillas de AAO (nanoreactores) se desarrolló para la polimerización radical del metacrilato de metilo (MMA). La reacción se estudió a diferentes temperaturas y a diferentes grados de confinamiento en función del tamaño de poro de la plantilla. Los resultados de la cinética de polimerización se compararon con los obtenidos en bulk y se interpretaron en base a un modelo matemático. Las principales diferencias que se observaron se resumen en la fase inicial donde la velocidad de polimerización es más rápida en confinamiento por la descomposición acelerada de la molécula iniciadora. En la siguiente etapa se observó que el inicio de las limitaciones de difusión ocurría antes y fue atribuida a la mayor temperatura de transición vítrea de los polímeros bajo confinamiento. En la

última etapa, se observó que la combinación de dos radicales ocurría más rápidamente en el sistema confinado debido al menor volumen efectivo, aumentando así la velocidad de terminación. Estos efectos de confinamiento dieron como resultado un polímero de menor peso molecular y de menor polidispersidad. El envejecimiento físico junto con el estudio químico, demostraron una restricción de la movilidad de las cadenas de polímero a lo largo de la pared de alúmina.

Para generalizar el concepto a otros monómeros se estudió la polimerización radical de un monómero fluoroacrílico (FA). La reacción de polimerización en masa se hizo a de forma similar al caso anterior y se comparó con la reacción de polimerización en confinamiento. Los resultados mostraron una disminución en la velocidad de polimerización producido por el aumento de la reacción de terminación, ya que la probabilidad de encontrarse dos radicales en un menor volumen es mayor, como se vio en el caso del MMA. Para justificar estos resultados los datos fueron ajustados a un modelo matemático. Como aplicación de este estudio se prepararon nanoestructuras de PFA con plantillas AAO consiguiendo un material superhidrofóbico.

El estudio se completó con la reacción de polimerización por pasos. Se sintetizó un poliuretano en confinamiento dentro de las plantillas AAO a partir de la reacción entre un diol y un diisocianato. La polimerización se llevó a cabo en diferentes tamaños de confinamiento y se compararon con la reacción en bulk. En este caso se observó que los grupos hidroxilo de la alúmina reaccionan con los grupos isocianatos dando lugar a una disminución del peso molecular y la polidispersidad. Esta reacción adicional junto con el confinamiento físico de las cadenas a crecer en un volumen confinado, da como resultado un aumento de la velocidad de polimerización en las primeras etapas de reacción. Para explicar los resultados se estableció un modelo matemático teniendo en cuenta las interacciones químicas y físicas encontradas en la plantilla de alúmina.

La preparación de polímeros nanoestructurados en plantillas AAO mediante infiltración de polímeros (nanomoldes) dio lugar a nuevas estructuras *core-shell* no recogidas en la bibliografía. Por un lado se sintetizaron nanoestructuras metal/polímero donde nanocables de níquel son recubiertos por nanotubos de poliestireno. La caracterización magnética de la doble nanoestructura indica la presencia de un eje de fácil magnetización paralelo a los nanocables y atribuido principalmente a la anisotropía de los nanocables de níquel.

También se consiguió una estructura *core-shell* polímero/polímero mediante doble infiltración por fundido de dos polímeros: policaprolactona (*core*) y poliestireno (*shell*). El estudio de la cristalización de la PCL mostró un comportamiento fraccionado, observándose dos

picos de cristalización, uno a altas temperaturas debido a la nucleación heterogénea y otro a menor temperatura asumible a una nucleación homogénea.

Por último, se realizó un estudio preliminar para imitar la huella del dedo de la rana. Para ello se desarrolló un sistema polimérico en base a dos patrones de diferente escala, nano y micro. La nanoestructura se logró con nanopilares de PCL y PMMA por infiltración del polímero dentro de plantillas AAO, mientras que la microestructura se consiguió con micropilares de PDMS y pACAA por doble desmoldeo a partir de máscara obtenida por litografía. Los polímeros blandos (PDMS y pACAA) se estudiaron por fuerzas de adhesión y fricción, observando diferencias en las superficies planas y microestructuradas. La estructura doble constituida por microestructuras compuestas por nanopilares no resultó ser lo más adecuada la propiedad buscada. Estos resultados fueron el punto de partida en un estudio posterior donde se consiguió la estructura deseada.

Summary

Anodic aluminium oxide templates (AAO) are ordered systems, formed by a matrix of uniformly sized cylindrical pores. These templates have been widely used in our group to obtain polymer nanostructures such as nanorods, nanofibers and nanotubes through the process of polymer infiltration (nanomolding). Also, numerous studies have shown that the properties of the polymer in confinement inside the nanopores change according to the properties of the same polymer in bulk. However, when we need to infiltrate thermosetting polymers or the infiltration process must be carried out at high temperature and / or for a relatively long time, from hours to days, the polymer may be degraded and it is required to use other method. This doctoral thesis proposes the in situ polymerization of a monomer within the pores of the AAO template (nanoreactor) as an alternative method to produce polymer nanostructures. Once it polymerized, the polymer can be extracted for the study of its properties and can be the use in different applications.

This thesis is based on the use of AAO templates and comprises two important aspects, their use as nanoreactors and nanomolds. The objectives of this thesis are: the study of the reactions of polymerization of different monomers in the nanocavities and the preparation of new polymer nanostructures never reported in the literature, by the polymer infiltration process in AAO. The first objective also proposes the modelling of the polymerization in confinement by studying the differences with respect to the bulk.

To achieve these objectives, alumina templates were prepared by the double anodization process. The use of different anodizing conditions (temperature, nature and concentration of electrolyte, voltage and time) allowed the development of templates of different sizes of pore diameter and pore length, between 15-400 nanometers and 0.7-100 microns, respectively.

The first study on confinement polymerization in AAO templates (nanoreactors) was developed for the radical polymerization of methyl methacrylate (MMA). The reaction was studied at different temperatures and different degrees of confinement depending on the pore size of the template. The results of polymerization kinetics were compared with those obtained in bulk and were interpreted by a mathematical model. The main differences observed are summarized in the initial phase where the rate of polymerization is faster in confinement by the faster decomposition of the initiator molecule. In the next step, it was observed that the onset of diffusion limitations occurred earlier and was attributed to the higher glass transition temperature of the polymers under confinement. In the last step, it was observed that the combination of two radicals occurred more rapidly in the confined system due to the lower effective volume, thus increasing the termination rate. These confinement effects resulted in a lower molecular weight

and lower polydispersity polymer. Physical aging and the chemical study demonstrated a restriction of the mobility of the polymer chains along the alumina wall.

In order to generalize the concept to other monomers the radical polymerization of a fluoroacrylic monomer (FA) was studied. The bulk polymerization reaction was carried out similar to the previous case and compared to the polymerization reaction in confinement. The results showed a decrease in the rate of polymerization produced by the increase of the termination reaction, since the probability of finding two radicals in a smaller volume is higher, as it was observed in the case of MMA. These results were fitted to a mathematical model to confirm the results. As an application of this study, PFA nanostructures with AAO templates were prepared by obtaining a superhydrophobic material.

The study was completed with the step-growth polymerization reaction. A polyurethane was synthesized inside AAO nanocavities from the reaction between a diol and a diisocyanate. The polymerization was carried out in different confinement sizes and compared with the bulk reaction. In this case it was observed that the hydroxyl groups of the alumina react with the isocyanate groups resulting in a decrease in molecular weight and polydispersity. This additional reaction together with the physical confinement of the chains to grow in a confined volume result in an increase of the rate of polymerization in the first reaction stages. To explain the results, a mathematical model was established taking into account the chemical and physical interactions found in the alumina template.

The preparation of nanostructured polymers in AAO templates by polymer infiltration (nanomoldes) gave rise to new core-shell structures not reported in the literature. On the one hand, polymer/polymer core-shell structure was also achieved by double melt infiltration of two polymers: polycaprolactone (core) and polystyrene (shell). The study of the crystallization of the PCL showed a fractional behaviour, observing two peaks of crystallization, one at high temperatures due to heterogeneous nucleation and another at a lower temperature assuming to a homogeneous nucleation.

A metal/polymer nanostructure was synthesized where nickel nanowires are coated with polystyrene nanotubes. The magnetic characterization of the double nanostructures indicates the presence of an axis of easy magnetization parallel to the nanowires and attributed mainly to the anisotropy of the nanowires of nickel.

Finally, a preliminary study was carried out to replicate the toe pad of the tree frog. For this, a polymer system was developed based on patterns at two different scales, nano and micro. The nanostructure was achieved with PCL and PMMA nanopillars by polymer infiltration process in AAO template, whereas the microstructure was achieved with PDMS and pACAA

micropattern by double soft-molding from a mask obtained by lithography. The soft polymers (PDMS and pACAA) were studied by adhesion and friction forces, observing differences between flat and microstructured surfaces. The double structure constituted by microstructures composed of nanopillars did not prove to be the most satisfactory property required. These results were the starting point in a later study where the desired structure was achieved.

Chapter 1

GENERAL INTRODUCTION AND OBJECTIVES

The present PhD Thesis work “*Advances in Patterned Polymer Nanostructures. In-situ Polymerization and Polymer Infiltration in AAO Templates*”, aims to bring new insights in the framework of the research line “*Polymer Nanotechnology*”, in which the group has been involved for the last years. This work proposes new objectives and challenges to develop new and effective fabrication methods to obtain polymer nanostructures which could be precursors of applications. Along this 4 years period, it has been undertaken a huge study on “*Polymerization Reactions in AAO Templates*”, scarcely reported in the literature, with emphasis on the influence of confinement effects on the polymerization kinetics and on the molecular weight of resulting polymer. On the other hand, it has also been carried out a large study to develop novel methods to obtain sophisticated (next generation) of polymer nanostructures by “*Polymer Infiltration in AAO Templates*”

The reason to undertake such a challenging objective is because polymers for nanotechnology are highly demanded in medicine, sensing, electronics and other fields of applications and the research behind it plays an important role within regional, national and European Research Programs (VII Framework Program and Horizon 2020). In fact, it is generally accepted that in nanotechnology applications, especially in those where uniformity and organization of structures at the nanoscale is required, polymer materials have a predominant position in the development of new nanomaterials, since they combine specific chemical functions together with the feasibility of nanoscale manufacturing process. The fabrication of polymer nanomaterials started more than twenty years ago with the aid of different methods and technologies, i.e. self-assembling, soft lithography, microprinting, electrospinning, microfluidic, among others, and, more recently by means of templating methods. The development of these processes allowed to reproducibly fabricate different polymer nanostructures, such as, nanoparticles, thin films, nanopillars, nanotubes, and even more sophisticated hierarchical shaped structures¹.

Among templating methods, the versatility of porous anodic aluminum oxide (AAO) templates to pattern a polymer melt or solution into sophisticated polymer nanostructures with different shapes and morphologies has been a matter of research in many laboratories world-wide, as well as in our group, as a relevant method in the rapid development of polymer nanotechnology.¹ Today, it is possible to fabricate, by replication of AAO hard templates, “tailored” polymer nanostructures, such as rod-like, nanotubes, and other more sophisticated hierarchical shaped structures, such as, branched, pyramidal or nanostructured surfaces.

In connection to the fabrication of tailored polymer nanostructures by AAO templating, in the first PhD work² entitled “*Nanoestructuras Poliméricas Unidimensionales “a la carta”*”. Del

Confinamiento a las potenciales aplicaciones”, we started to widely explore the fabrication and characterization of different one dimensional (1D) polymer nanostructures. Firstly, with the setting up of an anodization laboratory for the fabrication of ordered AAO templates, we were able to fabricate a wide range of shaped-defined hard AAO devices with adjusted pore diameter and length, by using different anodization strategies. The subsequent development of **polymer infiltration methods**, mainly by wetting phenomena (complete wetting and partial regimes), allowed the preparation of the desired one-dimensional polymer nanostructures. The combination of these two strategies generated a variety of different polymer and polymer based composite nanostructures of polyvinyl fluoride (PVDF), polyethylene oxide (PEO), polyvinyl alcohol (PVA), polylactic acid (PLLA), polyvinyl chloride (PVC) and polystyrene (PS), with structural definition of size and morphology. Secondly, the investigation of the influence of confinement effects on the physical properties, such as crystallization and molecular dynamics of different polymers, confirmed that crystallinity and perfection of crystal (nucleation and growth processes) were significantly altered when the polymer is confined in the AAO nanocavities. Thirdly, of special interest were the results concerning the study of nanostructured polymer materials such as 1D magneto-polymeric nanostructures and nanostructured matrices based on PLLA substrates used as synthetic extracellular matrices of quasi-three dimensional scaffolds.²

Due to the great interest and relative success of this kind of polymer nanomaterials, then, it was undertaken the PhD work³ entitled “*Fabrication of Polymer Nanostructures by “Template Synthesis” and Polymer Properties under Confinement*” with the aim of expanding the acquired knowledge on the fabrication methods of AAO templates. This 2nd PhD work was, in some ways, the continuation of the previous one but new strategies and requirements were introduced. The main purpose was to extend and if possible to generalize the influence of polymer confinement on the polymer properties and, to test the feasibility of new polymer composite nanostructures for technological applications. Briefly, the most important contributions were i) the fabrication of ordered AAO templates of diameter up to 400 nanometers, never done in the laboratory before, and the preparation of polymer nanospheres and nanopillars, by solution wetting and capillarity infiltration methods, thus opening the range of production of polymer nanostructures from porous alumina templates; ii) the effect of confinement on the crystallization process of different polymers was confirmed. Moreover, the mechanism of nucleation and growth was suggested to be an efficient route to control the crystal orientation of nanostructures and, therefore, the polymer microstructure and iii) two types of polymer nanocomposite nanostructures, PVDF/SWCNT and PMMA/Lu₂O₃ NPs, with potential technological interest were prepared and tested³.

Apart these PhD works, in the following years, the investigations on the process of fabrication of tailored polymer nanostructures from AAO templates with potential scientific and/or technological interest continued through a Master Thesis,⁴ “*Electrically conducting polymer nanostructures confined in anodized aluminum oxide templates - From synthesis to characterization*”, and other international and collaborative projects⁵⁻⁸. A review with the most important results *on polymer nanostructures with modulated morphologies and functionalities using nanoporous AAO templates* was recently reported in the literature.¹

Nevertheless, in the preparation of polymer nanostructures by polymer infiltration in AAO templates, some drawbacks were found. For instance, in the preparation of polymethyl methacrylate (PMMA) solid nanofibers or PMMA/Lu₂O₃ NPs composite nanorods, in both cases, a long time of polymer infiltration and a high temperature was needed. On the other hand, the infiltration of polyisoprene (PI) lead to a high thermal degradation of the polymer. Therefore, the infiltration process of a polymer melt in the AAO nanocavities is not the most convenient route when i) the polymer infiltration takes very long time (days in some cases) and/or it is an energetic consuming process; ii) the polymer degrades as a consequence of the very high temperature needed for infiltration; and iii) for the preparation of nanostructures of a thermoset polymer (no melting). Thus, the exploration and development of alternative approaches to overcome the above limitations seem necessary.

A way to overcome the disadvantages of polymer infiltration methods could be the fabrication of polymer nanostructures from the in-situ synthesis of the polymer within the AAO template. As a result, the **in-situ polymerization method** of a monomer in the AAO templates emerges as an easy and direct approach to fabricate polymer nanostructures of many polymers not envisaged until the present, and being, therefore, complementary to the polymer infiltration method. In fact, when the research plan of this PhD work was set up, there were not systematic studies in the literature regarding the polymerization reaction in confinement in AAO templates. There was only a report concerning the synthesis of polyaniline (PANI) in AAO templates in which no kinetics studies neither the characterization of obtained polymer were undertaken⁹. Therefore, it seemed necessary to carried out a basic study of in-situ polymerization reaction in AAO templates. This study was tackled as an exploratory work of different mechanisms and monomers rather than a deep study on the polymerization process of a particular monomer. A short-term PhD stay carried out in the team of Prof JM Asúa BERC POLYMAT-UPV/EHU aided to this end.

Concerning the conventional preparation methods in AAO templates, the search for **innovative polymer infiltration methods** to obtain novel polymer structures via sophisticated infiltration methods and the concomitant study of size-dependency polymer properties is currently very active in the literature and in our group. In order to increase the knowledge on the conventional infiltration method in AAO templates along this PhD period, it was tackled an exploratory work for the preparation of three different hierarchically nanostructured polymers, each of them for a particular purpose. For instance, with the objective to study the polymer crystallization under no influence of AAO walls, the surface of the alumina nanopores was covered by an amorphous polymer through a double polymer infiltration method. Similar methodology could be applied to prepare metallic polymeric material. The combination of AAO templates with soft lithography methods proposed during the short-term PhD stay carried out in the group of Prof A del Campo, Max Planck Institute, Mainz.

Taken into account the challenges and opportunities that AAO templates offer to study and develop new polymer nanostructures, **the general objective** of this PhD work is to *Develop new fabrication routes to prepare polymer nanostructures, by in-situ polymerization and by the combination polymer infiltration methods, from AAO templates*. So, it represents a new step in the development of polymer nanostructures in which new strategies and requirements have been introduced. To achieve the requisites, a general methodology was developed in our laboratory. In the case of *In-situ Polymerization in AAO Templates* it was planned, firstly, to control the polymerization process to obtain polymer nanostructures of defined size and shape, either from free-radical or step-growth polymerization of selected and appropriate monomers and to compare the results (the discrepancies) with polymerization in bulk. Secondly, the implementation of a model that could explain the influence, if any, of confinement effects on the polymerization kinetics and on the molecular weight when the reaction is carried out in AAO “nanoreactors”. In the case of *Polymer Infiltration in AAO Templates*, it was planned to develop new methods to obtain sophisticated structures that enlarge the catalog list of polymer nanostructures offered by our laboratory. In particular to obtain new polymer morphologies such as, new core/shell polymer/polymer nanostructures that could help in the comprehensive understanding of fundamental problems or core/shell metallic/polymer nanostructures with emphasis on potential applications and new polymer micro-nanostructures.

For this PhD work, methylmethacrylate has been selected as a suitable monomer of gel effect free-radical polymerization; perfluoroacrylate acrylate as a suitable monomer of non-gel effect free-radical polymerization, and a diol and a diisocyanate as suitable monomers of step-growth

polymerization studies. Based on the previous experience of the group, for studies of preparation of new morphologies by polymer infiltration processes, PCL has been selected as appropriate core polymer and PS for the shell. For micro-nanostructures PCL and PDMS has been selected as appropriate polymers.

In order to get the general objective of the PhD work "*Advances in Patterned Polymer Nanostructures. In-situ Polymerization and Polymer Infiltration in AAO Templates*", the manuscript is structured in 8 chapters, corresponding two of them to introductory sections, four of them to main objectives of the PhD work, one to the general conclusions and an Annex to describe an exploratory work about atom transfer radical polymerization (ATRP).

The first chapter, *General Introduction and objectives*, intends to establish the scientific framework in which the present work is carried out.

The second chapter, *Brief state of the art*, is mainly devoted to the state of the art of *Polymerization in confinement in different materials*: AAO nanotemplates, controlled pore glasses (CPG), mesoporous silica, and metal organic framework (MOF). Moreover, it also includes a brief summary of the main characteristics of the AAO templates and a brief summary of the last works reported on polymer infiltration process.

The third chapter, entitled *Preparation of AAO Templates*, gives a detailed description of the fabrication of Anodized Aluminium Oxide (AAO) templates used as nanoreactor or nanomolds in the following chapters. It includes a brief description of the main characteristic of alumina templates.

The fourth chapter, entitled *Radical Polymerization of MMA in AAO Nanoreactors*, describes the study of **free radical polymerization** of methyl methacrylate in bulk and in confinement in AAO nanoreactors. It includes the methodology followed to synthesize PMMA nanostructures, the kinetics of reaction and the modelling of radical polymerization. A mathematical model is implemented to perform the results concerning reaction kinetics and molecular weight of the obtained polymer on the basis of confinement effects. Moreover, a brief characterization of the obtained PMMA nanostructures is also reported

The fifth chapter, entitled *Radical Polymerization of Hydrophobic FA in AAO Nanoreactor*, describes the study of **radical polymerization** of a perfluoroacrylate acrylate (FA) monomer and follows a similar methodology to that of the previous chapter, that is, polymer synthesis, reaction kinetics and modelling of polymerization reaction. It also includes the wettability study of PFA polymer surfaces.

The sixth chapter, entitled *Step Polymerization of Diol and Diisocyanate in AAO Nanoreactor*, describes the study of **step-growth polymerization** of a dialcohol and a diisocyanate and also follows a similar methodology to the previous chapters, that is, synthesis, polymerization kinetics study and modelling of polymerization reaction to discuss the results on the basis of confinement effects.

The seventh chapter, entitled *Polymer Infiltration. Advances in Novel Nanostructures*. This chapter contains three sections. Every section describes the fabrication of a new combined nanostructure, such as, Polycaprolactone-Polystyrene (PCL-PS) core-shell nanocylinders, Nickel-Polystyrene (Ni-PS) magnetic flexible nanowires and Polycaprolactone-Polydimethylsiloxane (PCL-PDMS) nano-micro patterned structures. For each particular purpose, a different property of the polymer nanostructure has been characterized and studied.

The eighth chapter, entitled *General conclusions and perspectives*, summarizes the most general conclusions of the work and proposes new subjects of research in this field

The manuscript also includes an Annex Section describing an exploratory attempt to prepare polymer nanostructures by ATRP polymerization. A Reference Section, reported along the chapters, including more than 300 references related to the most relevant and updated works on *In-situ Polymerization and Polymer Infiltration methods in AAO Templates* and finally an Abbreviation Section and the List of publications obtained from this PhD Thesis.

REFERENCES

1).- *A review on the progress of polymer nanostructures with modulated morphologies and functionalities using nanoporous templates.*

C Mijangos, R Hernández and J. Martín

Progress in Polymer Science, 54-55, 2016, 148-182

2).- *Nanoestructuras Poliméricas Unidimensionales “a la carta”. Del Confinamiento a las potenciales aplicaciones*

PhD work, Jaime Martín, 2010.

Universidad Complutense de Madrid.

3).- *Fabrication of Polymer Nanostructures by “Template Synthesis” and Polymer Properties under Confinement*

PhD work, Jon Maiz, 2013.

Universidad UPV/EHU, San Sebastián-Donostia.

4).- *Electrically conducting polymer nanostructures confined in anodized aluminum oxide templates - From synthesis to characterization*

MD work, Vincent Desmaret, 2013.

University of Louvaine, Louvaine, Belgium

5).- *Producción a escala comercial de de polímeros con morfologías nanoscópicas aplicables en biotecnología*

MICINN-PRI-PIBAR-2011-1400, 3 years, Proyecto Internacional España-Argentina.

6).- *“New developments on nanostructured and functional polymers and gels for technological applications*

MICINN-MAT 2011-24797, 3 years.

7).- *Nanomateriales poliméricos con morfologías y funciones definidas mediante templating (extrínseco) y autoensamblado (intrínseco)*

MINECO-MAT 2014-53437-C2-1P, 4 years.

8).- *Nanostructured polymer and functional polymer-based materials and nanocomposites*

Action to support active NoE , VII EU, “NMP.2011.4.0-5 Support.

9).- *Template-Synthesized Polyaniline microtubules*

R.V.Parthasarathy and C.R. Martin, Polymer Chemistry 1995, 6(10), 61-68

Chapter 2

STATE OF THE ART

The second chapter mainly describes the state of the art of polymerization in confinement. It also includes the key concepts about AAO templates and polymer infiltration process.

2.1. Porous Anodic Aluminium Oxide Template (AAO)

Nanotechnology is currently one of the most studied scientific areas. Nanomaterials made of oxides, metals, semiconductors, piezoelectric and polymers have demonstrated great potential for applications in different fields of science like catalysis, electronics, energy storage or drug delivery¹. Among them, one-dimensional nanostructures, such as nanowires, nanotubes and nanorods, have become subject of great scientific interest.

Polymer nanostructures can be achieved by the application of different techniques namely lithographic, electrospinning or self-assemble techniques. Nevertheless, these techniques have some major disadvantages. For instance, via lithographic techniques low aspect ratio (the ratio of length to diameter) nanostructures can be solely produced, the patterned area is limited to few square mm and the cost of manufacturing is high.^{2,3} Electrospinning does not offer precise control over the fiber diameter and diameters smaller than 100nm are difficult to achieve, not the mention that, the obtained nanofiber mat presents a low degree of organization.⁴ In the case of self-assemble techniques, because the polymer compound must have the intrinsic ability to self-organize, the range of patternable the materials is limited.⁵

In the last years, the demand for highly ordered nanostructures has been accomplished with the aid of the anodic aluminium oxide (AAO) template, i.e. AAO templates are used as a pattern for the creation of nanostructures. The synthesis of polymer materials in confinement on the pores of anodic aluminium oxide template has propelled the rapidly increasing interest of hierarchical systems with potential applications. Anodic aluminium oxide template has been investigated and utilized in the preparation of many different polymer and polymer based nanostructures.

AAO templates consist of a dense array of columnar hexagonal cells with central cylindrical, uniformly sized pores. The pore diameter size can cover almost the entire range from 10-400nm, and densities as high as 10^{11} pores/cm² can be achieved. As will

show in chapter 3, these templates are prepared by a two-step anodization process of aluminium in an acidic electrolyte.

In 1995 Masuda and Fukuda⁶ reported a major advance for the preparation of AAO. Since then, various works have been developed to improve the fabrication process of porous alumina templates. There are several ways to obtain AAO templates, but the most important are by mild and hard anodizations. The mild anodization (MA) is the conventional way to produce self-ordered pore structures in a laboratory, but is a slow process with a narrow range of processing conditions.⁷ The hard anodization (HA) is widely used in the aluminium industry, is faster, but it produces disordered porous structures.⁸ Later, Lee and co-workers developed a new process from the combination of both anodizations called pulse anodizing. This method combines the advantages of the mild and hard anodization processes to fabricate well-defined nanoporous alumina membrane sheets and a novel three-dimensional nanostructures.⁹ Very recently, a review about the anodization and templated synthesis of functional nanostructures was reported by Woo Lee and Sang-Joon Park.¹⁰ They presented the last developments of various anodization methods (mild, hard, pulse, cyclic and guided anodization), the diameter, density and aspect ratio of pores that can be tightly controlled by appropriate selection of the anodizing conditions.

Currently, the focus of the research is centered on self-organized nanostructured materials with a periodic arrangement of nanopores, due to the high expectations regarding their applications. The AAO template synthesis derived from different approaches seen previously will further expand the field of application, therefore the uses found for the templates are numerous.

Over the past decade, several applications have appeared about AAO membranes such as separation, biomedical, chemical/biological sensing, and electronics. These four fields of research have been studied for different applications. These applications have been collected in more details by Jani *et al.*¹¹ in a recent review. Figure 2.1 shows a scheme of AAO template being applied in advanced applications across a wide area, including sensing (chemo and bio), molecular separation, catalysis, biomedical applications for local drug delivery, implants and cell growth, molecular electronics, optics, photonics, solar cells, fuel cells and energy store.

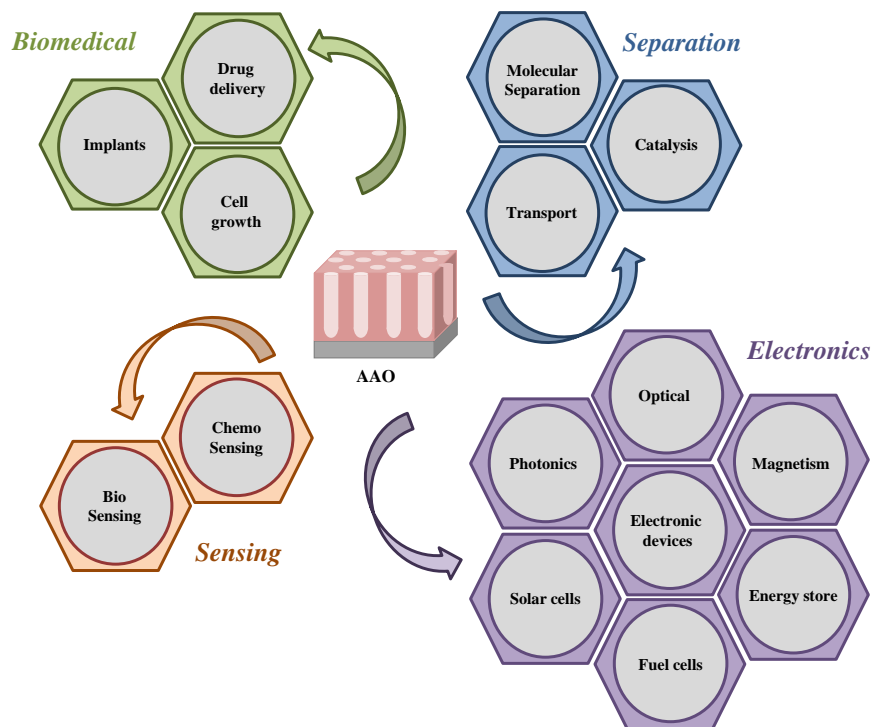


Figure 2.1. Scheme of the typical AAO structure and the major applications. Modified figure from Ref. ¹¹

The importance of the AAO membrane for *separation applications* in selective molecular transport, is that its parameters, such as, pore diameters, narrow pore distribution, high porosity and surface chemistry can be controlled. In fact, AAO templates have been applied for separation tasks including separation of multivalent ions, proteins, amino acids and DNA. AAO membranes with high surface area per unit volume and chemical inertness are ideal platforms for catalytic applications. Numerous studies have focused on the placement of various catalytic active components, including metal, metal oxide nanoparticles, organic catalysts or enzymes inside of AAO nanopores.^{12, 13} Moreover, both catalytic and molecular separation applications can be combined in AAO. For instance, Stair *et al.* prepared a catalytic membrane by depositing 10nm of alumina by atomic layer deposition into an AAO with 40nm pores. Subsequently, a single vanadium monolayer was deposited by wet impregnation using ammonium metavanadate. Oxidative dehydrogenation of cyclohexane and benzene through a V_2O_5 coated AAO membrane showed high catalytic activity and selectivity.¹⁴

The main *biocompatibility* studies that have been performed on nanoporous AAO are related to in vitro cell culture studies and applications as orthopedic implants.¹⁵⁻¹⁷ Bones are a naturally occurring porous ceramic material composed of nanosize organic and

mineral phases that forms a hierarchical macrostructure. In previous studies using oxide ceramics with porous surfaces of 100 μm of diameter, it was observed that the size was the main factor for the bone growth to maintain blood supply to the connective tissue. Lately, La Flamme *et al.* found that AAO membranes have smaller pores permitting the bone growth.¹⁸ AAO template has also become in excellent candidates as nanostructured substrates for cell-interface studies due to its biocompatibility, increased surface area and the possibility to tailor this nanomaterials with a wide range of surface modifications. Dorothea Brüggemann summarized surveys on cell adhesion and proliferation on different AAO nanopore geometries and surface modifications and reported that the employ as implant, coculture substrates or immunoisolation devices can be used as future applications in biotechnology and medicine fields.¹⁹

In recent years, a variety of nanoscale materials has been investigated for drug delivery applications. Mainardes *et al.* studied by means of AAO templates how to deal with problems associated with conventional drug therapies such as limited drug solubility, poor bio distribution, lack of selectivity and unfavorable pharmacokinetics.^{20, 21} Manzano and coworkers²² reported that systems based on ordered AAO mesoporous structures with good mechanical stability, chemical inertness, biocompatibility and controllable pore size and volume are excellent platform for loading large amount of drugs and facilitate their controlled release.

Fan *et al.* studied the main advantages of using nanoporous AAO as a device for *chemical and biological sensors*. The principal characteristics of this template are their chemical inertness and the large surface area.²³ Moreover, the reasonable transparency of AAO membranes in the UV and IR regions has allowed direct detection by the absorbance in transmission mode. Various biomolecules such as proteins, enzymes, antibodies, DNA and whole cells have been selected to develop optical biosensors on the pores of AAO.

Optical sensing applications have been studied by Kumeria *et al.* The ability to engineer the structure and surface chemistry of AAO and its optical properties have led to the establishment of distinctive photonic structures. Moreover, AAO templates are explored for developing low-cost, portable, rapid-response and highly sensitive sensing devices in combination with Surface Plasmon Resonance (SPR) and Reflective Interference Spectroscopy (RIFS) techniques, for optical sensing and biosensing devices.²⁴

Others emerging applications focused on *electronic* topics, such as fuel cells, solar cells,²⁵²⁶ molecular junctions and photonic crystals using AAO substrates have increased their interest. For example, Banerjee *et al.*²⁷ fabricated the AAO based metal-insulator-metal (MIN) nanocapacitors for energy storage. They also deposited the sequence of TiN-Al₂O₃-TiN multilayer structures on AAO by atomic layer deposition.

All of these mentions works are examples of different applications that can be found in the AAO templates, but the use is not limited to the devices since they can also be used as host materials.

The use of AAO template as host material attracted the attention of scientists in the area of nanotechnology since 1995, when Masuda *et al.* reported the use of the AAO as negative structure followed by the formation of the positive structure with gold metal resulted in a honeycomb metallic structure.⁶ The tuneable structural features of porous AAO have been intensively exploited for synthesizing a diverse range of nanostructured materials in the forms of nanorods, nanowire and nanotubes and also for developing functional nanodevices. Moreover, many types of nanocomposites have been fabricated with anodic alumina used as a host material.

In the last years, numerous reviews about nanostructures obtained from this template have been published. For example, several articles are focused on the magnetic properties of ferromagnetic nanowires and nanotubes. Wang *et al.*²⁸ collected investigations about the synthesis of these materials inside the pores of the ordered anodic aluminium oxide membranes. Authors reported that the diameter, orientation and crystal structure of ferromagnetic nanowires and nanotubes can be controlled using the AAO templates by changing deposition parameters in the process of direct-current electrochemical deposition. The corresponding magnetic properties can be controlled according to the structure and morphology of the one-dimension magnetic nanomaterials.

In 2006, Lee *et al.*²⁹ reported a review about the synthesis of porous carbon material, using anodic aluminium oxide as a template to create one-dimensional carbon nanostructured materials. Niko Haberkorn carried out a wide work about the synthesis of organic and hybrid materials in anodic alumina membranes to find applications in optoelectronic devices.³⁰

In 2011, Platschek *et al.*³¹ emphasized the great progress about understanding the different synthetic processes and the structure formation mechanisms relevant for the preparation of host mesostructured materials within porous alumina. Potential functionality and applications include molecular sieves or host materials for the inclusion of conducting or semiconducting nanostructures. Moreover, the fabrication of AAO templates has also interested in the design of heterogeneous 1 D nanostructure array for energy applications. Wen *et al.*³² reported how to develop efficient energy-conversion-storage devices via optimizing the compositional morphological parameters of the heterogeneous 1D nanostructure arrays.

Nowadays, nanoporous AAO templates have typically been used in the polymer field with two general objects, for the polymer nanostructure fabrication by replication using the AAO as host material and as a confining medium for the study of low dimensionality effects on the properties of polymers. The polymer template synthesis is widely studied and developed by many different groups, such as Steinhart³³⁻³⁶, Russell^{37, 38}, Gösele³⁹⁻⁴¹, Chen⁴²⁻⁴⁴, Wendorff^{41, 45}, Jin⁴⁶⁻⁴⁸, Wang^{49, 50} and more recently by our group. Very recently a completed review about AAO templates describing polymer nanostructures with modulated morphologies and properties was reported by Mijangos *et al.*,⁵¹ This review summarizes the hundreds of works reported in the literature to fabricate nanostructured materials from polymers and polymer based composites, prepared by template synthesis method using anodic aluminium oxide templates (AAO) as nanomold and nanoreactor.

As such, there is no doubt that AAO membranes play and will continue show an important role in the nanoscience. In this PhD work, the use of anodic aluminium oxide template has been chosen for two aims: i) as nanoreactors to study polymerization in confinement and ii) for the fabrication of nanostructured polymers and the study of its corresponding properties.

2.2. Polymerization in confinement

Nowadays, high performance functional polymers have become in an interesting material in modern society. By the end of 2014, nearly 311 million tons per year of plastic materials are estimated to be produced worldwide.⁵² These polymers are closely related to their chemical structures, molecular weight and molecular weight distribution and these parameters are controlled by the polymerization process. Moreover, the chemical reactions

are strongly sensitive to the reactions environment due to the highly reactive species, such as radicals, anions, cations, or the impacting factors, including reaction medium, concentration, catalysts, molecular diffusions/interactions and so on.⁵³

In the biological events, natural polymers are produced by enzymatic catalysis, where stereoselective, regioselective and chemoselective polymerizations are developed within regulated and well organized molecular scale spaces.⁵⁴ Therefore, to create these elegant systems, scientists have used channel structures,⁵⁵ layered materials⁵⁶ or nanolevel templates⁵⁷. In some cases, the need to design uniformity within the pore size, shape and volume has increased over the last years since it can lead to superior application properties.

In polymers, there are different polymerization mechanisms, such as, free radical, step-growth and ATRP polymerization reactions that will be briefly mention because they will be study in confinement.

The free radical polymerization is one of the most widely used polymerization method in synthetic polymer chemistry and accounts for about a half of industrial production of common polymers, because of it is relatively easy to introduce on an industrial plant, it is compatible with water and it could accommodate a wide variety of functional monomers.^{58, 59} This kind of polymerization is defined by three processes: slow initiation, very fast propagation and fast termination. The chain propagation is the most relevant step to the generation of radical species, which is very short. Finally, the reaction ends via combination or disproportionation termination leading to “dead chain”. Therefore, the continual propagation of neighbouring monomers could not be reached.⁵⁸ Moreover, there are some important characteristics of the free radical bulk polymerization such as the presence of diffusion controlled, the cage effect, the glass effect and the gel effect that also affect the reaction kinetics, as well as the molecular weight and the molecular weight distribution of the final product. The cage effect is determined by physical and transport properties of the reaction mixture.⁶⁰ In the case of glass effect, the propagation rate decreases due to the decrease in the mobility of monomer molecules and the propagation rate constant becomes diffusion controlled.⁶¹ The gel effect or Trommsdorff-Norrish effect affects to the viscosity, when the conversion increases the viscosity of the reaction mixture also increases but the diffusion of the free radicals decreases leading a faster propagation rate instead of termination rate. The results of these effect is a broader molecular weight

distribution of the produced polymer.⁶² Methyl methacrylate is a typical monomer that show up these effects and therefore it will be study more deeply in this work.

The polymerization of free radicals is carried out mainly in bulk or in solution phase and under these conditions the obtained products are of low molecular weight and with poor control of the structure. All of these questions do not easily allow the control over properties such as tacticity, chain sequence, molecular weight and its distribution, which are an important topic for both industrial and academic worlds. Nowadays, there are two ways to resolve these problems: increasing the lifetime of radicals (enough time for the propagation chain) or improving the initiation rate (all radicals propagate simultaneously). One strategy is to obtain reversible activation-deactivation of propagation radicals in a catalytic way: for example by atom transfer radical polymerization (ATRP)⁶³, or by stable radical mediated polymerization (SRMP)⁶⁴. On the other hand, another strategy is to apply degenerate transfer between propagating radicals and dormant species based on a chain transfer reagent: for example by reversible addition-fragmentation chain-transfer polymerization (RAFT)⁶⁵. All of these methods have greatly changed the synthesis of the polymerization reaction because can control the structure of polymer with very narrow molecular weight distribution (1.1~1.5) and well-defined block copolymer. However, it still cannot meet the requirements well, due to it introduces residual halide as impurities and the catalysts are relatively expensive.⁶⁶

Other type of polymerization reaction is the step-growth polymerization. In this mechanism bi-functional or multifunctional monomers react to form first dimers, than trimers, longer oligomers and eventually long chain polymers. The slow build-up of molecular weight is the primary disadvantage of step-growth polymerization. Due to the nature of this mechanism, it is necessary to reach high conversion of reaction to achieve high molecular weight. Moreover, if the polymer is soluble and the reaction employed is of high yield, a high polymer can be obtained. However, if the oligomers precipitate before they react with another, or if the yield of the reaction is low, the degree of polymerization may be very low. This problem is often found in the synthesis of conjugated polymer.⁶⁷ This kind of reaction in confinement has been poorly studied. Recently, studies have revealed that this reaction is much faster in confinement. Also, kinetic curves follow an exponential trend suggesting a strong reduction of the initial part of the step-growth polymerization and the Tg depression appears to be nonlinear function of inverse confinement size.^{68, 69}

Template synthesis is an efficient preparation method to obtain ordered nanopores. Each of these nanocavities can be viewed as a reactor, in which one-dimensional nanostructure of desired material can be synthesized, only depending on the pore form and the size of the template. Up to now, several kinds of porous materials such as microporous zeolites, mesoporous silicates, clays, etc., have been used as hosts for the synthesis of functional polymer with controlled structures.^{55, 57, 70} These systems can provide internal spaces large enough to hold diverse monomers in a highly systematic manner.^{71, 72} Moreover, the geometrical constraints of the well-defined nanochannels structure affect the pattern of monomer insertion and chain growth process, which offers a way to control the polymer chain structures and its macroscopic morphologies.^{73, 74}

There are several important structural characteristics of porous materials that should be described, such as pore geometry, pore size or pore surface functionality. The pore geometry includes tubular, spherical or network-type morphologies, that can be disordered or assembled into ordered arrays. The pore size, as said before, is an important parameter since pores with a smaller size produce materials with high surface area. The pore surface functionality can be designed by post modification processes or through the use of functional monomers.^{75, 76} The possibility to control the structure pores and the functionality into the porous materials has improved the study of polymerization reaction.

The SCOPUS® search providing the data in Figure 2.2 was drawn over the broad classifications of “polymerization in confinement” as a function of the year of publication. The study of the polymerization reaction in confined spaces has been increased because this phenomenon needs a comprehension that demands further investigation. The last year, 2016, is not completed the total number of publications of whole year.

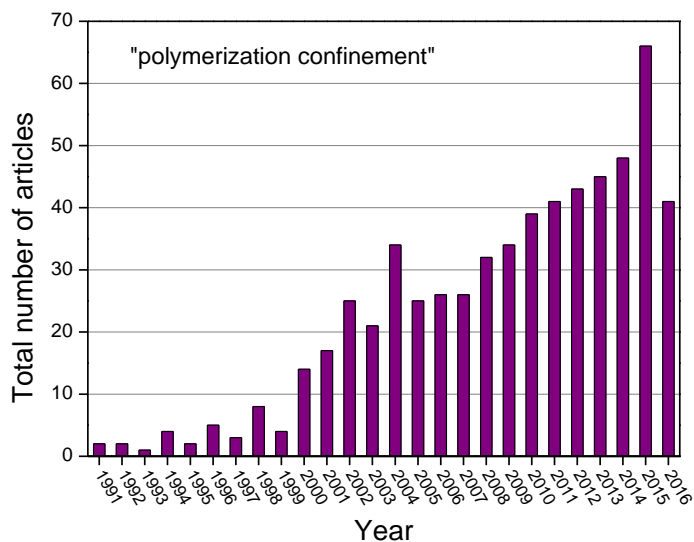


Figure 2.2. Total number of articles and reviews published on the topic of Polymerization Confinement since 1991. Data source: SCOPUS®.

2.2.1. Polymerization reaction in Porous materials

At the end of the 20th century, significant advances were achieved in the fabrication of new porous solids with ordered structures for a wide range of different materials. Henceforth, we include a brief description of the works based on polymerizations reactions within the following porous materials: mesoporous silicas, metal-organic framework and controlled pore glasses.

Mesoporous silicas

In 1992, researchers of the company Mobil Oil patented and subsequently published⁷⁷ a new family of mesoporous materials called M41S characterized by having a regular pore system in the range the mesoporous and narrow pore distribution. The formation of these materials was based on the use of surfactants as structure directing agents. The synthesis of these materials was the beginning of the preparation of new catalysts controlled porosity within the range of mesoporous. Mobil Composition of Matter (MCM) is the initial name given for a series of mesoporous materials. A member of this family of materials is the number 41 (MCM-41). This material is characterized by a regular hexagonal arrangement of cylindrical pores, with a diameter size between 2.5-6 nm and a sharp pore distribution. The inorganic walls are generally microporous and constituted by amorphous silica.⁷⁸ From the same family of materials (see Figure 2.3) is the solid MCM-48 that consist of a

cubic mesophase crossed by intertwined three-dimensional channels and the uncalcined solid MCM-50 which consists of a layered mesophases. Both are less widely used than MCM-41.⁷⁹

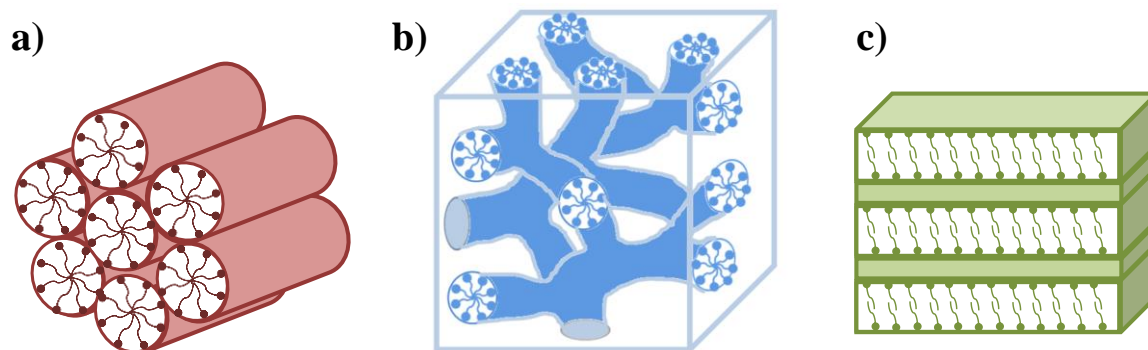


Figure 2.3. Schematic diagram of the M41S materials: a) MCM-41 (hexagonal), b) MCM-48 (Cubic) and c) MCM-50 (layered).

In 1998, Zhao *et al.* performed the synthesis of a new mesoporous material obtained in acid media, called Santa Barbara Amorphous or SBA-15.⁸⁰ The characteristics of the SBA-15 structure are defined by a system of unidirectional channels of uniform size between 4.6 and 30 nm hexagonal packed with heavy wall thickness (3.1 to 6.4 nm). The main differences of this material with respect to MCM-41 structure are the larger pore size and wall thickness, giving them greater thermal and hydrothermal stability, and high physical strength, something that also provide mechanical steadiness.⁸¹

These mesoporous silicas, MCM-41 and SBA-15, are used as templates for carrying out polymerization reactions. Wu *et al.* described the polymerization of aniline into the 3nm wide hexagonal channel system of the MCM-41, obtaining polyaniline filaments of high conductivity.⁸² In 1997, Ng *et al.* reported the free radical polymerization process of methyl methacrylate (MMA) within the uniform channels of the mesoporous zeolite MCM-41 at 100°C to give a high molecular weight polymer. The formation of long-living propagating polymer-radicals was detected by electron paramagnetic resonance (EPR), and the molecular weight of PMMA controlled over a wide range by changing the monomer/initiator mole ratio.⁸³ Moller *et al.* also reported the polymerization of methylmethacrylate (MMA) within the pores of microporous (zeolites) and mesoporous (MCM-41 and MCM-48) materials. In this case, the conversion of PMMA was followed

by FTIR spectroscopy, observing that the polymers confined in channels show different characteristic in the behaviour of glass transition temperature with respect to bulk.⁸⁴

Later, Choi *et al.* conducted the free-radical polymerization, of various vinyl monomers, inside mesoporous silicas in order to open a route to achieve a functional polymer-silica composite material with well-defined mesoporosity. These composites obtained by in situ polymerization demonstrated that the nanocoatings remarkably enhanced catalytic activity and selectivity, as compared to that bulk polymer resins.⁷¹

At the same time, Guo *et al.* polymerized ethylene in SBA-15 supported zirconium catalyst and found that the molecular weight and melting point were much higher compared with bulk polymer. This observation indicates that the mesoporous SBA-15 can effectively control the direction and dimension of the growth of polymers in the process of polymerization, yielding polymers with improved properties.⁸⁵

Recently, Tang *et al.* have polymerized 1,3-butadiene by immobilizing salicylaldehyde cobalt complexes on the mesoporous silica nanoparticles. The nanocatalysts in combination with methylaluminoxane (MAO) showed both excellent catalytic efficiency, and dependence of the molecular weight of the poly-butadiene product with the particle size of the catalyst support.⁸⁶

Scelta *et al.* reported the polymerization of acetylene in the channels of a noncatalytic, pure SiO₂ zeolite, silica in a diamond cell, using only high pressure (~4 Gpa) as the driving force. Thus, they made the first step toward the synthesis of a new generation of conducting polymers embedded in nanostructured hosts and the development of mechanochemistry in highly confined systems.⁸⁷

In spite of the development made so far, there are still several questions that need to be solved for these host materials, such as pore size control, pore width, stability, surface functionality, etc. Therefore, the improvement of others porous materials are of interest to control the polymerizations of a wide range of monomers.

Metal-Organic Framework (MOF)

Since the early 1990s, Metal-Organic Framework (MOFs), also called porous coordination polymers (PCPs) are composed of a transition-metal ions and organic ligands. These materials have been developed owing to the scientific interest in the creation of the

nanometer-sized spaces for new studies of research and for the applications in molecular storage, gas separation, heterogeneous catalysis, etc.⁸⁸⁻⁹⁰ These materials have attracted much attention as intriguing porous materials due to their high structural regularity and diversity, control of size and shape of pores, easy modification of frameworks, high porosity and structural flexibility.⁹¹ Therefore, MOF's exhibit significant characteristic features shown in the Figure 2.4.

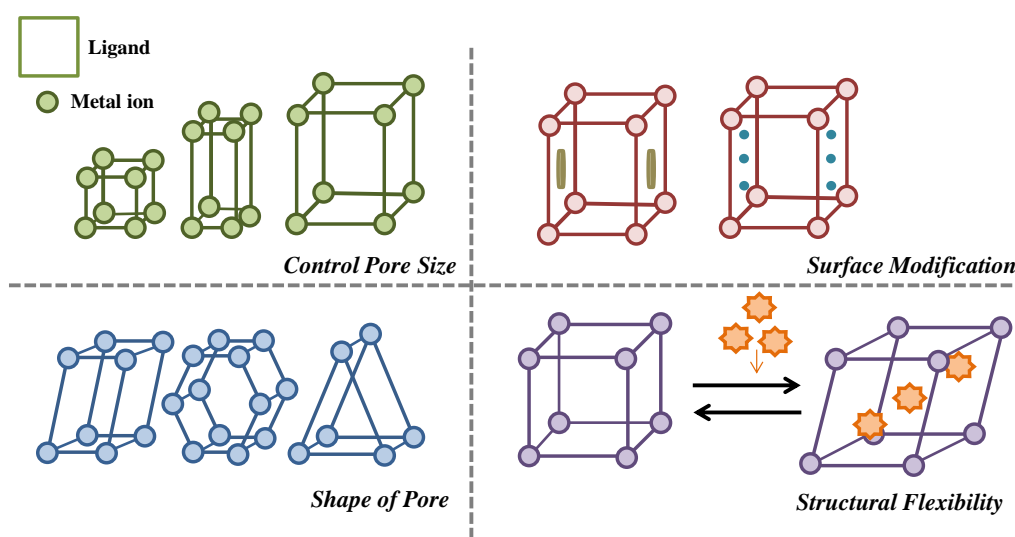


Figure 2.4. Scheme of porous coordination polymers (PCPs). Modified figure from Ref. ⁹¹

As a consequence, the polymerization within the nanocavities of these materials will be affected by the confinement effect together with the functionality of the nanopores. The pore size of MOFs is in the range of 4 to 20Å ⁹², so the confinement effect cause steric barriers for the monomer insertion and the propagation. On the other hand, MOFs with functional groups in the pores allow stronger guest trapping as well as control of the orientation of the monomer.⁹³

Kitagawa's group has studied the radical polymerization of different vinyl monomers such as styrene, methyl methacrylate, and vinyl acetate within MOFs. The principal factors to control in the free radical polymerization within MOFs can be summarized into four features:

a) Reaction pathways:

A coordination network comprising 2-vinyltriphenylene was reacted with AIBN at a high temperature, but it was observed that the radical polymerization of the vinyl monomer was completely suppressed by spatial separation and the hidden aerobic oxidation pathways

were enhanced. Nevertheless, these oxidation pathways are considerably slower than polymerization under relatively high concentration of vinyl monomer.⁹⁴

b) Molecular weight, distribution and stereoregularity:

In this polymerization system, the polymeric growth radicals were remarkably stabilized by efficient suppression of termination reactions in the nanochannels, provided by an isolated reaction environment for growing polymer radical, with narrow molecular weight distributions. Besides, the isotacticity increased in the resulting polymers.^{95, 96}

c) Properties of polymer products:

Confined molecules in nanospaces have distinctly different properties to those in the bulk state because of the formation of specific molecular assemblies and conformations. The result of the encapsulation of single polystyrene chains in one-dimension regular crystalline nanochannels was observed by molecular dynamics, where the homogeneous mobility of phenyl was significantly with lower activation energy.^{95, 97}

d) Chain sequences and compositions of copolymers:

Radical copolymerizations of vinyl monomers, such as, styrene and methylmethacrylate and styrene and vinyl acetate were examined in the nanochannels. In this system, it is observed that the composition of styrene in the copolymers prepared in the nanochannels is lower than that obtained from corresponding in bulk. The interaction potential between the molecules and the nanochannels are related to the size. This study suggest that the copolymerization in MOFs nanochannels could have a significant influence on the composition and sequence of copolymer structures by efficient through-space inductions.⁹⁸

The control in polymer primary structures is very difficult in conventional bulk and solution polymerizations. Therefore, these polymerization systems can provide a new aspect of controlled radical polymerizations and is fundamentally important for the understanding of the role of pore size and geometry.

Metal organic-frameworks have been also studied for other kind of polymerization reactions. For example, oxidative polymerization within MOFs with redox-active metal ions and fine channel structures are believed to be able to catalyse the polymerization of pyrrole and endow the linear alignment of the polymeric chains along the nanochannels, leading to polypyrrol (PPy) with much higher conductivity. Firstly, Yanai *et al.* carried out

the polymerization of pyrrole within a redox-active 2D layered MOF⁹⁹ and observed that the conductivity along the direction parallel to the sheet was 20 times higher than that perpendicular to it, showing the importance of polymeric chain alignment for polymer conductivity.

Later, Wang *et al.*¹⁰⁰ described the use of MOFs with 1 nm channels as template for the preparation of single PPy. The one-dimension polymer had a high-ordered linear structures and excellent conductivity, being five orders of magnitude higher than that of 2D PPy. The disadvantage of this process is the difficulty to scale up the redox MOFs and the difficult recovery of PPy from the template. Also, MOFs have been used in order to catalyse polymerization reaction. For that, the surface of the nanochannels is functionalized by acidic or basic sites. The use of porphyrin as catalysts is interesting topic in the heterogeneous catalysis, for example the copolymerization of cyclohexene oxide and CO₂ to produce poly(cyclohexene carbonate).¹⁰¹ However, the integration of metaloporphyrin into the nanochannels of MOFs, for the catalytic polymerizations, is a quite complicated step. The transition metal containing MOFs can be used as initiator for ring-opening polymerization reactions. Chuck *et al.* reported that titanium alkoxide based MOFs can be used as initiator for the polymerization of cyclic esters such as ϵ -caprolactone and L-lactide.¹⁰²

The progress of polymerization using MOF as template offers several advantages over the traditional methods such as the control of polymer microstructure and macrostructure (molecular weight, stereostructure, dimensions, sequence in block copolymer, etc.). However, the use of MOFs has challenges to improve. For example, the process for monomers and initiators encapsulation is labour-intensive and after polymerization reactions, the digestion of MOFs templates and recovery of polymers is also costly.⁵³ There are still varied issues that need to be solved for this perspective can be accepted in the field of polymer synthesis.

Controlled Pore Glasses (CPG)

Controlled pore glass is a silica material that includes pores, usually in the nano or micrometer range. GPC is produced from a borosilicate base material which is heated to separate the borates and the silicates¹⁰³. The original preparations and characterizations of controlled pore glasses were done by Haller.^{104, 105}

The starting material is composed of 50-75% SiO₂, 1-10% Na₂O and the remainder B₂O₃. The molten glass is phase separated by cooling between 500 and 750°C. The time taken for this treatment determines the resulting average of the pore size and the extent of phase separation. The borate phase is leached out by acid solutions at high temperatures. The remaining glass contains colloidal silica particles, which can be removed by a treatment with NaOH followed by washing with water. The final CPG with a porosity between 50-75% and an average pore size between 4.5-400nm has a surface area between 10 and 350 m²/g, depending on the pore size.¹⁰⁶

Among nanoporous materials, GPC shows many advantages, such as a high chemical, thermal and mechanical resistance, which results from a rigid and incompressible silica network and a high surface area with uniform pore size distribution. The morphology of these materials is a network of cylindrical pores, rather than isolated pores with one end closed. An easy functionalization of the inner surface opens a wide field of applications for porous glasses. For example, the CPG can be modified with hexamethyldisilazane to convert the hydroxyl groups of the surface into trimethylsilyl groups. This treatment makes the glass pores more hydrophobic and promote wetting by organic liquids.¹⁰⁷ Although controlled pore glasses were developed for use in size-exclusion chromatography, derivative glasses can show a high chemical affinity for certain biomolecules and can even be used as catalytic agents and bioreactors.¹⁰⁸ An image obtained by scanning electron microscopy of GPC sample with 300nm pores is shown in Figure 2.5.

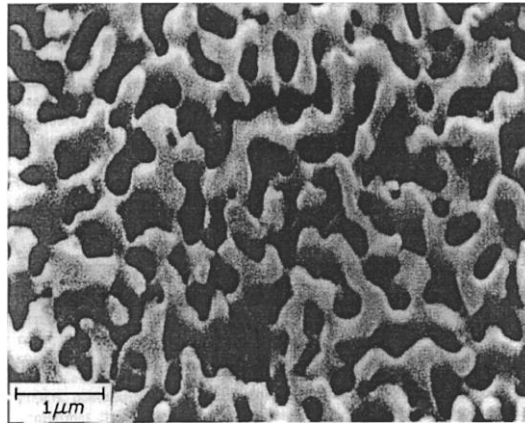


Figure 2.5. Scanning electron micrograph of controlled-pore glass of 300 nm mean pore diameter. Ref. ¹⁰⁷

This material has also been used as template for polymerization in confinement. The Simon's group started with the free radical polymerization of methyl methacrylate using the nanoporous of CPG. Firstly, Begum *et al.*¹⁰⁹ extended the model used by Verros *et al.*¹¹⁰ (2005), for free radical polymerization of MMA in nanopores. The model of Verros incorporates diffusion effects and is capable of describing the conversion and the number and weight average molecular weights of the resulting poly(methyl methacrylate) as a function of polymerization time and process conditions. The model was extended by incorporating the effect of nanoconfinement on diffusivity using the parameters reported in the literature. The calculations indicate that nanoconfinement lead to higher molecular weights and lower polydispersity and the gel effect occur earlier.

Later, Zhao *et al.*¹¹¹ used CPG with pore diameters of 13, 50 and 110nm for the experimental confinement polymerization reaction of MMA. They compared the hydrophilic and hydrophobic pores, observing that the effective reaction polymerization rate and the apparent activation energy at low conversion, before autoacceleration, are unchanged in hydrophobic pores. In the case of hydrophilic pores, the reaction rate increases in the smallest pore sizes, and the effective activation energy decreases. For both porous surfaces, the time needed to reach the Trommsdorff effect decreases with decreasing pore size, even though the effect is much more pronounced in the hydrophilic pores. The decrease in time to reach the autoacceleration is presumed to be due to the decrease in the diffusivity of the long chains under nanoconfinement with results in a decrease in the rate of termination of free radicals.

The same authors carried out a deeper study of the reaction in hydrophilic nanopores,¹¹² showing an increase in the reaction rate at low conversion before the gel point and a higher

limiting conversion with decreasing pore size. Authors suggested that the increase in initial rate and the decrease in activation energy could be due to the catalytic effect of silanol groups present on the native surface. The higher diffusion coefficients may arise from flux due to a concentration gradient because the reaction occurs favourably in the pore wall. The model on hydrophobic pores was also studied in profundity¹¹³. The kinetic model of Verros was simplified using the Doolittle free volume theory and two additional parameters, one accounting for the magnitude in the change of chain diffusivity on confinement and the other accounting for the modest increase in T_g. According to the fit of the experimental data, chain diffusivity is 20-50% of the bulk value in pores with 13nm of diameter size.

Finally, Zhao *et al.* characterized the properties of PMMA synthesized in the nanopores¹¹⁴. Gel permeation chromatography (GPC), ¹H nuclear magnetic resonance (¹H NMR), and differential scanning calorimetry (DSC) were used to characterize molecular weight, tacticity, and the glass transition temperature, respectively. The initial number average molecular weight prior to autoacceleration is similar for PMMA synthesized in the bulk and hydrophobic pore, but higher molecular weights were observed for hydrophobic pores due to higher initial reaction rates. The growth of the weight average molecular weight, M_w, follows the same trend as the growth of M_n. Hence, the final polydispersity of samples synthesized is lower than that in bulk (2.3 vs 2.5), whereas the effect in hydrophilic pores is even more pronounced (~1.5). The glass transition temperature of PMMA in the CPG increases for both porous surfaces (8K in hydrophobic and 12 K in hydrophilic) respect to the bulk polymer. Moreover, the isotacticity is found to increase in hydrophilic pores due to interaction with silanol groups at the wall surface.

Other completed study about the polymerization within CPG described by Simon's group is the curing of thermosetting resins under nanoscale constraint. Li *et al.* started the study with the isothermal curing of bisphenol M dicyanate ester (BMDC), which trimerizes to form a polycyanurate network material.⁶⁸ Differential scanning calorimetry was used to monitor the conversion during the cure and the evolution of the glass transition temperature (T_g) as a function of the diameter of GPC. Nanoscale constraint strongly accelerates the cure of bisphenol M dicyanate ester, and the acceleration factor increases with decreasing pore size. The glass transition temperature of the obtained polymer decreases up to 56 K for polycyanurate networks confined in the 11.5 nm pore diameter. A second T_g is observed in the 11.5 nm pore size, which reflects the less-mobile surface

layer in a two-layer model the lower bound of which is less than the generally accepted length scale for cooperativity.

A similar study was carried out by Koh *et al.*, with a monocyanate monomer.¹¹⁵ From isothermal reaction studies, the trimerization reaction of monocyanate ester in 8 nm pores is found to be faster as pore size decreases with an acceleration of 21 relative to the bulk reaction rate. Both the monocyanate ester reactant and cyanurate product show lower T_gs upon nanoconfinement, as compared to the bulk. The heat of reaction, activation energy, and reaction kinetic model are unchanged under nanoconfinement, suggesting that intrinsic size effects are the origin of the enhanced reactivity for the nanopore confinement.

Later, Lopez *et al.* reported a study about a monomer mixture containing the previous mono and diffusional cyanate ester.¹¹⁶ The polymerization rate in CPG of 8.1 nm pores is accelerated by 12 compared to the bulk, less than half of the observed value for the individual mono- and bifunctional monomers previously studied. This is in spite of the fact that the reaction of the mixture in the bulk case is faster than that of the individual components. The reaction is accelerated due to monomer layering on the pore surface giving changes in reactivity under nanoconfinement. The molecular weight of the produced polymer decreases a 20% in the case of the smallest pores, and the T_g is depressed by 44 K relative to the T_g of the material after extraction. The origin of the T_g depression in nanopores has been suggested to arise from intrinsic size effects and appears to be unrelated to the changes in reactivity observed for the nanoconfined monomers.

As a final conclusion, control pore glasses have been studied for the kinetics and thermodynamics of polymerization reactions in confinement. An increase in reactivity was observed with increased confinement in both free radical and step-growth polymerization reactions. In addition the results can be explained and modelled by competition between changes in local packing and diffusivity under confinement coupled with entropic and surface effects. Nevertheless, these systems are based on a network of interconnected channels therefore the results different from the nanoscale of reactors like isolated cavities. Moreover, the principal disadvantage of this system is the difficult to recover the nanostructured polymer for a resulting application.

2.2.2. Polymerization in Anodic Aluminium Oxide (AAO) template

The in situ polymerization of a monomer inside of AAO template (nanoreactor) is a method to produce polymer nanostructures, alternative to the infiltration of polymers (nanomolding). In fact, it is a complementary way to obtain tailored thermoplastic polymer nanostructures when the polymer infiltration process must be carried out at high temperature and/or for a relatively long time, from hours to days. Furthermore, it is the only process to obtain nanostructures from thermoset polymers, for which the polymer infiltration by melting is impossible.⁵¹ In the nanoporous of AAO template is possible to study the polymerization kinetics and reaction modelling in confinement, because each nanocavity is a watertight compartment and can be considered as a nanoreactor. Moreover, the dimensions of nanoporous are well-defined, easily designed and the polymer properties can be studied in confinement or extracted for testing of potential applications.⁵¹ Figure 2.6 illustrates a schematic diagram of in situ polymerization inside AAO template, from the monomer infiltration to the obtained polymer nanostructures, after removing of the template.

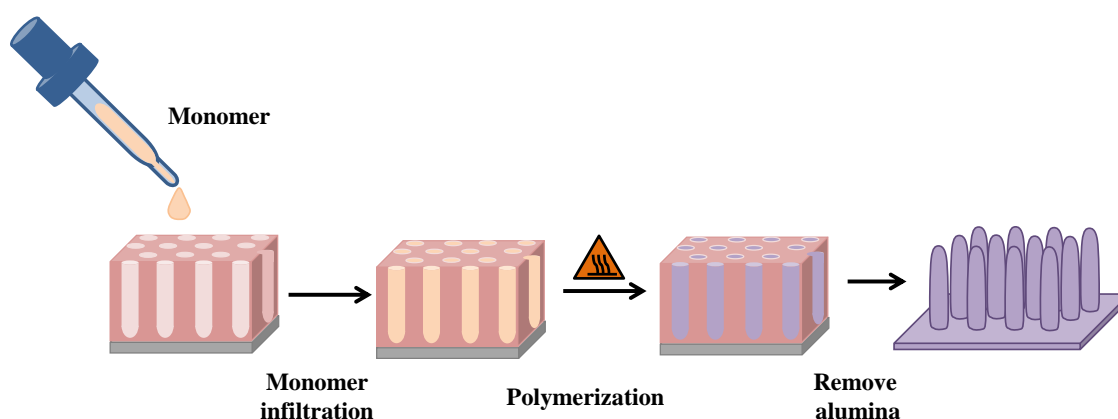


Figure 2.6. Schematic diagram of in-situ polymerization inside AAO obtaining free-standing nanorod arrays.

The first works of direct polymerization in the nanoporous of AAO were reported by Martin.^{39, 117, 118} They studied the polymerization of the polypyrrole and observed that if the monomers were polymerized within the nanopores, it was possible to adjust the wall thickness of the resulting polymer by choosing the right polymerization conditions, mainly the polymerization time: nanotubes with thin walls (short polymerization times) or thick walls (long polymerization times). For example, for polypyrrole, the nanotubes ultimately

“close up” to form solid fibrils. Hence, by controlling the polymerization time they can make hollow polypyrrole nanotubes or solid fibrils.¹¹⁹ Later, Nair *et al.*¹²⁰ carried out the fabrication of functional polypyrrole nanotubes inside nanopores of AAO, in liquid phase polymerization (LPP) conditions.

In contrast, the polyaniline (PANI) nanotubes did not close up, even a long polymerization times.¹²¹ This was explained by the fact that the surface layers eventually grow completely across the membrane surface and block the pore ends. As a result of this, the monomer and the oxidant cannot longer enter into the pores and further polymerization within the pores is not possible. Therefore, solid polyaniline fibers cannot be formed by this method. Moreover, enhancements in conductivity were observed in the confined polymers compared to bulk samples because of the polymer chains in confinement are highly aligned.¹²²

Li *et al.*¹²³ reported the synthesis of the copolymer composed of pyrrole and aniline in the pores of AAO. The microstructure study was performed by SEM and TEM microscopy and authors observed that they formed nanofiber. The result of FTIR spectroscopy and thermogravimetric analysis (TGA) indicated that both polymers were involved in the formation of a copolymer rather than in a composite.

Continuing with the aniline, Xiong *et al.* studied the highly ordered polyaniline nanotubes array prepared by in situ polymerization using AAO as nanoreactors. The doping degree of PANI nanotube is higher than that of PANI bulk sample, because the crystal form of polyaniline nanotubes makes the molecular chain of polymer arrange more ordered.¹²⁴ Blaszczyk-Lezak *et al.* also reported the enhance of the electrical conductivity by dielectric spectroscopy of polyaniline nanofibers polymerized in the nanocavities of AAO, and with Raman confocal was detected that the emeraldine salt of PANI was obtained correctly along the length of the nanopores. In this study, the polymerization rate was critical and needed to be well-controlled to achieve the desired morphology.¹²⁵

Grim *et al.*³⁴ photopolymerized an oligotheracrylate with the aid of free radical photoinitiator into the AAO hard templates at room temperature. The nanofibers were photopolymerized by UV light with a cross-linked polyacrylate film on the top of the template in order to extract the arrays of polyacrylate nanofibers from AAO hard templates by a nondestructive mechanical way. Choi *et al.*¹²⁶ reported high-aspect-ratio nanopillars of polyurethanes by reaction of a functionalized prepolymer with acrylate group acting as

crosslinker. The nanopillars do not show lateral collapse either the sticking problem between the mold and the nanopillars.

Duran and coworkers applied the optical waveguide spectroscopy (OWS) to characterize in situ the surface-initiated polymerization of polybenzyl glutamate (PBLG) within a nanoporous of 60-70nm in diameter. Thin films of Poly(γ -benzyl-L-glutamate) PBLG were surface grafted within nanoporous anodic alumina (AAO) by surface-initiated polymerization of the N-carboxy anhydride of benzyl-L-glutamate (BLG-NCA). Optical waveguide spectroscopy was able to track the PBLG layer thickness increase in situ, and ex situ FT-IR gave complementary information on the PBLG chain's secondary structure. The use of a nanoporous AAO matrix, combined with the surface grafting of a thin film of PBLG chains with multiple modifiable side chains, could potentially offer a nanoporous platform with a very high density of functional sites.^{33, 127}

Back *et al.*¹²⁸ obtained nanotubes of poly(3,4-ethylenedioxythiophene) (PEDOT) highly conductive and highly ordered by a vapor-phase deposited polymerization process in the pores of AAO membrane. These high conductivity and desirable work function of PEDOT nanotubes can provide great potential advantages for optimization of the performance of organic devices and sensors. Liu *et al.* reported the fast charging/discharging capability of poly(3,4-ethylenedioxythiophene) nanotubes by electrochemical polymerization for high-powered supercapacitor.¹²⁹ Lee *et al.* studied a functional monomer thermally polymerized inside the AAO channels into nanotubes in order to be utilized as nano-containers of Fe₃O₄ nanoparticles to form magnetic nanocomposites.¹³⁰

Other type of polymerization process in AAO templates is the photopolymerization reaction. For applications in materials science or biomedical engineering, the monomers with dianthrance polymer precursor was synthesized and used to form molecular crystal nanorods using anodized aluminum oxide templates. The polymer nanorods are flexible, resistant to breakage, insoluble in organic solvents and strong acid/base solutions.¹³¹ AAO template has been used for the synthesis of a cross-linkable siloxane-derivatized tetraphenylbenzidine (DTMS-TPD) for the fabrication of nanorods with potential application in the fabrication of multilayered divided architectures for building well-ordered bulk-heterojunction solar cells.¹³²

Likewise, there is the possibility to carry out of the electrochemically polymerization inside the AAO nanoporous. Liu *et al.*¹³³ synthesized pyrrole by electrochemically

polymerization to obtain polypyrrole nanotubes. The presence of hollow nanotubes suggests that PPy initially deposits on the surface of the pore walls.

Atom transfer radical polymerization (ATRP) and reversible addition fragmentation chain transfer polymerization (RAFT) have been used for some monomer systems in AAO templates. The possibility of combining AAO templates with controlled/"living" radical polymerization techniques leads to more controlled polymerization systems.

Polymerization process provides a special way to synthesize polymer nanotubes, especially for responsive polymers that are sensitive to the environment, such as electrical or thermal characterization, pH value or solvent. Poly(*N*-isopropylacrylamide) (PNIPAM) is an interesting thermosensitive polymer. ATRP method has been used to synthesis PNIPAM grafted on AAO templates. Li *et al.*¹³⁴ first immobilized (3-Aminopropyl)triethoxysilane (APTES) on the AAO nanoporous, followed by post-modification with initiator 2-bromoisobutyryl bromide (BIBB), and subsequently polymerized NIPAM from the surface. The grafting density of PNIPAM on AAO template was controlled by changing the density of the ATRP initiator. Several polymers and copolymers have been also synthesized by this method¹³⁴⁻¹³⁷ that is represented in the Figure 2.7.

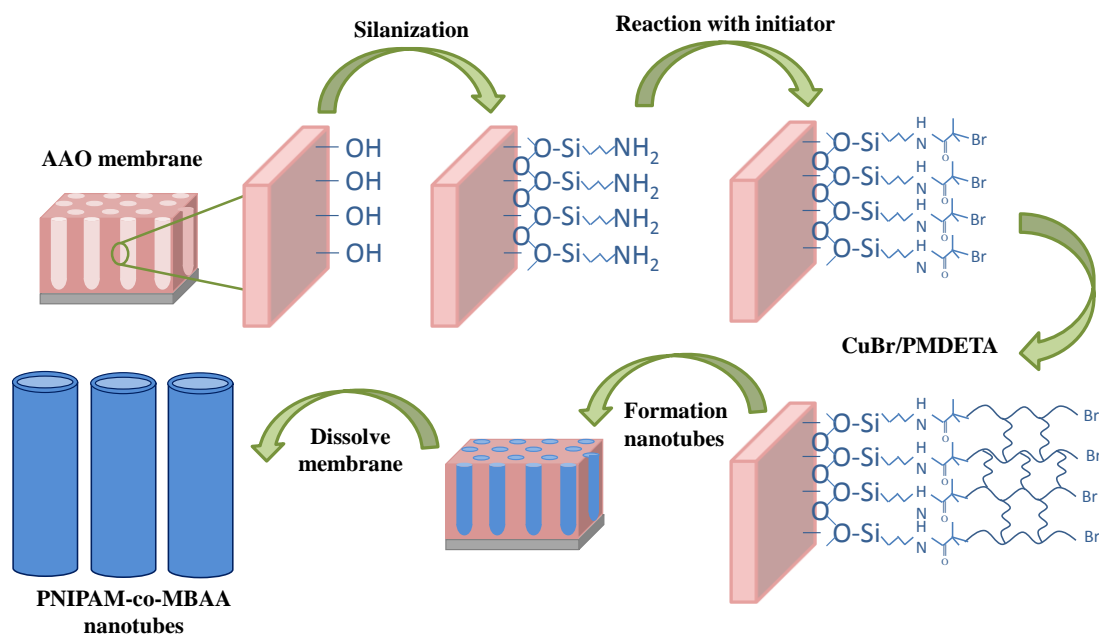


Figure 2.7. Scheme of the synthesis of Thermosensitive PNIPAM-co-MBAA Nanotubes by Atom Transfer Radical Polymerization within a Porous Membrane. Adapted figure from Ref.¹³⁵

Nevertheless, with a few exceptions, for systematic studies in the polymerization inside the AAO templates there are still many parameters to be studied, such as how the reaction kinetics is affected by the confinement and how is the chemical structure of the synthesized polymers with respect to the bulk polymerization.

Polymerization kinetics in AAO confinement

The majority of research studies about polymerization process have focused on the basic structural properties of the polymer in the template or once the AAO has been removed. A few and recent works are based on how is the polymerization kinetics within the alumina nanoporous. For example, Giussi *et al.*¹³⁸ reported the in situ polymerization of styrene inside porous AAO of 35 nm of diameter used as nanoreactors. By monitoring the monomer conversion at different times of polymerization by Confocal Raman Microscopy (CRM), it was possible to establish the polymerization kinetics in confinement. The reaction carried out in the AAO nanoreactor exhibits a value of polymerization rate almost three times higher than the reaction rate for the same polymerization conditions carried out in bulk. Authors also observed that the average molecular weight and polydispersity index are lower than those obtained for bulk polymer. Moreover, the nanoconfined PS has a greater stereospecificity, higher thermal stability and greater glass transition temperature than PS bulk.

Recently, the dynamics and kinetics of a curing epoxy system under confinement were analyzed and compared with the reaction in bulk.¹³⁹ The speed of reaction is enhanced in nanochannels, because the initial step of reaction is reduced or even suppressed. Besides, the rate of reaction is different at the surface with respect to the core of pores due to the lower reactivity of the functional units close to the pore walls. The dielectric measurements revealed that there is a characteristic change in the slope of the segmental relaxation times plotted as a function of the time of reaction under confinement. Further, a new study about radical polymerization of ionic liquid monomer in confinement has been reported by Paluch's group. They employed broadband dielectric spectroscopy (BDS) and differential scanning calorimetry (DSC) to investigate dynamics and charge transport of 1-butyl-3-vinylimidazolium bis-(trifluoromethanesulfonyl)imide ([bvim][NTf₂]) confined in native uniaxial AAO pores, in addition to study the kinetics of radical polymerization of the compound examined according to the degree of confinement. It was observed an

enhancement of the dc conductivity (σ_{dc}) and an increase in Mw, showing that this process can be tuned and controlled by the application of the appropriate confinement.¹⁴⁰

These results indicate the influence of nanoconfinement both on the polymerization and the properties of the polymer. However, considering that confinement and surface effects may not be identical for all the monomer, polymerization reaction and porous templates, it seems obvious the need of systematic studies of polymerization in confinement, polymer characterization and modelling.

2.3. Polymer infiltration process.

In the last decade, our group has been working in the development of polymer infiltration methods. Polymer infiltration process is a versatile technique for the formation of nanostructures since the size and shape of the resulting structures can be easily tuned by choosing the appropriate AAO template dimensions. Moreover, the infiltration of polymers within AAO nanopores is an interesting and versatile route to study the confinement effect on the polymer properties such as crystallization process, the conformation of the chain, molecular dynamics and so on. The direct infiltration processes are based on three different steps: a) the infiltration of the melting polymer or polymer solution, b) solidification of the distributed polymer and c) the removal of the template if necessary.

In the following, we briefly describe the infiltration process that is based on a fundamental physical phenomenon, the wetting process being the reason for the first advantage of this method. Basically, all polymer-containing liquids with a low surface energy can be processed by this way.¹⁴¹ Polymer melts or polymer solutions are infiltrated into the spaces of the templates, and the polymer is solidified within the cavities. The final structure of the obtained polymer is controlled by two main factors: the properties of the AAO templates, such as surface chemistry and pore sizes, and the properties of the infiltrated polymer, such as molecular weight, polymer chain conformation, concentration of solutions, and viscosity.¹⁴²

Normally, there is no need to modify the surface of the pores of the AAO template because metal oxide has high surface energy and almost all fluids that has a low surface energy can freely spread over inner walls of AAO^{141, 143, 144}. This phenomenon is applicable in the preparation of one dimension (1D) polymer nanostructures.

The SCOPUS® search providing the data in Figure 2.8 was drawn over the broad classifications of “polymer infiltration process” as a function of the year of publication. The study of the nanostructured polymer by infiltration in templates has been increased because this phenomenon needs an understanding that demands further investigation.

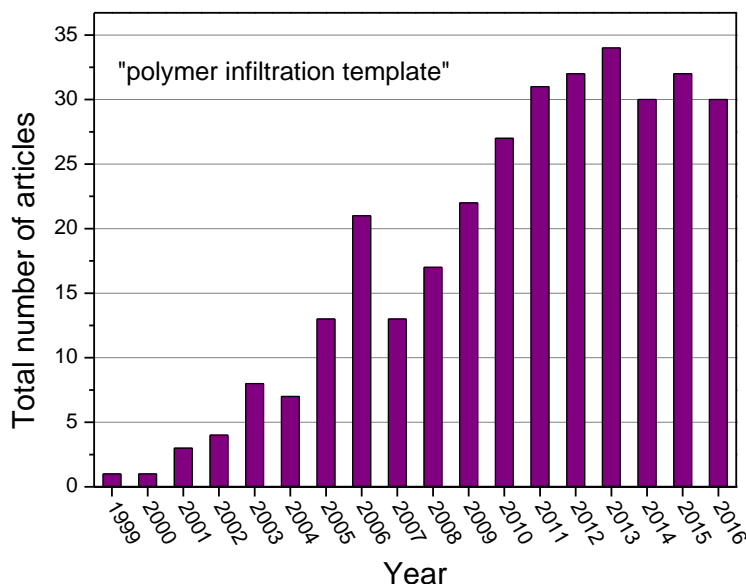


Figure 2.8. Total number of articles and reviews published on the topic polymer infiltration process in template since 2002. Data source: SCOPUS®.

2.3.1. Classification of template synthesis methods

Depending on the polymer infiltration process, Martín *et al.* classified the preparation methods in the following groups:¹⁴⁵

1. *Methods based on wetting phenomena.* This method is the most commonly used. It is based on the wetting properties of liquids onto solid surfaces, and they have the particularity of being spontaneous. Depending on the process involved in the infiltration, different methods can be considered: i) melt wetting, classified at the same time in completed wetting regime, known as precursor film method, and partial wetting regime, known as capillary method and ii) solution wetting.
2. *Methods based on applied forces.* This method has the use of external forces that are responsible of the fluid infiltration. This is used when the fluid cannot

spontaneously infiltrate into the pores because of the viscosity. Therefore, they are usually employed with polymer solutions. This method is no longer described in the manuscript.

Diagram 2.1 summarizes the infiltration methods of polymer within AAO membranes.¹⁴⁵

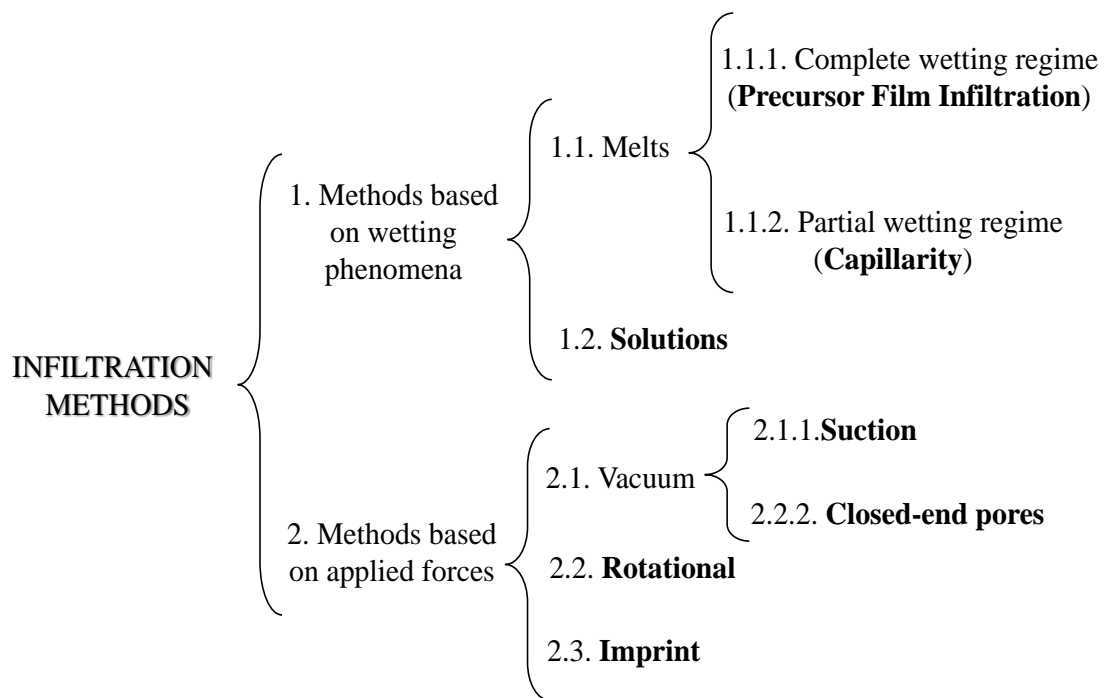


Diagram 2.1. Summary of different infiltration methods of polymer within AAO membranes. Diagram taken from Ref. ¹⁴⁵

In order to know which is the appropriate infiltration method to fabricate polymer nanostructure, Martín *et al.* reported the following advices: when is possible the use of melts, this method is preferred instead of solutions one. Usually this method is recommended in order to obtain both nanofibers and nanotubes (in both wetting regimes: capillary and precursor wetting infiltration).¹⁴⁵ Moreover, spontaneous melt infiltrations are usually more reproducible since problems related to solvents, such as evaporation time, incomplete evaporation, deficiency of material in nanotubes or nanofibers, etc. are avoided. The advantage in solution wetting infiltration process is that the number of parameters than can be adjusted is higher than in melt wetting (concentration, quality of the solvent, etc.), in this way, a higher number of characteristic parameters in the

nanostructures can be tuned, such as, wall thickness or periodic modulations in nanotubes.^{146, 147}

The main difference between the two melt-wetting methods, i.e. precursor film infiltration and capillarity, is the infiltrating time. In the precursor film method, the wetting is completed in relative short time, while the time needed for capillary action range from tens of minutes of several hours. The differences can be explained by the spreading coefficient (S), proposed by Zhang³⁷, which is defined by,

$$S = \gamma_{SV} - \gamma_{SL} - \gamma_{LV} \quad 2.1$$

where, γ_{SL} , γ_{SV} , γ_{LV} represent the solid-vapour, solid-liquid, and liquid-vapour interfacial tensions, respectively. In function of S values, the different wetting regimes can be classified:

For precursor film wetting, $S \geq 0$, where a complete wetting would occur and the liquid droplet spreads spontaneously on the pore. In the case of partial wetting or capillarity, $S < 0$, and the liquid droplet spreads on partially and eventually reached an equilibrium shape with a define contact angle.¹⁴⁸ The first case leads to the production of nanotubes or nanofibers depending on each template-polymer system and the second to the production of nanofibers.

Very recently, a new growth mechanism named two-step growth mechanism has been proposed by Yang *et al.*¹⁴⁸ The intermediate state of the polymer nanotube arrays growth process by polymer solution and melt wetting in AAO was observed and named a wax seal method. The first step is the vertical growth (formation of the precursor film) and the second step is the horizontal growth, the increase of the wall thickness. The whole growth process of the polymer nanotubes is driven by “Marangoni flow” which is caused by surface tension gradient.

In the fabrication of polymer nanotubes, precursor wetting is recommended, but in the case of possible degradation, solution wetting should be used. Recently, Ho and co-workers¹⁴⁹, Ji and co-workers¹⁵⁰ and Chen and co-workers⁴² developed the solvent-annealing-induced wetting method using AAO templates, in which the polymer chains wet the nanocavities with the help of solvent vapours. This method is also called the solvent-annealing-induced nanowetting in templates (SAINT) method. In the SAINT method, the annealing step at high temperatures is avoided and the problem of thermal degradation is resolved.

2.3.2. Polymer nanostructures from infiltration method

As has been seen previously, Martín *et al.* studied the possibility to prepare various 1D polymer nanostructures, such as, nanotubes or nanofibers by different infiltration methods.¹⁵¹ Furthermore, in this study several polymers were infiltrated with different chemical nature, such as, poly(methyl methacrylate), poly(vinyl chloride), poly(vinyl alcohol), poly(vinylidene fluoride), etc., or even polymer based on nanocomposites.

Multitude of materials, including some that until now have been difficult to use, such as PEEK^{141, 152} or PTFE^{141, 145} have been infiltrated to obtain polymer nanostructures. These polymers are insoluble in all solvents and the common polymer nanostructuring techniques such as electrospinning, spin coating, and many forms of nanoprinting techniques are not applicable methods. Template wetting also makes possible to produce PEEK nanotubes (being the melting point of the PEEK about 340°C), by melting a film of the polymer on a template surface at 380 ° C. In the case of experiments with Teflon CN (DuPont, Wilmington), it was observed that the wetting of pore walls happened at a temperature of 400°C when the polymer is moderately pressed against the template surface. The walls of the resulting Teflon nanotubes were slightly ribbed.¹⁴¹

Further, spherical polymer nanoparticles can also be obtained using AAO templates using various procedures: (i) controlling the evaporation of polymer solutions within pores.⁴⁶ (ii) promoting instabilities of infiltrated solutions and subsequent swelling of the formed nanoblock,⁴⁷ or (iii) wetting of curved polymer films in contact to a non-solvent liquid.¹⁵³

Therefore, by an adequate polymer and infiltration condition, it is possible to prepare a huge variety of polymer and polymer based composite of well-defined shape and dimensions, from nanorods, nanospheres, nanotubes, nanofibers and other systems. Recently, the combination of polymer/polymer system has been reported by Chen *et al.*⁴³ and Ko *et al.*¹⁵⁴ inside AAO templates for the formation of new polymer morphologies like nanopeapods or core-shell nanospheres. These polymer nanostructures were obtained by a double-solution wetting method and based on the Rayleigh-instability, where the shell and the core are composed of PMMA and PS, respectively.

Not only polymer systems can be infiltrated in the templates, but also multicomponent systems formed by the combination of polymer-metal can also be made into nanotubes. Thus, polymers which act as carriers in the wetting process can be mixed with inorganic

components and can be chemically transformed within the walls of the composite nanotubes. One example of this is the formation of palladium nanotubes,¹⁵⁵ where the preparation of Pd nanotubes occurs by wetting of porous templates with a mixture of palladium (II) acetate and polylactide polymer in a solvent common to both.

The following table, Table 2.1, summarizes some of the most recently polymers infiltrated in the template, the morphology of the nanostructure, infiltration method and the corresponding reference to each work. These works refer about single and double polymer infiltrations, copolymers, polymer infiltration with embedded nanoparticles and polymer/metal coaxial nanostructures.

Table 2.1. Polymers, morphology, AAO template dimension, infiltration method and conditions and references

Polymer	Morphology	AAO template (diameter/length)	Infiltration method	Conditions T ^a (°C)/ time	Ref
PP	Nanofibers	50nm/120μm	Precursor film	165-225°C/5min	156
PMMA	Nanotubes	330nm/70μm	Precursor film	250°C/2h	157
PA6	Nanofibers	200nm/70μm	Solution Wetting	RT/72h	48
P3HT	Nanowires	15-350nm	Partial wetting	260°C/45min	158
P3HT	Nanowires	15-350nm	Solution wetting	0.5wt% in CHCl ₃ 1day	158
P3HT	Nanopillars	50nm/200nm	Vacuum	230°C/10min	159
PEEK	Nanorods	120nm	Precursor film	390°C/25min	160
PLLA	Nanorods	40,75,200,385	Precursor film	225°C/3h	49
PFO	Nanowires	25, 35 and 60nm	Precursor film	200°C/4h	161
F8BT	Nanotubes	150-400nm//60μm	Solution wetting	2.5wt% in CHCl ₃	162
PS/PMMA	Core-shell Nanospheres	240nm/60μm	Solution Wetting	5wt% PSinDMF(10s) 5wt% PMMA;A.Acid(10s)	154
PS/PMMA	Nanopeapods PS spheres PMMA tubes	240nm/60μm	Solution Wetting	5wt% PSinDMF(10s) 10wt% PMMA;A.Acid(5min)	43
PS-b-PE	Core-shell nanofibers	60nm/100μm	Precursor film	180°C/5h	163
PS-b-PDMS	Porous nanotubes	150-400nm/60μm	SAINT	30°C/24h	44
PS-b-P2VP	Spiral nanofibers	200nm	Solution Wetting	RT/12h	164
PS-b-P4VP_Au	Nanorods	25-330nm	Capillarity	195°C/48h	165
PMMA_Lu2O3	Nanorods	330nm	Capillarity	130°C/1week	166
PMMA_Lu2O3	Nanotubes	330nm	Precursor film	190°C/1h	166
Ni-PA66	Core-shell nanotubes	200nm/60 μm	Solution wetting	3wt% PA66 in Formic Acid	167
Ag-PS	Core-shell nanocables	200nm/60 μm	Solution wetting	Toluene	168

Finally, it should be noted that the size of the polymer in confinement determines the physical behaviour and thus can be used to change its properties. Since the polymer molecules have nanoscale dimensions many of physical process are sensitive to the confinement. That is the case of structural features such as crystallization process,¹⁶⁹ the conformation of the chain,¹⁷⁰ enthalpy driven molecular self-assembly of block copolymers,¹⁷¹ etc. A number of dynamical processes are also affected by the reduced size, namely segmental dynamics, chain reptation or Rouse dynamical.¹⁷² Henceforth, all the polymer properties that depends on any of the physical processes are also sensible to confinement, i.e., rheological,¹⁷³ thermal¹⁷⁴ and mechanical¹⁷⁵ properties. Further studies on the effect of confinement on polymers have been reported in the review of Mijangos *et al.*⁵¹ and will not be further mentioned in this manuscript.

2.4. References

- (1). Md Jani, A. M.; Losic, D.; Voelcker, N. H. Nanoporous anodic aluminium oxide: Advances in surface engineering and emerging applications. *Progress in Materials Science* **2013**, 58, (5), 636-704.
- (2). Ito, T.; Okazaki, S. Pushing the limits of lithography. *Nature* **2000**, 406, (6799), 1027-1031.
- (3). Ji, Q.; Chen, Y.; Ji, L.; Jiang, X.; Leung, K.-N. Ion beam imprinting system for nanofabrication. *Microelectronic Engineering* **2006**, 83, (4-9), 796-799.
- (4). Lu, X.; Wang, C.; Wei, Y. One-dimensional composite nanomaterials: Synthesis by electrospinning and their applications. *Small* **2009**, 5, (21), 2349-2370.
- (5). Shimizu, T., Advances in Polymer Science: Preface. In *Advances in Polymer Science*, 2008; Vol. 219, pp IX-X.
- (6). Masuda, H.; Fukuda, K. Ordered metal nanohole arrays made by a two-step replication of honeycomb structures of anodic alumina. *Science* **1995**, 268, (5216), 1466.
- (7). Masuda, H.; Yada, K.; Osaka, A. Self-ordering of cell configuration of anodic porous alumina with large-size pores in phosphoric acid solution. *Japanese Journal of Applied Physics* **1998**, 37, (11A), L1340.
- (8). Lee, W.; Ji, R.; Gösele, U.; Nielsch, K. Fast fabrication of long-range ordered porous alumina membranes by hard anodization. *Nature materials* **2006**, 5, (9), 741-747.
- (9). Lee, W.; Schwirn, K.; Steinhart, M.; Pippel, E.; Scholz, R.; Gösele, U. Structural engineering of nanoporous anodic aluminium oxide by pulse anodization of aluminium. *Nature Nanotechnology* **2008**, 3, (4), 234-239.
- (10). Lee, W.; Park, S.-J. Porous anodic aluminum oxide: anodization and templated synthesis of functional nanostructures. *Chemical reviews* **2014**, 114, (15), 7487-7556.
- (11). Jani, A. M. M.; Losic, D.; Voelcker, N. H. Nanoporous anodic aluminium oxide: advances in surface engineering and emerging applications. *Progress in Materials Science* **2013**, 58, (5), 636-704.
- (12). Mitchell, D. T.; Lee, S. B.; Trofin, L.; Li, N.; Nevanen, T. K.; Söderlund, H.; Martin, C. R. Smart Nanotubes for Bioseparations and Biocatalysis. *Journal of the American Chemical Society* **2002**, 124, (40), 11864-11865.
- (13). Dotzauer, D. M.; Dai, J.; Sun, L.; Bruening, M. L. Catalytic Membranes Prepared Using Layer-by-Layer Adsorption of Polyelectrolyte/Metal Nanoparticle Films in Porous Supports. *Nano Letters* **2006**, 6, (10), 2268-2272.
- (14). Stair, P.; Marshall, C.; Xiong, G.; Feng, H.; Pellin, M.; Elam, J.; Curtiss, L.; Iton, L.; Kung, H.; Kung, M. Novel, uniform nanostructured catalytic membranes. *Topics in catalysis* **2006**, 39, (3-4), 181-186.
- (15). Leary Swan, E. E.; Papat, K. C.; Desai, T. A. Peptide-immobilized nanoporous alumina membranes for enhanced osteoblast adhesion. *Biomaterials* **2005**, 26, (14), 1969-1976.

- (16). Swan, E. E. L.; Popat, K. C.; Grimes, C. A.; Desai, T. A. Fabrication and evaluation of nanoporous alumina membranes for osteoblast culture. *Journal of Biomedical Materials Research - Part A* **2005**, *72*, (3), 288-295.
- (17). Popat, K. C.; Leary Swan, E. E.; Mukhatyar, V.; Chatvanichkul, K. I.; Mor, G. K.; Grimes, C. A.; Desai, T. A. Influence of nanoporous alumina membranes on long-term osteoblast response. *Biomaterials* **2005**, *26*, (22), 4516-4522.
- (18). La Flamme, K. E.; Popat, K. C.; Leoni, L.; Markiewicz, E.; La Tempa, T. J.; Roman, B. B.; Grimes, C. A.; Desai, T. A. Biocompatibility of nanoporous alumina membranes for immunoisolation. *Biomaterials* **2007**, *28*, (16), 2638-2645.
- (19). Brüggemann, D. Nanoporous aluminium oxide membranes as cell interfaces. *Journal of Nanomaterials* **2013**, *2013*, 32.
- (20). Vallet-Regí, M.; Izquierdo-Barba, I.; Colilla, M. Structure and functionalization of mesoporous bioceramics for bone tissue regeneration and local drug delivery. *Philosophical Transactions of the Royal Society A: Mathematical, Physical and Engineering Sciences* **2012**, *370*, (1963), 1400-1421.
- (21). Mainardes, R. M.; Silva, L. P. Drug delivery systems: Past, present and future. *Current Drug Targets* **2004**, *5*, (5), 449-455.
- (22). Manzano, M.; Vallet-Regí, M. New developments in ordered mesoporous materials for drug delivery. *Journal of Materials Chemistry* **2010**, *20*, (27), 5593-5604.
- (23). Fan, X.; White, I. M.; Shopova, S. I.; Zhu, H.; Suter, J. D.; Sun, Y. Sensitive optical biosensors for unlabeled targets: A review. *Analytica Chimica Acta* **2008**, *620*, (1-2), 8-26.
- (24). Kumeria, T.; Santos, A.; Losic, D. Nanoporous anodic alumina platforms: engineered surface chemistry and structure for optical sensing applications. *Sensors* **2014**, *14*, (7), 11878-11918.
- (25). Martinson, A. B. F.; Elam, J. W.; Hupp, J. T.; Pellin, M. J. ZnO nanotube based dye-sensitized solar cells. *Nano Letters* **2007**, *7*, (8), 2183-2187.
- (26). Haberkorn, N.; Gutmann, J. S.; Theato, P. Template-assisted fabrication of free-standing nanorod arrays of a hole-conducting cross-linked triphenylamine derivative: Toward ordered bulk-heterojunction solar cells. *ACS Nano* **2009**, *3*, (6), 1415-1422.
- (27). Banerjee, P.; Perez, I.; Henn-Lecordier, L.; Lee, S. B.; Rubloff, G. W. Nanotubular metal-insulator-metal capacitor arrays for energy storage. *Nature Nanotechnology* **2009**, *4*, (5), 292-296.
- (28). Wei Wang, X.; Cheng He, Z.; Shan Li, J.; Hao Yuan, Z. Controllable synthesis and magnetic properties of ferromagnetic nanowires and nanotubes. *Current Nanoscience* **2012**, *8*, (5), 801-809.
- (29). Lee, J.; Kim, J.; Hyeon, T. Recent progress in the synthesis of porous carbon materials. *Advanced Materials* **2006**, *18*, (16), 2073-2094.
- (30). Haberkorn, N.; Lechmann, M. C.; Sohn, B. H.; Char, K.; Gutmann, J. S.; Theato, P. Templated organic and hybrid materials for optoelectronic applications. *Macromolecular Rapid Communications* **2009**, *30*, (14), 1146-1166.

- (31). Platschek, B.; Keilbach, A.; Bein, T. Mesoporous structures confined in anodic alumina membranes. *Advanced Materials* **2011**, *23*, (21), 2395-2412.
- (32). Wen, L.; Wang, Z.; Mi, Y.; Xu, R.; Yu, S. H.; Lei, Y. Designing heterogeneous 1D nanostructure arrays based on AAO templates for energy applications. *Small* **2015**, *11*, (28), 3408-3428.
- (33). Duran, H.; Gitsas, A.; Floudas, G.; Mondeshki, M.; Steinhart, M.; Knoll, W. Poly (γ -benzyl-L-glutamate) peptides confined to nanoporous alumina: Pore diameter dependence of self-assembly and segmental dynamics. *Macromolecules* **2009**, *42*, (8), 2881-2885.
- (34). Grimm, S.; Giesa, R.; Sklarek, K.; Langner, A.; Gösele, U.; Schmidt, H.-W.; Steinhart, M. Nondestructive replication of self-ordered nanoporous alumina membranes via cross-linked polyacrylate nanofiber arrays. *Nano Letters* **2008**, *8*, (7), 1954-1959.
- (35). Ok, S.; Steinhart, M.; Serbescu, A.; Franz, C.; Vaca Chávez, F. n.; Saalwächter, K. Confinement effects on chain dynamics and local chain order in entangled polymer melts. *Macromolecules* **2010**, *43*, (10), 4429-4434.
- (36). Wang, Y.; Gösele, U.; Steinhart, M. Mesoporous polymer nanofibers by infiltration of block copolymers with sacrificial domains into porous alumina. *Chemistry of Materials* **2007**, *20*, (2), 379-381.
- (37). Zhang, M.; Dobriyal, P.; Chen, J.-T.; Russell, T. P.; Olmo, J.; Merry, A. Wetting transition in cylindrical alumina nanopores with polymer melts. *Nano Letters* **2006**, *6*, (5), 1075-1079.
- (38). Dobriyal, P.; Xiang, H.; Kazuyuki, M.; Chen, J.-T.; Jinnai, H.; Russell, T. P. Cylindrically confined diblock copolymers. *Macromolecules* **2009**, *42*, (22), 9082-9088.
- (39). Penner, R. M.; Martin, C. R. Controlling the morphology of electronically conductive polymers. *Journal of the Electrochemical Society* **1986**, *133*, (10), 2206-2207.
- (40). Steinhart, M.; Wendorff, J.; Greiner, A.; Wehrspohn, R.; Nielsch, K.; Schilling, J.; Choi, J.; Gösele, U. Polymer nanotubes by wetting of ordered porous templates. *Science* **2002**, *296*, (5575), 1997-1997.
- (41). Steinhart, M.; Senz, S.; Wehrspohn, R. B.; Gösele, U.; Wendorff, J. H. Curvature-directed crystallization of poly (vinylidene difluoride) in nanotube walls. *Macromolecules* **2003**, *36*, (10), 3646-3651.
- (42). Chen, J. T.; Lee, C. W.; Chi, M. H.; Yao, I. Solvent-Annealing-Induced Nanowetting in Templates: Towards Tailored Polymer Nanostructures. *Macromolecular Rapid Communications* **2013**, *34*, (4), 348-354.
- (43). Chen, J.-T.; Wei, T.-H.; Chang, C.-W.; Ko, H.-W.; Chu, C.-W.; Chi, M.-H.; Tsai, C.-C. Fabrication of polymer nanopeapods in the nanopores of anodic aluminum oxide templates using a double-solution wetting method. *Macromolecules* **2014**, *47*, (15), 5227-5235.
- (44). Chu, C.-J.; Cheng, M.-H.; Chung, P.-Y.; Chi, M.-H.; Jeng, K.-S.; Chen, J.-T. Reversible morphology control of three-dimensional block copolymer nanostructures by the solvent-annealing-induced wetting in anodic aluminum oxide templates. *International Journal of Polymeric Materials and Polymeric Biomaterials* **2016**, *65*, (13), 695-701.
- (45). Schlitt, S.; Greiner, A.; Wendorff, J. H. Cylindrical polymer nanostructures by solution template wetting. *Macromolecules* **2008**, *41*, (9), 3228-3234.

- (46). Feng, X.; Jin, Z. Spontaneous formation of nanoscale polymer spheres, capsules, or rods by evaporation of polymer solutions in cylindrical alumina nanopores. *Macromolecules* **2009**, *42*, (3), 569-572.
- (47). Mei, S.; Feng, X.; Jin, Z. Fabrication of polymer nanospheres based on Rayleigh instability in capillary channels. *Macromolecules* **2011**, *44*, (6), 1615-1620.
- (48). Xue, J.; Xu, Y.; Jin, Z. Interfacial Interaction in Anodic Aluminum Oxide Templates Modifies Morphology, Surface Area, and Crystallization of Polyamide-6 Nanofibers. *Langmuir* **2016**, *32*, (9), 2259-2266.
- (49). Guan, Y.; Liu, G.; Ding, G.; Yang, T.; Müller, A. J.; Wang, D. Enhanced crystallization from the glassy state of poly (l-lactic acid) confined in anodic alumina oxide nanopores. *Macromolecules* **2015**, *48*, (8), 2526-2533.
- (50). Guan, Y.; Liu, G.; Gao, P.; Li, L.; Ding, G.; Wang, D. Manipulating crystal orientation of poly (ethylene oxide) by nanopores. *ACS Macro Letters* **2013**, *2*, (3), 181-184.
- (51). Mijangos, C.; Hernández, R.; Martín, J. A review on the progress of polymer nanostructures with modulated morphologies and properties, using nanoporous AAO templates. *Progress in Polymer Science* **2016**, *54-55*, 148-182.
- (52). Europe, P. An analysis of European plastics production, demand and waste data. www.plasticseurope.org
- (53). Hu, Z.; Zhao, D. A. N. Polymerization within confined nanochannels of porous metal-organic frameworks. *Journal of Molecular and Engineering Materials* **2013**, *01*, (02), 1330001.
- (54). Tajima, K.; Aida, T. Controlled polymerizations with constrained geometries. *Chemical Communications* **2000**, (24), 2399-2412.
- (55). Moller, K.; Bein, T. Inclusion chemistry in periodic mesoporous hosts. *Chemistry of Materials* **1998**, *10*, (10), 2950-2963.
- (56). Matsumoto, A. Polymer structure control based on crystal engineering for materials design. *Polymer journal* **2003**, *35*, (2), 93-121.
- (57). Davis, S. A.; Breulmann, M.; Rhodes, K. H.; Zhang, B.; Mann, S. Template-directed assembly using nanoparticle building blocks: a nanotectonic approach to organized materials. *Chemistry of Materials* **2001**, *13*, (10), 3218-3226.
- (58). Moad, G.; Solomon, D. H., *The chemistry of radical polymerization*. Elsevier: 2005.
- (59). Matyjaszewski, K.; Davis, T. P., *Handbook of radical polymerization*. Wiley Online Library: 2002.
- (60). Odian, G., *Principles of polymerization*. John Wiley & Sons: 2004.
- (61). Cook, W. D. Thermal aspects of the kinetics of dimethacrylate photopolymerization. *Polymer* **1992**, *33*, (10), 2152-2161.
- (62). Wisanrakkit, G.; Gillham, J. The glass transition temperature (T_g) as an index of chemical conversion for a high-T_g amine/epoxy system: chemical and diffusion-controlled reaction kinetics. *Journal of Applied Polymer Science* **1990**, *41*, (11-12), 2885-2929.

- (63). Matyjaszewski, K.; Xia, J. Atom transfer radical polymerization. *Chemical reviews* **2001**, *101*, (9), 2921-2990.
- (64). Tobita, H. Effect of small reaction locus in free-radical polymerization: Conventional and reversible-deactivation radical polymerization. *Polymers* **2016**, *8*, (4).
- (65). Chiefari, J.; Chong, Y.; Ercole, F.; Krstina, J.; Jeffery, J.; Le, T. P.; Mayadunne, R. T.; Meijs, G. F.; Moad, C. L.; Moad, G. Living free-radical polymerization by reversible addition-fragmentation chain transfer: the RAFT process. *Macromolecules* **1998**, *31*, (16), 5559-5562.
- (66). Zhang, H. Controlled/"living" radical precipitation polymerization: A versatile polymerization technique for advanced functional polymers. *European Polymer Journal* **2013**, *49*, (3), 579-600.
- (67). Brédas, J. L.; Silbey, R., *Conjugated polymers: the novel science and technology of highly conducting and nonlinear optically active materials*. Springer Science & Business Media: 2012.
- (68). Li, Q.; Simon, S. L. Curing of bisphenol M dicyanate ester under nanoscale constraint. *Macromolecules* **2008**, *41*, (4), 1310-1317.
- (69). Tarnacka, M.; Dulski, M.; Starzonek, S.; Adrjanowicz, K.; Mapesa, E. U.; Kaminski, K.; Paluch, M. Following kinetics and dynamics of DGEBA-aniline polymerization in nanoporous native alumina oxide membranes - FTIR and dielectric studies. *Polymer (United Kingdom)* **2015**, *68*, 253-261.
- (70). Comotti, A.; Bracco, S.; Beretta, M.; Perego, J.; Gemmi, M.; Sozzani, P. Confined Polymerization in Highly Ordered Mesoporous Organosilicas. *Chemistry - A European Journal* **2015**, *21*, (50), 18209-18217.
- (71). Choi, M.; Kleitz, F.; Liu, D.; Lee, H. Y.; Ahn, W.-S.; Ryoo, R. Controlled polymerization in mesoporous silica toward the design of organic-inorganic composite nanoporous materials. *Journal of the American Chemical Society* **2005**, *127*, (6), 1924-1932.
- (72). Wight, A.; Davis, M. Design and preparation of organic-inorganic hybrid catalysts. *Chemical reviews* **2002**, *102*, (10), 3589-3614.
- (73). Guo, C.; Jin, G. X.; Wang, F. Preparation and characterization of SBA-15 supported iron (II)-bisimine pyridine catalyst for ethylene polymerization. *Journal of Polymer Science Part A: Polymer Chemistry* **2004**, *42*, (19), 4830-4837.
- (74). Lee, K.-S.; Oh, C.-G.; Yim, J.-H.; Ihm, S.-K. Characteristics of zirconocene catalysts supported on Al-MCM-41 for ethylene polymerization. *Journal of Molecular Catalysis A: Chemical* **2000**, *159*, (2), 301-308.
- (75). Rzyayev, J.; Hillmyer, M. A. Nanochannel array plastics with tailored surface chemistry. *Journal of the American Chemical Society* **2005**, *127*, (38), 13373-13379.
- (76). Nagai, A.; Guo, Z.; Feng, X.; Jin, S.; Chen, X.; Ding, X.; Jiang, D. Pore surface engineering in covalent organic frameworks. *Nature communications* **2011**, *2*, 536.
- (77). Kresge, C.; Leonowicz, M.; Roth, W.; Vartuli, J.; Beck, J. Ordered mesoporous molecular sieves synthesized by a liquid-crystal template mechanism. *Nature* **1992**, *359*, (6397), 710-712.

- (78). Soler-Illia, G. J. d. A. A.; Sanchez, C.; Lebeau, B.; Patarin, J. Chemical Strategies To Design Textured Materials: from Microporous and Mesoporous Oxides to Nanonetworks and Hierarchical Structures. *Chemical reviews* **2002**, *102*, (11), 4093-4138.
- (79). Huo, Q.; Leon, R.; Petroff, P. M.; Stucky, G. D. Mesostructure design with gemini surfactants: Supercage formation in a three-dimensional hexagonal array. *Science* **1995**, *268*, (5215), 1324-1327.
- (80). Zhao, D.; Feng, J.; Huo, Q.; Melosh, N.; Fredrickson, G. H.; Chmelka, B. F.; Stucky, G. D. Triblock copolymer syntheses of mesoporous silica with periodic 50 to 300 angstrom pores. *Science* **1998**, *279*, (5350), 548-552.
- (81). Zhao, D.; Sun, J.; Li, Q.; Stucky, G. D. Morphological control of highly ordered mesoporous silica SBA-15. *Chemistry of Materials* **2000**, *12*, (2), 275-279.
- (82). Wu, C.-G.; Bein, T. Conducting polyaniline filaments in a mesoporous channel host. *Science* **1994**, 1757-1759.
- (83). Ng, S. M.; Ogino, S. i.; Aida, T.; Koyano, K. A.; Tatsumi, T. Free radical polymerization within mesoporous zeolite channels. *Macromolecular Rapid Communications* **1997**, *18*, (12), 991-996.
- (84). Moller, K.; Bein, T.; Fischer, R. X. Entrapment of PMMA polymer strands in micro-and mesoporous materials. *Chemistry of Materials* **1998**, *10*, (7), 1841-1852.
- (85). Guo, C.; Zhang, D.; Wang, F.; Jin, G.-X. Nanofibers of polyethylene produced by SBA-15 supported zirconium catalyst [N-(3-tert-butylsalicylidene)-4'-allyloxylanilinato] 2 Zr (IV) Cl 2. *Journal of Catalysis* **2005**, *234*, (2), 356-363.
- (86). Tang, D.; Zhang, L.; Zhang, Y.; Qiao, Z.-A.; Liu, Y.; Huo, Q. Mesoporous silica nanoparticles immobilized salicylaldehyde cobalt complexes as high efficient catalysts for polymerization of 1, 3-butadiene. *Journal of Colloid and Interface Science* **2012**, *369*, (1), 338-343.
- (87). Scelta, D.; Ceppatelli, M.; Santoro, M.; Bini, R.; Gorelli, F. A.; Perucchi, A.; Mezouar, M.; Van Der Lee, A.; Haines, J. High pressure polymerization in a confined space: conjugated chain/zeolite nanocomposites. *Chemistry of Materials* **2014**, *26*, (7), 2249-2255.
- (88). Li, J.-R.; Sculley, J.; Zhou, H.-C. Metal-organic frameworks for separations. *Chemical reviews* **2011**, *112*, (2), 869-932.
- (89). Long, J. R.; Yaghi, O. M. The pervasive chemistry of metal-organic frameworks. *Chemical Society Reviews* **2009**, *38*, (5), 1213-1214.
- (90). Kitagawa, S.; Kitaura, R.; Noro, S. i. Funktionale poröse Koordinationspolymere. *Angewandte Chemie* **2004**, *116*, (18), 2388-2430.
- (91). Uemura, T.; Horike, S.; Kitagawa, S. Polymerization in coordination nanospaces. *Chemistry - An Asian Journal* **2006**, *1*, (1-2), 36-44.
- (92). Eddaoudi, M.; Kim, J.; Rosi, N.; Vodak, D.; Wachter, J.; O'Keeffe, M.; Yaghi, O. M. Systematic design of pore size and functionality in isorecticular MOFs and their application in methane storage. *Science* **2002**, *295*, (5554), 469-472.

- (93). Rowsell, J. L.; Yaghi, O. M. Effects of functionalization, catenation, and variation of the metal oxide and organic linking units on the low-pressure hydrogen adsorption properties of metal-organic frameworks. *Journal of the American Chemical Society* **2006**, *128*, (4), 1304-1315.
- (94). Inokuma, Y.; Nishiguchi, S.; Ikemoto, K.; Fujita, M. Shedding light on hidden reaction pathways in radical polymerization by a porous coordination network. *Chemical Communications* **2011**, *47*, (44), 12113-12115.
- (95). Uemura, T.; Yanai, N.; Kitagawa, S. Polymerization reactions in porous coordination polymers. *Chemical Society Reviews* **2009**, *38*, (5), 1228-1236.
- (96). Uemura, T.; Uchida, N.; Higuchi, M.; Kitagawa, S. Effects of unsaturated metal sites on radical vinyl polymerization in coordination nanochannels. *Macromolecules* **2011**, *44*, (8), 2693-2697.
- (97). Uemura, T.; Horike, S.; Kitagawa, K.; Mizuno, M.; Endo, K.; Bracco, S.; Comotti, A.; Sozzani, P.; Nagaoka, M.; Kitagawa, S. Conformation and molecular dynamics of single polystyrene chain confined in coordination nanospace. *Journal of the American Chemical Society* **2008**, *130*, (21), 6781-6788.
- (98). Uemura, T.; Ono, Y.; Kitagawa, S. Radical copolymerizations of vinyl monomers in a porous coordination polymer. *Chemistry letters* **2008**, *37*, (6), 616-617.
- (99). Yanai, N.; Uemura, T.; Ohba, M.; Kadowaki, Y.; Maesato, M.; Takenaka, M.; Nishitsuji, S.; Hasegawa, H.; Kitagawa, S. Fabrication of Two-Dimensional Polymer Arrays: Template Synthesis of Polypyrrole between Redox-Active Coordination Nanoslits. *Angewandte Chemie International Edition* **2008**, *47*, (51), 9883-9886.
- (100). Wang, Q. X.; Zhang, C. Y. Oriented Synthesis of One-Dimensional Polypyrrole Molecule Chains in a Metal-Organic Framework. *Macromolecular Rapid Communications* **2011**, *32*, (20), 1610-1614.
- (101). Darensbourg, D. J. Making plastics from carbon dioxide: Salen metal complexes as catalysts for the production of polycarbonates from epoxides and CO₂. *Chemical reviews* **2007**, *107*, (6), 2388-2410.
- (102). Chuck, C. J.; Davidson, M. G.; Jones, M. D.; Kociok-Köhn, G.; Lunn, M. D.; Wu, S. Air-stable titanium alkoxide based metal-organic framework as an initiator for ring-opening polymerization of cyclic esters. *Inorganic chemistry* **2006**, *45*, (17), 6595-6597.
- (103). Mazurin, O. V.; Porai-Koshits, E., *Phase separation in glass*. Elsevier: 1984.
- (104). Haller, W. Chromatography on glass of controlled pore size. **1965**.
- (105). Haller, W. Rearrangement kinetics of the liquid—liquid immiscible microphases in alkali borosilicate melts. *The Journal of Chemical Physics* **1965**, *42*, (2), 686-693.
- (106). Schnabel, R.; Langer, P. Controlled-pore glass as a stationary phase in chromatography. *Journal of Chromatography A* **1991**, *544*, 137-146.
- (107). Jackson, C. L.; McKenna, G. B. The melting behavior of organic materials confined in porous solids. *The Journal of Chemical Physics* **1990**, *93*, (12), 9002-9011.
- (108). Haller, W., *In Solid Phase Biochemistry*. New York, 1983.

- (109). Begum, F.; Simon, S. L. Modeling methyl methacrylate free radical polymerization in nanoporous confinement. *Polymer* **2011**, *52*, (7), 1539-1545.
- (110). Verros, G.; Latsos, T.; Achilias, D. Development of a unified framework for calculating molecular weight distribution in diffusion controlled free radical bulk homo-polymerization. *Polymer* **2005**, *46*, (2), 539-552.
- (111). Zhao, H.; Simon, S. L. Methyl methacrylate polymerization in nanoporous confinement. *Polymer* **2011**, *52*, (18), 4093-4098.
- (112). Begum, F.; Zhao, H.; Simon, S. L. Modeling methyl methacrylate free radical polymerization: Reaction in hydrophilic nanopores. *Polymer* **2012**, *53*, (15), 3238-3244.
- (113). Begum, F.; Zhao, H.; Simon, S. L. Modeling methyl methacrylate free radical polymerization: Reaction in hydrophobic nanopores. *Polymer* **2012**, *53*, (15), 3261-3268.
- (114). Zhao, H. Y.; Yu, Z. N.; Begum, F.; Hedden, R. C.; Simon, S. L. The effect of nanoconfinement on methyl methacrylate polymerization: T_g, molecular weight, and tacticity. *Polymer (United Kingdom)* **2014**, *55*, (19), 4959-4965.
- (115). Koh, Y. P.; Simon, S. L. Trimerization of monocyanate ester in nanopores. *The Journal of Physical Chemistry B* **2010**, *114*, (23), 7727-7734.
- (116). Lopez, E.; Simon, S. L. Trimerization Reaction Kinetics and T_g Depression of Polycyanurate under Nanoconfinement. *Macromolecules* **2015**, *48*, (13), 4692-4701.
- (117). Martin, C. R. Template synthesis of polymeric and metal microtubules. *Advanced Materials* **1991**, *3*, (9), 457-459.
- (118). Martin, C. R. Nanomaterials: A membrane-based synthetic approach. *Science* **1994**, *266*, (5193), 1961-1966.
- (119). Parthasarathy, R.; Martin, C. R. *Synthesis of polymeric microcapsule arrays and their use for enzyme immobilization*; DTIC Document: 1994.
- (120). Nair, S.; Naredi, P.; Kim, S. H. Formation of high-stress phase and extrusion of polyethylene due to nanoconfinements during Ziegler-Natta polymerization inside nanochannels. *The Journal of Physical Chemistry B* **2005**, *109*, (25), 12491-12497.
- (121). Parthasarathy, R. V.; Martin, C. R. Template-synthesized polyaniline microtubules. *Chemistry of Materials* **1994**, *6*, (10), 1627-1632.
- (122). Cai, Z.; Lei, J.; Liang, W.; Menon, V.; Martin, C. R. Molecular and supermolecular origins of enhanced electric conductivity in template-synthesized polyheterocyclic fibrils. 1. Supermolecular effects. *Chemistry of Materials* **1991**, *3*, (5), 960-967.
- (123). Li, X.; Zhang, X.; Li, H. Preparation and characterization of pyrrole/aniline copolymer nanofibrils using the template-synthesis method. *Journal of Applied Polymer Science* **2001**, *81*, (12), 3002-3007.
- (124). Xiong, S.; Wang, Q.; Xia, H. Preparation of polyaniline nanotubes array based on anodic aluminum oxide template. *Materials Research Bulletin* **2004**, *39*, (10), 1569-1580.

- (125). Blaszczyk-Lezak, I.; Desmaret, V.; Mijangos, C. Electrically conducting polymer nanostructures confined in anodized aluminum oxide templates (AAO). *Express Polymer Letters* **2016**, *10*, (3), 259-272.
- (126). Choi, M. K.; Yoon, H.; Lee, K.; Shin, K. Simple fabrication of asymmetric high-aspect-ratio polymer nanopillars by reusable AAO templates. *Langmuir* **2011**, *27*, (6), 2132-2137.
- (127). Lau, K. A.; Duran, H.; Knoll, W. In situ characterization of N-carboxy anhydride polymerization in nanoporous anodic alumina. *The Journal of Physical Chemistry B* **2009**, *113*, (10), 3179-3189.
- (128). Back, J.-W.; Lee, S.; Hwang, C.-R.; Chi, C.-S.; Kim, J.-Y. Fabrication of conducting PEDOT nanotubes using vapor deposition polymerization. *Macromolecular Research* **2011**, *19*, (1), 33-37.
- (129). Liu, R.; Cho, S. I.; Lee, S. B. Poly(3,4-ethylenedioxythiophene) nanotubes as electrode materials for a high-powered supercapacitor. *Nanotechnology* **2008**, *19*, (21).
- (130). Lee, L.-C.; Han, H.; Tsai, Y.-T.; Fan, G.-L.; Liu, H.-F.; Wu, C.-C.; Shyue, J.-J.; Sun, S.-S.; Liu, C.-L.; Chou, P.-T. Template-assisted in situ polymerization for forming blue organic light-emitting nanotubes. *Chemical Communications* **2014**, *50*, (60), 8208-8210.
- (131). Al-Kaysi, R. O.; Dillon, R. J.; Kaiser, J. M.; Mueller, L. J.; Guirado, G.; Bardeen, C. J. Photopolymerization of organic molecular crystal nanorods. *Macromolecules* **2007**, *40*, (25), 9040-9044.
- (132). Haberkorn, N.; Weber, S. A. L.; Berger, R.; Theato, P. Template-Based Preparation of Free-Standing Semiconducting Polymeric Nanorod Arrays on Conductive Substrates. *ACS Applied Materials & Interfaces* **2010**, *2*, (6), 1573-1580.
- (133). Liu, L.; Zhao, C.; Zhao, Y.; Jia, N.; Zhou, Q.; Yan, M.; Jiang, Z. Characteristics of polypyrrole (PPy) nano-tubules made by templated ac electropolymerization. *European Polymer Journal* **2005**, *41*, (9), 2117-2121.
- (134). Li, P.-F.; Xie, R.; Jiang, J.-C.; Meng, T.; Yang, M.; Ju, X.-J.; Yang, L.; Chu, L.-Y. Thermo-responsive gating membranes with controllable length and density of poly (N-isopropylacrylamide) chains grafted by ATRP method. *Journal of Membrane Science* **2009**, *337*, (1), 310-317.
- (135). Cui, Y.; Tao, C.; Zheng, S.; He, Q.; Ai, S.; Li, J. Synthesis of Thermosensitive PNIPAM-co-MBAA Nanotubes by Atom Transfer Radical Polymerization within a Porous Membrane. *Macromolecular Rapid Communications* **2005**, *26*, (19), 1552-1556.
- (136). Barbey, R.; Lavanant, L.; Paripovic, D.; Schüwer, N.; Sugnaux, C.; Tugulu, S.; Klok, H.-A. Polymer brushes via surface-initiated controlled radical polymerization: synthesis, characterization, properties, and applications. *Chemical reviews* **2009**, *109*, (11), 5437-5527.
- (137). Wang, W. C.; Wang, J.; Liao, Y.; Zhang, L.; Cao, B.; Song, G.; She, X. Surface initiated ATRP of acrylic acid on dopamine-functionalized AAO membranes. *Journal of Applied Polymer Science* **2010**, *117*, (1), 534-541.
- (138). Giussi, J. M.; Blaszczyk-Lezak, I.; Cortizo, M. S.; Mijangos, C. In-situ polymerization of styrene in AAO nanocavities. *Polymer (United Kingdom)* **2013**, *54*, (26), 6886-6893.

- (139). Tarnacka, M.; Dulski, M.; Starzonek, S.; Adrjanowicz, K.; Mapesa, E. U.; Kaminski, K.; Paluch, M. Following kinetics and dynamics of DGEBA-aniline polymerization in nanoporous native alumina oxide membranes – FTIR and dielectric studies. *Polymer* **2015**, *68*, 253-261.
- (140). Tarnacka, M.; Chrobok, A.; Matuszek, K.; Golba, S.; Maksym, P.; Kaminski, K.; Paluch, M. Polymerization of Monomeric Ionic Liquid Confined within Uniaxial Alumina Pores as a New Way of Obtaining Materials with Enhanced Conductivity. *ACS Applied Materials & Interfaces* **2016**.
- (141). Steinhart, M.; Wehrspohn, R. B.; Gösele, U.; Wendorff, J. H. Nanotubes by template wetting: a modular assembly system. *Angewandte Chemie International Edition* **2004**, *43*, (11), 1334-1344.
- (142). Wu, D.; Xu, F.; Sun, B.; Fu, R.; He, H.; Matyjaszewski, K. Design and preparation of porous polymers. *Chemical reviews* **2012**, *112*, (7), 3959-4015.
- (143). Steinhart, M.; Wendorff, J. H.; Greiner, A.; Wehrspohn, R. B.; Nielsch, K.; Schilling, J.; Choi, J.; Gösele, U. Polymer Nanotubes by Wetting of Ordered Porous Templates. *Science* **2002**, *296*, (5575), 1997-1997.
- (144). Fox, H. W.; Hare, E. F.; Zisman, W. A. Wetting Properties of Organic Liquids on High-Energy Surfaces. *The Journal of Physical Chemistry* **1955**, *59*, (10), 1097-1106.
- (145). Martín, J.; Maiz, J.; Sacristan, J.; Mijangos, C. Tailored polymer-based nanorods and nanotubes by "template synthesis": From preparation to applications. *Polymer* **2012**, *53*, (6), 1149-1166.
- (146). Martín, J.; Hernández-Vélez, M.; de Abril, O.; Luna, C.; Munoz-Martin, A.; Vázquez, M.; Mijangos, C. Fabrication and characterization of polymer-based magnetic composite nanotubes and nanorods. *European Polymer Journal* **2012**, *48*, (4), 712-719.
- (147). Maiz, J.; Sacristan, J.; Mijangos, C. Probing the presence and distribution of single-wall carbon nanotubes in polyvinylidene difluoride 1D nanocomposites by confocal Raman spectroscopy. *Chemical Physics Letters* **2010**, *484*, (4), 290-294.
- (148). Yang, C.; Li, X.; Yang, S.; Song, G. Study on the Growth Mechanism of the Polymer Nanotube Arrays by Its Controlled Growth in Anodic Aluminum Oxide Template. *Journal of Nanoscience and Nanotechnology* **2016**, *16*, (7), 7758-7763.
- (149). Wang, T.-C.; Hsueh, H.-Y.; Ho, R.-M. Hundred-Nanometer-Size Crystalline Carbon Tubes from Poly (acrylonitrile) Pore-Filling Anodic Aluminum Oxide Templates via Solvent Annealing. *Chemistry of Materials* **2010**, *22*, (16), 4642-4651.
- (150). Mei, S.; Feng, X.; Jin, Z. Polymer nanofibers by controllable infiltration of vapour swollen polymers into cylindrical nanopores. *Soft Matter* **2013**, *9*, (3), 945-951.
- (151). Martín, J.; Mijangos, C. Tailored polymer-based nanofibers and nanotubes by means of different infiltration methods into alumina nanopores. *Langmuir* **2009**, *25*, (2), 1181-1187.
- (152). Martin, J.; Martin-Gonzalez, M. The use of PEEK nanorod arrays for the fabrication of nanoporous surfaces under high temperature: SiNx example. *Nanoscale* **2012**, *4*, (18), 5608-5613.
- (153). Chen, D.; Zhao, W.; Wei, D.; Russell, T. P. Dewetting on curved interfaces: a simple route to polymer nanostructures. *Macromolecules* **2011**, *44*, (20), 8020-8027.

- (154). Ko, H.-W.; Chi, M.-H.; Chang, C.-W.; Chu, C.-W.; Luo, K.-H.; Chen, J.-T. Fabrication of Core-Shell Polymer Nanospheres in the Nanopores of Anodic Aluminum Oxide Templates Using Polymer Blend Solutions. *ACS Macro Letters* **2015**, *4*, (7), 717-720.
- (155). Steinhart, M.; Jia, Z.; Schaper, A. K.; Wehrspohn, R. B.; Gösele, U.; Wendorff, J. H. Palladium Nanotubes with Tailored Wall Morphologies. *Advanced Materials* **2003**, *15*, (9), 706-709.
- (156). Muanchan, P.; Suzuki, S.; Kyotani, T.; Ito, H. One-dimensional polymer nanofiber arrays with high aspect ratio obtained by thermal nanoimprint method. *Polymer Engineering & Science* **2016**.
- (157). Tan, A. W.; Torkelson, J. M. Poly (methyl methacrylate) nanotubes in AAO templates: Designing nanotube thickness and characterizing the T g-confinement effect by DSC. *Polymer* **2016**, *82*, 327-336.
- (158). Martín, J.; Campoy-Quiles, M.; Nogales, A.; Garriga, M.; Alonso, M. I.; Goñi, A. R.; Martín-González, M. Poly (3-hexylthiophene) nanowires in porous alumina: internal structure under confinement. *Soft Matter* **2014**, *10*, (18), 3335-3346.
- (159). Chen, D.; Zhao, W.; Russell, T. P. P3HT nanopillars for organic photovoltaic devices nanoimprinted by AAO templates. *ACS Nano* **2012**, *6*, (2), 1479-1485.
- (160). Martín, J.; Martín-González, M. The use of PEEK nanorod arrays for the fabrication of nanoporous surfaces under high temperature: SiN x example. *Nanoscale* **2012**, *4*, (18), 5608-5613.
- (161). Martin, J.; Scaccabarozzi, A. D.; Nogales, A.; Li, R.; Smilgies, D.-M.; Stingelin, N. Confinement effects on the crystalline features of poly (9, 9-dioctylfluorene). *European Polymer Journal* **2016**.
- (162). Chu, C.-W.; Jeng, K.-S.; Chi, M.-H.; Tsai, C.-C.; Cheng, M.-H.; Chen, J.-T. Confinement Effects on the Optical Properties and Chain Conformations of Poly(9,9-di-n-octylfluorene-alt-benzothiadiazole) Nanotubes. *Macromolecular Chemistry and Physics* **2016**, *217*, (18), 2074-2080.
- (163). Casas, M. T.; Michell, R. M.; Blaszczyk-Lezak, I.; Puiggali, J.; Mijangos, C.; Lorenzo, A. T.; Mueller, A. J. Self-assembly of semicrystalline PE-b-PS diblock copolymers within AAO nanoporous templates. *Polymer* **2015**, *70*, 282-289.
- (164). Hou, P.; Fan, H.; Jin, Z. Spiral and mesoporous block polymer nanofibers generated in confined nanochannels. *Macromolecules* **2014**, *48*, (1), 272-278.
- (165). Maiz, J.; Zhao, W.; Gu, Y.; Lawrence, J.; Arbe, A.; Alegría, A.; Emrick, T.; Colmenero, J.; Russell, T. P.; Mijangos, C. Dynamic study of polystyrene-block-poly (4-vinylpyridine) copolymer in bulk and confined in cylindrical nanopores. *Polymer* **2014**, *55*, (16), 4057-4066.
- (166). Han, X.; Maiz, J.; Mijangos, C.; Zaldo, C. Nanopatterned PMMA-Yb: Er/Tm: Lu₂O₃ composites with visible upconversion emissions. *Nanotechnology* **2014**, *25*, (20), 205302.
- (167). Li, X.; Yang, C.; Han, P.; Zhao, Q.; Song, G. Facile synthesis and magnetic study of ni@polyamide 66 coaxial nanotube arrays. *Journal of Magnetism and Magnetic Materials* **2016**.
- (168). Wan, M.; Zhao, W.; Peng, F.; Wang, Q.; Xu, P.; Mao, C.; Shen, J. Facile fabrication of high-quality Ag/PS coaxial nanocables based on the mixed mode of soft/hard templates. *Scientific Reports* **2016**, *6*.

- (169). Michell, R. M.; Blaszczyk-Lezak, I.; Mijangos, C.; Müller, A. J. Confined crystallization of polymers within anodic aluminum oxide templates. *Journal of Polymer Science Part B: Polymer Physics* **2014**, *52*, (18), 1179-1194.
- (170). Noirez, L.; Stillings, C.; Bardeau, J.-F.; Steinhart, M.; Schlitt, S.; Wendorff, J.; Pepy, G. What happens to polymer chains confined in rigid cylindrical inorganic (AAO) nanopores. *Macromolecules* **2013**, *46*, (12), 4932-4936.
- (171). Shi, A.-C.; Li, B. Self-assembly of diblock copolymers under confinement. *Soft Matter* **2013**, *9*, (5), 1398-1413.
- (172). Shin, K.; Obukhov, S.; Chen, J.-T.; Huh, J.; Hwang, Y.; Mok, S.; Dobriyal, P.; Thiyagarajan, P.; Russell, T. P. Enhanced mobility of confined polymers. *Nature materials* **2007**, *6*, (12), 961-965.
- (173). Rowland, H. D.; King, W. P.; Pethica, J. B.; Cross, G. L. Molecular confinement accelerates deformation of entangled polymers during squeeze flow. *Science* **2008**, *322*, (5902), 720-724.
- (174). Cao, B.-Y.; Li, Y.-W.; Kong, J.; Chen, H.; Xu, Y.; Yung, K.-L.; Cai, A. High thermal conductivity of polyethylene nanowire arrays fabricated by an improved nanoporous template wetting technique. *Polymer* **2011**, *52*, (8), 1711-1715.
- (175). Duran, H.; Yameen, B.; Geuss, M.; Kappl, M.; Steinhart, M.; Knoll, W. Enhanced interfacial rigidity of 1D thermoset nanostructures by interface-induced liquid crystallinity. *Journal of Materials Chemistry C* **2013**, *1*, (46), 7758-7765.

Chapter 3

PREPARATION AND CHARACTERIZATION OF AAO TEMPLATES

This chapter describes the preparation of anodic aluminium oxide (AAO) templates. It includes the experimental method and conditions used to obtain ordered alumina templates, based on the two-step anodization process, and the characterization of the template by SEM microscopy and contact angle measurements.

3.1. Introduction

The anodic alumina template is the suitable choice for the preparation of polymers nanostructures since the pore diameters and lengths can be easily adjusted to the desired size. Moreover, AAO template synthesized in the laboratory has an aluminium part that acts as a support making the template easily manipulable and resistant to infiltrate the polymer into the pores, even if some pressure may be used to aid infiltration of melting polymer without breaking the template. In addition, the double anodization procedure allows control, accuracy and precision, keeping costs relatively low over the more costly processes of polymer nanostructuring. The highly desired densely packed hexagonal array nanopores structure can be obtained by a two step anodization process, which is a relatively easy process for the fabrication of nanostructured material.¹

At present, AAO membranes can be synthesized in the laboratory or supplied from the market. Whatman Company provides AAO membranes with irregularly ordered pores and a broad size distribution, mainly addressed to filter applications. This commercial alumina membrane tends to have imperfections and sometimes their pore size and structure are not regular. In Figure 3.1.a is observed the top of the surface where some pores are connected, increasing the number of the pores and causing smaller size of the pore diameter. In addition, the bottom of the surface (Figure 3.1b) is very different from the upper side because pore homogeneity does not remain across the membrane and a heterogeneous alumina network is formed on this side, in consequence, it is very important to differentiate both sides. In addition, these membranes are only available commercially in a very limited number of pore diameters (0.02 μm , 0.1 μm and 0.2 μm). Very recently, Synkera Technologies, Inc. Company has marketed a broad range of anodic alumina-based nanotemplates of three distinctly different architectures. It is possible to purchase AAO template attached to aluminium foil or free standing as membrane. Synkera offers more ordered nanostructures than Whatman but the disadvantage is the cost, is an expensive product. For this reason and the experience gained in the group with instrumental improvements

in the experimental anodization set-up, we prefer to prepare our own AAO templates with regular and ordered pores along the template (Figure 3.1 c and d) by anodization process of aluminium.

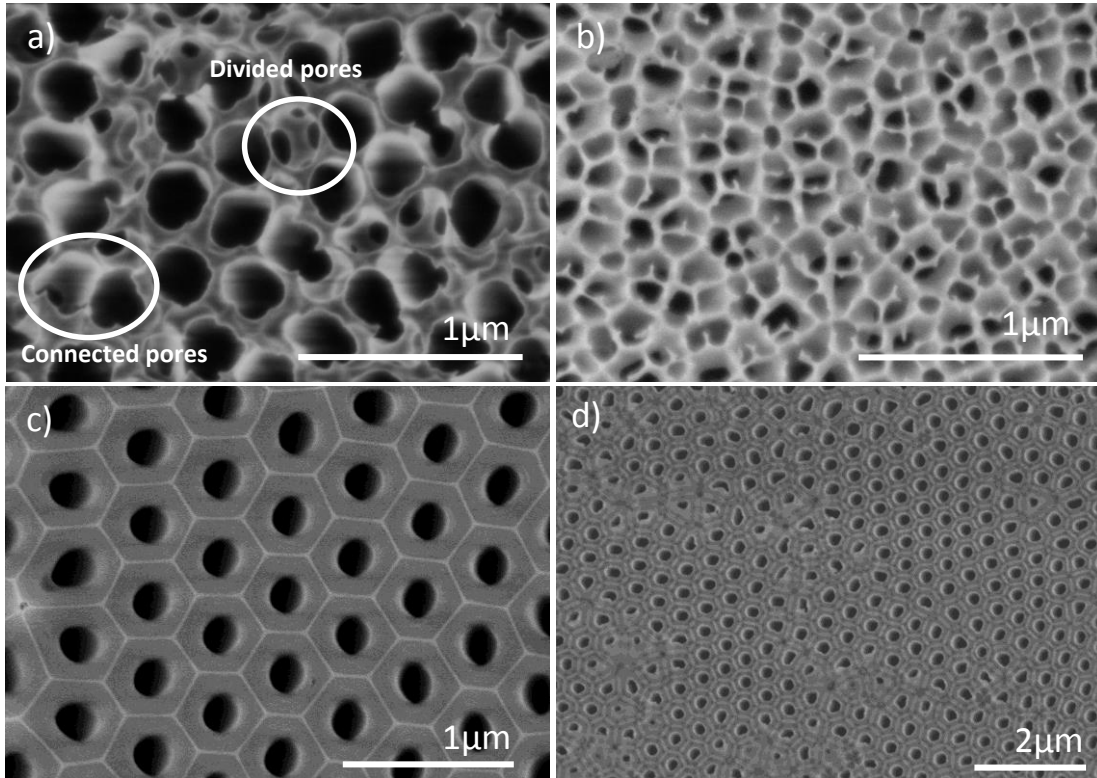


Figure 3.1. SEM images of commercially available Whatman[®] Nanopore (Anodic) membrane (0.2 μm pore diameter), a) Top surface and b) Bottom surface. SEM images of AAO template synthesized in our laboratory c) Top surface and b) Bottom surface after barrier layer removed.

The self-organization process occurs during the two-step anodization process of aluminium in acidic electrolytes and it has become in one of the most frequently employed methods to obtain a quasi monodomain nanopores system.

Anodization process

The formation of the AAO porous has been extensively investigated and reported by various groups, starting with the pioneering works of Masuda², Keller³, Thomson⁴ and others. In 1995 a major advance for the preparation of AAO was made by Masuda and Fukuda². They reported the fabrication of highly ordered porous AAO with a low pore size distribution by using a two-step anodization process⁵. Briefly, this process was based on three steps (see Figure 3.2). Firstly the aluminium foil is washed and degreased. Then, a smoothing of the surface via electro-polishing is performed in order to start the process from a homogeneous surface. In the first

anodization disordered pores are formed, oxide growth serves as a pre-texturing for aluminium. The disordered porous film on the surface is removed in the following step that consists of a wet chemical etching of the alumina layer with an aqueous solution of $\text{CrO}_3 + \text{H}_3\text{PO}_4$, during overnight. This solution leaves a formation of hexagonally ordered indentation on the aluminium surface. In the second anodization step, this indentation serves as seeds for the pore growth and results in an array of columnar hexagonal packed cells with central, cylindrical and uniformly sized pores. A more detailed overview about the pore dimensions at various anodization parameters can be found in the following references^{6,7}

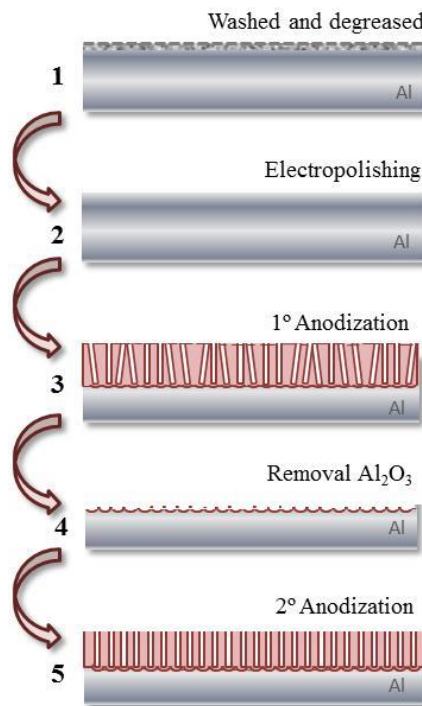
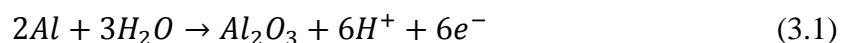


Figure 3.2. Schematic diagram of the fabrication of AAO templates by utilizing two-step anodization: 1) Washed and degreased. 2) Smoothing of the surface via electro-polishing. 3) First anodization step results in partially unordered pores. 4) Selective etching of the porous alumina by treatment with aqueous chromic acid. 5) Formation of hexagonally ordered pores during the second anodization.

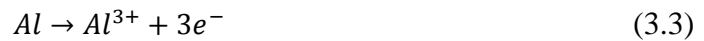
To understand the reactions that take place during the anodization process, the electrochemical principles of aluminium oxide formation have to be defined. This process has been described in detail in the Desmaret's Master manuscript.⁸ Briefly, the aluminium (anode) is electrochemically oxidized in a conductive aqueous electrolyte according to the equation 3.1 and hydrogen (cathode) is formed by proton reduction by the equation 3.2.



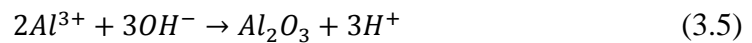


Depending on the properties of the electrolyte, two different types of oxide layers can be formed. If the electrolyte is neutral or basic ($5 < \text{pH} < 7$), such as boric acid or tartaric acid, a homogeneous nonporous oxide layer is formed. As opposed, if the electrolyte used during the anodization is weakly acidic, such as sulfuric, oxalic or phosphoric acid, a porous aluminium oxide layer is obtained. In order to understand the mechanisms of the formation of ordered porous morphology, several theories have been proposed.⁹⁻¹² The most accepted mechanism for the self-adjustment of pores in AAO is believed to be based on mechanical stress theory¹³. O'Sullivan *et al.*¹⁰ discussed the effect of the two basic chemical processes that take place during the anodization process:

1. The formation of aluminium oxide. At the beginning of the anodization process, in the oxidation reaction the aluminium metal is converted to Al^{3+} ions that migrate across the metal/oxide interface¹⁴

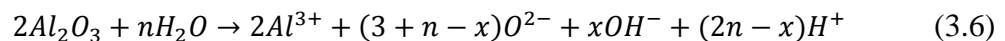


The Al^{3+} ions can remain at the metal/oxide interface and directly form Al_2O_3 with migrated oxide anions (O^{2-} and OH^-) from the electrolyte/oxide interface,



O^{2-} and OH^- anions migrate induced by the high electric field and are formed by dissociation of water at the electrolyte/oxide interface. These anions can also be formed by partial dissolution of Al_2O_3 , explained in the second process.

2. The dissolution of aluminium oxide at the interface between electrolyte/oxide.⁹ The overall reaction can be written as¹⁵:



where n indicates the ratio of the dissociation rate of water and the rate of Al_2O_3 dissolution, and x is the indicator of the ratio of O^{2-} and OH^- ¹³. Therefore the oxide layer thickness is increased by the formation of Al_2O_3 in reaction (3.4) and (3.5), and decreased by the described dissolution process in reaction (3.6).

During the oxide formation the barrier layer constantly regenerates with further oxide growth and transforms into a semi-spherical oxide layer of constant thickness that forms the pore bottom. The oxidation takes place over the entire pore base, with a perpendicular oxide growth occurring at the pore boundaries¹⁶, as shown in Figure 3.3. The review of Poinern and co-workers describes in detail the pore formation in AAO templates.

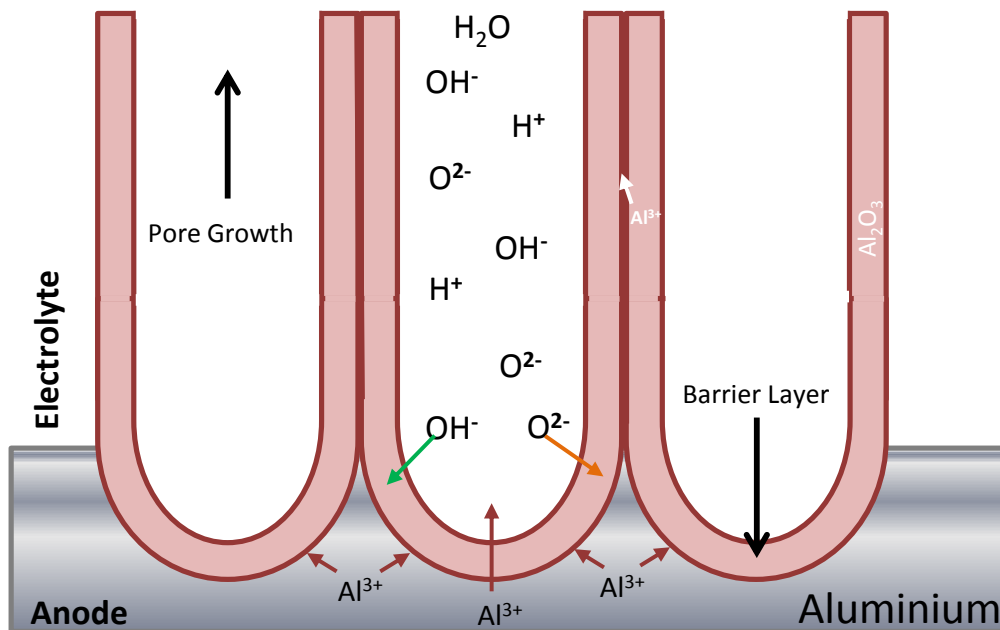


Figure 3.3. Schematic of pore formation mechanism in an acidic electrolyte. Modified figure from Ref.¹⁶

The formation of hexagonal oxide cell is also depending on the current and voltage conditions employed in the anodizing process. In fact, it can be carried out under constant current density or constant anodizing potential regime. The constant potential of anodizing instead of constant current regime has been commonly used for the fabrication of highly ordered anodic porous alumina and is the procedure that will be followed in this work. Hoar and Yahalom¹⁷ revealed that the constant anodizing potential is the result between two overlapping processes, current density and time (see Figure 3.4). As observed in the Figure 3.4, the barrier layer film formation is represented in red color and the process of pore formation is represented in blue color. The different steps of pore formation are also illustrated in the graphic. At the beginning of the anodization (step I) a thin barrier film layer is formed and its constant growth results in an exponential decrease of the current. As the time of anodizing progresses, the electric field is concentrated in surface defects to propagate in individual paths (precursors pore) through the

oxide film and the minimum current density is achieved rapidly (step II). Once the minimum current is reached, the rupture of the compact barrier layer occurs and pores begin to grow with increasing the current (step III). In the last stage, after reaching a local maximum in the current density, the growth of porous alumina maintains an equilibrated state (step IV). After a long time of anodization, the current density slightly decreases due to diffusion limits in the long pore channels.

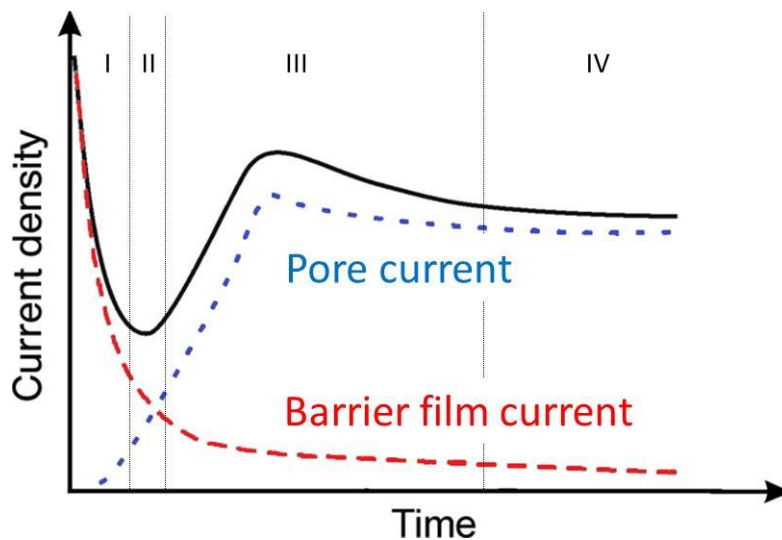


Figure 3.4. Schematic illustration of overlapping processes occurring during the porous oxide growth under constant anodizing potential regime. Ref. ¹⁷

In the anodization process, the evolution of current over time is an important parameter in the formation of pore but other factors, such as, temperature and voltage need to be controlled to achieve templates with great ordering and desired pore growth. The control of the above parameters is dependent on the electrolyte solution employed sulfuric, oxalic, or phosphoric acid.

In summary, the fabrication of the AAO template is based on a facile and economic electrochemical anodization self-ordering process, not requiring any lithography process. In fact, there is a great demand for the use of highly ordered nanopores arrays, which has generated enormous deal of works in function of the final applications. The advantage of this approach is that it does not require sophisticated instrumentation and allows the fabrication of uniform sizes of nanomaterials of broad origin with high yield.¹⁸⁻²¹

Wettability

As previously described, the size of pores (diameter, length and distance between pores) of AAO templates can be controlled as a function of anodization conditions. As known, wettability is highly dependent on the surface morphology, therefore, the wettability of AAO templates could be modified as a function of pore dimensions. In the case of the AAO templates the wettability has been merely studied, although it has a great influence on the infiltration process. The objective of this section is not to carry out a deep study of the wettability in porous systems, but to have a brief knowledge of the contact angle of water over the AAO template as a function of pore sizes.

In order to understand the wettability of AAO, some concepts related to wetting ability of porous surfaces are explained below.

In the partial wetting of ideal (chemically homogeneous, isotropic and topographically smooth) solid surfaces, the natural macroscopic parameter characterizing wetting behaviour is the contact angle θ value. This angle is the result of the balance at the three-phase contact of solid, liquid and vapour where equilibrium is represented in the Young's equation 3.7.

$$\gamma_{SG} = \gamma_{SL} + \gamma_{LG} \cdot \cos\theta_Y \quad (3.7)$$

where γ_{SG} , γ_{SL} , γ_{LG} are the surface tensions at the solid/gas, solid/liquid, and liquid/gas interfaces, respectively (see Figure 3.5.a).

The wettability of a rough surface can be studied by the behaviour of a water droplet on the surface. There are two theories to explain the state of equilibrium of a water droplet, Cassie and Wenzel models. The relationship between roughness and wettability was defined already in 1936 by Wenzel, who stated that the wetting properties of a solid substance should be directly proportional to the roughness of the surface wetted²². For example, if the surface is chemically hydrophobic, it will become even more hydrophobic when surface roughness is added. In this case the droplet penetrates the harshness (see Figure 3.5.b) and the presence of a roughness factor implies an increase/reduction of the static equilibrium contact angle if $\theta_Y > 90^\circ$ or $\theta_Y < 90^\circ$. Wenzel statement can be described by equation 3.8.

$$\cos\theta_w = r \cos\theta_Y \quad (3.8)$$

where θ_w is the contact angle of the rough surface, θ_Y is the Young angle of a flat surface of the same material and r is the roughness ratio defined as the relation between the actual surface area

to the projected surface area. When r is 1 the surface is smooth whereas if r is bigger than 1 the surface is rough.

The Cassie state is used in cases where the liquid does not penetrate into the grooves. The Cassie equation was first developed to describe chemically heterogeneous surfaces, with two different chemistries,²³ equation 3.9.

$$\cos\theta_c = \Phi_1 \cos\theta_{Y1} + \Phi_2 \cos\theta_{Y2} \quad (3.9)$$

where Φ_1 and Φ_2 are the fractions of the surface area occupied by each these species, and θ_{Y1} and θ_{Y2} are the contact angles between liquid and solid and liquid and air, respectively. Cassie and Baxter simplified the equation 3.9 taking into account two approach: if the second area is air, the contact angle between liquid and air is 180° and therefore the value of $\cos\theta_{Y2}$ is -1 , and with the relation between the $\Phi_2 = 1 - \Phi_1$ the equation 3.9 can be written as the equation 3.10 as the equation developed by²³

$$\cos\theta_{CB} = \Phi \cos\theta_Y + \Phi - 1 \quad (3.10)$$

As shown in Figure 3.5.c, in this case the droplet lays on the top of the harshness and the air is trapped in the nanostructures below the droplet. The most stable contact angle is associated with the absolute minimum of the Gibbs energy curve which can be connected to the Young contact angle. The contact angles calculated from the Wenzel and Cassie-Baxter equations have been found to be good approximations of experimentally determined contact angles²⁴

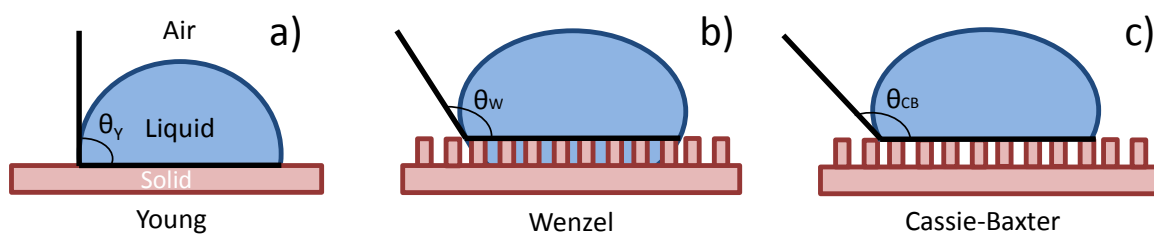


Figure 3.5. A droplet on a solid surface and surrounded by a gas forms a characteristic contact angle (θ). In Wenzel state the liquid penetrates in the solid asperities while in the Cassie state the liquid rest on the top of the asperities.

For AAO nanocavities, when the water droplet lies on the surface of the template, an equilibrium is achieved between the three phases.²⁵ During the wetting process two main forces come into play. The drop is driven into the nanopores by a capillary force (F_c), but the air that resides within the pore is compressed providing a counter force (F_v), preventing water from imbibition

into the nanopores. At nanoscopic scale the force of gravity is relatively small and can be neglected as the pore length is much greater than its diameter²⁶. The Figure 3.6 shows a diagram of the forces involved between the water and the AAO template.

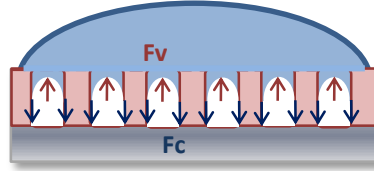


Figure 3.6. Scheme of the forces that take place when the water droplet lies on the top of the AAO template. Capillarity force (F_c) and counter force (F_v)

The capillary force (F_c) is defined by equation 3.11:

$$F_c = \pi \cdot \gamma \cdot d_p \cdot \cos\theta_Y \quad (3.11)$$

where γ is the liquid surface tension, θ_Y is the Young contact angle (CA), and d_p is the average pore diameter.

Counter force (F_v) is produced from the closed-air in the nanopore and is given by the equation 3.12,²⁷

$$F_v = \frac{P_0 \cdot H \cdot \pi \cdot d_p^2}{4(H-h)} \quad (3.12)$$

where P_0 is the atmospheric pressure, h is the invasion depth of water into the nanopore, and H is the length of the nanopore.

The aluminium oxide has a tendency to be wet by water, being a hydrophilic material. Nevertheless, there was a discrepancy in the literature about value of Young contact angle (θ_Y) for a smooth, flat, non-porous surface of alumina. First, Ran et al. gave a hydrophobicity value close to 85° ²⁸, and later Li et al. provided a lower value of 35° ²⁹. Both values are quite different from each other, and also well above the value more accepted for this type of material, which is in the order between $10-15^\circ$, found in previous studies of non-porous alumina by Lee et al.³⁰ and Megias-Alguacil.³¹

3.2. Experimental part

3.2.1. Fabrication of AAO template

This section describes the method of double anodization to fabricate alumina template based on the developed process of Masuda et al.², as well as, the pore widening process that modifies the wall thickness and pore diameter.

Description of equipment

The experimental set-up and the description of the equipment used for the anodizing process are illustrated in Figure 3.7. The equipment consists in a two electrode system connected to a power supply. In the anodization process the aluminium foil (anode) is placed in the electrolyte container in contact with a copper plate that is connected to the anode of the power supply. A platinum mesh, connected to the negative pole of the power supply, acts as a cathode, and it is localized in parallel with the aluminium foil. The interface between the aluminium and the container is a circular shape with a diameter of 3.2 cm and it is sealed with a Viton O-ring. A protective cover of PVC protects the container cell, also made of PVC, to minimize the heat transfer with the exterior. The cell is fixed and tightly pressed onto the ground plate in order to avoid leakage of the electrolyte solution. The electrolyte is continuously agitated by a motor with Teflon mechanical stirrer connected to the top of the cell, and it helps to homogenize the temperature of the system. It should be noted that the high-field applied during the anodization promotes much emission of heat, therefore, any excessive heat should be effectively removed from the sample in order to prevent burning. Due to this condition, the cell is plugged into a refrigerating plate, which is connected to a cooling bath continuously. The current of anodization process is controlled with an ammeter and the temperature is measured with a thermocouple.

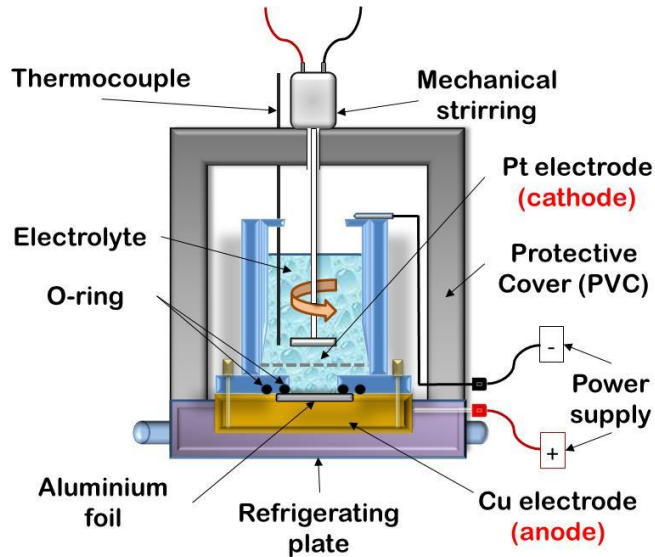


Figure 3.7. Experimental set-up for the fabrication of AAO templates.

This experimental set-up has been fabricated in our Institute (ICTP).^{8, 32, 33} Two apparatus, which are currently working in the group, have been designed depending on the desired size of AAO template. Figure 3.8 shows the experimental set-up used. a) Image of the equipment used for the phosphoric anodization. b) Equipment used for the sulfuric and oxalic anodization. The anodization with phosphoric acid is a more difficult process to stabilize because it is exposed to high voltages 195V, therefore the experimental set-up consists in only one anodization cell. However, in the case of the anodization with oxalic acid, the conditions are not too extreme and 40V voltages are easier to stabilize, therefore it can work with a parallel system and produce three templates at the same time.

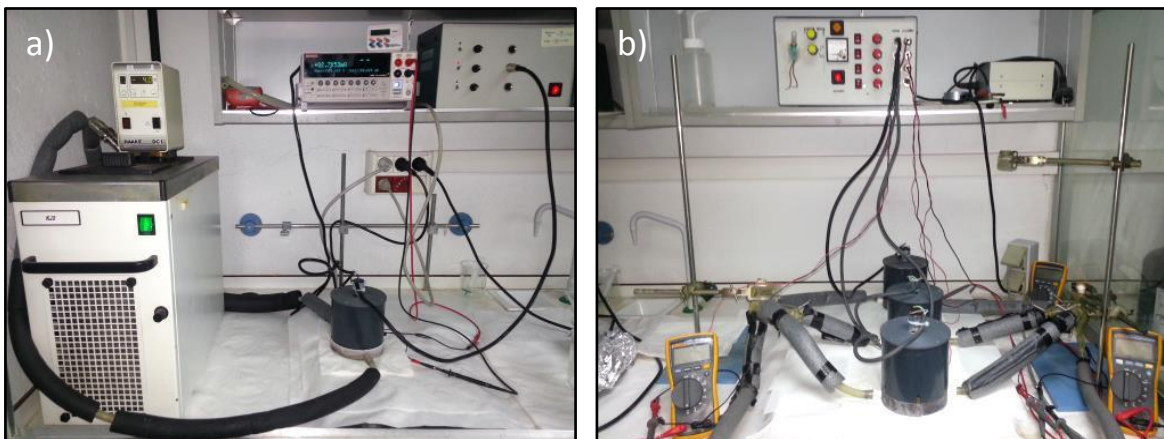


Figure 3.8. Experimental set-up for the fabrication of AAO template: a) Equipment for phosphoric anodization, b) equipment for sulfuric and oxalic anodization.

The most desirable starting material for self-organized nanopores array formation by anodizing is a high-purity, annealed aluminium foil.¹ The aluminium foil employed in our work is ultrapure (99.999%) aluminium foil supplied by Advent Research Materials (England), with a thickness of 0.5 mm. A pre-treatment process must be carried out to reduce the surface faults and to control and reproduce the generation of the required morphology. In order to this pre-treatment the aluminium foils must be first cleaned and degreased by sonication with three solvents of different polarity (water, ethanol and acetone). Then, to remove the oxide barrier layer formed by the air, the electropolished is carried out at constant voltage of 20 V during 4 minutes and a temperature below 10°C, in a mixture of perchloric acid and ethanol: HClO₄: C₂H₆O (25:75).

First and second anodization

In order to obtain the AAO templates of different dimensions the anodization process must be carried out under different conditions of the electrolyte type and concentration, voltage, temperature and time. During this work several templates have been synthesized for different purposes. The conditions used for anodization process are summarized in the Table 3.1. The time used in the second anodization determine the pore length, in the last column is reported the needed time to obtain AAO templates with 100 µm of pore depth.

Table 3.1. Experimental conditions for the first and second anodizations.

	Electrolyte (1st Anod.)	Electrolyte (2^{do} Anod.)	Voltage (V)	Temperature (°C)	Time (h) (1st Anod.)	Time (h) (2^o Anod.)
a)	10wt% H ₂ SO ₄ 50wt% C ₂ H ₆ O ₂	10wt% H ₂ SO ₄ 50wt% C ₂ H ₆ O ₂	19	0	24	72
b)	0.3 M H ₂ SO ₄	0.3 M H ₂ C ₂ O ₄	20	0	3	168
c)	0.3 M H ₂ SO ₄	0.3 M H ₂ C ₂ O ₄	25	1-2	24	24
d)	0.3 M H₂C₂O₄	0.3 M H₂C₂O₄	40	1-3	24	72
e)	2wt% H ₃ PO ₄ 0.02M Al ₂ C ₆ O ₁₂	2wt% H ₃ PO ₄ 0.02M Al ₂ C ₆ O ₁₂	195	0-1	6	24

The most used AAO templates during the next chapters are those obtained with the oxalic and phosphoric acids electrolytes, i.e., d) and e), which will call from now AAO templates of 35 and 140nm, respectively. These templates have been synthesized with different pore lengths from a less than 1µm to 100 µm.

Pore widening

A great advantage of the anodic alumina template is that the pore diameter can be designed from the initial template obtained by two-step anodization. Moreover, the pore diameter can be widened, while the interpore distance remains. An easy step to achieve bigger pores consists in the immersion of the AAO inside a solution of 5-10wt% H_3PO_4 at a fixed temperature. Under these conditions the rate of oxide wet etching depends on pore length, wall composition, initial pore diameter and time. This implies that the widening rate is not lineal with the time and is different for every template. In this work we study the pore widening of the templates obtained by using oxalic and phosphoric as electrolytes, with different acid concentration and temperature, as a function of time.

Thin alumina template

In order to carry out some experimental characterizations, the aluminium substrate must be removed. This procedure consists in the immersion of the AAO template in a mixture of copper chloride (II), hydrochloric acid and water. In this way, a redox reaction takes place, where the aluminium is oxidized and the copper is reduced. Although the aluminium is removed it still remains the barrier layer in the bottom of the surface, therefore there is one face opened and the other closed. This thin template, which is very brittle and more difficult to manipulate, is necessary for several experiments later explained. Besides, it is important to distinguish between the opened and closed side. In order to achieve a AAO membrane, with both side opened, the barrier layer has to be removed by dissolving in a 10% phosphoric acid solution. After a few hours the layer is removed and some bubbles can be observed coming out from the alumina nanocavities, indicating that the barrier layer has disappeared.

3.2.2. Characterization techniques

In order to characterize the morphology and to evaluate the dimensions of the nanocavities of templates Scanning Electron Microscopy (SEM) is used. Moreover, wettability of template has been studied by contact angle measurements.

- *Scanning electron microscopy (SEM)*

A scanning electron microscope (SEM), like a transmission electron microscope, consists of an electron optical column, a vacuum system, electronics, and software. The electron gun at the top of the column produces an electron beam that is focused into a fine spot as small as 1 nm in diameter on the specimen surface. This beam is scanned over the specimen and the intensities of various signals created by interactions between the beam electrons and the specimen are measured and stored in computer memory. The stored values are then mapped as variations in brightness on the image display. The secondary electron signal is the most frequently used signal. It varies with the topography of the sample surface much like an aerial photograph: edges are bright, recesses are dark. The ratio of the size of the displayed image to the size of the area scanned on the specimen gives the magnification.³⁴

In this work, two microscopies have been employed: a Philips XL-30 ESEM operated at 25 kV and a FESEM Hitachi model SU8000 with TE detector operated at 0.5-3 kV. Figure 3.9 shows the Hitachi model microscopy.



Figure 3.9. FESEM Hitachi model SU8000 used for morphological characterization

In order to analyze the measurement of the SEM images ImageJ software has been used. ImageJ is a public domain, Java-based image processing program developed at the National Institutes of Health³⁵. ImageJ can calculate area and pixel value statistics of user defined selections and intensity threshold objects. It can measure distances and angles. It can create density histograms and line profile plots. It does geometric transformations such as scaling, rotation, and flips. The program supports any number of images simultaneously, limited only by available memory. In this work this software has been used to measure the features of AAO templates and to study the pore diameter distribution and the error.

- ***Surface Characterization by Contact Angle***

The wettability of AAO template is measured by the contact angle technique. In this work, KSV Theta goniometer with a charge coupled device camera that was used to capture the images of the water droplets for the determination of the contact angles.

The wetting behaviour of ordered nanoporous template (AAO) is studied at ambient conditions measuring 2 μ L of water drop as can be seen in Figure 3.10.



Figure 3.10. Contact Angle System employed for wettability measurement.

3.3. - Results and discussion

3.3.1. Ordered AAO templates

AAO templates with different parameters were prepared by two-step anodization process using the conditions described before. SEM technique and ImageJ software are used to measure the pore diameter, pore length and interpore distance in order to determine the dimensions of the template. The Figure 3.11 shows SEM images of the top part of the alumina layer: a) after first anodization with unordered pores, b) the same template after second anodization, where ordered pores are finally obtained, and c) is the image of the bottom pore part, once the aluminium part is removed, the barrier layer is observed.

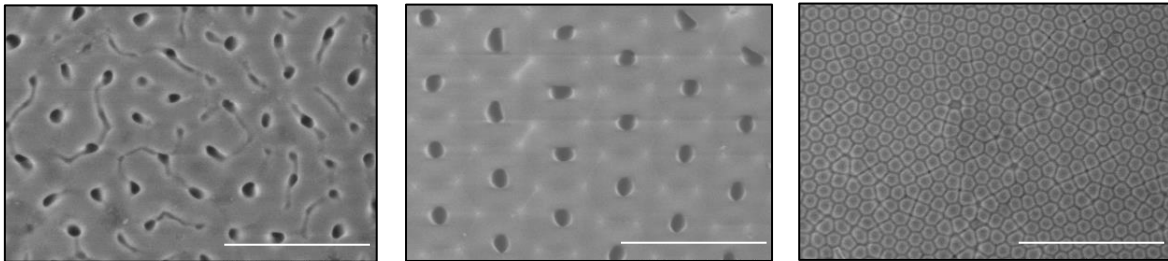


Figure 3.11. a) SEM images of the top part of the AAO after first anodization, b) the same template after second anodization and c) the bottom of the part of the template.

Table 3.2 summaries the growth rate of the pore the final diameter and the distance between pores. The calculation of errors in the measurement of diameters and interpore distance is calculated with the program ImageJ after the analysis of 100 pores. As shown in the

Table 3.2 not only the electrolytes determine the interpore distance and the growth rate of the nanocavities, but also the temperature and the voltage of the anodizing (see Table 3.1) are also important factors.

Table 3.2. Parameters (growth rate, pore diameters and interpore distances) of the obtained anodic alumina templates corresponding to the used acid electrolytes.

	Electrolyte (1st Anod.)	Electrolyte (2^{do} Anod.)	Growth rate ($\mu\text{m}/\text{h}$)	Pore diameter (nm)	Interpore distance (nm)
a)	10wt% H ₂ SO ₄ 50wt% C ₂ H ₆ O ₂	10wt% H ₂ SO ₄ 50wt% C ₂ H ₆ O ₂	0.7	17 \pm 2	50 \pm 3
b)	0.3 M H ₂ SO ₄	0.3 M H ₂ C ₂ O ₄	8.5	30 \pm 2	49 \pm 6
c)	0.3 M H ₂ SO ₄	0.3 M H ₂ SO ₄	2.5	31 \pm 3	64 \pm 5
d)	0.3 M H ₂ C ₂ O ₄	0.3 M H ₂ C ₂ O ₄	1.4	38 \pm 3	102 \pm 4
e)	2wt% H ₃ PO ₄ 0.02M Al ₂ C ₆ O ₁₂	2wt% H ₃ PO ₄ 0.02M Al ₂ C ₆ O ₁₂	3	134 \pm 7	485 \pm 26

Figure 3.12 shows the images of the AAO templates obtained under the anodization condition of the Table 3.2. As can be seen in all cases, the a-e samples, there is a homogeneous and uniformly distribution of pore size, as well as a highly densely packed hexagonal array nanoporous structure.

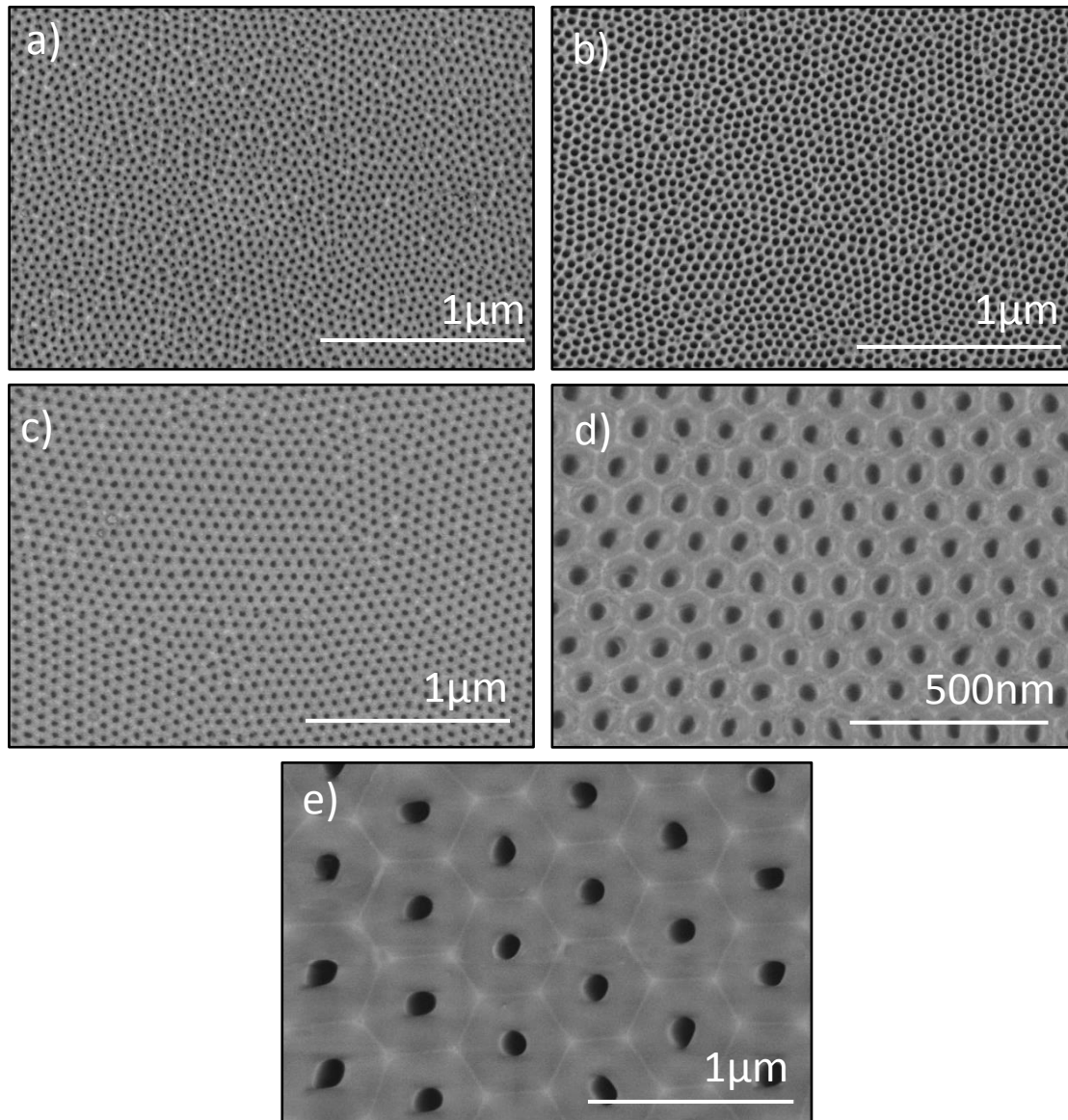


Figure 3.12. SEM images of the AAO surface obtained under different anodization conditions.

In this work the templates selected are those of oxalic and phosphoric acid electrolyte (d and e), with a pore size of 35 and 140 nm. In order to achieve bigger pore sizes is necessary to carry out a pore widening process. The length of the nanopores is controlled by the second anodization time. In this work we have employed templates from hundreds of nanometers to hundreds of microns, according to the aim of the experiment. The Table 3.3 summarizes the second anodization times and the obtained length.

Table 3.3. Anodization time to obtain AAO templates with different length

Electrolyte (2 ^{do} Anod.)	Time 2 ^o Anodization to obtain length of					
	0.7 μm	1 μm	1.5 μm	25 μm	50 μm	80 μm
0.3 M H₂C₂O₄	30min	43min	65min	17.5h	35h	57h
2wt% H₃PO₄ 0.02M Al₂C₆O₁₂	14min	20min	30min	8.3h	12h	19h

Figure 3.13 shows SEM images of the cross section of the AAO templates. This view shows homogeneous and regular nanocavities with 140nm pore diameter and the final length of the formed nanopores. Image shows in a) the short AAO template where the time of the second anodization is less than 15 minutes and 730 nm of length, image b) exhibits a longer pore length of 100 μm , where the needed time is 24 hours, and image c) presents an overview with lower magnifications, but enough to illustrate the regularity of the nanopores. The nanocavities are parallels in whole template, there are not crossed pores and the pore diameter is maintained constant along the alumina template. In order to observe this kind of images, the AAO template has been bent to break the alumina and separate the nanowires.

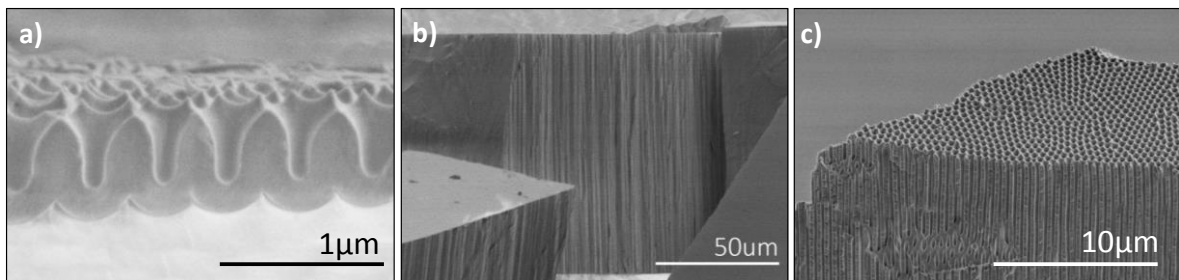


Figure 3.13. Cross section SEM images of the alumina templates obtained with different times of the second anodization. a) A short AAO template with 730nm pore length. b) A long AAO with 100 μm pore length. c) An overview with low magnification to observe the regularity of the nanocavities.

The repeatability of the process is satisfactory, so we can prepare many samples being very reliable. The diameter pore can be widened to achieve bigger nanocavities, in the next paragraph, we explain how this process is.

3.3.2. Pore widening

The widening of the pores has been described previously in the experimental part. The rate of the pore widening is studied as a function of time, for AAO templates formed from phosphoric and oxalic electrolytes. Every template has been characterized from images obtained by SEM microscopy and after measuring with ImageJ software. As an example, Figure 3.14 shows two different templates before and after widening pore process. Image a) shows an AAO template obtained using oxalic acid as electrolyte with a medium pore diameter of 38 ± 3 nm. Image b) illustrates the same template after broadening during 35 minutes in acid solution, getting a final pore diameter of 68 ± 3 nm. Image c) shows an AAO template obtained using phosphoric acid as electrolyte with a medium pore diameter of 134 ± 7 nm. Image d) illustrates the same template after broadening during 105 minutes in acid solution, getting a final pore diameter of 393 ± 12 nm.

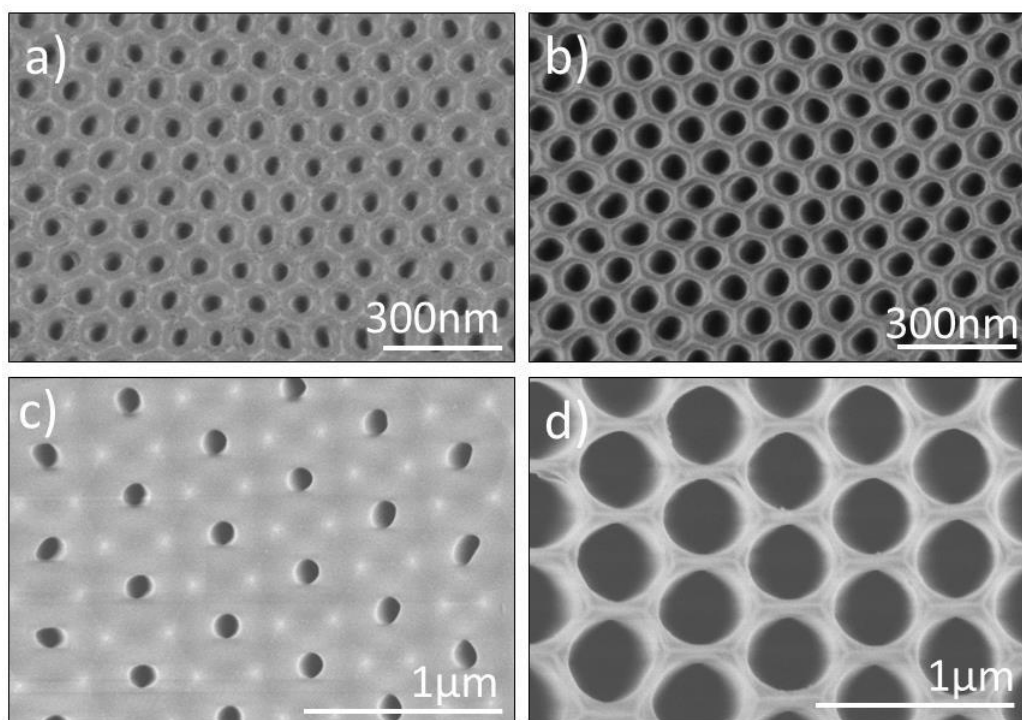


Figure 3.14. SEM images of the opened pore side AAO. Template fabricated with oxalic acid electrolyte a) before and b) after of the widening pore process. AAO fabricated with phosphoric acid electrolyte c) before and d) after of the widening pore process.

In order to study the rate of widening pore, several samples of different pore diameter have been measured at different time. The acid solution, for widening templates of 35 and 140, is 5wt% H_3PO_4 at $35^\circ C$. In addition, a complementary study in the phosphoric AAO template has been carried out, increasing the electrolyte concentration to 10wt% H_3PO_4 and decreasing the

temperature at 30°C. The resulting data of pore diameter versus time are fitted in a lineal equation. Figure 3.15 shows the dependence between the pore diameter with the time and the respective linear fit.

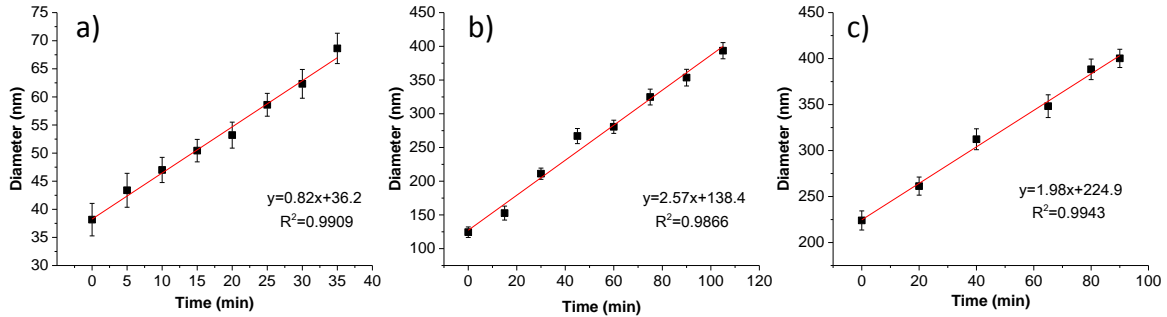


Figure 3.15. Dependence between pore diameter and duration of the pore widening. AAO obtained by two-step anodization in a) oxalic acid electrolyte and widening was carried out at 35°C in 5wt% H₃PO₄. Anodization process in phosphoric acid electrolyte widening carried out b) at 35°C in 5wt% H₃PO₄ and c) at 30°C in 10 wt% H₃PO₄

As observed in the Figure 3.15 the AAO template with pore diameter of 35 nm can be widened until 70 nm and in the case of templates with pore diameter of 140nm can be broadened until around 400nm. The rate of widening pore is calculated from the linear fit of the data, in function of the template and conditions. Where d_{final} is the desired diameter and $d_{initial}$ is the initial diameter, equations are the following:

$$\text{a) Oxalic electrolyte / 5wt\% H}_3\text{PO}_4\text{/35}^\circ\text{C: } d_{final} = 0.82 \cdot t + d_{initial}$$

$$\text{b) Phosphoric electrolyte / 5wt\% H}_3\text{PO}_4\text{/35}^\circ\text{C: } d_{final} = 2.57 \cdot t + d_{initial}$$

$$\text{c) Phosphoric electrolyte / 10wt\% H}_3\text{PO}_4\text{/30}^\circ\text{C: } d_{final} = 1.98 \cdot t + d_{initial}$$

The procedure of wet chemical etching in phosphoric acid was carefully optimized for all studied templates. It was shown that the pore diameter can be tuned by a careful fit of the etching conditions such as the electrolyte concentration and temperature. Finally an increasing in the temperature accelerates the rate of the widening pores to a greater extent than an increasing in the electrolyte concentration. Therefore, thanks to the anodization and widening processes it is possible to obtain AAO template with pore diameter from 17nm until 400nm.

3.3.3. Porosity and volume

The porosity of nanostructures templates of alumina depends on the anodization process. Parameters as the type of the electrolyte, the concentration of electrolyte, time of anodization, anodizing potential and temperature determine the diameter and the length of pores and, therefore the porosity. The structure of the template is characterized by a closed-packed array of hexagonal columns which have inside a cylindrical pore, normal to the aluminium metal surface. In Figure 3.16 illustrates a scheme of the alumina template with the characterize parameters.

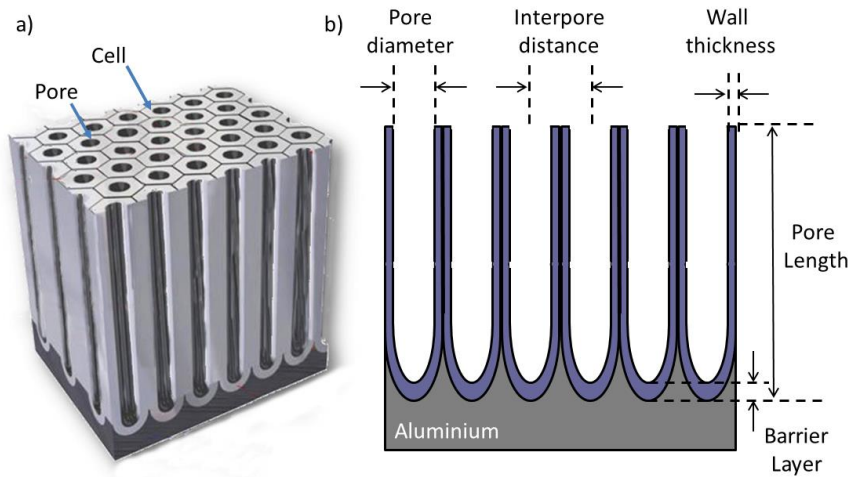


Figure 3.16. a) Idealized structure of anodic porous alumina, b) a cross-sectional view of the anodized layer

The porosity is defined as a ratio of a surface area occupied by pores (S_{pore}) to the whole surface area (S_{total}). For a single regular hexagon with one pore inside, the porosity formulation can be written as follows:

$$P = \frac{S_{pore}}{S_{total}} \quad (3.13)$$

Assuming that each single pore is a perfect circle, the following equations for S_{pore} and S_{total} can be further evolved:

$$S_{pore} = \pi \left(\frac{D_{pore}}{2} \right)^2 \quad (3.14)$$

$$S_{total} = \frac{\sqrt{3} \cdot D_c^2}{2} \quad (3.15)$$

Where D_{pore} and D_{int} are the diameter pore and the interpore distance, respectively. Substitution of the equation (3.13) and (3.14) into the equation (3.15) leads to the following expression for the porosity of a nanostructure with hexagonally arranged cells:

$$P = \frac{\pi}{2\sqrt{3}} \cdot \left(\frac{D_{pore}}{D_{int}}\right)^2 = 0.907 \cdot \left(\frac{D_{pore}}{D_{int}}\right)^2 \quad (3.16)$$

Nielsch et al.³⁶ reported that, for a perfect hexagonal arrangement of nanopores formed by self-organized anodization under optimum anodizing conditions, the ratio between pore diameter and interpore distance is almost constant and equal to 0.33–0.34. In general, the self-organized anodic porous alumina has a porosity near 10%, independently of the anodizing potential, type of electrolyte and anodizing conditions. From the equation 3.16 the porosity of the alumina template fabricated by sulfuric, oxalic and phosphoric acid and also the widening pore has been calculated and showed in Table 3.4.

Table 3.4. Calculation of the porosity by the diameter and the interpore distance.

Pore diameter(nm)	Interpore distance(nm)	Porosity (%)
17±2	50±4	8
30±2	49±6	18
31±3	64±5	13
35±3	102±4	11
60±4	102±4	29
140±7	485±26	7
300±9	485±26	34

Another factor that can be calculated to characterize the AAO template is the volume. Volume is a relevant parameter related with the amount of polymer infiltrated. AAO volume and surface area can be calculated based on structural parameters such as pore length, pore density and sample size. In this work, we have used alumina templates with a diameter of 3.2 cm. Assuming that the formed nanopores are straight and uniform, through the hexagonal structure, the length is 100 μm, and knowing the measurements of the parameters from the SEM images, we can calculate the total volume and pore density for every template. The obtained results are summarized in Table 3.5. From the difference between weight before and after infiltration process, we can calculate the infiltrated mass polymer which also depends on its density.

Table 3.5. Characteristic features of the obtained AAO Templates

Pore diameter(nm)	Interpore distance (nm)	Side hexagonal cell (nm)	Pore density (pore/cm ²)	Pore Volume (cm ³)
17±2	50±4	29	3.7·10 ¹¹	0.007
30±2	49±6	26	4.6·10 ¹¹	0.015
31±3	64±5	37	2.2·10 ¹¹	0.011
35±3	102±4	60	8.4·10 ¹⁰	0.008
60±4	102±4	60	8.4·10 ¹⁰	0.024
140±7	485±26	283	3.9·10 ⁰⁹	0.006
300±9	485±26	283	3.9·10 ⁰⁹	0.027

The results in the Table 3.5 shows that the pore density is a function of the primary template and the widening pores process does not affect the results, because the pore opening process maintains constant the numbers of the pore but increase the size and area of the pore. Therefore, it increases the alumina area of the nanocavities and their volume.

3.3.5. Wettability

The wettability has been studied by means of contact angle measurements for different AAO templates. This study has been carried out as a function of pore diameter and length. The effect of pore diameter from 15nm to 300nm has been studied in the AAO templates with the same pore length of 100 µm (black squares). While the effect of the pore length of 1, 6 and 100 microns has been studied in the AAO templates with the same pore diameter. The results are collected in Figure 3.17 where the difference has been observed between the pore length with solid symbols in red, blue and black respectively.

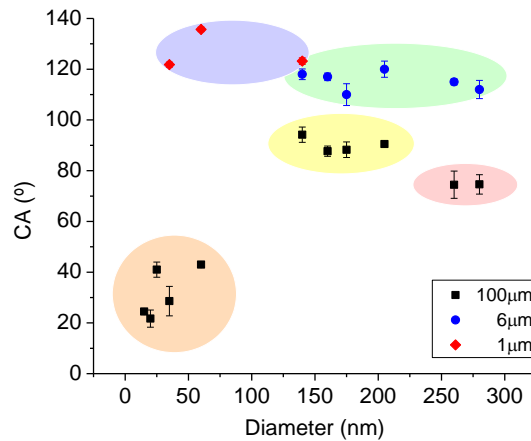


Figure 3.17. Evolution of the contact angle in function of pore diameter of AAO. Templates with pore length of 100 μm (black), 6 μm (blue) and 1 μm (red).

As can be observed in the Figure 3.17 all the values of contact angle are higher than 20°, this means that the fact of creating a porous surface of alumina increases the contact angle value since Young contact angle for smooth alumina surfaces is very hydrophilic (10-15°). The effect of the pore diameter is firstly studied. Observing the plot of **¡Error! No se encuentra el origen de la referencia.** Figure 3.17 we can conclude that there are three different cases depending on the pore diameter.

Case a), where the pore diameter is less than 60nm (orange area), the value of contact angle increase slightly from 20-40°. In this case, the values of contact angle (θ_w) are slightly higher than the flat alumina (θ_Y). This can be interpreted by the fact that the water droplet lays on the top of the pores without penetrating into the pores, because the air becomes trapped inside³⁷ (Figure 3.18 .a). Therefore, the values are close to Young contact angle, that give a largely hydrophilic character to the template.

Case b) where the pore diameter is between 140-205nm (yellow area), the values of contact angle are between 90-120°, very much higher than the values of previous case. The maximum value reached here, θ_w , is 120° for 205nm pore diameter. This can be interpreted by the fact that the drop of water does not longer wet the surface of the template, because the counter force (F_c) produced by the air trapped in the pores, is greater than the capillary force and this causes an increase in the value of the contact angle (Figure 3.18. b). This would correspond to the theory of Cassie, where the drop of water does not wet the inside of the pores increasing the hydrophobicity of the sample.

Case c), where the pore diameter is bigger than 205nm (pink area), the value of the contact angle decreases slightly as the pore diameter increases. This can be interpreted by the fact that the drop of water is placed above the surface, but part of the water invades the cavities. It increases the strength of capillarity, which causes water to penetrate into the pores (Figure 3.18.c). The length pores provides a high counterforce (F_v), which prevents that the water penetrates.

These results agree with those obtained by Li et al.²⁹, in literature, where they compared closed AAO templates (barrier layer) with open AAO templates (without barrier layer). They observed similar results with a smaller number pore diameter measurements.

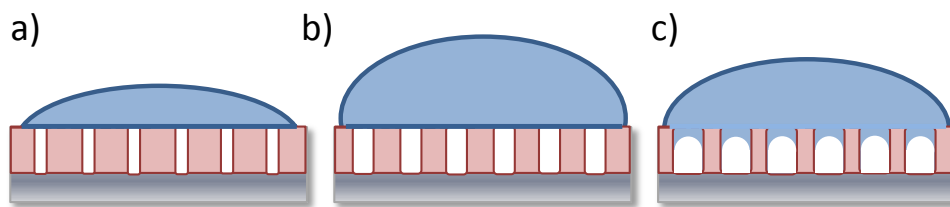


Figure 3.18. Schemes of the water drop behaviour on different type of AAO templates. There are three cases in function of pore diameter a) $dp < 60\text{nm}$, b) $60\text{nm} < dp < 200\text{nm}$ and c) $dp > 200\text{nm}$.

Concerning the pore length, the results show that as shorter pore depth the contact angle value is bigger (blue area). This means that increases the hydrophobicity of AAO templates with diameter shorter than 6 micron pores (green area). The result agrees with that found in the literature, where Buijnsters et al.³⁸ observed that porous templates undergo a transition from slightly to moderately hydrophobic surfaces when they have a pore length close to $6\mu\text{m}$. This situation would resemble Cassie theory, where the drop rests on the surface roughness produced by the pores, since air is trapped in the nanocavities preventing water penetration and increasing hydrophobicity.

3.4. Conclusions

The principal conclusions that can be drawn from the fabrication of porous anodic aluminium oxide template in this work are the following:

- Nanoporous AAO templates can be fabricated by a two-step anodization process from the aluminium foils. The result is a homogeneous and uniform distribution of pore size as well as a highly densely packed hexagonal array of nanoporous structure. Moreover, the process repeatability is satisfactory, so AAO nanocavities are very reliable.
- The experimental anodization conditions such as the nature and concentration of the electrolyte, voltage, temperature and time determine the features of the fabricated template. The concentration and the type of electrolyte with the temperature and the voltage define the interpore distance and the pore diameter. The time in the second anodization process determines the length of the nanocavities ranging from hundreds of nanometers to hundreds of microns. The pore widening rate is a function of time and the type of template.
- Features such as porosity and volume can be easily studied for every AAO template. Porosity of the templates is determined by the anodization conditions, while volume pore is also affected by the widening pore process.
- The hydrophobicity of the AAO templates has been determined from water contact angle measurements. Alumina is a hydrophilic material with a low contact angle (10-15°) but when the flat surface is changed to a porous one the contact angle value increases, therefore, changes their wettability towards a hydrophobic material. Template with the same pore length raises a maximum hydrophobicity at medium pore diameter and then it slightly decreases. Templates with smaller pore length are more hydrophobic.

3.5. Reference

- (1). Sulka, G. D., Highly Ordered Anodic Porous Alumina Formation by Self-Organized Anodizing. In *Nanostructured Materials in Electrochemistry*, Wiley-VCH Verlag GmbH & Co. KGaA: 2008; pp 1-116.
- (2). Masuda, H.; Fukuda, K. Ordered metal nanohole arrays made by a two-step replication of honeycomb structures of anodic alumina. *Science* **1995**, *268*, (5216), 1466.
- (3). Keller, F.; Hunter, M.; Robinson, D. Structural features of oxide coatings on aluminum. *Journal of the Electrochemical Society* **1953**, *100*, (9), 411-419.
- (4). Thompson, G.; Furneaux, R.; Wood, G.; Richardson, J.; Goode, J. Nucleation and growth of porous anodic films on aluminium. **1978**.
- (5). Masuda, H.; Hasegawa, F.; Ono, S. Self-ordering of cell arrangement of anodic porous alumina formed in sulfuric acid solution. *Journal of the Electrochemical Society* **1997**, *144*, (5), L127-L130.
- (6). Jeong, S. H.; Jung, S. H.; Lee, K. H. Preparation of Anodic Alumina Nanotemplate and its Applications. *J. Korean Ind. Eng. Chem.* **2005**, *16*, (4), 461-473.
- (7). Na, Y.; Farva, U.; Cho, S. M.; Park, C. Synthesis and optimization of porous anodic aluminum oxide nano-template for large area device applications. *Korean J. Chem. Eng.* **2009**, *26*, (6), 1785-1789.
- (8). Desmaret, V. Nanoestructuras poliméricas eléctricamente conductoras confinadas en aluminio anodizado. De la síntesis a la caracterización. Escuela Técnica Superior de Ingenieros Industriales Madrid, 2013.
- (9). Thompson, G. E.; Wood, G. C. Porous anodic film formation on aluminium. *Nature* **1981**, *290*, (5803), 230-232.
- (10). O'Sullivan, J. P.; Wood, G. C. The Morphology and Mechanism of Formation of Porous Anodic Films on Aluminium. *Proceedings of the Royal Society of London A: Mathematical, Physical and Engineering Sciences* **1970**, *317*, (1531), 511-543.
- (11). Jessensky, O.; Müller, F.; Gösele, U. Self-organized formation of hexagonal pore arrays in anodic alumina. *Applied Physics Letters* **1998**, *72*, (10), 1173-1175.
- (12). Patermarakis, G.; Tzouvelekis, D. Development of a strict kinetic model for the growth of porous anodic Al₂O₃ films on aluminium. *Electrochimica Acta* **1994**, *39*, (16), 2419-2429.
- (13). Su, Z.; Hahner, G.; Zhou, W. Investigation of the pore formation in anodic aluminium oxide. *Journal of Materials Chemistry* **2008**, *18*, (47), 5787-5795.
- (14). Patermarakis, G. Development of a theory for the determination of the composition of the anodizing solution inside the pores during the growth of porous anodic Al₂O₃ films on aluminium by a transport phenomenon analysis. *Journal of Electroanalytical Chemistry* **1998**, *447*, (1-2), 25-41.
- (15). Våland, T.; Heusler, K. E. Reactions at the oxide-electrolyte interface of anodic oxide films on aluminum. *Journal of Electroanalytical Chemistry and Interfacial Electrochemistry* **1983**, *149*, (1), 71-82.
- (16). Poinern, G. E. J.; Ali, N.; Fawcett, D. Progress in Nano-Engineered Anodic Aluminum Oxide Membrane Development. *Materials* **2011**, *4*, (3), 487.

- (17). Hoar, T. P.; Yahalom, J. The Initiation of Pores in Anodic Oxide Films Formed on Aluminum in Acid Solutions. *Journal of the Electrochemical Society* **1963**, *110*, (6), 614-621.
- (18). Bae C., Y. H., Kim S., Lee K., Kim J., Sung M., and Shin H. Template-Directed Synthesis of Oxide Nanotubes Fabrication, Characterization, and Applications. *Chem.Mater* **2008**, *20*, 756-767.
- (19). Hurst, S. J.; Payne, E. K.; Qin, L.; Mirkin, C. A. Multisegmented One-Dimensional Nanorods Prepared by Hard-Template Synthetic Methods. *Angewandte Chemie International Edition* **2006**, *45*, (17), 2672-2692.
- (20). Lai, M.; Riley, D. J. Templated electrosynthesis of nanomaterials and porous structures. *Journal of Colloid and Interface Science* **2008**, *323*, (2), 203-212.
- (21). Wirtz, M.; Yu, S.; Martin, C. R. Template synthesized gold nanotube membranes for chemical separations and sensing. *The Analyst* **2002**, *127*, (7), 871-879.
- (22). Wenzel, R. N. Resistance of solid surfaces to wetting by water. *Industrial & Engineering Chemistry* **1936**, *28*, (8), 988-994.
- (23). Cassie, A. B. D.; Baxter, S. Wettability of porous surfaces. *Transactions of the Faraday Society* **1944**, *40*, (0), 546-551.
- (24). Marmur, A., Solid-surface characterization by wetting. In *Annual Review of Materials Research*, 2009; Vol. 39, pp 473-489.
- (25). Daniel, R. C.; Berg, J. C. Spreading on and penetration into thin, permeable print media: Application to ink-jet printing. *Advances in Colloid and Interface Science* **2006**, *123-126*, 439-469.
- (26). de Gennes P-G., B.-W. F., Quere D., *Capillarity and Wetting Phenomena: Drops, Bubbles, Pearls, Waves*. New York, 2004.
- (27). Gast, A. W. A. a. A. P., Physical Chemistry of Surfaces. In *Chapter II*, Sons, J. W., Ed. New York, 1997; Vol. Section 4.
- (28). Ran, C.; Ding, G.; Liu, W.; Deng, Y.; Hou, W. Wetting on Nanoporous Alumina Surface: Transition between Wenzel and Cassie States Controlled by Surface Structure. *Langmuir* **2008**, *24*, (18), 9952-9955.
- (29). Li, Z.; Wang, J.; Zhang, Y.; Wang, J.; Jiang, L.; Song, Y. Closed-air induced composite wetting on hydrophilic ordered nanoporous anodic alumina. *Applied Physics Letters* **2010**, *97*, (23), 233107.
- (30). Lee, K. P.; Leese, H.; Mattia, D. Water flow enhancement in hydrophilic nanochannels. *Nanoscale* **2012**, *4*, (8), 2621-2627.
- (31). Megias-Alguacil, D.; Tervoort, E.; Cattin, C.; Gauckler, L. J. Contact angle and adsorption behavior of carboxylic acids on α -Al₂O₃ surfaces. *Journal of Colloid and Interface Science* **2011**, *353*, (2), 512-518.
- (32). Martín, J. Nanoestructuras poliméricas unidimensionales "a la carta". Del confinamiento a las potenciales aplicaciones. Universidad Complutense, Madrid, 2010.
- (33). Maiz, J. Fabrication of polymer nanostructures by "Template Synthesis" and polymer properties under confinement. Universidad del País Vasco, San Sebastián- Guipuzcoa, 2013.
- (34). FEI An Introduction to Electron Microscopy. The Scanning Electron Microscope.

- (35). Schneider, C. A.; Rasband, W. S.; Eliceiri, K. W. NIH Image to ImageJ: 25 years of image analysis. *Nat Meth* **2012**, *9*, (7), 671-675.
- (36). Nielsch, K.; Choi, J.; Schwirn, K.; Wehrspohn, R. B.; Gösele, U. Self-ordering Regimes of Porous Alumina: The 10 Porosity Rule. *Nano Letters* **2002**, *2*, (7), 677-680.
- (37). Raspal, V.; Awitor, K.; Massard, C.; Feschet-Chassot, E.; Bokalawela, R.; Johnson, M. Nanoporous surface wetting behavior: The line tension influence. *Langmuir* **2012**, *28*, (30), 11064-11071.
- (38). Buijnsters, J. G.; Zhong, R.; Tsyntsar, N.; Celis, J. P. Surface wettability of macroporous anodized aluminum oxide. *ACS Applied Materials and Interfaces* **2013**, *5*, (8), 3224-3233.

Chapter 4

RADICAL POLYMERIZATION OF MMA IN AAO NANOREACTORS

This chapter describes the study of free radical polymerization of methyl methacrylate in bulk and in confinement in the nanocavities of the AAO template, using the nanopores as nanoreactors. It includes a mathematical model to explain the differences between polymerization in bulk and in confinement. It also describes the chemical, thermal, morphological and surface characterization of the obtained PMMA nanostructures.

4.1 Introduction

Thermoplastics are among the most industrially important polymers and radical polymerization is still the most common process by which they are synthesized. The commercial importance of these polymers has driven extensive research into the polymerization kinetics and, at least for the most common vinyl monomers, a comprehensive picture has been built, allowing us to understand how reaction kinetics impact on macromolecular structure. Whilst these bulk scale materials have become essential for everyday life, there is a growing desire to produce nanomaterials with well-defined structural features, mimicking those of natural systems. As a consequence, over the last few years, there have been reported an extensive number of publications concerning the study of polymerization reactions in confined systems such as, inorganic zeolites, metal-organic frameworks (MOFs), porous glass, porous coordination polymers and the nanocavities of AAO templates¹⁻⁶ (see chapter 2. State of the art). Previous studies using different types of polymerization mechanism (radical, polyaddition, ring-opening and so on.) have shown that by confining the polymerization to dimensions approaching those of an individual polymer chain the reaction kinetics and resulting polymer structure are changed significantly.⁷⁻¹⁰

Focusing on the polymerization of methyl methacrylate (MMA), there are several studies of free radical polymerizations in different confinement systems. For instance, Uemura *et al.* studied the radical polymerization of methyl methacrylate in the nanochannels of porous coordination polymers (PCPs) and demonstrated a significant effect of the channel size on the yield, molecular weight, and stereoregularity of the resulting polymer. They also confirmed a narrow polydispersity and an increase in the degree of isotacticity in the obtained polymers and a pore size effect in the initiation step of polymerization.^{11, 12} Li *et al.*¹³ and Kalogeras and Neaegu¹⁴ reported that the polymerization of MMA in silica gel

nanopores led to an increase in molecular weight and in the glass transition temperature (T_g) of the obtained poly(methyl methacrylate) (PMMA). As already mentioned in the chapter 2, Simon's group reported a detail study about the polymerization of MMA in controlled pore glasses (CPG) with various pore diameters and observed a catalytic effect due to the silanol groups on the walls of the hydrophilic pores leading to a faster polymerization rate with decreasing pore size.⁸ In addition, they showed that molecular weight of the nanostructured polymer increases, polydispersity index decreases and glass transition temperature increases for reactions conducted in nanoconfinement compared to the corresponding bulk system.⁹

One of the major difficulties in establishing the impact of nanoconfinement on reaction kinetics is the variety of possible effects occurring simultaneously during the reaction. This also complicates the modeling of polymerization kinetics under confinement, which has been scarcely reported in the literature. However, two papers of Simon et al.^{15, 16} studied the modeling free radical polymerization under confinement in porous system using Control Pore Glasses (CPG). The authors also developed a mathematical approach to study the autoaccelerated radical polymerization process in confinement and found that chemical interactions, for instance wall effects on the rate of initiation, propagation, and termination, and also effects arising from the physical confinement of polymer chains affects the diffusion rate of macromolecules. The effects in the model of nanoconfinement were compared with experimental data.

One system that closely fulfills the requirements of a precision nanoreactor (or confined system) is nanoporous anodic aluminium oxide (AAO) templates prepared by a two-step electrochemical anodization process. In this case, the size of nanocavities can be adjusted and the pores are highly monodisperse, therefore the reactor should be easily modeled.

Therefore, the above mentioned AAO templates offer a good chance to study the polymerization of methyl methacrylate monomer (MMA) in confined. In order to gain a deeper understanding of the structural differences between polymers synthesized in bulk and those synthesized under nanoconfinement it is necessary to have a better appreciation of the different kinetic features of polymerizations conducted under nanoconfinement. Therefore, the main objective of this chapter is the kinetic study of autoaccelerated polymerization reaction of methyl methacrylate at different temperatures under confinement within AAO nanocavities of different dimensions as compared to bulk

polymerization. In order to explain the free radical polymerization of this monomer inside the nanoreactor a mathematical model was applied considering factors that arise from the chemical interactions of radical species with the pore wall and the physical effects due to changes in diffusivity under nanoconfinement. Besides, the properties such as thermal, chemical and surface of the confined PMMA have been studied.

4.2. Experimental part

Materials and AAO templates

Methyl methacrylate (MMA) and 2,2'-azobis-isobutyronitrile (AIBN) initiator were purchased from Sigma-Aldrich. The inhibitor was removed by distillation under reduced pressure with magnesium sulfate and the initiator was purified by recrystallization from methanol before use. Polymethylmethacrylate (PMMA) with $M_w = 64\ 000\ \text{g mol}^{-1}$. AAO templates having pores of 35, 60 and 140 nm diameter and 100 μm length were prepared by the two-step anodization method as reported in Chapter 3.2.

In-situ polymerization of MMA in AAO templates

A previous study of in situ polymerization of MMA was performed by Raman spectroscopy. With this technique is possible to monitor the progress of the reaction by the ratio of two bands, the band of $1640\ \text{cm}^{-1}$ which belongs to the group of C=C of the monomer and the band of $1720\ \text{cm}^{-1}$ which corresponds to the group of C=O that remains constant. In this case the polymerization of the MMA was carried in three different AAO templates (35, 60 and 140nm) with the aluminum support (for better handling) inside an oven with temperature, 55°C , and nitrogen atmosphere. The mixture of MMA and AIBN (0.5% in weight respect to monomer) was purged with nitrogen for 30 min and stored in a freezer at -20°C until use. The solution (monomer/initiator) was placed on the top of the template, open pore side, with a syringe. Absorption of the solution into the template occurs quickly as a result of the capillary force and polarity of the solution. The reaction was stopped by withdrawing the sample from the oven at different times and keeping the sample in the freezer (-18°C).

Polymerization reaction was studied by DSC. For that, first the aluminium was removed from the AAO with a solution of HCl, CuCl_2 and H_2O to obtain a thinner alumina template. Samples were prepared in two different AAO templates with varying pore diameter (only 35 and 60 nm) and placed inside hermetic pans of 50 μL , with an area of 19mm^2 . In order to achieve the highest possible volume of resin, several layers of alumina were placed inside the pan. The amount of template used was between 38-42mg. Depending on the pore volume of the AAO and taking into account the density of

alumina,¹⁷ 2.3 g cm^{-3} , and the density of MMA 0.94 g cm^{-3} , the final amount of resin inside the alumina was 2-5mg.

Polymerization reactions were performed in a Perkin Elmer differential scanning calorimeter (DSC) under isothermal conditions. The polymerizations were conducted at temperatures lower than the T_g of PMMA, therefore the polymerization did not reach full conversion due to the glass effect. This glass effect or the vitrification effect is observed when the glass transition temperature of the reaction rises above the reaction temperature, therefore the reaction can not achieve the total conversion. In order to achieve the 100% of polymer conversion, at the end of the isothermal process, the system was cooled down to $30 \text{ }^\circ\text{C}$ then heated to $150 \text{ }^\circ\text{C}$ at $10 \text{ }^\circ\text{C}/\text{min}$. This dynamic scan was performed twice. The effect of confinement on the polymerization reaction was studied in 35 and 60nm at 80°C , whilst kinetic study was performed at 60, 70, 80 and 90°C in AAO template of 60 nm pore diameter.

Bulk polymerization of MMA

Bulk polymerization of MMA was carried out in DSC equipment with the same mixture of MMA and AIBN, at different temperatures 60, 70, 80, 90°C following the same method described above.

Infiltration of PMMA in AAO

In order to study surface properties by contact angle, a PMMA film has been infiltrated in three different AAO templates with a length of 1 micron and diameter of 35, 60 and 140nm. Firstly a film of PMMA was prepared by solvent-casting. PMMA was dissolved in toluene solvent (10%wt). A thin film of thickness about $50 \text{ }\mu\text{m}$ was made by solvent-casting onto a clean Petri dish after drying the film for several days. In order to infiltrate PMMA in AAO nanocavities by capillarity forces the film was placed over the AAO open side in an oven at 180°C under vacuum. The equipment employed for polymer infiltration inside AAO is a cylindrical oven fabricated and designed in our laboratory, with controlled atmosphere and temperature. It was connected to a vacuum pump and a nitrogen bullet, and with a key it can be changed the atmosphere. Normally, the vacuum is used to dry the template and to infiltration process, but in some cases, nitrogen atmosphere was used to avoid oxidative degradation of the polymer. The temperature maximum reached was up to 250°C . The Figure 4.1 shows the set-up of the equipment.

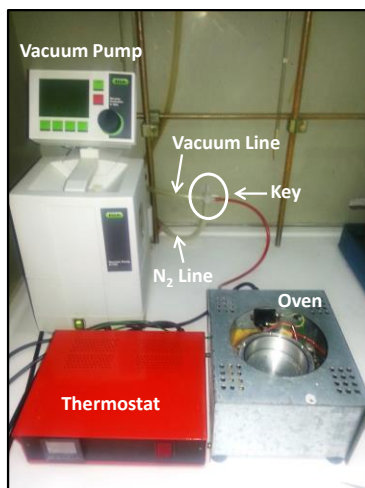


Figure 4.1. Imagen of the equipment employed for infiltration process. It consists of a vacuum pump, a thermostat, an oven and a key to control the vacuum or nitrogen atmosphere.

In order to help the infiltration of this polymer, a weight (55g) was placed on top during three days. The PMMA nanorods were obtained after removing the aluminum substrate with a mixture of HCl, CuCl₂, and H₂O, and the alumina was dissolved with a sodium hydroxide aqueous solution (5%wt) for 1hour.

Infiltration of AIBN in AAO

To infiltrate the initiator inside de AAO, a solution of 1% AIBN in acetone was prepared and placed in contact with the template until total evaporation of acetone. The residual AIBN on the surface was carefully removed with a blazer. Kinetic study was carried out in DSC by isothermal scan at three different temperatures (90, 92 and 94°C).

Characterization techniques

- ***Scanning electron microscopy***

Scanning Electron Microscopy (SEM) was used for the morphological study. The in-situ polymerized nanofibers and infiltrated PMMA were morphologically characterized by Hitachi microscopy model SU8000 with TE detector operated at 0.5-3 kV (described in Chapter 3.2.) In order to observe the polymer nanofibers inside the AAO, the preparation of these samples was carried out by fracture under cryogenic temperatures.

- *Raman spectroscopy*

Raman spectroscopy was used for the chemical and polymerization kinetics study. The spectroscopic technique is based on inelastic scattering of monochromatic light, usually from a laser source. Inelastic scattering means that the frequency of photons in monochromatic light changes upon interaction with a sample. Photons of the laser light are absorbed by the sample and then reemitted. Frequency of the reemitted photons is shifted up or down in comparison with original monochromatic frequency, which is called the Raman effect. This shift provides information about vibrational, rotational and other low frequency transitions in molecules.¹⁸ This equipment is particularly suited to the study of organic polymeric materials because of the sensitivity of the technique to the structure of molecules containing nonpolar species such as C-C and C=C which commonly make up the backbone of synthetic polymers. The ν (C=C) feature which is weak in infrared absorption is dominant in the Raman scattering for example. The study of the polymer sample can be carried out in powder, film, solid, filament, or solution with little sample preparation.

Confocal Raman spectroscopy has been used to study the composition gradient of one dimension system, through the depth of the sample in the micrometer scale.¹⁹⁻²² Moreover, Raman spectroscopy has been also employed to characterize the chemical composition of the polymers.

Raman scattering was excited with a laser diode near-infrared 320mW 785nm with maximum input power. A lens NA090 100x magnification was used to focus the laser beam with a power of 0.1W incident on the sample, giving a diameter of $\pm 1 \mu\text{m}$ laser spot. With this objective lens, the sampling depth is estimated at about 4-5 μm (average width profile confocal depth of a silicon wafer) and the lateral resolution is estimated of about 1 μm with the system operated in the confocal mode. Raman scattered radiation is focused through an aperture of a pinhole.

The equipment is a Renishaw InVia Raman Microscope (Renishaw plc, Wotton-under-Edge, UK) see Figure 4.2, which was used to fit with a grating spectrometer of 1200 lines per mm and a Peltier-cooled hargecoupled device (CCD) detector, coupled to a confocal microscope. All spectra were processed using Renishaw WiRE 3.3 software. The temperature control cell will be explain and used in the chapter 5.



Figure 4.2. Renishaw InVia Raman Microscope. Equipment employed for chemical characterization.

The study of the intensities of spectral bands can enable us to achieve quantitative measurements and identify the spectra given by different materials. Band area is statistically more significant than the band height, as they use more than one data point in the spectrum and can be independent of resolution.

Raman technique has been used to study the polymerization of methyl methacrylate inside the nanopores of AAO templates of 35nm pore diameter and 100 μ m of length. Once the polymerization reaction was stopped, measurements were carried out ex situ by Raman spectroscopy.

- ***Gel permeation chromatograph***

Gel Permeation Chromatograph (GPC) is used to study the molecular weight of the synthesized polymer. This technique is a type of size exclusion chromatography (SEC) that separates and analyses sample on the basis of size. For that, samples are dissolved in an appropriate solvent and after filtering the solution it is injected onto a column. The quantification is made from calibration patron curves. In our case, the GPC set up consisted of a pump (LC-20A, Shimadzu), an autosampler (Waters 717), a differential refractometer (Waters 2410) and three columns in series (Styragel HR2, HR4 and HR6 with pore sizes ranging from 102 to 106 Å). Chromatograms were obtained in THF (HPLC grade) at 35 °C using a flow rate of 1 ml/min⁻¹. The equipment was calibrated using narrow polystyrene standards ranging from 595 to 3.95 × 10⁶ Da (5th order universal calibration). In order to know the molecular weight of the synthesized polymer, the AAO templates filled with PMMA were placed in vials with 1ml of tetrahydrofuran (THF)

solvent and left in a digital shaker during 3 days to dissolve the polymer. The diluted polymer was filtered using a PTFE filter of 0.2 μm .

- ***Differential scanning calorimetry***

Differential Scanning Calorimetry (DSC) was used to study the polymerization kinetics and the physical aging. This technique considers the response of polymers to heating, and measures the difference in the amount of heat required to increase the temperature of the sample respect to the reference. DSC can be used to study crystallinity and melting process, glass transitions, phase changes, and polymerization reactions. In this chapter, this technique has been used to follow the kinetics of polymerization reaction and the properties of the PMMA polymerized inside the template. Besides, the physical aging of the bulk and confined polymers has been studied, with this technique. The equipment used was a Perkin Elmer differential scanning calorimeter DSC 8500 with intracooler 2P and nitrogen purge gas (see Figure 4.3). Indium was used to calibrate the enthalpy and temperature at 10 $^{\circ}\text{C}/\text{min}$. Samples were sealed in aluminium hermetic pans of 50 μL . Alumina templates, with solution of monomer and initiator, are placed inside aluminium.



Figure 4.3. Perkin Elmer DSC. The equipment employed for polymerization and thermal characterization.

- ***Contact Angle***

In this work contact angle measurements were performed using KSV Theta goniometer (described in Chapter 3.2). A charge coupled device camera was used to capture the images of the water droplets for the determination of the contact angles. The nanostructured film was deposited onto glassy supports and the contact angles were measured in the air-film surface using 2 μL of water drop.

4.3. Radical polymerization kinetic model

A number of models have been developed to describe the kinetics of diffusion controlled free radical polymerizations.²³⁻²⁷ Marten et al.²⁷ described the development of a semi-empirical model based on the *free volume theory* which assumed no chain length dependence and fitted number-average molecular weight data with adjustable constants obtained from polymerization rate data, nevertheless they failed to fit weight-average and higher average molecular weight data. Previous models assumed that the residual termination rate constant is proportional to the frequency of monomer addition to the radical chain end. Later Soh et al.²⁶ established a proportionality parameter A, in function of an efficiency factor. Later the parameters of the Achilias et al.²⁵ model had a physical meaning, but these were not available either for many monomer-polymer systems or for other components like solvents. Also, Achilias' model did not describe better the entire conversion range than the other models, especially in the region of high conversion. Later, Tefera et al.²⁴ studied the influence of diffusion process on the propagation rate of polymerization of MMA to a very high conversion, and found that this was negligible compared to the influence of the cage effect on the radical efficiency. The presented model was also tested for polymerizations conducted in the presence of solvent and/or chain transfer agents. Latter Achilias with Verros²³ increased the knowledge of two different approaches to model diffusion controlled free radical polymerization. Namely the free volume model, and the entanglement theory were compared. All the diffusion-controlled phenomena were taken into account, including gel, glass and cage effects as well as residual termination.

The kinetic model used here was based on the free volume approach.²⁷ In this model, the time dependent number of moles and volume is given by

$$\frac{dN_G}{dt} = V_{r_G} = V_0(1 + \epsilon X)r_G \quad (4.1)$$

$$\frac{dV}{dt} = V_0\epsilon(1 - X)k_p \sum R_n \quad (4.2)$$

where N_G is the number of moles of species G , V_0 is the initial volume of the reaction mixture, ϵ is the volume contraction factor, X is the conversion, r_G is the reaction rate of

species G , k_p is the propagation constant and R_n is the concentration of free radicals with n monomer units.

The kinetic model, based on the kinetic scheme in Table 4.1, considers the elementary processes of initiation, propagation and termination to give the following rate equations 4.3 - 4.6 for the reaction rate of initiator (r_I), monomer (r_M), active radicals with n monomer units (r_{R_n}) and dead polymer with n monomer units (r_{P_n}). The model makes the assumption that contributions to chain termination from chain transfer to monomer and termination by combination are insignificant, both fair assumptions for methyl methacrylate.

$$r_I = -k_d I \quad (4.3)$$

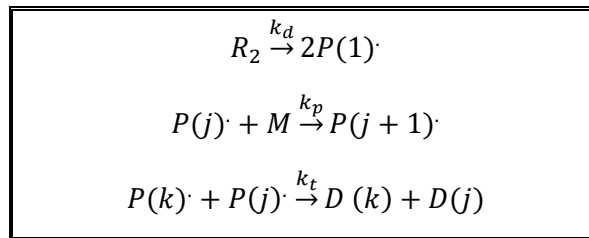
$$r_M = -k_p M \sum_{m=1}^{\infty} R_m \quad (4.4)$$

$$r_{R_n} = 2fk_d I \delta_{1n} + k_p M (R_{n-1} - R_n) - R_n k_t \sum_{m=1}^{\infty} R_m = 0 \quad (4.5)$$

$$r_{P_n} = R_n k_t \sum_{m=1}^{\infty} R_m \quad (4.6)$$

where M and I are monomer and initiator concentrations respectively and f is the initiator efficiency. k_d , k_p , k_t are the rate coefficients of initiator dissociation, propagation and termination by disproportionation, respectively, and δ is the Kronecker delta which gives $\delta=1$ where $n=1$ and $\delta=0$ for all other numbers. Equation 4.5 is set to 0 according to the assumption of the quasi steady state approximation.

Table 4.1. Kinetic scheme for free radical polymerization of MMA.



In order to account for the change in rate coefficients with conversion, the approach of Marten and Hamielec was followed.²⁷ Following this theory, it is assumed that the free volume, V_f , decreases with conversion according to

$$V_f = [0.025 + \Delta\alpha_p(T - T_{gp})]\Phi_p + [0.025 + \Delta\alpha_m(T - T_{gm})](1 - \Phi_p) \quad (4.7)$$

where α_m and α_p are the expansion coefficients of the monomer and polymer respectively, T is the reaction temperature, T_{gp} and T_{gm} are the glass transition temperatures of the polymer and monomer respectively and the volume fraction of polymer ϕ_p is given by

$$\Phi_p = \frac{X(1+\epsilon)}{1+\epsilon X} \quad (4.8)$$

The value of T_{gp} is calculated from

$$T_{gp} = T_{gp}^{\infty} - Q \left(\frac{1}{M_n} \right) \quad (4.9)$$

where Q is a constant that gives the molecular weight dependence of the T_{gp} . At some point in the polymerization, the free volume reaches a critical point where the termination reaction begins to become diffusion controlled. At this point the relationship

$$\overline{M}_w^{-m} \exp\left(\frac{A}{V_f}\right) = K_3 \quad (4.10)$$

is satisfied. A and m are constants which are taken from the work of Hamielec.²⁷ The cumulative molecular weight and free volume at this stage are designated as $\overline{M}_{w,cr}$ and $V_{f,cr1}$. After that, the diffusion controls the rate coefficient of termination, such that

$$k_{t'} = k_{t0} \left(\frac{\overline{M}_{w,cr}}{\overline{M}_w} \right)^n \exp\left(-A \left(\frac{1}{V_f} - \frac{1}{V_{f,cr1}} \right)\right) \quad (4.11)$$

At high conversion the diffusion of polymer chains is decreased to the point where $k_{t'}$ approaches zero. In this region the migration of the radical chain end by propagation of monomer units becomes significant²⁸. This so called “residual termination” term, $k_{t,res}$, is incorporated into the overall value of the termination rate coefficient by

$$k_t = k_{t'} + k_{t,res} = k_{t'} + f_{res} k_p [M] \quad (4.12)$$

where f_{res} is a proportionality constant. At high conversion another critical point, $V_{f,cr2}$ is reached in which the propagation becomes diffusion controlled (glass effect) and the rate coefficient for propagation is given by

$$k_p = k_{p0} \exp\left(-B \left(\frac{1}{V_f} - \frac{1}{V_{f,cr2}} \right)\right) \quad (4.13)$$

where B is a constant taken from the work of Hamielec²⁷. Similarly, the initiator efficiency is expected to decrease at high conversion. This decrease may be different from that of k_p but in order to reduce the number of parameters the same function was used due to the similar size of the monomer and initiator radicals.

$$f = f_0 \exp\left(-B\left(\frac{1}{V_f} - \frac{1}{V_{f,cr2}}\right)\right) \quad (4.14)$$

As reported in the literature,¹⁶ the rapid reduction in k_p and f at the later stages of the reaction results in a limiting conversion being reached. In addition, the glass transition temperature may be altered by nanoconfinement effects. The glass transition can be approximated to scale with the diameter of the AAO cylinder²⁹ and thus under nanoconfinement equation 4.9 is modified to give

$$T_{gp,nano} = T_{gp}^{\infty} - Q\left(\frac{1}{M_n}\right) + C/D \quad (4.15)$$

where C is a constant and D is the diameter of the porous template. In order to account for the increased rate of polymerization in the early stages under nanoconfinement we consider an increase in the rate coefficient for the decomposition of the initiator due to the enhanced decomposition of the initiator at the template walls, $k_{d,wall}$, to be such that

$$k_d = k_{d0} + \frac{k_{d,wall}}{D} \quad (4.16)$$

The molecular weights are determined from the k^{th} moments of the chain length distribution of the free radicals (λ_k) and dead chains (μ_k) given by

$$\lambda_k = \sum_{n=1}^{\infty} n^k R_n \quad (4.17)$$

$$\mu_k = \sum_{n=1}^{\infty} P_n \quad (4.18)$$

The number average molecular weight, M_n , of the material can be calculated from

$$\overline{M}_n = W_m \frac{(\mu_1 + \lambda_1)}{(\mu_0 + \lambda_0)} \quad (4.19)$$

4.4. Results and discussion

4.4.1. Free radical polymerization of the MMA in confinement and bulk

Morphological characterization

The first evidence that the synthesis of polymethylmethacrylate has been achieved in confinement is obtained by scanning electron microscopy (SEM). The free radical polymerization of MMA was conducted within AAO templates (with pore diameter of 35, 60 and 140nm) at 80°C during 90 min. SEM microscopy were used to determine the nanostructure of the obtained polymer. Figure 4.4 a, b and c shows PMMA nanofibers (colored to guide the eye) in the alumina pore of broken template (in grey) with different pore diameter 35, 60 and 140 nm respectively. The Figure 4.4 d, e and f corresponds to the free nanofibers after removing the template. From the images, it can be seen that the nanofibers formed by free radical polymerization filled the pores of the AAO templates. This shows that in-situ polymerization in AAO nanocavities is a convenient way to obtain nanofibers, being faster and requiring lower temperatures than the alternative method of polymer infiltration, which requires around 12 hours at temperatures of 220°C³⁰.

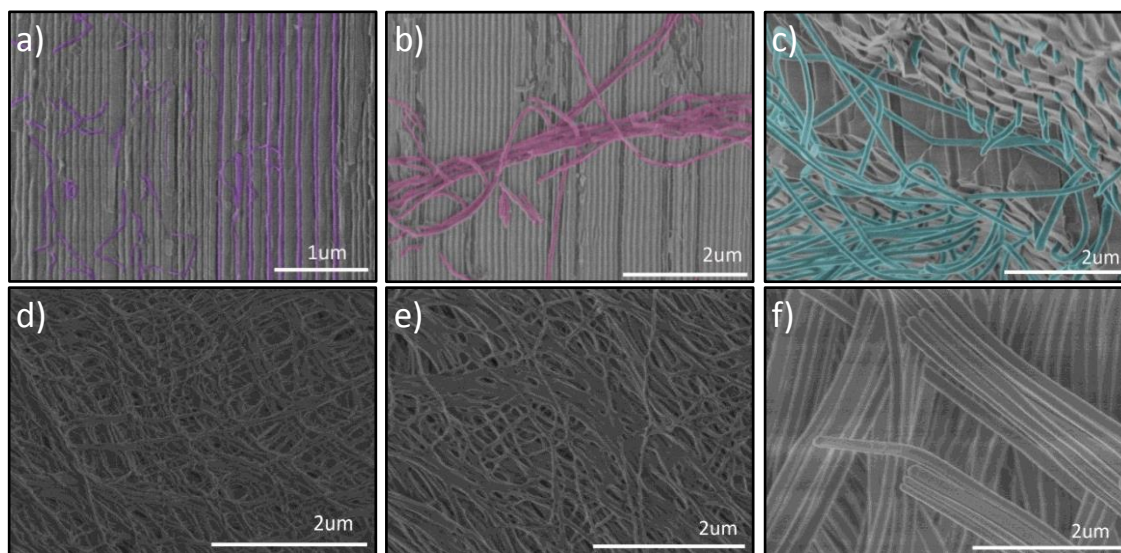


Figure 4.4. SEM images of broken AAO with PMMA nanofibers polymerized inside nanocavities: a) AAO 35, b) AAO 60 and c) AAO 140nm. Figures d), e) and f) correspond the respectively fibers after removing the template.

Monitoring by Raman spectroscopy

The characterization of the AAO template filled with the MMA monomer was carried out by Raman Confocal can demonstrate that the distribution of the monomer along the pore is homogeneous. Figure 4.5 shows the depth profiles by focusing the microscope stepwise, at 10 μm intervals, through the AAO template. The intensity of the bands remains constant along the depth and demonstrating that the monomer penetrates into the nanocavities.

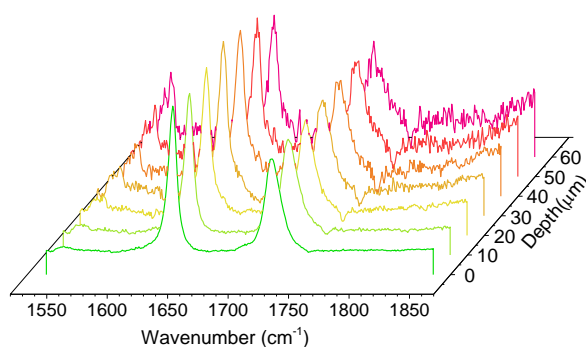


Figure 4.5. Raman spectra of infiltrated MMA inside the AAO template of 35nm at different pore depth.

Raman measurements have been carried out through the pore in depth with the confocal mode every 10 μm . The wavenumber range is between 1550-1850 cm^{-1} where two Raman scattering transitions have been observed in the sample, related to the monomer and polymer content in the sample. The main bands are located at 1720 and 1640 cm^{-1} , which are assigned to a stretching mode of the C=O bond in the ester carbonyl group present in both monomer and polymer and of stretching mode of the C=C bond present only in the monomer, respectively.

Figure 4.6 a) shows the evolution of the depth profile Raman spectra every 10 μm of the PMMA synthesized inside AAO with nanopores of 35nm after 30 minutes of polymerization. The bands ratio, between I_{1640}/I_{1720} , decrease as the pore depth increases, this result suggests that the reaction is faster in the bottom of the pore. Figure 4.6 b) shows the evolution of the bands with the time. The monomer band (1640 cm^{-1}) decreases as the polymerization reaction increases, furthermore 1720 cm^{-1} band is widening due to the appearance C=O carbonyl group α - β saturated.

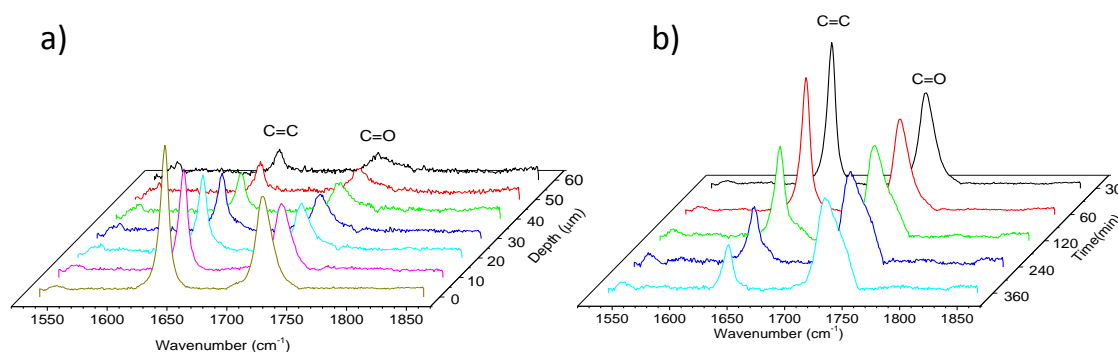


Figure 4.6. Raman spectra of the PMMA polymerized in side AAO template with nanopores of 35nm.
 a) Depth profile Raman spectra at 30min b) Time profile Raman spectra at 20μm depth

Although Raman spectroscopy is an appropriate technique to study the kinetic polymerization with the cell temperature (as will be seen in the chapter 5 for fluoroacrylate monomer), in this case due to evaporation of the monomer was not an accurate method. For this reason, we explored another method to study the MMA polymerization inside the nanoreactors, where the measurements were carried out ex-situ, once the reaction was stopped with low temperature. In this way, the measurements did not have the same reproducibility because an important factor, the induction time, was not taken into account as will be explained later. Therefore, the measurements were not reliable and good enough for the fitting of the model. For this reason, the experiment was redesigned to be studied by DSC.

Monitoring by DSC

Bulk polymerization of MMA was studied by thermal calorimetry. A droplet of solution (MMA+0.5%AIBN) was placed inside hermetic aluminium pans. The method followed by DSC to study bulk and in confinement polymerization has been the same. For that, three scans have been run. Firstly an isothermal heating is carried out in order to polymerize MMA at the selected temperature of 60, 70, 80 and 90°C and then, two dynamical processes. An example of the resulting thermogram is plotted in Figure 4.7. As observed, before the reaction starts, there is an induction period corresponding to the time needed to begin the reaction. Later an exothermic and intense peak appears as polymerization step. The heat of reaction is calculated with the enthalpy of the exothermic peak. After a cooling scan, a first dynamic scan is carried out from 30°C to 150°C at 10°C/min in order to check if the polymerization reaction is finished. In this case is observed a second exothermic

peak, which corresponds to possible residual heat of reaction. So, the total heat of reaction (ΔH_T) is calculated by the sum of the first and second exothermic peaks. Finally, a second dynamic scan is carried out to confirm if polymerization reaction is finished and to eventually observe the T_g of PMMA obtained after the reaction.

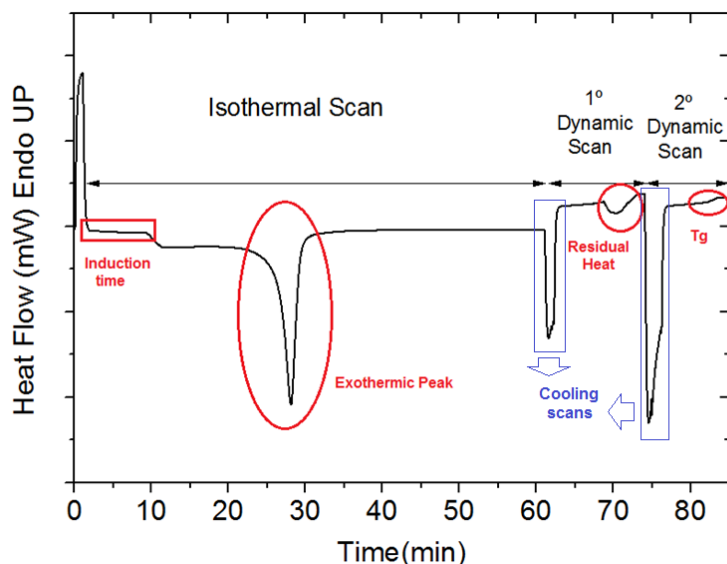


Figure 4.7. Thermogram of MMA polymerization by DSC

Figure 4.8 a, shows the heat generated during the reactions. As observed, the reactions are exothermic, and increasing the temperature accelerated the polymerization process yielding a narrower exothermic peak. Figure 4.8 b, represents the conversion versus time of polymerization for the four temperatures. The conversion (X) at different time was obtained by equation 4.20

$$X = \frac{1}{\Delta H_T} \int_{t_0}^t Q dt \quad (4.20)$$

where ΔH_T is the total heat of reaction and Q is the corresponding reaction heat flow. As the T_g of PMMA (110 °C) is higher than the reaction temperatures the polymerization was expected to suffer from a glass effect which leads to a limiting conversion lower than 100 %. In order to estimate the total heat of reaction, complete conversion was achieved by subjecting the samples to a dynamic scan at 10 °C/min up to 150 °C. Therefore, the total heat of reaction (ΔH_T) was calculated from the sum of the heat generated during the isothermal process and the dynamic scan. The average total of the heat of reaction is 55

KJ/mol, in agreement with the heat reported in literature³¹. Similar values were found for reactions conducted in nanoconfinement.

Figure 4.8 b presents the evolution of the conversions as a function of time and shows a strong gel effect for all polymerization temperatures, marked by the onset of rapid polymerization leading to a limiting conversion. The point in conversion at which the gel effect appears increases with increasing reaction temperature. At higher temperatures the molecular weight of the polymer is lower and the free volume higher, thus the critical point defined by equation 4.10 is reached at high conversion. Figure 4.8 b also shows that the maximum conversion obtained increases with increasing reaction temperature, which can be attributed to the T_g of the monomer polymer mixture reaching the reaction temperature at higher conversions.

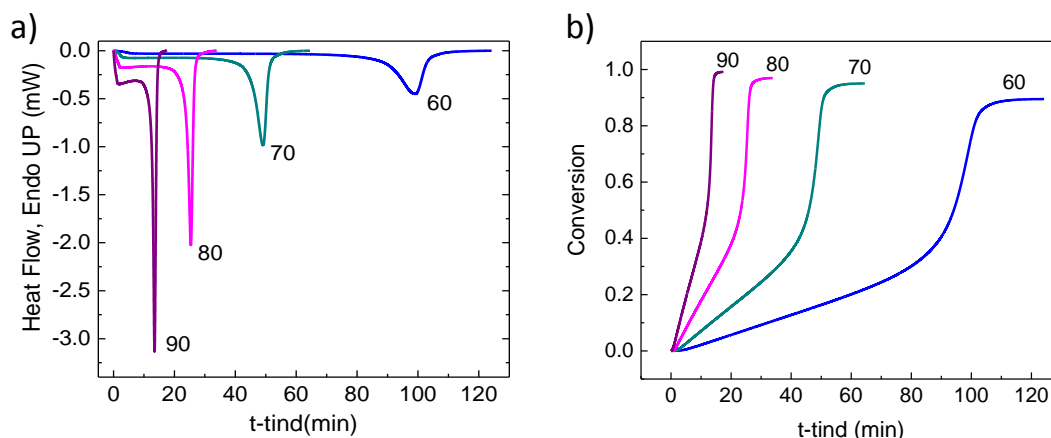


Figure 4.8. a) Heat Flow measured in the bulk polymerization of MMA at different temperatures under isothermal conditions. b) Evolution of conversion with time.

To study the confinement effects, polymerization was also studied in the AAO template within 60 nm pore diameter. Figure 4.9 presents the results obtained for this polymerization. Although the results were qualitatively similar to those obtained in bulk, the polymerization rates were faster and the limiting conversion lower than in bulk. This increase in the polymerization rate could be due to confinement effects and/or a catalytic effect due to surface hydroxyl groups of the native alumina pores¹⁵ as will be clarified below.

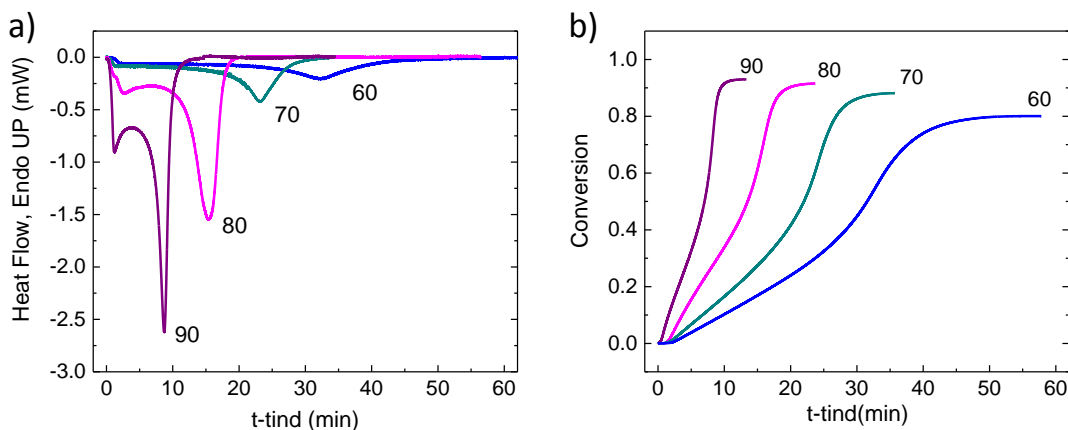


Figure 4.9. a) Heat Flow measured in the nanoconfined polymerization of MMA in AAO 60 at different temperatures under isothermal conditions. b) Evolution of conversion with time.

Figure 4.10 presents the effect of the size of the nanopores on the kinetics of polymerizations carried out at 80 °C. It can be seen that (1) the initial rate of polymerization was much faster in the nanoconfined system than in bulk, (2) the onset of the gel point occurs at slightly lower conversion, (3) the rate of polymerization after the gel point was slower, and (4) a lower limiting conversion is reached for polymerizations under nanoconfinement. The possible influence of the AAO walls will be study later.

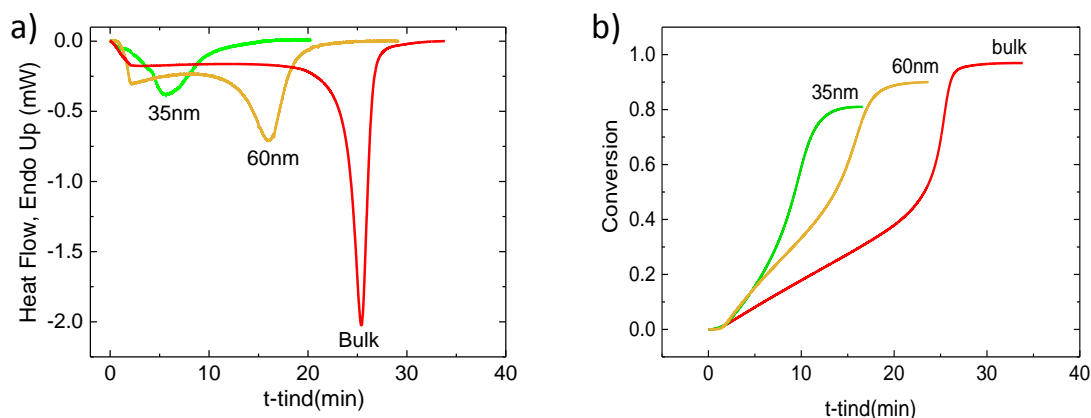


Figure 4.10. a) Heat Flow measured in the polymerization of MMA in bulk and within AAO templates of varying pore diameter under isothermal conditions. b) Evolution of conversion with time

Molecular weight by GPC

The molecular weight of polymer polymerized in AAO template was studied by extraction of the polymer from the template and measured by GPC. Table 4.2 summarizes the average

molecular weight of the final polymers. It is observed that weight and number average molecular weight and polydispersity index values are higher for bulk polymerization than for polymerization inside the nanoreactors, therefore, polymer chain decrease with decreasing pore size.

Table 4.2. Effect of the pore diameter of the AAO on the average molecular weights of the final polymer obtained at 80 °C.

Sample	Mw(g/mol)	Mn(g/mol)	PDI(Mw/Mn)
35nm	79000	47000	1.68
60nm	201000	85000	2.36
Bulk	480000	99500	4.82

This trend in molecular weights is also in agreement with those reported by Giussi *et al.* in the polymerization of styrene with AIBN confined in AAO.⁷ Moreover, Pallikari-Viras³² also observed a decrease of M_w with the degree of confinement at much smaller pore diameters than those used here and ascribed this reduction to the propagation mobility of the free radicals.

On the contrary, Begum *et al.*¹⁵ and Kalogeras and Neagu¹⁴ have reported that molecular weight was higher in the polymerization of MMA conducted in a porous glass membrane consisting of interconnected pores. The increase in molecular weights was attributed to the reduced diffusion under nanoconfinement which leads to lower rate of termination.

One major difference between the result of this work and those works in which the molecular weight increases compared to bulk polymerization, is the nature of the template. In the present case, each pore is physically isolated and, as such, the local radical concentration will stay for longer time at the site at which radical decomposition occurs, leading to higher rates of termination. In contrast, most systems in the literature are based on a network of pores. In a series of interconnected pores, after initiator decomposition, once radicals encounter different channels the probability of termination is reduced, thus higher molecular weights may be expected.

Catalytic effect of the pore alumina walls

To study the influence of the alumina walls on the initiator and therefore on the polymerization kinetic, thermal decomposition of AIBN inside nanopores was studied by

isothermal scan, at three different temperatures (90, 92 and 94°C). The thermal decomposition of AIBN in solution (i.e., without AAO) was monitored as a reference. The results are plotted in thermogram, Figure 4.11, where the exothermic peak shows the AIBN decomposition at 90, 92 and 94°C. As observed in Figure 4.11, the decomposition of the initiator was faster when the temperature increases, moreover, the decomposition rate increased with the presence of the alumina and also with the degree of confinement.

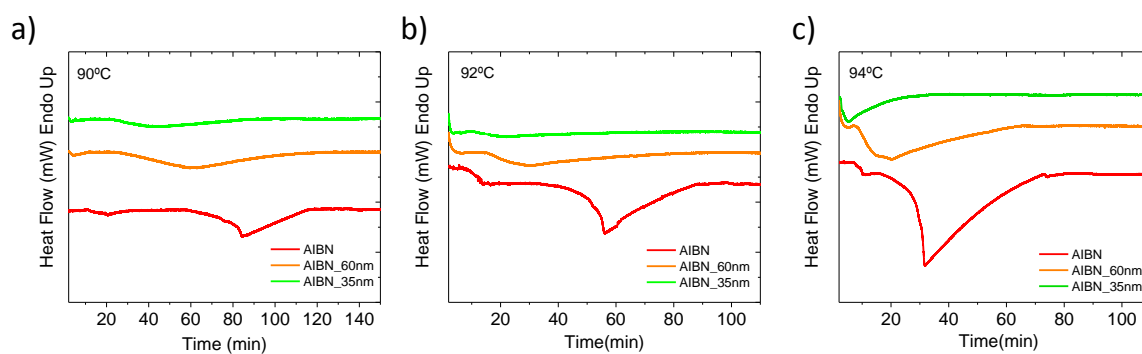


Figure 4.11. Thermograms of the decomposition of AIBN (red), and AIBN infiltrated inside the AAO template with diameter size of 35nm (green) and 60nm (orange). In isothermal scan at different temperatures: a) 90°C, b) 92°C and c) 94°C.

The isothermal heat flow data are converted to decomposition percentage versus time data, using the equation 4.20, where X is the AIBN decomposition percentage instead of conversion. Figure 4.12 shows three graphs a), b) and c), where the decomposition of AIBN is studied at different temperature 90, 92 and 94°C respectively. Each plot illustrates that the AIBN decomposition is faster within the AAO template, confinement degree and with the temperature.

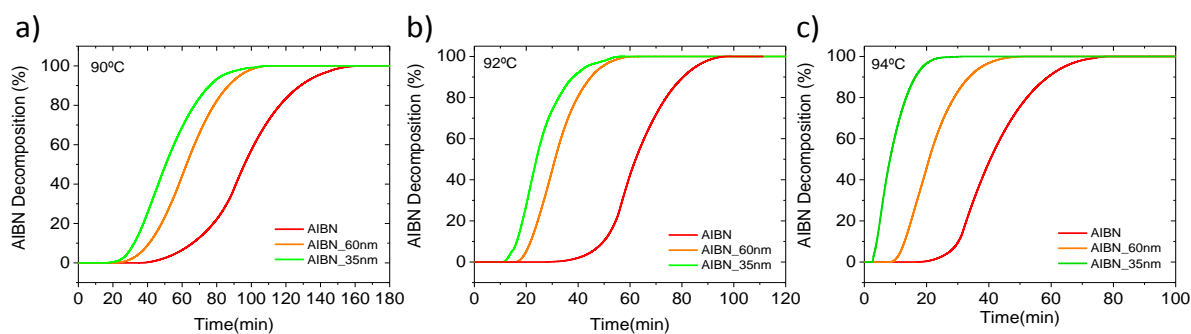


Figure 4.12. Decomposition curves of AIBN (red line) over time and in function with confinement: 35nm (green line) and 60nm (orange line). Thermal study at different temperatures: a) 90°C, b) 92°C and c) 94°C.

Induction time and gel effect

The induction time is a period of time before the polymerization reaction occurs, see Figure 4.13 a. Figure 4.13 b shows the induction time for bulk and nanoconfined (60nm) samples in function of the temperature, values are taken from Figure 4.8 and 4.9. This induction time depends on the temperature and it becomes more significant at lower temperatures due to the fact that polymerization is slower at low temperature, therefore, this time increases as shown in Figure 4.13 b. In nanoconfined case this time is higher than bulk case, since confined reactions have little monomer and initiator hence it needs more time to remove all the oxygen in the system.³³

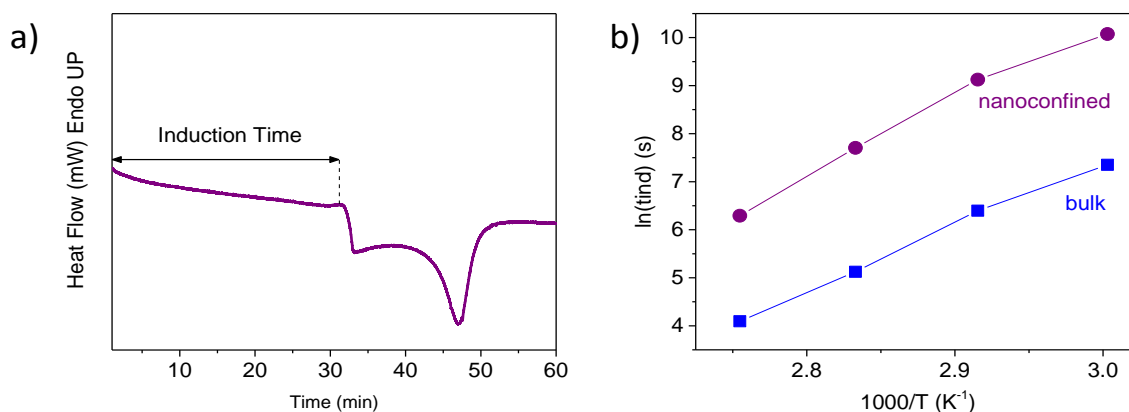


Figure 4.13. a) Graphic representation of induction time in the thermogram for the polymerization reaction at 80°C in confinement. b) Induction time for bulk and samples in nanoconfined system in function of reciprocal temperature.

Another effect that can be observed in the free radical polymerization process is the onset of gelation. Gel effect is an important effect in MMA free radical reaction, since the reactivity and the molecular weight, increase at this point in the reaction. As already discussed, autoacceleration occurs at earlier times and conversion with the increase of temperature.

In order to calculate the gel point, graphically, two tangents are drawn in the graphic of the conversion versus time. Each tangent is drawn in the first and second linear part of the conversion curve. The cut off of the two tangents determines the gel time (t_{gel}), see Figure 4.14 a. This effect is quantified by plotting the ratio of the time required to reach the gel point for bulk and nanoconfined system in Figure 4.14 b. This intersection point decreases with increasing temperature due to the fact that temperature accelerates the polymerization

reaction. The difference in time of gelation between bulk and nanoconfined reaction is higher at low temperature (60°C) and decreases when temperature increases. The onset of gelation occurs at the point in which diffusion of polymer chains is significantly reduced, resulting in a reduction in the rate of termination. As has been observed before, the point of conversion at which the gel effect appears increases with increasing reaction temperature. In our system, a little effect of the diffusion limited termination would be expected, because the pore diameter is significantly larger than the diameter of an individual polymer chain. However, for very small pore diameters the point at which this diffusion limited termination becomes important would be expected to be lower. In this case, the onset of the increase in the rate of polymerization at slightly lower conversion in the nanoconfined system can be attributed to the higher glass transition temperature of the nanoconfined polymer.^{9, 34}

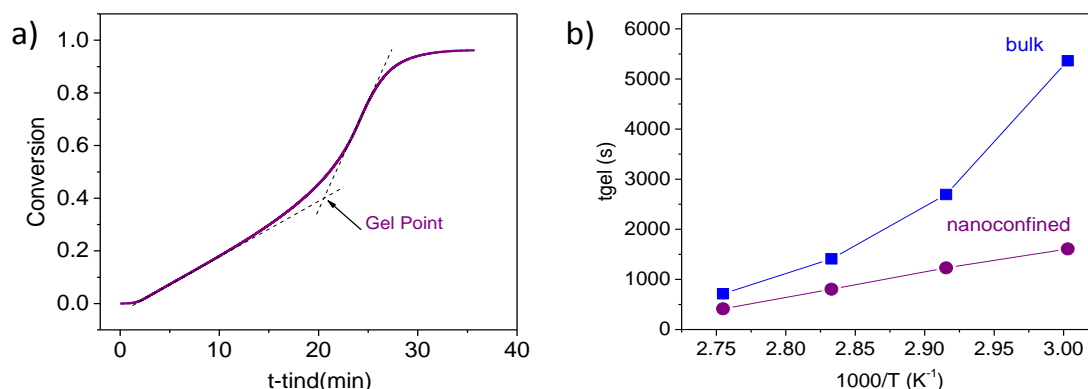


Figure 4.14. a) Graphic representation of gel point in the conversion curve for the polymerization reaction at 70°C in confinement. b) Gel time for bulk and samples in nanoconfined system in function of temperature.

Finally, at higher conversions it may be expected that the rate of termination is higher for the nanoconfined system because under nanoconfinement the likelihood of two radicals being in close proximity to each other is higher, thus, both the rate of polymerization and the limiting conversion are lower than the corresponding bulk polymerization. Unlike bulk polymerization, upon decomposition of the initiator, the two radicals generated are not free to move in all 3 dimensions, leading to higher rates of termination.^{35, 36} This is similar to the increased probability of termination of pairs of radicals generated by decomposition of oil soluble thermal initiators in nano sized droplets in heterogeneous polymerization techniques such as (mini)emulsion polymerization.^{11, 37} These effects are shown schematically in Figure 4.15.

In the initial region, there are no diffusional constraints and the increased rate of polymerization can only be related to an increased rate of initiator decomposition, a higher rate coefficient of propagation, or a lower rate coefficient of termination. Since the latter two would both result in a higher molecular weight, which is not observed experimentally, the increased rate was attributed to the catalytic effect of the pore walls on initiator decomposition. The decrease in molecular weight is in agreement with the arguments laid out above and shown schematically in Figure 4.15, with a lower molecular weight being expected in both the early stages of the reaction where the radical concentration is high and in the latter stages of the reaction where the effective rate of termination is increased.

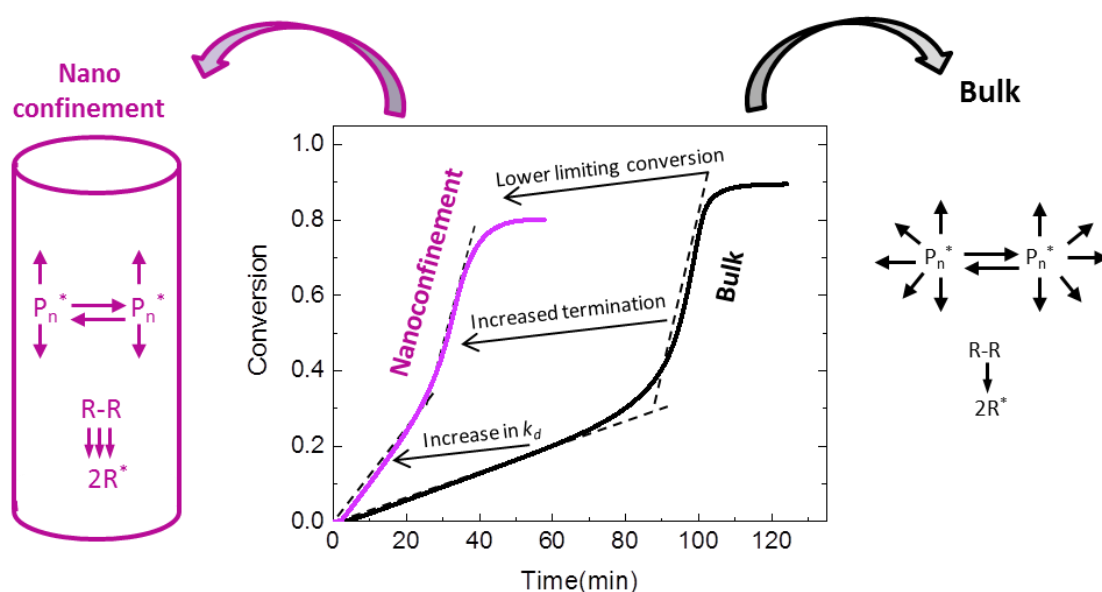


Figure 4.15. Scheme showing the difference of reaction kinetics of MMA polymerized in bulk and in nanoconfinement (60 nm) at 60 °C.

4.4.2. Modeling of polymerization in bulk and in confinement

Implementation of the model and model fit

In order to implement the model, the equations related to the rates of change of monomer, initiator, and free radicals must be solved. In this work, we use MATLAB software to do the numerical calculation. The upper limit of the chain length was considered to be $n = 2 \times 10^5$. A continuous variable approximation was used in order to reduce the number of equations from 2×10^5 to 1×10^4 using a discretization step of 20 (i.e., $n=1,21,41\dots$). The differential equations (4.1,4.2,4.3,4.4,4.5 and 4.6) were solved using a 4th order Runge-

Kutta solver with variable time step. This method allowed for a reasonable computation time whilst maintaining accuracy around critical points. In each loop, the values of f , k_p , k_t and the concentration of the free radical species were updated. The simulation is conducted in three stages. For a given value of K_3 the simulation is conducted assuming no diffusion effects ($k_p = k_{p0}$, $k_t = k_{t0}$ and $f = f_0$) until equation 4.10 is satisfied. The simulation is then continued using the appropriate parameters of $M_{w,cr}$ and $V_{f,cr1}$ to calculate the value of k_t . Then the simulation is conducted until the free volume is equal to $V_{f,cr2}$. Finally, taking into account the reduction in initiator efficiency and propagation rate coefficient according to equations 13 and 14, the simulation is conducted from the point where $V_{f,cr2} \geq V_f$ until the end of the desired reaction time. The free radical concentration at each time step was obtained by iteratively solving equation 4.5. The parameters of the model were estimated by fitting the experimental conversion using as starting values those from Stickler *et al.*³⁸ The literature values used for the rate constants are shown in Table 4.3.

Table 4.3. Values used for the rate constants.

Parameter	Value	Reference
k_{d0} (min^{-1})	$6.32 \times 10^{16} \exp(-30660/RT)$	25
k_{p0} ($\text{M}^{-1} \text{min}^{-1}$)	$1.6 \times 10^8 \exp(-5344/RT)$	39
k_{t0} ($\text{M}^{-1} \text{min}^{-1}$)	$5.88 \times 10^9 \exp(-701/RT)$	25
R ($\text{cal.K}^{-1} \text{mol}^{-1}$)	1.9872	
V_0 ($\text{cm}^3 \cdot \text{g}^{-1}$)	$1/(0.968-1.225 \times 10^{-3} T(^{\circ}\text{C}))$	25
ε	$(V_0/1.18) - 1$	25
f_0	0.63	23
Q (K g mol^{-1})	2.208×10^5	40
T_{gp}^{∞} (K)	387	40
T_{gm} (K)	167	40
$\Delta\alpha_p$	0.48×10^{-3}	40
$\Delta\alpha_m$	1.00×10^{-3}	40
A	1.11	27
B	1.0	27

m	0.5	27
n	1.75	27
K_3	$\exp(-0.75+4460/T)$	Activation energy ³⁸ , Preexponential factor (this work)
$V_{f,cr2}$	$\exp(-9.0+1800/T)$	Activation energy ³⁸ , Preexponential factor (this work)
$V_{f,cr2}$ (nanoconfined)	$\exp(-10.9+2700/T)$	This work
f_{res}	10	This work
f_{res} (nanoconfined)	100	This work
$C(nm)$	267	This work
$k_{d,wall}(nm \cdot min^{-1})$	$\exp(-12.7+5900/T)$	This work

Modeling of polymerization in bulk

The experimentally determined conversion curves for the polymerizations conducted in bulk were fitted by the mathematical model described above as shown in Figure 4.16. All parameters were taken from literature with the exception of the values of K_3 and $V_{f,cr2}$, calculated in this work (Table 4.3), which determine the onset of the gel point and the limiting conversion respectively. The value of K_3 is slightly higher than that reported by Stickler *et al.*³⁸ and is likely due to the higher accuracy of the DSC measurements conducted here. The value of $V_{f,cr2}$ is also similar to that reported by Stickler but here we include in this value the effect of the decrease in initiator efficiency which prevents the unrealistic buildup of radicals at the latter stages of the reaction. The value for the “residual termination” constant, f_{res} , is similar to those reported in literature. The constant, C , is calculated from the linear fit of T_g versus $1/D$. The kinetics can be divided into two distinct kinetic regimes. In the first part the rate of polymerization proceeds without diffusion control and the rate of polymerization is given by

$$R_p = [M]k_p \sqrt{\frac{fk_d[I]}{k_t}} \quad (4.21)$$

After a certain conversion is reached, a rapid increase in the viscosity results in a decrease in the diffusion of the radical chains. At this point the rate of termination decreases drastically and thus the rate of polymerization is increased. The rate coefficient of termination becomes diffusion controlled and is largely dominated by the migration of the radical chain end by propagation, known as “residual termination”. At high conversion, when the T_g of the reaction mixture approaches the polymerization temperature, the propagation reaction becomes diffusion controlled and the rapid decrease in k_p results in a limiting conversion. The two kinetic regimes (diffusion and non-diffusion controlled) can also be seen in the simulated and, to a lesser extent, the experimental molecular weight distributions of the chains as shown in Figure 4.17 a) The lower molecular weight region consists of chains that are formed in the early stages of the reaction, while the higher molecular chains are generated during the second part of the reaction where, due to the low rate of termination, the kinetic chain length is increased. The simulated MWD in Figure 4.17 b) are in good agreement with the experimental MWD, although due to broadening of the distribution in the SEC measurement the bimodal nature of the experimental distribution is poorly defined.

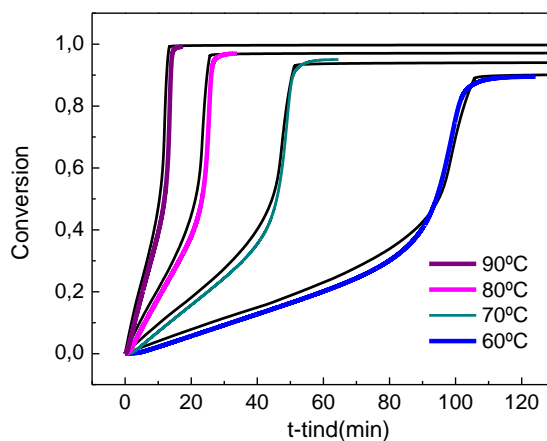


Figure 4.16. Kinetic plot of MMA polymerization in bulk at 60°C (blue), 70°C (turquoise), 80°C (pink) and 90 °C (purple). The bold lines indicate the fit of the kinetics to the mathematical model described herein.

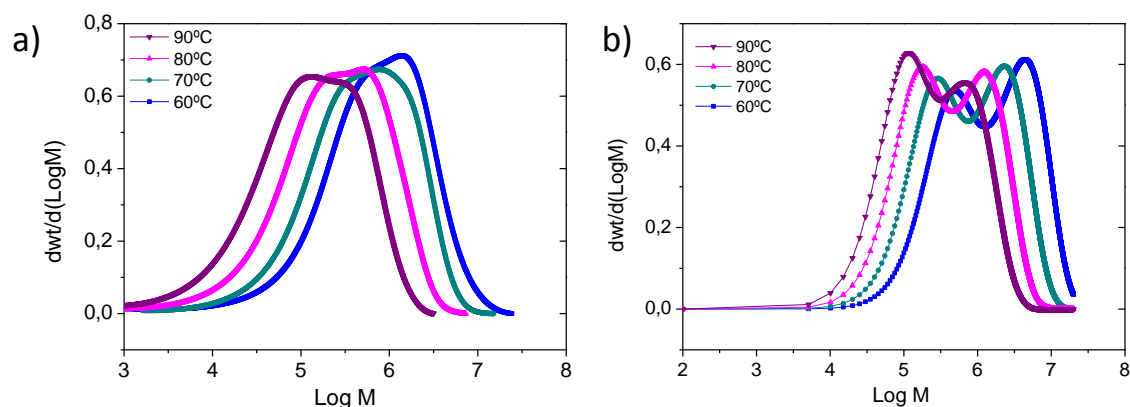


Figure 4.17. a) Experimental and b) simulated molecular weight distributions of MMA polymerization in bulk at 60°C (blue), 70°C (turquoise), 80°C (pink) and 90 °C (purple).

Modeling of polymerization in confinement

The experimental data of polymerizations conducted under nanoconfinement were fit using the mathematical model as shown in Figure 4.18, taking into account the increased rate of initiator decomposition, the higher glass transition temperature and the increased rate of “residual termination”. In order to accurately describe the data, a higher value of the residual termination rate coefficient, f_{res} , was used and the value at which the onset of the reduction in the rate coefficient of propagation and f , $V_{f,cr2}$, was estimated for the reactions conducted with 60 nm pore diameter. One reason for the difference in $V_{f,cr2}$ compared to the reactions conducted in bulk, may be that the initiator efficiency is reduced due to higher probabilities of recombination (as opposed to propagation) of pairs of radicals in confined spaces. It should be noted that in order to reduce the number of parameters estimated the value of $V_{f,cr2}$ is used to describe changes in both the propagation rate and the initiator efficiency, although only the latter is expected to be significantly affected by confinement of the system. The small increase in the glass transition temperature under nanoconfinement was determined from the experimentally determined T_g of polymers synthesized under nanoconfinement (see Table 4.4) and is in agreement with the values determined by Begum *et al.*¹⁵ With these considerations a good fit of the data was achieved.

Table 4.4. Glass transition Temperatures of PMMA bulk and confined

PMMA	T _g (°C)	Onset(°C)
Bulk	107,8±0,5	104,5±1,5
60nm	125,7±0,2	122,6±0,7
35nm	127,5±1,6	121,8±2,5

The increased radical flux in the early stage of the reaction, and the increase in termination in the latter stage results in a reduction in the molecular weight of the polymers synthesized within the AAO template as can be seen from the simulated and experimental molecular weight distributions shown in Figure 4.19. For the reaction conducted at 60 °C there was insufficient sample to obtain a reliable chromatogram in the GPC and therefore this result is omitted. Compared to the bulk experiments there is not such a large difference in the molecular weights obtained during the two kinetic regimes which results in a lower polydispersity and a reduction in the bimodal character of the molecular weight distributions. The molecular weight distribution is in reasonable agreement with the experimental GPC data previously shown in Table 4.2, confirming the origin of the difference between the rate of polymerization in the nanoconfined system and in bulk.

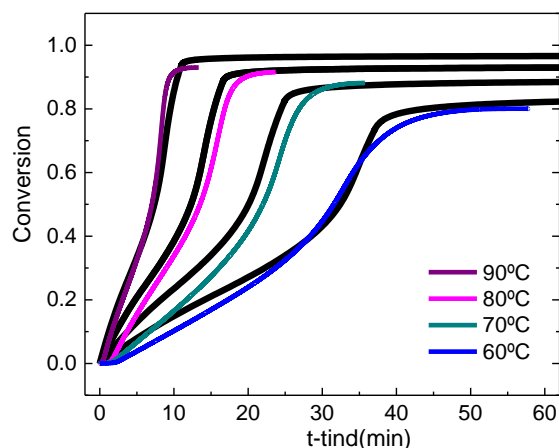


Figure 4.18. Kinetic plot of MMA polymerization conducted in AAO templates with nanopore of 60 nm of diameter at 60°C (blue), 70°C (turquoise), 80°C (pink) and 90 °C (purple). The bold lines indicate the fit of the kinetics to the mathematical model described herein.

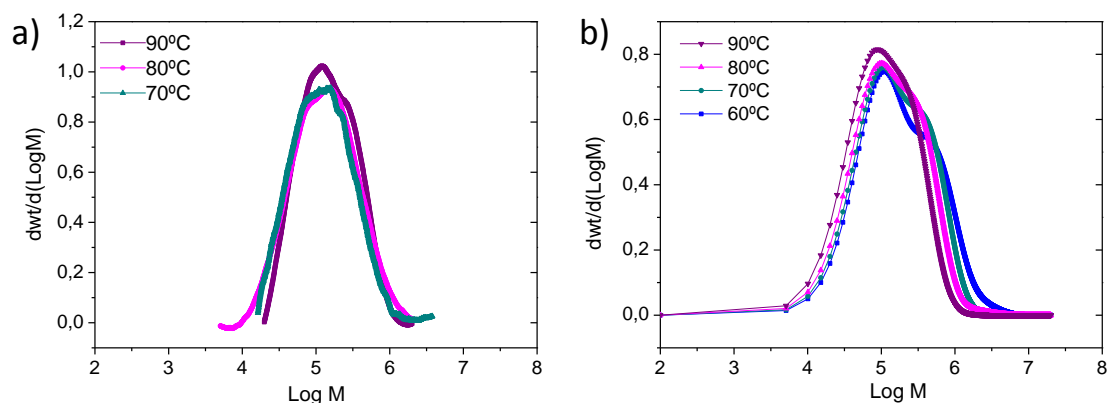


Figure 4.19. a) Experimental and b) simulated molecular weight distributions of MMA polymerization conducted in AAO templates with nanopore of 60 nm diameter at 60°C (blue), 70°C (turquoise), 80°C (pink) and 90 °C (purple).

4.4.3. Properties of synthesized PMMA nanostructures

Thermal properties and polymer aging

Differential Scanning Calorimetry has been used to determine thermal properties of the polymer once the synthesis of PMMA has been performed. Based on the structural criterion, the mobility of chains in a closely packed system is primarily determined by the degree of packing of the system or by its inverse measure.⁴¹ In the literature, there are some examples of the influence of the confinement on PMMA properties, for instance, JL Keddie et al. found that the T_g of PMMA on the surface of the native oxide of silicon increases slightly with decreasing film thickness.⁴² Also Priestley et al. produced PMMA nanocomposites with untreated silica. As a result of the hydrogen bonding between PMMA and the silica nanoparticles they found a more moderate increase in T_g with respect to the previously bulk systems.⁴³ Recently Tan *et al.* observed an agreement on confinement effects of PMMA nanotubes in the AAO. They demonstrated by the measurements carried out by DSC and by ellipsometry they demonstrated an increment of T_g of 12°C respect to bulk polymer.³⁴

The physical aging study has been carried out to observe the influence of confinement effect. This property can be explained in a straightforward way from the free-volume concept For this study every sample was heated and cooled from 30°C to 160°C at

40°C/min three times before annealing during 30 minutes at 10°C below its T_g (Taging). The results of the physical aging are shown in the Figure 4.20. before (solid line) and after (dotted line) annealing.

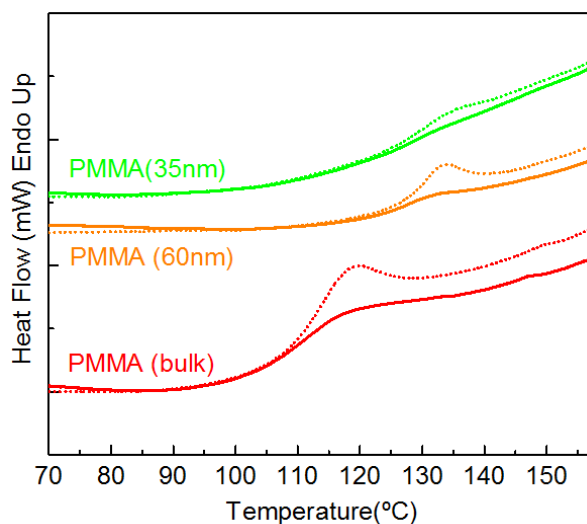


Figure 4.20. Thermogram of PMMA (solid line) polymerized in bulk (green) and inside of nanopores of 60nm (orange) and 35nm (green) of diameter. Effect of physical aging (dotted line).

As observed in the Figure 4.20, the glass transition of PMMA, before annealing (T_{g1}), increases with the confinement. For nanopores of 60nm the T_g increases 18°C and for nanopores of 35nm the T_g increases around 20°C. After that, a fourth cooling and heating were done to compare the physical aging effect. Results in Table 4.5 show that the difference between T_{g1} and the glass transition after annealing (T_{g2}) decreases with the confinement, as well as the different of heat flow (ΔY). These results can be explained by the fact of the restriction of mobility of the polymer chains along the interface of the wall of alumina nanopore, caused by hydrogen bonding between PMMA and surface hydroxyl groups.⁴² Besides, the interactions with the interfacial hydrogen bonds and confinement effects can suppress smaller motions associated to structural relaxation, this suppression as reported in the literature can result in a near elimination of physical aging within 25 nm.⁴⁴

Table 4.5. Thermal parameters of MMA polymerized in bulk and in side nanoporous alumina.

PMMA	Tg1(°C)	Taging(°C)	Tg2(°C)	$\Delta Y(\text{mW})$
35nm	127.5±1.6	117	131.2	0.027
60nm	125.7±0.2	115	131.4	0.130
Bulk	107.8±0.5	100	114.6	0.174

Raman spectroscopy is used to deeper study the confinement effects. Figure 4.21 shows Raman spectra of PMMA bulk and in situ polymerized in AAO template of different sizes of nanopores 35, 60 and 140nm. All spectra show all characteristic bands of PMMA found in the literature.^{45, 46} Peaks which arise in the range 900-1300 cm^{-1} correspond to C-O stretching, peaks in 1450 cm^{-1} are associated to C-H bending, the peak 1724 cm^{-1} is identified with C=O stretching and peaks in the range 2800-3100 cm^{-1} correspond to C-H vibrations of CH_2 and CH_3 groups. The principal difference is in the range 930-1230 cm^{-1} shown in the Table 4.6.

The intensity ratio of the peak at 979 cm^{-1} (II) , O- CH_3 stretching, respect to the intensity of the peak at 1158 cm^{-1} (I), C-O stretching, is decreasing from the bulk until the samples obtained confined in lower diameter.

Table 4.6. Intensity Ratio for bulk PMMA and in situ polymerized into AAO templates with different diameters of nanopores

MMA	Intensity Ratio (II/I)
Bulk	4.30
140	1.70
65	1.31
35	1.01

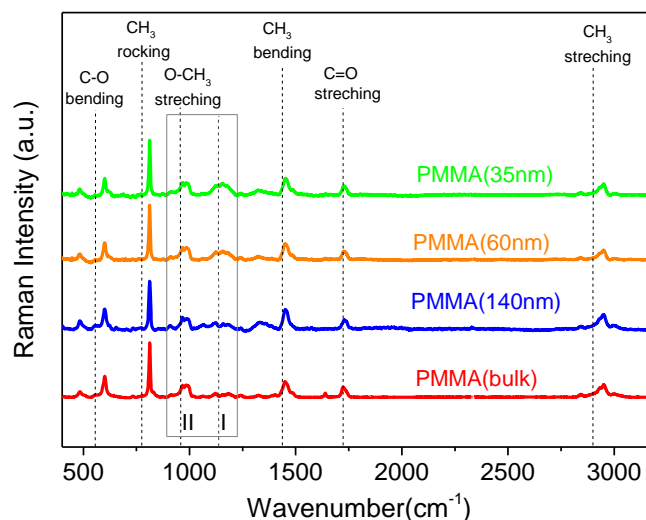


Figure 4.21. Raman spectra of PMMA in situ polymerized inside AAO 35nm, 60nm, 140nm and bulk.

The difference in the intensity ratio can be due to the changes in the chemical structure with degree of nanoconfinement. In fact, it can be observed smaller share of O-CH₃ bonds because of the interaction of PMMA chains with the alumina walls of nanopores.³⁰ The literature tells about the change of the spectra of PMMA is related to the rotations of the side ester group and the principal chain influence with the alumina walls of AAO.⁴⁷

Wettability

It is very well known that surface roughness plays an important role in wettability. In this work templates have been used as the mold to create roughness in the surface of PMMA film. The roughness is created by removal of a supported polymer infiltrated template and can be modulated. Due to the different geometry of the AAO templates. The procedure is illustrated in Figure 4.22 and 4.23. Figure 4.22 shows an example of PMMA polymer infiltrated inside a template of 140 nm of pore diameter and 1 μm of pore length. As can be seen, part of the polymer remains on the top of the template being the support layer of nanostructured polymer. After the removal of alumina nanopillars are supported on the polymer layer.

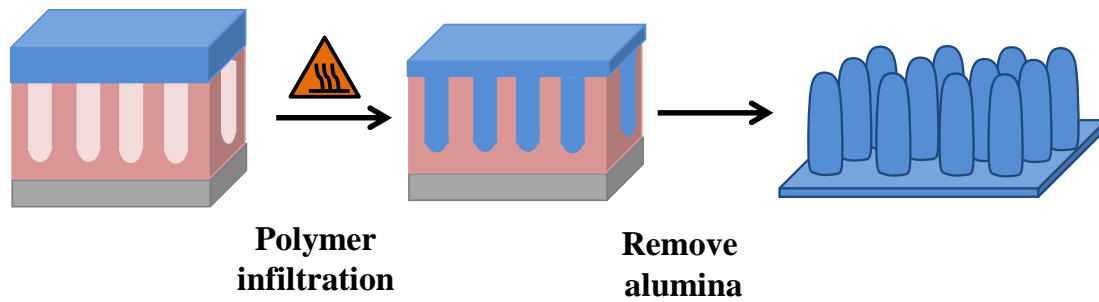


Figure 4.22. Process of polymer infiltration of PMMA inside the AAO template and remove the alumina.

Nanostructured surface is formed by pillars of controlled geometry. This geometry is determined by the pore diameter, pore length and distance between the pores of the AAO template. In order to compare the wettability of PMMA surfaces, three different nanostructures were made from AAO templates with the same length of depth, one micron, but diameters of 35, 60 and 140nm. Figure 4.23 shows a scheme of three PMMA nanostructured surface and the smooth film: a) is the flat polymer surface, b), c) and d) are the pattern obtained from infiltration of PMMA inside different AAO templates of 35, 60 and 140nm respectively, following the process of Figure 4.22. To explain the results we have to consider not only the pillars size but also the interpore distance of the AAO template. In case b) the interpore distance is 485nm and in the case c) and d) is 102 nm, therefore the distance between pillars are 345, 42 and 67 nm for the cases b, c and d respectively.

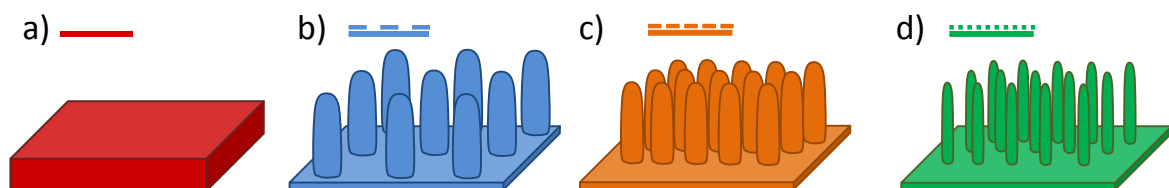


Figure 4.23. Schematic drawing of the theoretically patterns obtained of PMMA from AAO templates. a) Flat surface, nanostructured surfaces with pillars with diameters of a) 140nm, b) 60nm, c) 35nm.

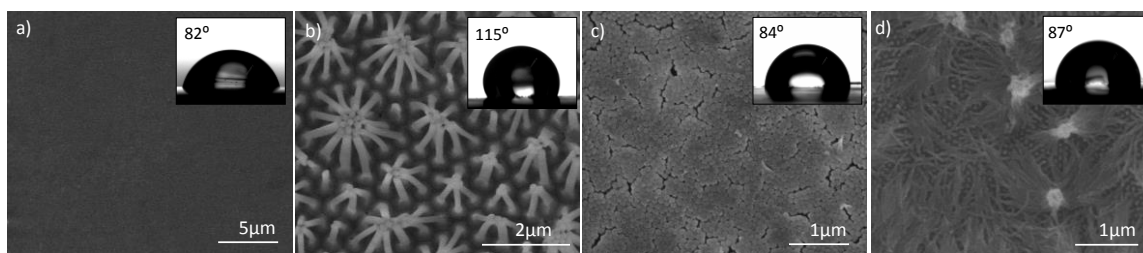






Figure 4.24. SEM images of the real patterns obtained of PMMA from AAO templates. a) Flat surface, b) nanostructured surfaces with pillars with diameters of 140nm; c) 60nm, d) 35nm and the corresponding initial contact angle images.

PMMA nanopillars have been studied by scanning electron microscopy to determine the morphology of the nanostructures (Figure 4.24). In the case b) the nanopillars are standing up but with a slight inclination that causes the formation of clusters. In case c), the nanopillars are standing up and very close each others. This can be interpreted because the short distance between the nanopillars (42nm) kept the nanopillars straight without falling, observing a dense surface of the polymer heads. Finally, in case d) the aspect ratio of the nanopillars is very high. This causes that nanopillars do not stand up and fall down, forming clusters.

The contact angle has been measured by observing the change of the water droplet with the time during droplet evaporation. Experiments were performed with 2µL droplets which were deposited on the top of the surface by a calibrated mechanical syringe. The results are summarized in Table 4.7 where the contact angles initials, finals and average are shown.

Table 4.7. Initial and final contact angle values of PMMA nanostructures.

	PMMA	Structure	CA
a)	Flat		74±1
b)	140nm		103±8
c)	60nm		69±3
d)	35nm		76±2

The results can be explained as following. In the case d) all nanopillars fell down, forming clusters. This is because the aspect ratio is too high, causing the fall of the pillars, forming a similar surface to the flat one. Hence the contact angle in the case a:74° and d: 76° are very similar values. In the case c) the pillars stand up and they tend to stay close one to the other, without gaps between them. Observing the behaviour of the contact angle, 69°, it

slightly decreases below the value of the flat surface and therefore decreases the hydrophobicity of the sample. This behaviour resemble to that of the Wenzel theory. Finally, in the case b) the formed pillars stand up and create a well-defined nanostructured surface. The evolution of the contact angle is quite different from the flat one, observing an increase in the value to 103° and therefore an increase in the hydrophobicity of the sample. This behaviour resemble to that of the Cassie-Baxter theory.

4.5. Conclusions

In the study of radical polymerization of MMA in AAO nanoreactors the following conclusions can be drawn:

The nanoporous structure of AAO templates can be successfully replicated by infiltration of liquid monomer followed by its polymerization. The reaction is significantly faster when is conducted within the AAO template compared to the bulk polymerization and the PMMA synthesized in confinement has significantly lower molecular weight than bulk. The total conversion is close to 90% in two hours which is slower time than the needed time for infiltration.

A mathematical model was developed to account for the differences in the reaction kinetics and molecular weight for reactions conducted under nanoconfinement. In the initial phase of polymerization in confinement, a quick decomposition of the initiator molecule leads to a faster rate of polymerization. Later, the onset of diffusional limitations occurs earlier, attributed to the higher glass transition temperature of polymers under nanoconfinement. Lastly, the pairwise combination of the radicals in the diffusion limiting region occurs faster in the nanoconfined system due to the lower effective volume experienced by each radical when placed under nanoconfinement. These confinement effects combine to give a PMMA of lower molecular weight and of lower dispersity than obtained in bulk. Therefore, confinement effects of AAO templates have not only a strong influence on the physical processes of polymers (crystallization, dynamics and so on) but also on the chemical process (polymerization kinetics, molecular weight, etc.).

The morphological characterization confirms that PMMA nanofibers have been formed inside the AAO templates. The glass transition increases with the degree of confinement until around 20°C. Moreover, physical aging together with the chemical Raman study, suggest a restriction of mobility of the polymer chains along the interface of a alumina nanopore wall. Finally, nanostructured surface based on PMMA nanopillars with different pore size and interpillar distances leads to different wettability, from hydrophilic to hydrophobic behaviour.

4.6. References

- (1). Mijangos, C.; Hernández, R.; Martín, J. A review on the progress of polymer nanostructures with modulated morphologies and properties, using nanoporous AAO templates. *Progress in Polymer Science* **2016**, *54-55*, 148-182.
- (2). Distefano, G.; Suzuki, H.; Tsujimoto, M.; Isoda, S.; Bracco, S.; Comotti, A.; Sozzani, P.; Uemura, T.; Kitagawa, S. Highly ordered alignment of a vinyl polymer by host-guest cross-polymerization. *Nat Chem* **2013**, *5*, (4), 335-341.
- (3). Hu, Z.; Zhao, D. A. N. Polymerization within confined nanochannels of porous metal-organic frameworks. *Journal of Molecular and Engineering Materials* **2013**, *01*, (02), 1330001.
- (4). Davis, M. E. Ordered porous materials for emerging applications. *Nature* **2002**, *417*, (6891), 813-821.
- (5). Uemura, T.; Horike, S.; Kitagawa, S. Polymerization in coordination nanospaces. *Chemistry - An Asian Journal* **2006**, *1*, (1-2), 36-44.
- (6). Comotti, A.; Bracco, S.; Beretta, M.; Perego, J.; Gemmi, M.; Sozzani, P. Confined Polymerization in Highly Ordered Mesoporous Organosilicas. *Chemistry - A European Journal* **2015**, *21*, (50), 18209-18217.
- (7). Giussi, J. M.; Blaszczyk-Lezak, I.; Cortizo, M. S.; Mijangos, C. In-situ polymerization of styrene in AAO nanocavities. *Polymer (United Kingdom)* **2013**, *54*, (26), 6886-6893.
- (8). Begum, F.; Simon, S. L. Modeling methyl methacrylate free radical polymerization in nanoporous confinement. *Polymer* **2011**, *52*, (7), 1539-1545.
- (9). Zhao, H. Y.; Yu, Z. N.; Begum, F.; Hedden, R. C.; Simon, S. L. The effect of nanoconfinement on methyl methacrylate polymerization: Tg, molecular weight, and tacticity. *Polymer (United Kingdom)* **2014**, *55*, (19), 4959-4965.
- (10). Tarnacka, M.; Dulski, M.; Starzonek, S.; Adrjanowicz, K.; Mapesa, E. U.; Kaminski, K.; Paluch, M. Following kinetics and dynamics of DGEBA-aniline polymerization in nanoporous native alumina oxide membranes - FTIR and dielectric studies. *Polymer (United Kingdom)* **2015**, *68*, 253-261.
- (11). Uemura, T.; Ono, Y.; Kitagawa, K.; Kitagawa, S. Radical polymerization of vinyl monomers in porous coordination polymers: Nanochannel size effects on reactivity, molecular weight, and stereostructure. *Macromolecules* **2008**, *41*, (1), 87-94.
- (12). Uemura, T.; Ono, Y.; Hijikata, Y.; Kitagawa, S. Functionalization of coordination nanochannels for controlling tacticity in radical vinyl polymerization. *Journal of the American Chemical Society* **2010**, *132*, (13), 4917-4924.
- (13). Li, X.; King, T. A.; Pallikari-Viras, F. Characteristics of composites based on PMMA modified gel silica glasses. *Journal of Non-Crystalline Solids* **1994**, *170*, (3), 243-249.
- (14). Kalogeras, I. M.; Neagu, E. R. Interplay of surface and confinement effects on the molecular relaxation dynamics of nanoconfined poly(methyl methacrylate) chains. *European Physical Journal E* **2004**, *14*, (2), 193-204.
- (15). Begum, F.; Zhao, H.; Simon, S. L. Modeling methyl methacrylate free radical polymerization: Reaction in hydrophilic nanopores. *Polymer* **2012**, *53*, (15), 3238-3244.

- (16). Begum, F.; Zhao, H.; Simon, S. L. Modeling methyl methacrylate free radical polymerization: Reaction in hydrophobic nanopores. *Polymer* **2012**, *53*, (15), 3261-3268.
- (17). Sanz, R.; Jensen, J.; Johansson, A.; Skupinski, M.; Possnert, G.; Boman, M.; Hernandez-Vélez, M.; Vazquez, M.; Hjort, K. Well-ordered nanopore arrays in rutile TiO₂ single crystals by swift heavy ion-beam lithography. *Nanotechnology* **2007**, *18*, (30).
- (18). Larkin, P., Chapter 1 - Introduction: Infrared and Raman Spectroscopy. In *Infrared and Raman Spectroscopy*, Elsevier: Oxford, 2011; pp 1-5.
- (19). Maiz, J.; Sacristan, J.; Mijangos, C. Probing the presence and distribution of single-wall carbon nanotubes in polyvinylidene difluoride 1D nanocomposites by confocal Raman spectroscopy. *Chemical Physics Letters* **2010**, *484*, (4-6), 290-294.
- (20). Hajatdoost, S.; Olsthoorn, M.; Yarwood, J. Depth profiling study of effect of annealing temperature on polymer/polymer interfaces in laminates using confocal raman microspectroscopy. *Applied Spectroscopy* **1997**, *51*, (12), 1784-1790.
- (21). Sacristán, J.; Mijangos, C.; Reinecke, H.; Spells, S.; Yarwood, J. Depth profiling of modified PVC surfaces using confocal Raman microspectroscopy. *Macromolecular Rapid Communications* **2000**, *21*, (13), 894-896.
- (22). Froud, C. A.; Hayward, I. P.; Laven, J. Advances in the raman depth profiling of polymer laminates. *Applied Spectroscopy* **2003**, *57*, (12), 1468-1474.
- (23). Verros, G. D.; Latsos, T.; Achilias, D. S. Development of a unified framework for calculating molecular weight distribution in diffusion controlled free radical bulk homopolymerization. *Polymer* **2005**, *46*, (2), 539-552.
- (24). Tefera, N.; Weickert, G.; Westerterp, K. R. Modeling of free radical polymerization up to high conversion. I. A method for the selection of models by simultaneous parameter estimation. *Journal of Applied Polymer Science* **1997**, *63*, (12), 1649-1661.
- (25). Achilias, D. S.; Kiparissides, C. Development of a general mathematical framework for modeling diffusion-controlled free-radical polymerization reactions. *Macromolecules* **1992**, *25*, (14), 3739-3750.
- (26). Soh, S. K.; Sundberg, D. C. Diffusion-controlled vinyl polymerization. I. The gel effect. *Journal of Polymer Science: Polymer Chemistry Edition* **1982**, *20*, (5), 1299-1313.
- (27). Marten F. L., H. A. E., *Polymerization reactors and processes* American Chemical Society: Washington, 1979; Vol. 104, p 43-70.
- (28). Soh, S. K.; Sundberg, D. C. Diffusion-controlled vinyl polymerization. IV. Comparison of theory and experiment. *Journal of Polymer Science: Polymer Chemistry Edition* **1982**, *20*, (5), 1345-1371.
- (29). Forrest, J. A.; Dalnoki-Veress, K. The glass transition in thin polymer films. *Advances in Colloid and Interface Science* **2001**, *94*, (1-3), 167-196.
- (30). Blaszczyk-Lezak, I.; Hernández, M.; Mijangos, C. One Dimensional PMMA Nanofibers from AAO Templates. Evidence of Confinement Effects by Dielectric and Raman Analysis. *Macromolecules* **2013**, *46*, (12), 4995-5002.

- (31). J.Brandrup, E. H. I., E.A. Grulke, Polymer Handbook. A Wiley-Interscience Publication: Canada, 1999; p 2366.
- (32). Pallikari-Viras, F.; Li, X.; King, T. A. Thermal analysis of PMMA/gel silica glass composites. *Journal of Sol-Gel Science and Technology* **1996**, 7, (3), 203-209.
- (33). Zhao, H.; Simon, S. L. Methyl methacrylate polymerization in nanoporous confinement. *Polymer* **2011**, 52, (18), 4093-4098.
- (34). Tan, A. W.; Torkelson, J. M. Poly(methyl methacrylate) nanotubes in AAO templates: Designing nanotube thickness and characterizing the Tg-confinement effect by DSC. *Polymer* **2016**, 82, 327-336.
- (35). Berezhkovskii, A. M.; Pustovoit, M. A.; Bezrukov, S. M. Channel-facilitated membrane transport: Average lifetimes in the channel. *Journal of Chemical Physics* **2003**, 119, (7), 3943-3951.
- (36). Hernandez, H. F.; Tauer, K. Radical desorption kinetics in emulsion polymerization. 1. Theory and simulation. *Industrial and Engineering Chemistry Research* **2008**, 47, (24), 9795-9811.
- (37). Autran, C.; De La Cal, J. C.; Asua, J. M. (Mini)emulsion polymerization kinetics using oil-soluble initiators. *Macromolecules* **2007**, 40, (17), 6233-6238.
- (38). Stickler, M.; Panke, D.; Hamielec, A. E. Polymerization of methyl methacrylate up to high degrees of conversion: Experimental investigation of the diffusion-controlled polymerization. *Journal of Polymer Science: Polymer Chemistry Edition* **1984**, 22, (9), 2243-2253.
- (39). Beuermann, S.; Buback, M.; Davis, T. P.; Gilbert, R. G.; Hutchinson, R. A.; Olaj, O. F.; Russell, G. T.; Schweer, J.; Van Herk, A. M. Critically evaluated rate coefficients for free-radical polymerization, 2: Propagation rate coefficients for methyl methacrylate. *Macromolecular Chemistry and Physics* **1997**, 198, (5), 1545-1560.
- (40). Horie, K.; Mita, I.; Kambe, H. Calorimetric investigation of polymerization reactions. I. Diffusion-controlled polymerization of methyl methacrylate and styrene. *Journal of Polymer Science Part A-1: Polymer Chemistry* **1968**, 6, (9), 2663-2676.
- (41). Struik, L. C. E., *Physical Aging in Amorphous Polymers and Other Materials*. Amsterdam, 1978.
- (42). Keddie, J. L.; Jones, R. A. L.; Cory, R. A. Interface and surface effects on the glass-transition temperature in thin polymer films. *Faraday Discussions* **1994**, 98, (0), 219-230.
- (43). Rodney, D. P.; Perla, R.; Linda, J. B.; Koji, F.; John, M. T. Evidence for the molecular-scale origin of the suppression of physical ageing in confined polymer: fluorescence and dielectric spectroscopy studies of polymer-silica nanocomposites. *Journal of Physics: Condensed Matter* **2007**, 19, (20), 205120.
- (44). Priestley, R. D.; Ellison, C. J.; Broadbent, L. J.; Torkelson, J. M. Structural Relaxation of Polymer Glasses at Surfaces, Interfaces, and In Between. *Science* **2005**, 309, (5733), 456-459.
- (45). Fazio, B.; Trusso, S.; Fazio, E.; Neri, F. Structural characterization of pulsed laser deposited poly(methylmethacrylate) thin films. *Journal of Raman Spectroscopy* **2008**, 39, (2), 182-185.

- (46). Mahanandia, P.; Schneider, J. J.; Khanef, M.; Stuhn, B.; Peixoto, T. P.; Drossel, B. Polymer confinement effects in aligned carbon nanotubes arrays. *Physical Chemistry Chemical Physics* **2010**, *12*, (17), 4407-4417.
- (47). Furer, V. L.; Abdullin, S. N.; Alekseev, V. V. Calculation of band intensities in the raman scattering spectrum of polymethyl methacrylate. *Journal of Applied Spectroscopy* *50*, (2), 179-183.

Chapter 5

RADICAL POLYMERIZATION OF HYDROPHOBIC FLUORINATED MONOMER IN AAO NANOREACTOR

In order to expand the knowledge of in situ polymerization inside AAO template acquired in the preceding chapter, the fifth chapter describes the radical polymerization of a perfluoroacrylate monomer in confinement. It includes a mathematical model to explain the differences between polymerization in bulk and in confinement. Moreover, the hydrophobicity of the nanostructured surface prepared from the AAO template is studied as a potential application.

5.1 Introduction

The rapidly increasing interest in the nanoscale materials and their outstanding applications offered by anodic aluminum oxide (AAO) templates is related to the remarkable trajectory of innovation they found. As demonstrated in the previous chapter, the in-situ polymerization approach is a complementary strategy to the well-known polymer infiltration methods, therefore, they can expand the interest of AAO patterning in the preparation of polymer nanostructures. In fact, the nanocavities of nanoporous alumina templates have been largely employed as nanomolding or nanoreactor to obtain short or long nanofibers, hollow or solid nanorods, core-shell nanostructures, free or supported nanofibers, or even more complex structures with structural and morphological definition on the nanometric scale.¹⁻³ These methods can produce nanostructured polymer morphologies.

It is well known that the morphology of a polymer surface plays an important role in the physical properties and applications of the material. Polymers with the same chemical composition can provide different properties to the surface simply by altering the nanostructure and thus increasing its versatility. In this content, porous AAO templates are emerging as one of the most promising patterning methods to produce nanostructured polymer surfaces.⁴⁻⁶ The selection of the appropriate monomer or polymer as well as the most favorable patterning conditions, together with the adjusted dimensions of template, lead to obtain a variety polymer surfaces with different morphologies, i.e., ordered or irregular nanotopographies (supported standing pillars, collapsed long pillars, etc.). It is worth to mention that a pillared nanostructure surface is generally obtained by placing a film on the top of a polymer filled AAO template of low aspect ratio and the chemical removing of the template.

These kinds of “patterned” polymer pillared nanostructures can stand up and scaled to tens of cm^2 of hydrophobic/hydrophilic surfaces, tissue engineering scaffolds, biosensors and other, for potential applications in coatings, biomedicine, and other fields.^{1, 4, 7} In particular, the hydrophobicity is an important characteristic of the polymer surfaces which depends not only on the chemical nature of the material but also on the surface roughness, therefore, is a suitable property to be controlled by polymer nanostructuring.^{5, 8-11}

Acrylic fluoropolymers exhibit very interesting properties such as good mechanical and thermal properties and chemical stability. Moreover, these materials show hydrophobic character due to their low surface energies. In addition, the wettability of this kind of materials can be heavily influenced by the chemical structure, surface preparation (spin coating, spraying, etc.), surface treatment with plasma, surface morphology and so on. For instance, Shang et al.⁸ reported the facile creation of superhydrophobic surfaces with a fluorine-silicon polymer using a phase separation technique. The surface morphologies of the polymer films were controlled by the degree of phase separation, which could be tuned easily by the ethanol/THF volume ratio and the initial solution concentration. Other techniques, such as electrospinning of fluorinated polymers or spraying of non-fluorinated supercritical solutions, were also described to improve the surface hydrophobicity.^{12, 13} Several other groups have used supercritical fluids as a part of their manufacturing method to create superhydrophobic particles or thin films.¹⁴⁻¹⁶

It is explored that a fluorinated and nanostructured polymer surface prepared by confinement in AAO nanocavities, either by in-situ polymerization or polymer infiltration would improve the hydrophobicity of the polymer surface. In order to generalize the previous results and to spread the impact of the in-situ polymerization of vinyl monomers in AAO nanoreactors and the associated confinement effects, in this chapter, we undertake the study of the radical polymerization of a perfluorodecyl acrylate monomer following the same methodology than in the previous chapter, including the modelisation of the reaction. Furthermore, in order to check the improvement of polymer properties by nanostructuring, the hydrophobicity characteristic of samples was studied by contact angle measurements and different model approaches.

5.2. Experimental part

Materials and AAO templates

The initiator, azoisobutyronitrile (AIBN), was the same that was used in the previous chapter. The monomer 1H,1H,2H,2H perfluorodecyl acrylate, 96 % (FA) was supplied by Interchin. AAO templates were fabricated with phosphoric acid solution and widening pores until obtaining sizes of different length such as 0.7, 1.5 and 50 μm and the pore diameter from 200-350nm. These templates were prepared by the two-step anodization method following the same procedure as reported in Chapter 3.2.

Bulk polymerization of FA

Previously to polymerization of FA in the AAO nanoreactors, the polymerization reactions in bulk were performed by differential scanning calorimetry (DSC) under isothermal and dynamic conditions, similar to the procedure performed in the chapter 4. Isothermal polymerization was carried out at 80, 90, 100 and 110 $^{\circ}\text{C}$ for a time sufficient to achieve 100% of conversion. For that purpose, approximately 10-15mg of FA monomer with AIBN (1% w/w) was weighted, put into hermetic TA Instruments sample pan, sealed and placed into the appropriate position of the instrument. The polymerizations were conducted under nitrogen atmosphere and it was maintained constant in all cases during the whole polymerization process. The reaction exotherms (in normalized values, W g^{-1}) were recorded as a function of time. After the isothermal polymerization process, a dynamic scan from 0 to 150 $^{\circ}\text{C}$ was applied in order to check any residual heat of reaction and to determine the crystallization and melting processes of obtained PFA. The procedure was repeated twice.

Moreover, for subsequent infiltration of the bulk polymer in the AAO template, PFA was synthesized by polymerization of FA at 90 $^{\circ}\text{C}$ under nitrogen atmosphere using AIBN (1% in weight respect to monomer) as initiator and used.

In-situ polymerization of FA in AAO

In order to study the in situ polymerization kinetics of FA in the AAO template, the reaction was followed by Raman spectroscopy as a function of time. The polymerization of FA was carried out in an AAO template with cavities of 250 nm diameter and 50 μm of length. In order to dissolve the initiator in the monomer, the mixture of FA and AIBN (1% in weight respect to monomer) was previously heated at 40 $^{\circ}\text{C}$. Then the mixture was poured onto the surface of AAO template, which was placed in the oven at 40 $^{\circ}\text{C}$ and in nitrogen atmosphere for overnight to provide a template wetting. Once the sample was prepared, the Raman measurements have been performed following the methodology described in the chapter 4. For that purpose, a temperature cell was fixed at 70 $^{\circ}\text{C}$ during 165 minutes, and registered static spectra centre was at 1641 cm^{-1} and 725 cm^{-1} . Raman characterization was also carried for PFA polymer in-situ synthesized at 90 $^{\circ}\text{C}$ for one hour and a half.

Infiltration of PFA in AAO

Nanostructured PFA surfaces were obtained by infiltration of PFA bulk polymer into AAO templates. To compare the morphology with the in situ PFA nanostructure, the PFA bulk was infiltrated in the same template of 250 nm diameter and 50 μm . Before the infiltration process, the AAO template was dried in the oven under vacuum at 200 $^{\circ}\text{C}$ for 2 h. The melting temperature of PFA is around 75 $^{\circ}\text{C}$, so the temperature for infiltration was 120 $^{\circ}\text{C}$ during 8 hours and under nitrogen atmosphere.

For hydrophobicity study we used short templates of several pore sizes/lengths: 200, 250, and 350 nm of diameter and 1.5 and 0.7 μm of length. The temperature of infiltration was 120 $^{\circ}\text{C}$, during 2 hours and under nitrogen atmosphere. The infiltration was favoured by application of manual force when the polymer reached rubbery-liquid flow state.

Characterization techniques

- *Scanning electron microscopy*

The in-situ polymerized nanofibers and infiltrated PFA were morphologically characterized by Scanning Electron Microscopy (SEM), Philips XL-30 ESEM (described in Chapter 3.2.) In order to observe the free nanostructure, nanofibers and nanorods, the aluminium substrate was removed with a mixture of HCl, CuCl₂, and H₂O, and the alumina was dissolved with a sodium hydroxide aqueous solution (5% wt) for 1hour.

- *Differential scanning calorimetry*

Differential scanning calorimetry (DSC) experiments were performed by using a TA Q 2000 instrument equipped with a refrigerant cooling system. The bulk polymerization kinetics was studied with this technique as described above.

- *Raman spectroscopy*

Two types of experiments have been carried out by Raman spectroscopy to study both the infiltration of PFA and the in situ polymerization of FA in AAO nanocavities. The equipment used is the Renishaw InVia Raman Microscope (Renishaw plc, Wottonunder-Edge, UK) described in the chapter 4. In the case of the following of the polymerization with temperature a temperature control cell has been used. The temperature range of cell is between -196 °C to 600°C, using liquid nitrogen to cool.

- *Contact angle and sliding angle.*

The contact angle measurements were performed using Contact Angle System OCA (Dataphysics) equipment described in the chapter 3. The films were deposited onto glassy supports and the contact angles were measured at the air-film interface using 12 mL and 8 mL of water drops. The sliding angle was measured manually as a function of the angle needed to slide the water drop down of the surface.

5.3. Results and discussion

5.3.1. Free radical polymerization of the FA in confinement and bulk

Morphological characterization

Similar to the polymerization of methylmethacrylate (chapter 4) in order to evidence that the synthesis of polyfluoroacrylate has been achieved in confinement, scanning electron microscopy (SEM) was performed. Figure 5.1a shows that nanofibers were successfully obtained by radical polymerization of FA monomer in the AAO nanocavities. The diameter of the nanofibers was around 300 nm, very similar to the template used, although a small difference of diameter between the AAO's pores and nanofibers is produced due to the dilatometer effect. Figure 5.1b shows the nanofibers of PFA obtained by infiltration of PFA bulk into the same AAO nanocavities. As can be observed the morphology of the nanostructures obtained by in situ polymerization and by infiltration is the same.

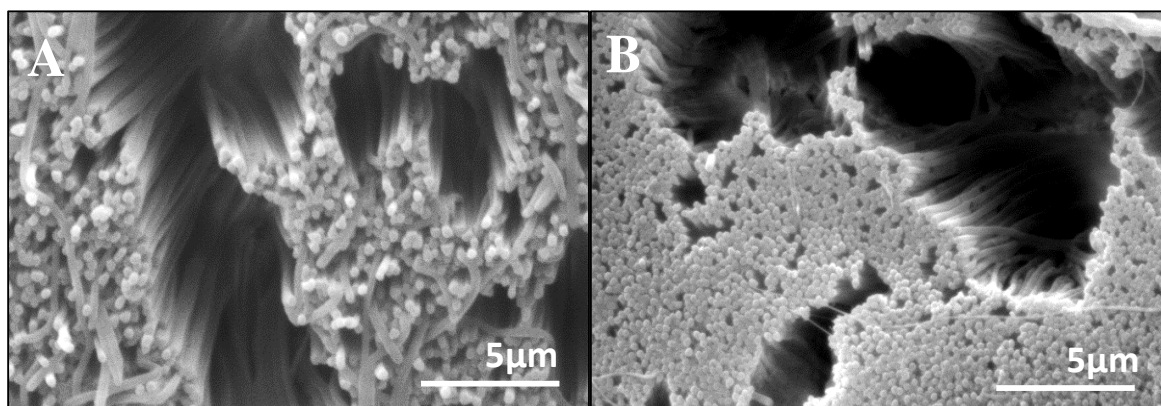


Figure 5.1. SEM of nanofibers of PFA: A) in-situ polymerized into the AAO nanocavities; B) infiltrated polymer into the AAO nanocavities. (AAO templates pore size: 250 nm of diameter and 50 μm of length).

Monitoring by DSC

Free radical polymerization of a fluorinated acrylic monomer (FA) under confinement was carried out in AAO nanocavities and the kinetics of the reaction was compared to bulk polymerization. Figure 5.2 represents the evolution of the heat of the reaction (W g^{-1}) at different temperatures and the polymerization enthalpies obtained are summarized in the Table 5.1. In order to study the conversion of these processes, the polymerization enthalpy (ΔH_T) for the total conversion of the FA to PFA was experimentally measured by DSC

being 160 J g^{-1} . This value was determined experimentally from an average of 3 dynamic DSC experiments in which after isothermal polymerization the samples were heated to high temperatures to polymerize any residual double bonds and calculated the residual heat release. The total enthalpy was calculated from the sum of the integrals of both the isothermal and dynamic parts of the experiment.

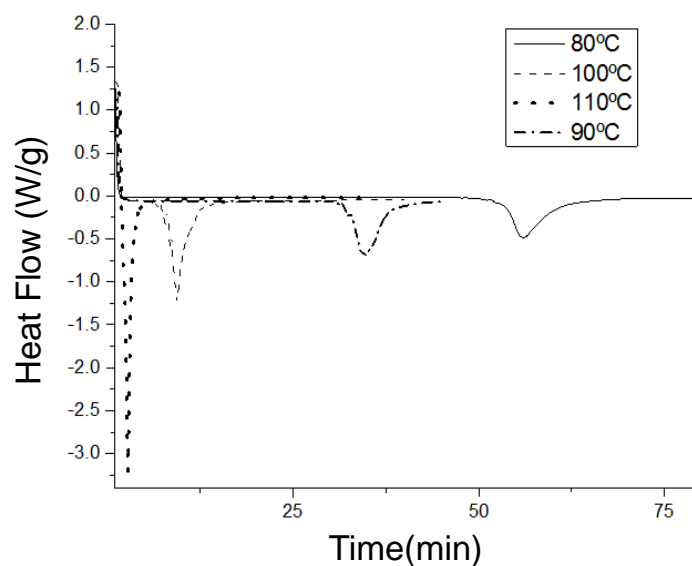


Figure 5.2. The heat release measured by the DSC in the bulk polymerization of PFA at different reaction temperatures (80, 90, 100, 110 °C).

Table 5.1. The heat releases (ΔH) obtained by DSC in PFA polymerized at different isothermal processes (80, 90, 100, 110 °C)

Sample	Polymerization T^a (°C)	ΔH (J g^{-1})
PFA-80	80	149
PFA-90	90	163
PFA-100	100	161
PFA-110	110	139

Monitoring by Raman Spectroscopy

After bulk polymerization, the reaction in confinement was carried out within the AAO templates. For this purpose, templates with pores of 250 nm and 50 μm of length were selected and Raman spectroscopy was used to monitor the polymerization inside the template. The polymerization of FA monomer within the AAO templates was conducted at 70 $^{\circ}\text{C}$ and followed with time by Raman spectroscopy. In Figure 5.3, the Raman spectra of FA monomer and PFA polymer film are plotted between 100 and 3200 cm^{-1} , where the most significant bands are observable. The kinetics of the polymerization was monitored by following the decreasing C=C stretching signal of the monomer, which appears at 1641 cm^{-1} . Figure 5.4 shows the evolution of that band during polymerization at 70 $^{\circ}\text{C}$ at increasing time until 165 minutes. In order to calculate the conversion, the spectrum was normalized with the signal at 725 cm^{-1} , which corresponds to the C-C stretching band that appears in both, the monomer and the polymer. Table 5.2 shows the evolution of the conversion.

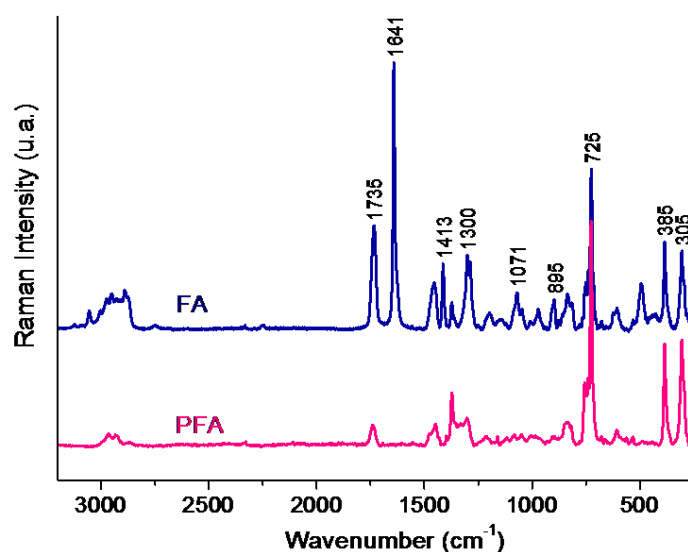


Figure 5.3. Raman spectra of FA and PFA bulk with assignation of characterization bands

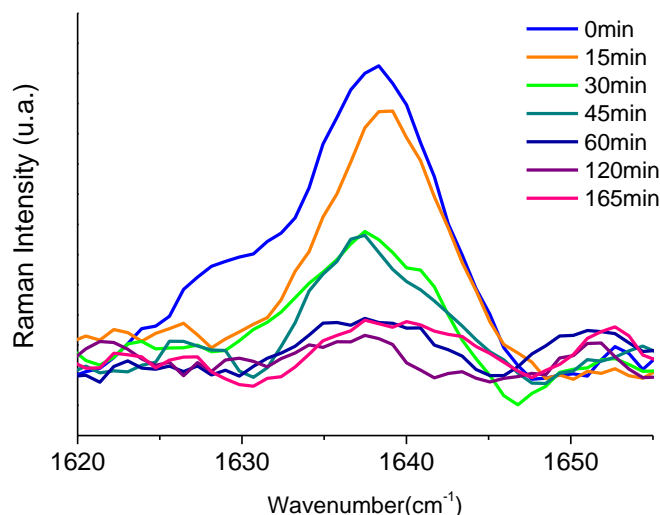


Figure 5.4. Raman spectra of in situ polymerization of FA in AAO template

The determination of monomer conversion by Raman Microscopy in AAO template was carried out by a linear regression obtained with different composition (equivalent to monomer conversion) of samples contained FA and PFA, see Figure 5.5. With these different samples we determine the $I_{C=C}/I_{CF_2}$ relationship for each monomer conversion. The signal at $\sim 1640\text{ cm}^{-1}$ corresponds to C=C stretching band, which is present only in the monomer (FA); while the signal at $\sim 725\text{ cm}^{-1}$ corresponds to the skeletal C-C stretching band, present in monomer and polymer, so it represents 100%. The spectrum has been normalized with the signal at 725 cm^{-1}

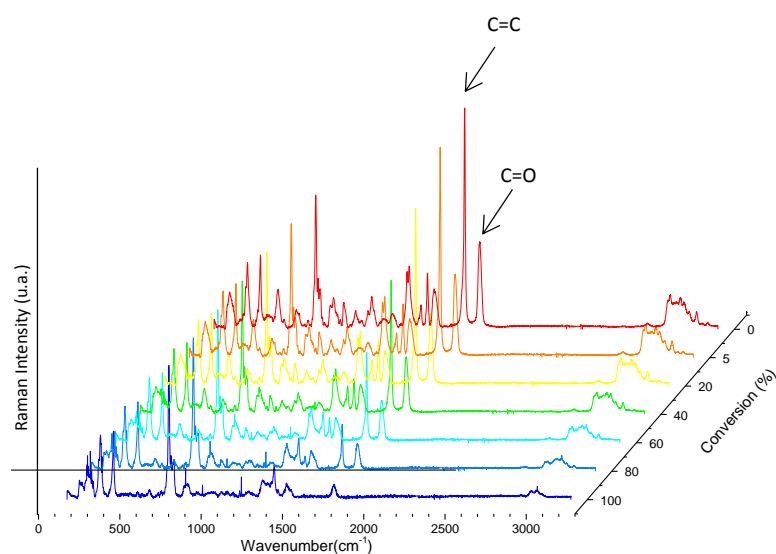


Figure 5.5. Raman spectra of FA polymerization.

Table 5.2. Raman intensity of 1641 cm⁻¹ band and its corresponding conversion at different times.

Time (min)	I ₁₆₄₁	Normalized	Conversion (%)
0	2563,43	1,663	0
15	2183,31	1,417	15,1
30	1122,51	0,728	56,6
45	1017,41	0,66	60,7
60	436,15	0,283	83,4
120	303,18	0,197	88,5
165	426,25	0,277	83,7

5.3.2. Modelling of Polymerization in bulk and confinement

For the case of a free radical polymerization in bulk media the rate of monomer consumption is given by equation 5.1:

$$-\frac{d[M]}{dt} = k_p[M][P\cdot] \quad (5.1)$$

where k_p is the polymerization rate constant, $[M]$ is monomer concentration and $[P\cdot]$ is the radical concentration. The overall concentration of radicals in solution is given by the equation 5.2, as the rate of production of radicals by decomposition of the thermal initiator minus the rate of consumption of radicals by termination, it equated to 0 by steady state approximation:

$$\frac{d[P\cdot]}{dt} = 2k_d f[I] - 2k_t[P\cdot]^2 = 0 \quad (5.2)$$

Where k_d is the initiator decomposition constant, f is the initiator efficiency, $[I]$ is the initiator concentration and k_t is the termination constant. The radical concentration is therefore given by equation 5.3:

$$[P\cdot] = \sqrt{\frac{k_d f [I]}{k_t}} \quad (5.3)$$

Substitution of this value back to the original rate equation 5.1, gives us the equation 5.4,

$$-\frac{d[M]}{dt} = k_p[M] \sqrt{\frac{k_d f [I]}{k_t}} \quad (5.4)$$

And subsequent integration gives the time dependence on conversion.

$$-\ln(1 - X_M) = k_p \sqrt{\frac{k_d f [I]}{k_t}} t \quad (5.5)$$

Assuming the initiator concentration to be constant for the duration of the polymerization and there to be no diffusional constraints as conversion increases, the evolution of conversion in a bulk free radical polymerization is given by

$$-\ln(1 - X_M) = kt \quad (5.6)$$

where X_M is the conversion of monomer expressed as a fraction, k is the overall kinetic rate coefficient and t is the time. The assumption of constant initiator concentration is only valid for short times so from a plot of $-\ln(1-X_M)$ versus time at short times yields a straight line with gradient proportional to the overall kinetic rate constant, k . The conversion, X_M , at a given time is given from the heat release and the total reaction enthalpy, which was taken to be 160 J g^{-1} according to the experimentally determined value detailed in the previous section. The plot of $-\ln(1-X_M)$ versus time for polymerization of the fluoroacrylate monomer at various temperatures can be seen in Figure 5.6.

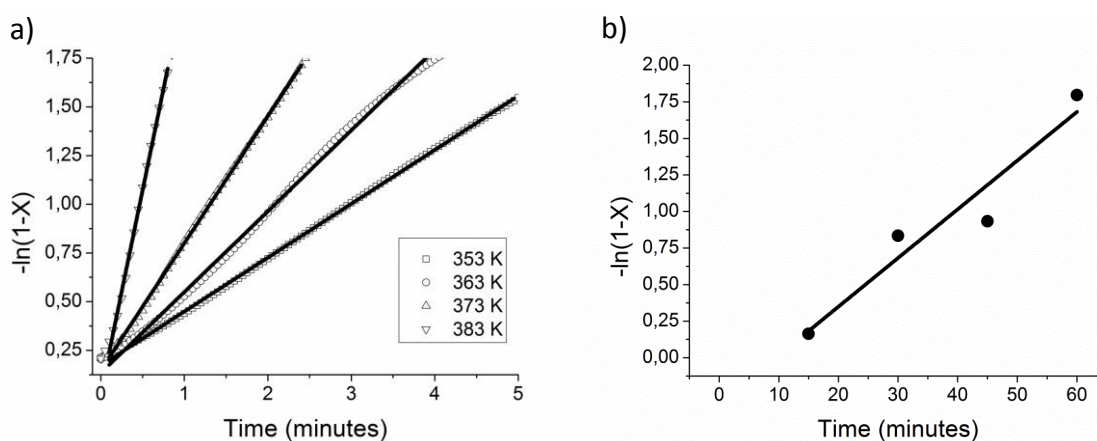


Figure 5.6. a) Linear plots of bulk free radical polymerization of PFA at varying temperatures. The open symbols represent experimental data points and the straight lines correspond to the linear fit of the data in this region. b) Linear plot of confined free radical polymerization of PFA in AAO template.

The overall rate constants calculated from Figure 5.6 follow a linear trend in the Arrhenius plot presented in Figure 5.7. This figure also includes the overall rate constant for a reaction conducted under confinement in the AAO template from the data in Table 5.2. It can be seen that the value was much lower than that obtained from the unconfined

reactions which indicates that confinement affects the concentration of radicals.

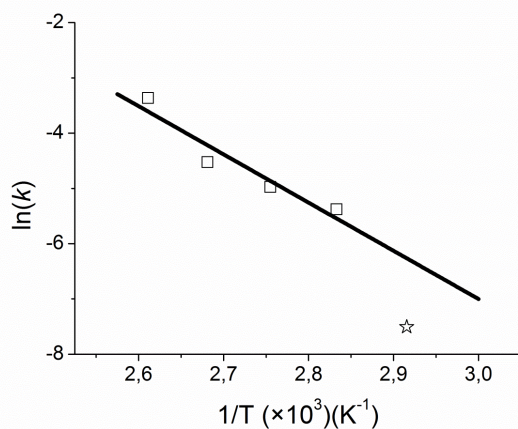


Figure 5.7. Arrhenius plot shows the difference in rate constants between bulk polymerization (\square) and nanoconfined polymerization (\star). The line represents the linear fit to the bulk polymerization data giving the Arrhenius parameters $\ln(A) = 19.1$, $E_a = 72.6 \text{ kJ mol}^{-1}$

In order to explain the significantly reduced rate of polymerization we considered the confinement effects experienced by propagating radicals. The situation observed here is similar in nature to dispersed phase polymerizations such as miniemulsion and emulsion polymerization where the concentration of radicals in the dispersed phase varies depending on the volume of monomer droplets/polymer particles dispersed in water.^{17, 18} In this work, rather than being confined to droplets within a continuous medium, the reaction is confined to a cylindrical space defined by the dimensions of the AAO template used. We developed a mathematical model to account for the compartmentalization effects in such a case.

The model was constructed assuming the radicals were confined to short cylindrical sections of an infinite cylinder. The confinement of radicals to a volume defined by the radius of the compartment and a given length is a result of the lower effective volume experienced by the radicals in a cylindrical space compared to an infinite 3 dimensional space as in bulk polymerization. This has been demonstrated in Brownian dynamic simulations and diffusional models that predict the probability of escape of a particle from a cylindrical space is significantly lower than from a spherical/unconfined space of equivalent volume.¹⁹⁻²² The volume of the individual nanocompartments was given by assuming the length to be equal to the characteristic length of the system, given here by the diameter of the cylindrical compartment, D . Radicals exit and entry between the cylindrical sections was assumed to be nonexistent. Such an assumption is valid based on the zero net

diffusion of radicals along the cylinder. The net diffusion of zero would be expected because a concentration gradient along the cylinder is induced only by the ends of the cylinder. In a system where the length of the cylinder is much greater than its diameter this effect is insignificant and the system can be modelled as a series of individual cylindrical sections with diameter, D , and no net movement of species between them (see Figure 5.8).

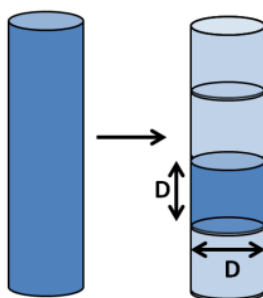


Figure 5.8. Schematic showing the volume of each cylindrical section according to the model.

In each compartment the material balance for the monomer is

$$\frac{dM}{dt} = -k_p[M][P\cdot]v_P \quad (5.7)$$

where k_p is the polymerization rate constant, $[M]$ is monomer concentration and $[P\cdot]$ is the radical concentration which is affected by the compartmentalization effects, and v_P is the volume of the individual compartments. To account for these a modified Smith-Ewart type equation can be used that describes the number of compartments containing n propagating radicals. Let us consider a population of N nanocompartments of volume, v_P , with a distribution of propagating radicals, N_0, N_1, N_2, \dots that correspond to the number of nanocompartments with 0, 1, 2, ... radicals. The number of radicals per compartment varies with time due to termination and initiation events only. These processes are shown in Figure 5.9. The population balance of nanocompartments with n radicals is given by

$$\frac{dN_n}{dt} = 2k_d f [I] N_a v_P (N_{n-2} - N_n) + \frac{k_t}{N_a v_P} ((n+2)(n+1)N_{n+2} - n(n-1)N_n) \quad (5.8)$$

where k_d is the initiator decomposition constant, $[I]$ is the initiator concentration, f is the initiator efficiency, k_t is the termination constant and N_a is Avogadro's number. The average rate of polymerization in one compartment is described by

$$R_P = -\frac{dM}{dt} = k_p[M] \frac{\bar{n}}{N_A \nu_P} \quad (5.9)$$

where \bar{n} is the average number of radical per compartment given by

$$\bar{n} = \frac{\sum n N_n}{\sum N_n} \quad (5.10)$$

The rate constants used were taken from literature values for n-butyl acrylate and are shown in Table 5.2, namely no adjustable parameters were used in the model. No gel effect was taken into account in the model but given the typically low value of \bar{n} ($\bar{n} \approx 0.075$) this omission is acceptable.

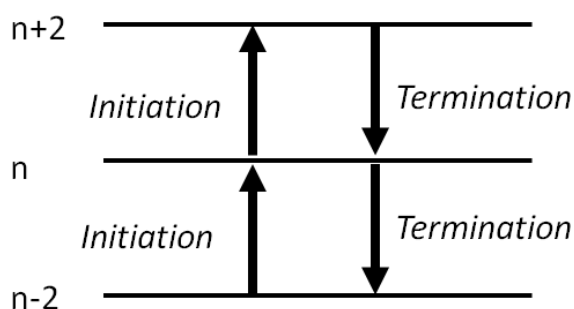


Figure 5.9. Process leading to change in radical concentration within a single compartment.

Table 5.3. Rate constants used in kinetics model

Reaction step	Parameter	Value	Ref
Initiator decomposition	k_d (s^{-1})	$2.8 \times 10^{15} \exp(-15685/T)$	23, 24
AIBN \rightarrow 2I	f	0.4	This work
Propagation	k_p ($M^{-1}s^{-1}$)	$2.2 \times 10^7 \exp(-2152/T)$	25
$P_n \cdot + M \rightarrow P_{n+1} \cdot$			
Termination	k_t ($M^{-1}s^{-1}$)	$1.3 \times 10^{10} \exp(-1010/T)$	26
$P_n \cdot + P_m \cdot \rightarrow D$			

The results of the model along with the experimental data and the predicted rate for a bulk polymerization are shown in Figure 5.10. It can be seen that a good agreement between the experimental data and the compartmentalized model is obtained while the corresponding bulk free radical polymerization would proceed at a much faster rate. Thus, the current model accurately predicts that as the nanocompartment diameter is decreased the probability of termination is increased due to a higher local radical concentration resulting in a slower rate of polymerization.

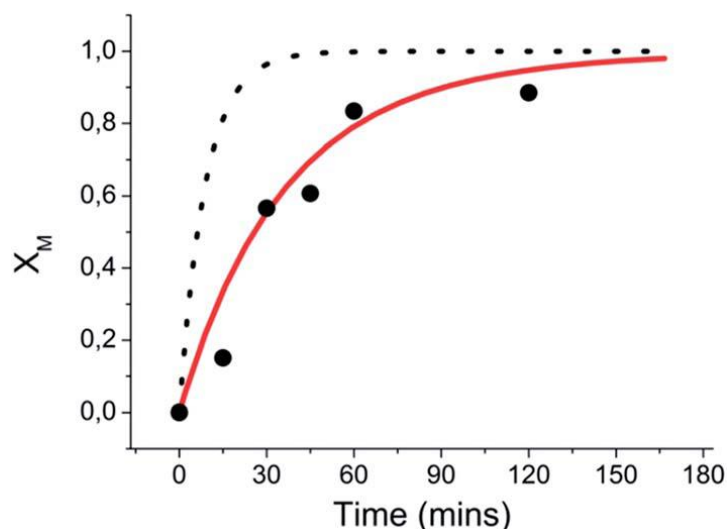


Figure 5.10. Graph of conversion versus time for polymerization of PFA in AAO template. Symbols represent experimental points while the dotted and solid lines represent the model prediction for bulk and nanoconfined polymerization respectively. The rate constants used are shown in Table 3.

The results are also quantitatively in agreement with the Arrhenius plot in Figure 5.7 which predicts a value of $\ln(k) = -6.27$ compared to the simulated value in Figure 5.10 of -6.38 for the bulk polymerization, and an experimental value of $\ln(k) = -7.54$ compared to the simulated value of -7.82 for the compartmentalized polymerization. It is thought that this model and experimental system may prove useful for the detection and quantification of compartmentalization effects in many other radical systems, most notably controlled radical polymerizations, since complications arising from radical entry/exit and partitioning effects can be neglected.²⁷⁻²⁹

5.3.3. Nanostructured PFA surface and applications

In the experiments documented above the nanostructured polymer surfaces were obtained by in situ polymerization of FA under confinement into AAO templates. In order to expand the application of nanostructured polymers produced by this technique, the infiltration of the preformed polymer into the template was carried out. PFA was previously polymerized in bulk and then infiltrated into AAO templates of different pore diameters 200, 250 and 350 nm and length of 1,5 and 0.7 μm . Afterwards, the alumina and aluminum of AAO were removed following the procedure mentioned before. Evidence of the polymer infiltration into the nanocavities was achieved through the morphological study of the film using SEM. Figure 11 A-C shows the SEM images of nanofibers obtained with templates of 1.5 μm of length and different pore diameters, while Figure 11 D shows nanofibers of 0.7 μm of length and the 350 nm of pore diameters. Samples are named: n(B)PFA/200 fibers, n(B)PFA/250 and, n(B)PFA/350 fibers. No apparent difference in the fiber morphology neither in the crystallinity was obtained when comparing the PFA nanofibers synthesized inside the AAO templates and those obtained by infiltration in the same template.

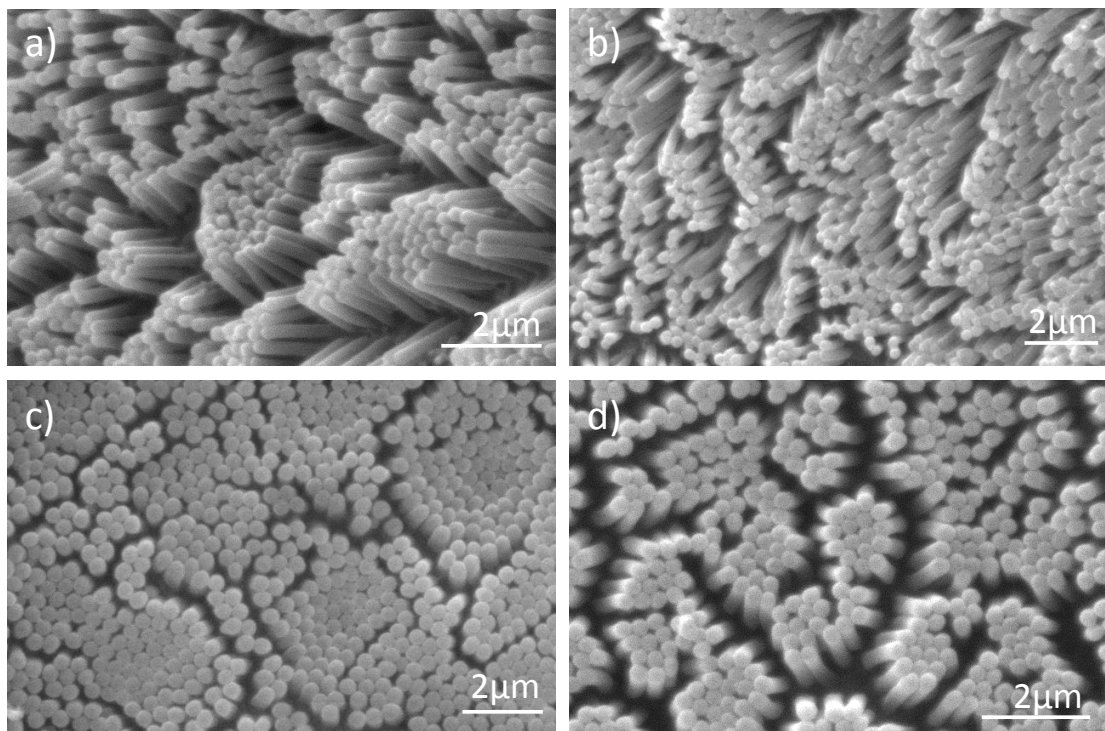


Figure 5.11. n(B)PFA infiltrated into AAO templates with different pore sizes: a) 200 nm of diameter and 1.5 μm of length; b) 250 nm of diameter and 1.5 μm of length; c) 350 nm of diameter and 1.5 μm of length; d) 350 nm of diameter and 0.7 μm of length.

One of the most interesting properties of the fluorinated polymer surfaces is the hydrophobicity. However, the water-repellent character of a film is not only controlled by the chemical composition, but also by the surface morphology, that affects the contact angle of a water droplet placed on it. In rough morphologies, air pockets can be trapped between the surface and the liquid droplet and highly hydrophobic surfaces can be achieved. In this regard, and with Cassie's model very much in mind,³⁰ the contact angle of nanostructured PFA surfaces obtained after infiltration of the polymer into AAO nanocavities were measured. Table 5.4 summarizes the results obtained. For the sake of comparison the contact angle of a flat PFA (no infiltrated) surface is included. These results demonstrated the increase in hydrophobicity of the same starting material after nanostructuration by using AAO templates. The nanocavities induced the roughness on the PFA surfaces increasing the amount of air cubicles trapped between the surface and water droplet, and superhydrophobic films were achieved as a consequence. This way, starting from hydrophobic PFA surfaces of around 114° of contact angle, superhydrophobic surfaces with contact angle above 150° were obtained by a nanostructuration of the material (see Figure 5.12).

Table 5.4. Values of contact angle and f_2 (the surface occupied by air when the porous PFA surface contacted the water droplet) corresponding to the n(B)PFA surfaces with different nanostructuring.

Sample	Characteristics	θ (8 μ L drop)	f_2 (%)
PFA	Flat	114	-
n (B)PFA ₁	$\varnothing \approx 200\text{nm}/L \approx 1.5\mu\text{m}$	137	54.8
n (B)PFA ₂	$\varnothing \approx 250\text{nm}/L \approx 1.5\mu\text{m}$	159	88.8
n (B)PFA ₃	$\varnothing \approx 350\text{nm}/L \approx 1.5\mu\text{m}$	141	62.4
n (B)PFA ₄	$\varnothing \approx 350\text{nm}/L \approx 0.7\mu\text{m}$	151	78.9



Figure 5.12. Hydrophobicity enhancement of the fluorinated surface (PFA) after nanostructuring by AAO templates.

Furthermore, the effect of the AAO nanocavities pore size/ length on the hydrophobicity of the PFA surfaces was studied. In an ideal system, when the pore size of the AAO templates increases the diameter of the resulting nanofibers is bigger, thus lowering the amount of air pockets trapped between the surface and water droplet, resulting in a contact angle that should be closer to that of the corresponding smooth surface. However, no clear correlation between the pore size (200, 250 and 350 nm) of the template and the final contact angle (n(B)PFA₁ = 137°, n(B)PFA₂ = 159°, n(B)PFA₃ = 141°) was observed. This can be attributed to the random collapse of PFA nanofibers after removing the AAO nanocavities used as templates. PFA pillars are not rigid enough to maintain their individuality after removing the template and they tend to collapse. The same collapsing effect was observed using 0.7 μm pore length template (Figure 5.11 D) and a contact angle of 151° was achieved. In all cases, it can be observed that there is a clear enhancement in the hydrophobic property of the surface by molding the material with AAO templates, which is attributed to the roughness of the new surfaces. As explained above, air pockets trapped between the surface and water droplet were responsible for the enhancement in the hydrophobicity of the surface. According to Cassie's model, the surface occupied by the air can be calculated by the following equation:

$$\cos \theta^* = f_1 \cos \theta_1 + f_2 \cos \theta_2 \quad (5.11)$$

where f_1 and f_2 are corresponding to a fraction interfacial areas of the liquid in contact with the solid and the air, respectively, thus $f_1 + f_2 = 1$. When $\theta_2 = 180^\circ$ (contact angle of a liquid on air in the case of suspended droplets) the equation can be modified in the following way:

$$\cos \theta^* = (1 - f_2) \cos \theta_1 - f_2 \quad (5.12)$$

Considering the contact angle of 114° for PFA in a smooth surface (θ_Y), f_2 was calculated for each sample taking the contact angle values corresponding to 8 μL of water drop (see Table 5.4). The values of f_2 given in Table 5.4 for n(B)PFA2,3,4 are much higher than the values that can be calculated from the AAO templates, indicating that the nanopillar collapse induced an additional degree of roughness.

Another characteristic of superhydrophobic surfaces is the sliding angle, which is defined as the critical angle where a water droplet with a certain weight begins to slide down the inclined plane³¹. An interesting superhydrophobic material is found in the nature, the “lotus leaf”, where the water droplet rolls off the leaf spontaneously when slightly tilted. Miwa et al. described the effect of the surface roughness on the sliding angle of the water droplet and they concluded by microstructural observation that surface structures that can trap air were important for the preparation of low-sliding-angle surfaces³¹. Therefore, the sliding angle of the n(B)PFA surface was measured to obtain a small angle of 8° using a water droplet with a volume of around 8 μL . As a result of obtaining a superhydrophobic surface with structures that can trap air, the water droplet easily rolled off it when the substrate was inclined at a slight angle and a lotus effect was observed on the surface.

5.4. Conclusions

The polymerization kinetics of perfluoroacrylate monomer within an AAO nanoreactor was studied as a function of time and a mathematical model was derived to explain the decrease in polymerization rate compared to bulk free radical polymerization.

The free radical polymerization of a fluorinated acrylic monomer can be also satisfactorily studied in confinement in an AAO nanoreactor by Raman spectroscopy. The polymerization conversion in two hours is near 95%, so in-situ polymerization is a faster process than polymer infiltration. The morphology was observed by SEM microscopy and shows that the nanostructures by in situ polymerization and by polymer infiltration are the same, nanofibers. A simpler mathematical model than the previous one is implemented to describe the differences between polymerization in bulk and in AAO nanocavities. In this case, the decrease in polymerization rate is directly related to the increase in the termination step, due to a lower effective volume experienced by the radicals when confined to a cylindrical volume.

Furthermore, when PFA is nanostructured by infiltration into AAO nanocavities of 200nm of pore diameter and 1 μ m of pore length, a superhydrophobic surface is achieved, deduced from the value of water contact angle of 159°, much higher than its analogous non-nanostructured PFA, 114°. The “lotus effect” is observed in the superhydrophobic surface, since the low sliding angle is of 8°.

5.5. References

- (1). Martín, J.; Maiz, J.; Sacristan, J.; Mijangos, C. Tailored polymer-based nanorods and nanotubes by "template synthesis": From preparation to applications. *Polymer* **2012**, *53*, (6), 1149-1166.
- (2). Martín, J.; Mijangos, C. Tailored Polymer-Based Nanofibers and Nanotubes by Means of Different Infiltration Methods into Alumina Nanopores. *Langmuir* **2008**, *25*, (2), 1181-1187.
- (3). Steinhart, M.; Wendorff, J. H.; Greiner, A.; Wehrspohn, R. B.; Nielsch, K.; Schilling, J.; Choi, J.; Gösele, U. Polymer Nanotubes by Wetting of Ordered Porous Templates. *Science* **2002**, *296*, (5575), 1997-1997.
- (4). Giussi, J. M.; Blaszczyk-Lezak, I.; Allegretti, P. E.; Cortizo, M. S.; Mijangos, C. Tautomerizable styrenic copolymers confined in AAO templates. *Polymer* **2013**, *54*, (18), 5050-5057.
- (5). Lee, J. A.; McCarthy, T. J. Polymer Surface Modification: Topography Effects Leading to Extreme Wettability Behavior. *Macromolecules* **2007**, *40*, (11), 3965-3969.
- (6). Gupta, M.; Gleason, K. K. Surface modification of high aspect ratio structures with fluoropolymer coatings using chemical vapor deposition. *Thin Solid Films* **2009**, *517*, (12), 3547-3550.
- (7). Grimm, S.; Lange, A.; Enke, D.; Steinhart, M. Imprinting macropore arrays into mesoporous silica monoliths. *Journal of Materials Chemistry* **2012**, *22*, (19), 9490-9493.
- (8). Shang, Q.; Fu, B.; Liu, H.; Wang, M.; Xiao, G. Facile creation of superhydrophobic surface with fluorine-silicon polymer under ambient atmosphere. *J Coat Technol Res* **2012**, *9*, (5), 589-595.
- (9). Cengiz, U.; Erbil, H. Y. Superhydrophobic perfluoropolymer surfaces having heterogeneous roughness created by dip-coating from solutions containing a nonsolvent. *Applied Surface Science* **2014**, *292*, (0), 591-597.
- (10). Bilgin, S.; Isik, M.; Yilgor, E.; Yilgor, I. Hydrophilization of silicone-urea copolymer surfaces by UV/ozone: Influence of PDMS molecular weight on surface oxidation and hydrophobic recovery. *Polymer* **2013**, *54*, (25), 6665-6675.
- (11). Peng, C.-W.; Chang, K.-C.; Weng, C.-J.; Lai, M.-C.; Hsu, C.-H.; Hsu, S.-C.; Li, S.-Y.; Wei, Y.; Yeh, J.-M. UV-curable nanocasting technique to prepare bio-mimetic super-hydrophobic non-fluorinated polymeric surfaces for advanced anticorrosive coatings. *Polymer Chemistry* **2013**, *4*, (4), 926-932.
- (12). Agarwal, S.; Horst, S.; Bognitzki, M. Electrospinning of Fluorinated Polymers: Formation of Superhydrophobic Surfaces. *Macromolecular Materials and Engineering* **2006**, *291*, (6), 592-601.
- (13). Ovaskainen, L.; Rodriguez-Meizoso, I.; Birkin, N. A.; Howdle, S. M.; Gedde, U.; Wågberg, L.; Turner, C. Towards superhydrophobic coatings made by non-fluorinated polymers sprayed from a supercritical solution. *The Journal of Supercritical Fluids* **2013**, *77*, (0), 134-141.

- (14). Desbief, S.; Grignard, B.; Detrembleur, C.; Rioboo, R.; Vaillant, A.; Seveno, D.; Voué, M.; De Coninck, J.; Jonas, A. M.; Jérôme, C. Superhydrophobic aluminum surfaces by deposition of micelles of fluorinated block copolymers. *Langmuir* **2009**, *26*, (3), 2057-2067.
- (15). Rao, A. V.; Hegde, N. D.; Hirashima, H. Absorption and desorption of organic liquids in elastic superhydrophobic silica aerogels. *Journal of colloid and interface science* **2007**, *305*, (1), 124-132.
- (16). Jagannathan, R.; Mehta, R. V. Continuous, atmospheric process to create organic clusters and nanostructured, functional films. *Advanced Functional Materials* **2006**, *16*, (5), 633-639.
- (17). Alduncin, J. A.; Forcada, J.; Barandiaran, M. J.; Asua, J. M. On the main locus of radical formation in emulsion polymerization initiated by oil-soluble initiators. *Journal of Polymer Science Part A: Polymer Chemistry* **1991**, *29*, (9), 1265-1270.
- (18). Autran, C.; de la Cal, J. C.; Asua, J. M. (Mini)emulsion Polymerization Kinetics Using Oil-Soluble Initiators. *Macromolecules* **2007**, *40*, (17), 6233-6238.
- (19). Berezhkovskii, A. M.; Pustovoi, M. A.; Bezrukov, S. M. Channel-facilitated membrane transport: Transit probability and interaction with the channel. *The Journal of Chemical Physics* **2002**, *116*, (22), 9952-9956.
- (20). Bezrukov, S. M.; Berezhkovskii, A. M.; Pustovoi, M. A.; Szabo, A. Particle number fluctuations in a membrane channel. *The Journal of Chemical Physics* **2000**, *113*, (18), 8206-8211.
- (21). Berezhkovskii, A. M.; Pustovoi, M. A.; Bezrukov, S. M. Channel-facilitated membrane transport: Average lifetimes in the channel. *The Journal of Chemical Physics* **2003**, *119*, (7), 3943-3951.
- (22). Hernandez, H. F.; Tauer, K. Radical Desorption Kinetics in Emulsion Polymerization. 1. Theory and Simulation. *Industrial & Engineering Chemistry Research* **2008**, *47*, (24), 9795-9811.
- (23). Tefera, N.; Weickert, G.; Westerterp, K. R. Modeling of free radical polymerization up to high conversion. II. Development of a mathematical model. *Journal of Applied Polymer Science* **1997**, *63*, (12), 1663-1680.
- (24). Tefera, N.; Weickert, G.; Westerterp, K. R. Modeling of free radical polymerization up to high conversion. I. A method for the selection of models by simultaneous parameter estimation. *Journal of Applied Polymer Science* **1997**, *63*, (12), 1649-1661.
- (25). Asua, J. M.; Beuermann, S.; Buback, M.; Castignolles, P.; Charleux, B.; Gilbert, R. G.; Hutchinson, R. A.; Leiza, J. R.; Nikitin, A. N.; Vairon, J.-P.; van Herk, A. M. Critically Evaluated Rate Coefficients for Free-Radical Polymerization, 5. *Macromolecular Chemistry and Physics* **2004**, *205*, (16), 2151-2160.
- (26). Barth, J.; Buback, M.; Hesse, P.; Sergeeva, T. Termination and Transfer Kinetics of Butyl Acrylate Radical Polymerization Studied via SP-PLP-EPR. *Macromolecules* **2010**, *43*, (9), 4023-4031.
- (27). Zetterlund, P. B. Controlled/living radical polymerization in nanoreactors: compartmentalization effects. *Polymer Chemistry* **2011**, *2*, (3), 534-549.
- (28). Zetterlund, P. B.; Okubo, M. Compartmentalization in Nitroxide-Mediated Radical Polymerization in Dispersed Systems. *Macromolecules* **2006**, *39*, (26), 8959-8967.

- (29). Kagawa, Y.; Zetterlund, P. B.; Minami, H.; Okubo, M. Compartmentalization in Atom Transfer Radical Polymerization (ATRP) in Dispersed Systems. *Macromolecular Theory and Simulations* **2006**, *15*, (8), 608-613.
- (30). Cassie, A. B. D.; Baxter, S. Wettability of porous surfaces. *Transactions of the Faraday Society* **1944**, *40*, (0), 546-551.
- (31). Miwa, M.; Nakajima, A.; Fujishima, A.; Hashimoto, K.; Watanabe, T. Effects of the Surface Roughness on Sliding Angles of Water Droplets on Superhydrophobic Surfaces. *Langmuir* **2000**, *16*, (13), 5754-5760.

Chapter 6

STEP-GROWTH POLYMERIZATION OF DIOL AND DIISOCYANATE IN AAO NANOREACTOR

The sixth chapter studies the step-growth polymerization reaction between two monomers, a diol with diisocyanate, in AAO nanoreactor. It includes a mathematical model to explain the differences with polymerization in bulk and in confinement. Moreover, the hydrophobicity of the nanostructured surface prepared in the AAO template is studied.

6.1. Introduction

In previous chapters, we have explored the ability to replicate the well defined geometry of anodic aluminum oxide (AAO) templates by the successful infiltration of liquid vinyl monomer followed by its radical polymerization.

Interestingly, while it is increasing the number of studies on radical polymerizations of vinyl monomers including styrene¹, acrylates and even ionic liquid² conducted in AAO nanoconfined system, the study of step-growth polymerization is relatively scarce. Simon's group studied the curing behaviour of bisphenol M dicyanate ester (BMDC) under defined nanoscale constraints in GPC to give a thermoset resin by trimerization reaction³⁻⁵. They found that the BMDC physically confined in the pores had a higher curing rate than the resin in the bulk state. Similar results were obtained by Amanuel and Malhotra when studied the effect of confinement on the curing behaviour of phenolic resin confined in the nanopores of a porous silica substrate.⁶ Recently, Tarnacka *et al.*⁷ reported the curing epoxy system under confinement of AAO by step-growth polymerization and observed that the polymerization is faster under confinement, compared to the analogous reaction carried out in the bulk system at the same temperature conditions. Moreover, the rate of reaction is slower at the surface of the pores with respect to the polymerization at the core of nanochannels.

These works are the only examples recently reported in the literature, while to the best of our knowledge the synthesis of polyurethanes in AAO templates has never been reported, even if polyurethanes are of particular interest since their physical properties can be easily tuned by altering the diol and diisocyanate monomers from which they are typically polymerized. Although, PU are formed by step-growth polymerization of a macroglycol and polyisocyanate,⁸ the direct addition of the diisocyanate to the glycol was found to be more satisfactory over other preparative methods, with the advantage that it involves a simple addition reaction and proceeds with the formation of no secondary product.⁹

Polyurethanes are a versatile family of polymers that have found a wide range of industrial applications (adhesives, biomedicine, foams, clothes or coatings) due to the easy fabrication of a huge range of tailored chemical structures. Moreover, nano and microstructured polyurethanes have also attracted increasing interest as functional coating and adhesives with growing range of applications. For instance, polyurethane acrylate nanopillars obtained by polymer infiltration AAO molds and asymmetrically bent in one direction have anisotropic shear adhesion behavior and directional wetting characteristics.¹⁰ Thermoplastic polyurethanes (TPU) nanofibers are widely used class of polymer with good mechanical properties that open the application perspectives of non-conducting for nano-device¹¹, and the good biocompatibility is used as an alternative material for drug delivery system¹² or tissue engineering applications¹³. TPU nanofibers are successfully produced by electrospinning technique while there are scarce works reported in the bibliography about thermal polyurethanes in anodic alumina templates. Most of them are based on infiltration the polymer by solution or melt in the template in order to obtain nanotubes¹⁴⁻¹⁶. The solution concentration, the volume of solution, and the pore size of the template, are major factors affecting the morphology of nanostructures in the template wetting with polymer solutions.

Molecular simulation have shown that diffusion effects have unique implications in step-growth polymerizations^{17, 18} and these effects are heightened for reactions conducted under nanoconfinement¹⁹. Polyurethanes are of particular interest since their physical properties can be easily tuned by altering the diol and diisocyanate monomers from which they are typically polymerized.

This work focuses on the synthesis of nanostructured polyurethanes by the infiltration, and subsequent polymerization, of a diol and a diisocyanate within the porous structure of an AAO template. The kinetics of the polymerization is followed using Fourier transform infrared spectroscopy and molecular weight of polymer by GPC. A mathematical model was developed to explain these results, taking into account the effects of confinement and chemical interactions of OH with the pore walls. Finally, the SEM characterization of in-situ synthesis of polyurethanes within the AAO template is shown to proof the viable route to nanostructured polymers, whereby the dimensions of the template used dictate the surface wettability.

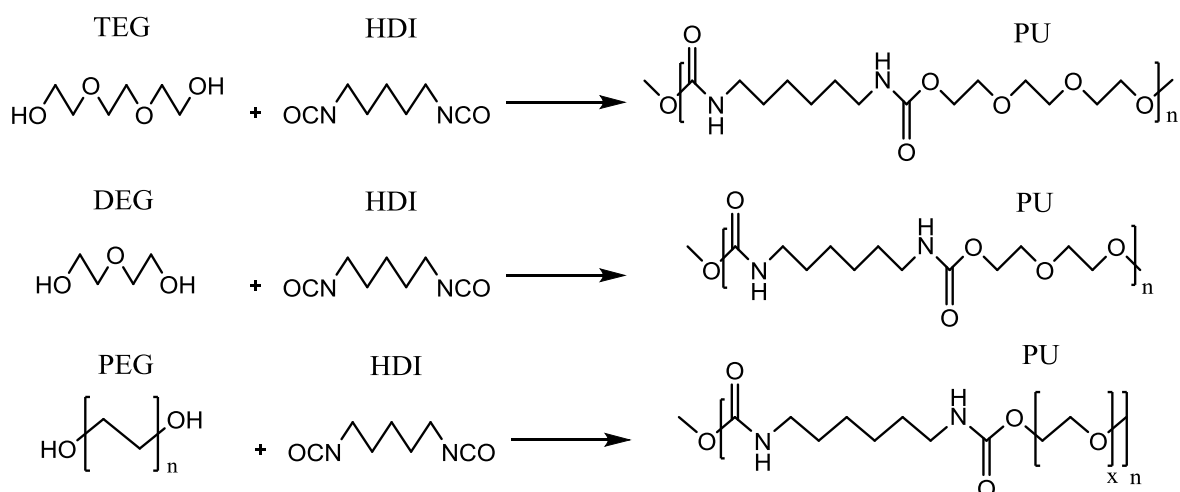
6.2. Experimental part

Materials and AAO templates

Three different diglycol were used: triethylene glycol, 99%, (TEG), diethylene glycol, 99%, (DEG) and Polyethylene glycol, 99%, (PEG) from Aldrich. The diisocyanate, hexamethylenediisocyanate (HDI) was also purchased from Aldrich. HDI was purified by distillation under vacuum at 145°C. AAO templates having pores of 35, 60 and 140 nm diameter and 100 μm length for polymerization and 140nm and one micrometer length for studying the wettability was prepared by the two-step anodization method as reported in Chapter 3.2.

Bulk polymerization of Polyurethane

The polymerization between diisocyanate (OCN-R-NCO) and diglycol (HO-R'-OH) is an addition reaction, where hydroxyl molecules begin to join for both sides of diisocyanate group to give a high molecular weight polymer. To control the molecular weight is necessary to take into account in the stoichiometric balance of the two bifunctional monomers. The same molar ratio 1:1 was used in all the reactions. Firstly, the reaction of polymerization was studied between the diisocyanate and each diglycol monomer TEG, DEG and PEG. The mixture of monomers was prepared with stoichiometry (1:1) and stirred, for 15 minutes, to obtain a homogeneous solution. The polyurethane bulk polymerization was carried out in an oven at 80°C, but without agitation, catalyst and no inert atmosphere. The samples were measured by ATR every 20 minutes for the first hour and later every 60 minutes until the isocyanate band disappeared. The reactions, that take place between the TEG, DEG, PEG and HDI, are described in the Scheme 6.1.



Scheme 6.1. Polymerization reaction between diglycols and diisocyanate.

The molecular weight of formed monomer unit is 319, 274 and 568 g mol⁻¹ in the case of the reaction between HDI with TEG, DEG and PEG respectively. Initially the catalyst tin(II) octoate (SnOct₂) was to be used, but in the case of TEG and DEG the polymerization reactions of the polyurethane was instantaneous when the catalyst is added, therefore it was only used in the case of PEG.

In-situ polymerization of Polyurethane in AAO

Similar to the study of polymerization in confinement by DSC, to study the polymerization in alumina nanopores by infrared spectroscopy is necessary to remove the aluminium support from the template with a solution of HCl, CuCl₂ and H₂O. The alumina templates used in this experiment has 100 μm of length and 35, 60 and 140 nm of diameter. In order to compare both polymerizations, bulk and confined reactions were carried out from the same solution of TEG and HDI under the same conditions. The mixture of TEG and HDI (1:1) was stirred for 15 minutes to obtain a homogeneous solution. This solution was poured onto the surface of the AAO template to infiltrate the solution, for 10 minutes at 25°C. The template was placed at 80°C in an oven and measured by FTIR at different reaction times.

Polymerization progress was monitored by attenuated total internal reflectance-Fourier transform infrared (ATR-FTIR) using a PerkinElmer Spectrum One infrared spectrometer equipped with an ATR accessory. The absorbance spectra were subtracted and normalized

with respect to a specific band corresponding to a stretching aliphatic vibration (2935 cm^{-1}), for a visual demonstration of the changes. Bulk infrared spectra were accumulated in the $600\text{-}4000\text{cm}^{-1}$ range, while spectra of the AAO templates were collected from 2500 to 4000 cm^{-1} due to the absorption alumina in the low frequency range. All spectra were recorded with 4 scans.

Infiltration of Polyurethane in AAO

In order to study the wettability of the samples, bulk polymer was infiltrated in a short AAO with 140nm of pore size and $1\mu\text{m}$ length to study the contact angle. The infiltration temperature was 110°C under vacuum for 120 minutes. The polyurethane nanorods were obtained after removing the aluminium support and the alumina template as have been described in the previous chapters. The bulk part that has not infiltrated in the template was remained and used as the supported of the nanorods.

Characterization techniques

- ***Thermal characterization***

In order to decide with what diglycol continue the work, the differential scanning calorimetry technique is used to study the thermal behaviour. Bulk polyurethane samples were encapsulated in aluminium pans and tested in the Perkin Elmer 8500 under ultrahigh nitrogen atmosphere. All the samples were cool down until -30°C and after 3 min are heated up until 150°C at $10^\circ\text{C min}^{-1}$. After cooling down until -30°C at the same rate, samples were heated up until 200°C .

- ***Morphological characterization***

The in-situ polymerized nanofibers were morphologically characterized by Scanning Electron Microscopy (SEM), Philips XL-30 ESEM. For the observation of nanofibers obtained in the template, the preparation of the samples was carried out by fracture of the template under cryogenic conditions. For the observation of morphologies obtained in the short templates, the AAO template was removed.

- ***Molecular weight***

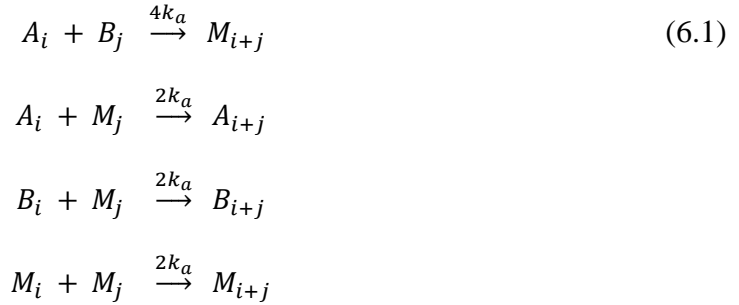
Molecular weight of the polymer were determined by size exclusion chromatography (SEC) in a Perkin Elmer chromatography system with Styragel (300 x 7.8 mm, 5 μ m nominal particle size) water columns. Dimethylformamide (DMF) was used as eluent. The measurements were carried out at 25 °C at a flow rate of 1.0 ml/min using a refractive index detector series 200. The polymer concentration was 3 mg/ml. The calibration was performed with monodispersed polystyrene standards in the range of 2.0 to 9000kDa. In order to remove the polyurethane from the template, alumina with the polymer inside was immersed in 1 ml of dimethylformamide (DMF) with stirring for 4 days.

- ***Surface characterization by contact angle***

Water contact angle (CA) measurements were performed with a KSV Theta goniometer equipment. The nanostructured polymers were deposited onto glass supports and the contact angles were measured at the air-film interface using 2 μ L droplet and a charge coupled device camera was used to capture the images for the determination of contact angles.

6.3. Polymerization model inside nanopores

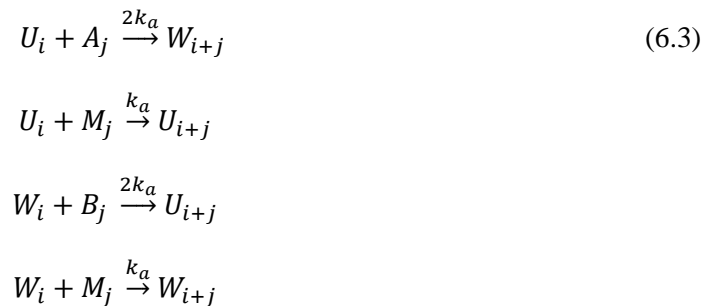
The reaction between diol and diisocyanate follows proceeds according to a classical A-A, B-B monomer system as shown in equation 6.1



where A_i , B_i and M_i are molecules with chain length i and two OH chain ends, two NCO chain ends and one OH and one NCO chain end respectively. k_a is the rate coefficient for reaction between the alcohol and the isocyanate groups. In the presence of alumina the Al-OH groups present on the wall may also react with NCO groups leading to the additional reactions shown in equation 6.2



Where U_i and W_i are molecules with chain length i which are tethered to the pore wall, at one end and at the other contain an NCO group and an OH group, respectively. k_x is the reaction constant between isocyanates and hydroxyl of alumina wall (see scheme 6.2). These can subsequently react with the other alcohol/isocyanate groups in the system according to equation 6.3

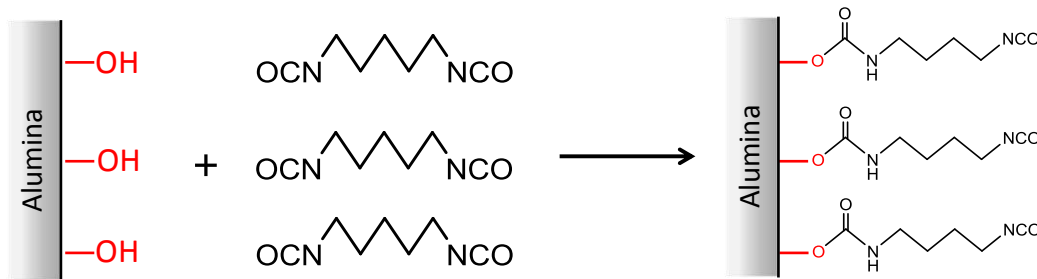


The introduction of alumina into the system results in an increase in the rate of polymerization because there are more reactive group available and also a reduction in molecular weight due to employing an effective stoichiometric imbalance. However,

experimentally the rate of polymerization is greater than can be accounted for than, by considering only the reactivity of the pore walls, without using unrealistically high density of OH groups on the alumina surface and reducing the molecular weight such that only very low molecular weight materials ($M_w < 1000$ g/mol) are expected to be obtained, in disagreement with experiment. In order to account for this, we consider the catalytic effect that the acidic alumina groups may have on the reaction between alcohol and isocyanate such that in equation 6.4

$$k_a = k_{a0} + k_{a_cat}/d \quad (6.4)$$

where k_{a0} is the rate coefficient for reaction between the alcohol and isocyanate in bulk, k_{a_cat} accounts for the acceleration of the reaction due to the acidic alumina hydroxyl groups,²⁰ and d is the diameter of pores. Since the concentration of alumina hydroxyl groups scales with the inverse of the diameter of the pore, this acceleration is enhanced as the pore size decreases. This constant also encompasses other factors that may contribute to an increased rate as pore diameter is decreased such as the increased collision frequency upon confinement which has been shown by Malvadi *et al.*¹⁹.



Scheme 6.2. Reaction between -OH from pore wall (alumina) and isocyanate group.

In order to account for the limiting termination and the lower than expected polydispersity of all the reactions, the effects of diffusion limitations were considered according to the work of Guzmán *et al.*²¹. In this framework, the Hatta number (Ha) is employed, which is a dimensionless parameter that relates the relative importance of intrinsic reaction rate coefficient (k_{int}) to the diffusional rate coefficient for the reaction between a molecule length i and a molecule with length j such that in equation 6.5

$$Ha(i, j) = \frac{k_{int}}{k_{diff}(i, j)} = \frac{\phi}{(\sqrt{i} + \sqrt{j})(i^{-m1} + j^{-m2})} \quad (6.5)$$

The constant $m1$ and $m2$ are related to the entanglement length of the polymer and are equal to 1 if $i < N_{ent}$ and $j < N_{ent}$. If $i > N_{ent}$ and $j > N_{ent}$ then $m1$ and $m2$ are equal to 2. The value of N_{ent} is related with the molecular weight between entanglements (M_e) and the molecular weight of the monomer (M_0), as show in the equation 6.6

$$N_{ent} = \frac{M_e}{M_0} \quad (6.6)$$

The value for the entanglement length is approximated to be equal as the structurally similar polymer Nylon 6 ($N_{ent}=21$)²².

The constant of ϕ represents the importance of diffusion effects on the reaction rate, diffusion limitations becoming increasingly negligible as ϕ tends to 0. The larger the value of ϕ , the more important diffusion limitations. For reactions between macromolecules and the alumina walls the Ha number can be expressed as a function of the chain length of the polymer, equation 6.7, only such that

$$Ha(i, Al) = \frac{\phi}{4^{(i^{0.5}-m)}} \quad (6.7)$$

The Hatta number can be used to get the effective rate constant by the equation 6.8

$$k_{i,j} = \frac{k_{int}}{1+Ha(i,j)} \quad (6.8)$$

The population balance, equation 6.9, for the various chemical species as indicated by the reactions shown in equations 6.1-6.3 are given by

$$\begin{aligned} \frac{dAl}{dt} &= -Al \sum_{i=1}^{\infty} k_{x(i,Al)} (2B_i + M_i) \\ \frac{dA_i}{dt} &= 2 \sum_{j=1}^{i-1} k_{a(i-j,j)} (M_{i-j} A_j) - 2A_i \sum_{j=1}^{\infty} k_{a(i,j)} (M_j + 2B_j + U_j) \\ \frac{dB_i}{dt} &= -2k_{x(i,Al)} B_i Al + 2 \sum_{j=1}^{i-1} (k_{a(i-j,j)} M_{i-j} B_j) - 2B_i \sum_{j=1}^{\infty} k_{a(i,j)} (M_j + 2A_j + W_j) \\ \frac{dM_i}{dt} &= -k_{x(i,Al)} M_i Al + \sum_{j=1}^{i-1} k_{a(i-j,j)} (4B_{i-j} A_j + M_{i-j} M_j) - 2M_i \sum_{j=1}^{\infty} k_{a(i,j)} (M_j + A_j + B_j) - M_i \sum_{j=1}^{\infty} k_{a(i,j)} (U_j + W_j) \\ \frac{dW_i}{dt} &= k_{x(i,Al)} M_i Al + \sum_{j=1}^{i-1} k_{a(i-j,j)} (M_{i-j} W_j + 2A_{i-j} U_j) - W_i \sum_{j=1}^{\infty} k_{a(i,j)} (2B_j + M_j) \\ \frac{dU_i}{dt} &= 2k_{x(i,Al)} Al B_i + \sum_{j=1}^{i-1} k_{a(i-j,j)} (M_{i-j} U_j + 2B_{i-j} W_j) - U_i \sum_{j=1}^{\infty} k_{a(i,j)} (2A_j + M_j) \end{aligned} \quad (6.9)$$

The method of moments is used to solve molecular weight distribution. Moments are redefined as the equation 6.10

$$\lambda_m = \sum_{i=1}^{\infty} i^m (A_i + B_i + M_i) \quad (6.10)$$

The zero moment (λ_0) is the concentration of all polymer chains, the first moment (λ_1) is the concentration of polymer segments, and the second moment is an average of the concentration of polymer segment with larger molecules being more heavily weighted.

Integration of this series of differential equations yields the chain length distributions of all species. The molecular weight distributions MWD (W_i) for every degree of polymerization can be calculated, with the equation 6.11, from the sum of the species A , B and M , which are not tethered to the pore walls

$$W_i = i(A_i + B_i + M_i)/\lambda_1 \quad (6.11)$$

The number average molecular weight (M_n) can be calculated by the equation 6.12

$$\overline{M}_n = \frac{\sum i(A_i + B_i + M_i)}{\sum (A_i + B_i + M_i)} w_m \quad (6.12)$$

where w_m is the mean average molecular weight of the monomer (diisocyanate or dialcohol).

Similarly the weight average molecular weight (M_w) is calculated by the equation 6.13

$$\overline{M}_w = \frac{\sum i^2 (A_i + B_i + M_i)}{\sum i (A_i + B_i + M_i)} w_m \quad (6.13)$$

Finally, the conversion of the isocyanate groups in the system is given by the equation 6.14

$$X_{NCO} = 1 - \frac{\sum 2B_i + \sum M_i + \sum U_i}{2[NCO]_0} \quad (6.14)$$

In this work we use MATLAB software, as in the chapter 4, in order to do the numerical calculation.

6.4. Results and discussion

6.4.1. Monitoring polyurethane polymerization

A previous study of the synthesis of polyurethane is carried out with different diglycols in order to obtain a thermoplastic polymer with defined thermal characteristics under suitable conditions. For this reason, a brief study of bulk polymerizations between HDI and TEG, DEG and PEG were conducted in an oven at 80°C and the reaction was monitored by ATR-FTIR spectroscopy. Figure 6.1 shows the polymerization reaction for the three diglycol with the diisocyanate. Each graphic shows the evolution of the monomers characteristic bands with increasing time. The rate of reaction is determined by HDI consumption observed in the band of isocyanate group at 2260 cm⁻¹. All spectra are normalized with the reference band at 2936 cm⁻¹. The analysis of the bands of spectra will be analyzed in more detail later.

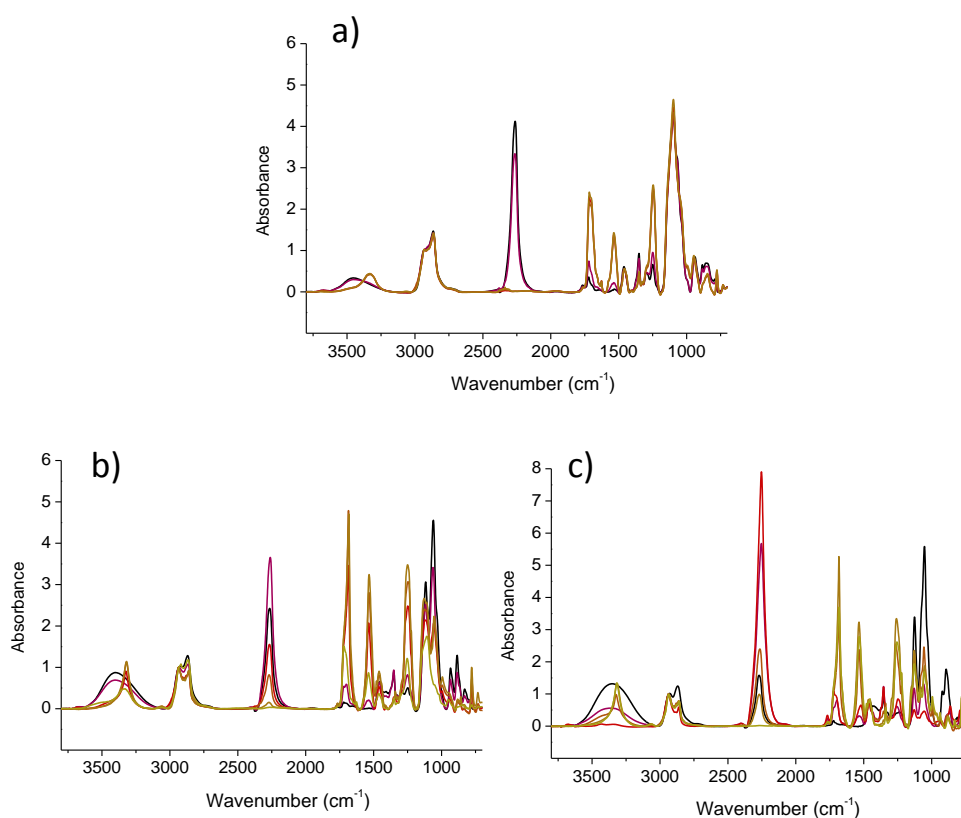


Figure 6.1. Time dependent infrared spectra data for bulk polymerization in the spectral region 650-3800 cm⁻¹. Polymerization reaction between HDI with a) PEG, b) TEG and c) DEG.

The evolution of the reaction is determined from the consumption of isocyanate group. From the infrared spectra (Figure 6.1), the isocyanate group consumption can be calculated from the rapport between the intensity of the absorbance at different time, respect to the sample at initial time. This relation is represented versus time in the Figure 6.2. This graphic shows that the faster reaction is for PEG monomer, probably because of the use of the catalyst. The polymerization reaction between HDI with TEG is more homogeneous than the reaction with DEG where the follow-up of the reaction is more fluctuating.

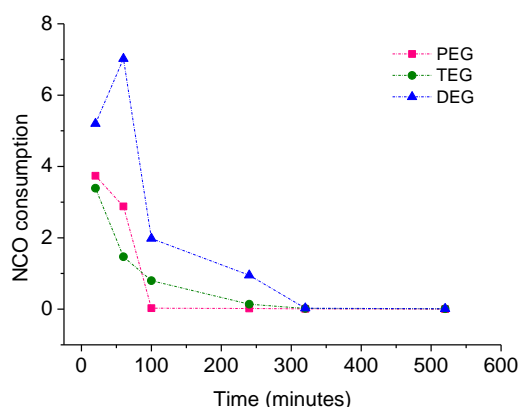


Figure 6.2. Relation of consumption of NCO group with the time.

The bulk polyurethanes obtained after the polymerization reaction at 80 ° C were characterized by DSC to observe their thermal transitions. Figure 6.3 shows the thermograms corresponding to the cooling and second heating scan of the three samples.

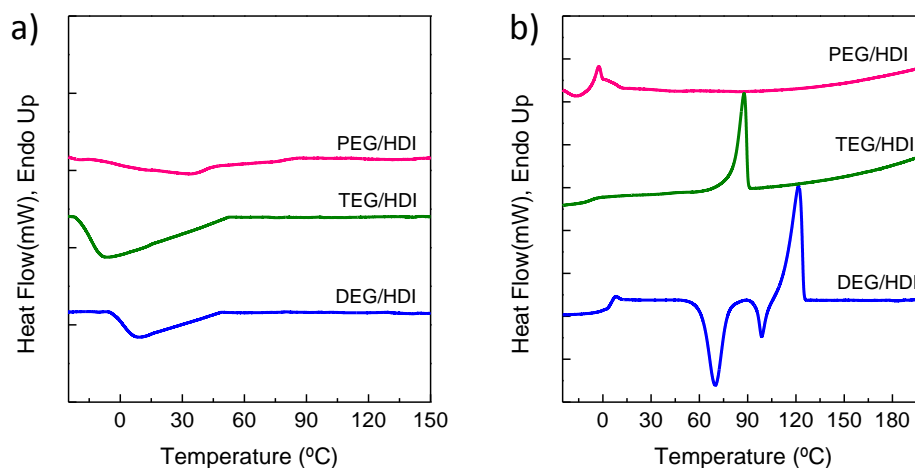


Figure 6.3. a) DSC cooling scans and b) subsequent heating scans at 20 °C min⁻¹

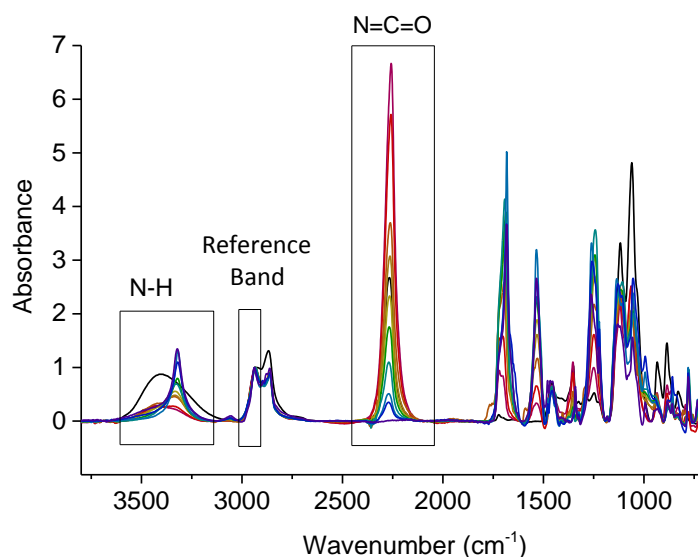
The polyurethane obtained from polyethylene glycol turns out to be an amorphous polyurethane with two possible glassy transitions due to the long chains of polyethylene

glycol and that of the isocyanates, its appearance being gluey and soft. The polyurethane obtained from DEG presents a glass transition temperature at -2.8°C , two exothermic peaks corresponding a cool crystallization at 60°C and a recrystallization at 90°C , respectively. After that, a melting temperature is observed at 118°C . In this polyurethane is detected several crystallization peaks corresponding to the formation of crystals of different sizes possibly formed after a polymerization with a broad molecular weight distribution. Finally, in the case of the polymerization between HDI with TEG the thermogram shows only a glass transition temperature at -6.7°C and a melting temperature at 90°C . From the point of view of thermal characterization, this polyurethane seems the simpler polymer to study. Consequently, the work will be developed using TEG as glycol to react with the HDI in the study of step-growth polymerization.

In the following, the study of the infrared reaction between HDI and TEG was deeply studied. The main signals and their assignments are shown in Table 6.1. Figure 6.4 shows the evolution of the spectra during the course of the reaction. All spectra have been normalized with a reference band at 2935 cm^{-1} which represents the tension and stretching aliphatic C-H bonds, that remains constant in the course of the polymerization. It can be seen that the intensity of the isocyanate band ($\text{N}=\text{C}=\text{O}$) at 2260 cm^{-1} decreases over time due to reaction with the diol, forming the urethane group. The near disappearance of the isocyanate peak indicates high conversion of monomer to form PU. Further evidence of the formation of the N-H bond arising from the urethane group is given by the development of a peak at 3320 cm^{-1} . Methylene groups (CH_2) present in the system show symmetric as well as asymmetric absorbance at approximately 2865 and 2935 cm^{-1} , respectively. The peak at 1725 cm^{-1} belongs to non-hydrogen bonded $\text{C}=\text{O}$ present in the isocyanate group, which is shifted during the reaction to 1687 cm^{-1} , indicating a strongly hydrogen-bonded carbonyl group. These values agree with other studies where polyurethanes were synthesized.²³

Table 6.1. Infrared band assignments for HDI and TEG reaction polymerization to obtain polyurethane.

Frequency (cm ⁻¹)	Assignment	Type of vibration
3320	N-H	Stretching urethane group
2935	CH ₂	Stretching, asymmetric (Reference Band)
2865	CH ₂	Stretching, symmetric
2260	N=C=O	Isocyanate group
1725	C=O	Tension and stretch (Non hydrogen bonded)
1687	OCN-H	Amide (H-bonded)
1534	N-H	Vibrations
1465, 1350	CH ₂	Vibrations

Figure 6.4. Time dependent infrared spectra data for bulk polymerization in the spectral region 650-3800 cm⁻¹. The boxed bands are the regions used to follow the reaction.

The FTIR spectra of the polymerization reaction corresponding to three different alumina templates used in this work were measured in the absence of any monomer (see Figure 6.5 A). Wavenumbers lower than 2000cm⁻¹ are not represented because of the strong absorption of alumina in this range. The spectra clearly show the presence of a stretching vibration of varying intensity which is attributed to the hydroxyl moieties on the pore walls. An additional peak can be observed at 2400-2300 cm⁻¹ which is of higher intensity in those templates synthesized in the presence of oxalic acid (35 and 60nm templates). The relative hydroxyl intensity, which is reflected by the intensity of the peak, follows the order: 60nm > 35 nm > 140 nm which agrees with the values of the porosity of the template, for a constant pore length the surface area is proportional to porosity. The percentage of porosity for the studied templates is 10, 29 and 7% for templates with pore

diameter 35, 60 and 140 nm respectively. This concept was described in detail in the chapter 3.3 (Porosity).

Figure 6.5 B, C and D represent the time evolution of the FTIR spectra of the polymerizations conducted inside the three alumina templates. All the spectra were rescaled with respect to the asymmetric vibration of CH₂ band (2935 cm⁻¹) because the intensity of this band remains unchanged during the reaction. Comparison with Figure 6.5 A shows that additional bands appear after infiltration of the monomer mixture which correspond to the isocyanate group (NCO) at 2270 cm⁻¹ as well as CH₂ stretching symmetric and asymmetric vibrations at 2865 cm⁻¹ and 2935 cm⁻¹, respectively. In the high frequency range (3600-3100cm⁻¹) the band of hydroxyl moieties⁷ attached to the pore wall can still be seen.

Focusing in the range between 3600-3100 cm⁻¹, which corresponds to OH groups and the NH groups of urethane bonds, the bands arising from OH groups of the alumina (3448 cm⁻¹) and the hydroxyl of the diol overlap. As the reaction progresses, the isocyanate group undergoes reaction with the OH moieties from the pore wall and with OH group from the diol, generating in both cases a urethane bond. The intensity of the band at 3448 cm⁻¹ disappears with time, indicating that hydroxyl groups from the alumina surface are being depleted by reaction with the isocyanate,²⁵ whilst there was an increase in the intensity of the peak corresponding to the NH groups . In the case of the 140nm template, the OH groups from the alumina walls are depleted faster than in the case of 60 or 35 nm templates, due to the lower number of alumina OH groups. The reactions of the isocyanate groups leads a concurrent decrease in the peak at 2270 cm⁻¹.

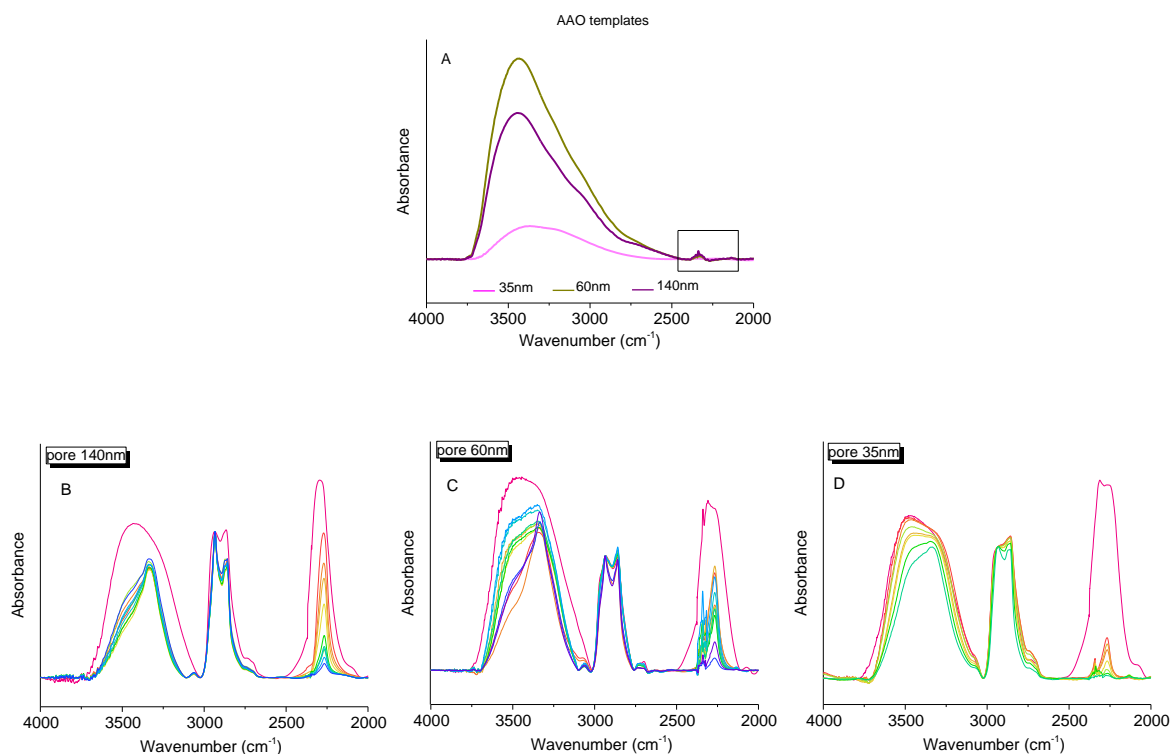


Figure 6.5. FTIR spectra of empty AAO template of different pore size (A); and time evolution of the spectra during the polymerization in confinement (B:140, C:60 and D:35nm)

The kinetic of polymerizations carried out in bulk and in AAO nanocavities were monitored by analysis of the integral intensity of the isocyanate peak at 2270 cm^{-1} . It is worth remembering that each spectrum was normalized with respect to the reference band at 2935 cm^{-1} . Conversion was calculated from the NCO/CH₂ peak area ratio, by equation 6.15

$$X_{NCO} = 1 - \frac{(A_{NCO}/A_{ref})_{t=t}}{(A_{NCO}/A_{ref})_{t=0}} \quad (6.15)$$

Where A_{NCO} is the area of the isocyanate band and A_{ref} is the area of the reference band calculated by the intensity integral of each measurement. Figure 6.6 shows the time evolution of the reactions conducted in the different templates and in bulk. It can be seen that as the pore diameter is decreased, the rate of polymerization is increased. Moreover, the reactions substantially slow down at high conversions higher to 90%.

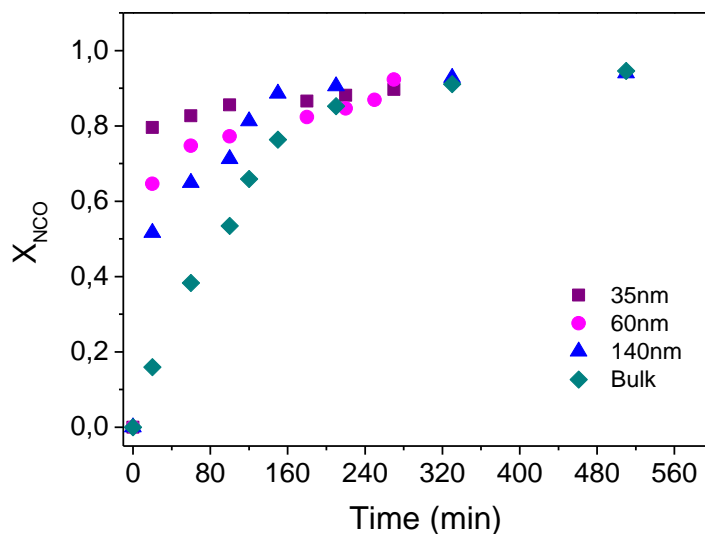
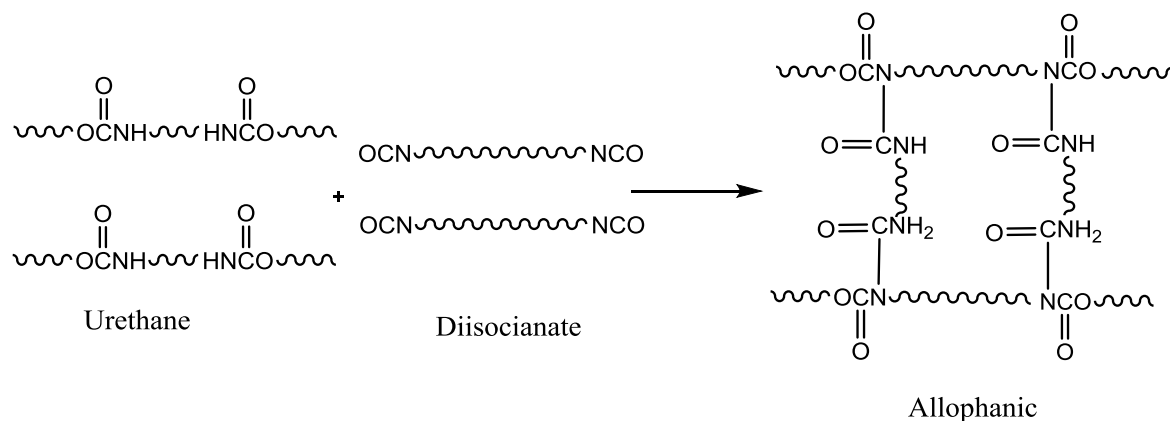


Figure 6.6. Conversion reaction versus time of polyurethanes polymerization in bulk (\blacklozenge), as well as in 35nm (\blacksquare), 60 (\bullet) and 140nm (\blacktriangle) pores at 80°C. Symbols indicate experimental data.

Due to the imbalance of the stoichiometry derived by the influence of the hydroxyl groups on the walls of the alumina, the reaction was tested for a 10% excess of diisocyanate. The observed result was a crosslinked polymer impossible to dissolve. In the case of the confinement, it was attempted to extract the polymer from the AAO with DMF and measured, but no GPC signal was observed, because the polymer was cross-linked within the pores of the template. This crosslinking reaction is because the free NCO groups of the terminal isocyanate react with the urethane groups to form allophanate groups.²⁶ The added percentage of 10% of diisocyanate does not achieve the stoichiometric balance and the reaction is affected by excess HDI. This reaction is shown in Scheme 6.3.



Scheme 6.3. Scheme of creation of allophanate groups by excess of diisocyanate.

6.4.2. Modeling results

The mathematical model described above was used in order to understand the effect of confinement on the rate of polymerization of the polymers resulting from in-situ polymerization. The rate coefficient for the reaction between HDI and TEG was obtained from the experimental rate data for polymerization in bulk. The other parameters of the model were estimated from the rate data, show in Table 6.2.

Table 6.2. Values of model parameters.

Parameter	Description	Expression or values
$[\text{NCO}]_0$	Diisocyanate initial concentration (mol/L)	3.39
$[\text{OH}]_0$	Dialcohol initial concentration (mol/L)	3.39
k_a	Reaction constant between isocyanates and alcohol (M/s)	$5.11 \cdot 10^{-5}$
k_x	reaction constant between isocyanates and hydroxyl of alumina wall (M/s)	$1.95 \cdot 10^{-5}$
$k_{a,cat}$	Catalytic alumina activity constant (M·nm/s)	0.007
$\sigma_{\text{Al-OH}}$	-OH molecules per alumina area(molecules/nm ²)	19.3^{27}
ϕ	Constant that acts as a measure of extent of diffusion effects	0(bulk), 0.1 (140 nm) 1.2 (60 nm) 3.4(35 nm)

The molecular weight and molecular weight distributions are shown in Table 6.3. Slightly lower molecular weights were obtained from simulation in comparison to the experimental values which may be an indication of the uncertainty in the absolute molecular weights which were measured in reference to polystyrene standards.

Table 6.3. Results of molecular average weight (Mw), number (Mn), and polydispersity index (PDI) of polyurethanes polymerized in bulk and confined at final conversion. Comparison of values obtained by model prediction with experimental data.

	Model			Experimental		
	Mw	Mn	PDI	Mw	Mn	PDI
Bulk	41400	21000	1.98	90000	39000	2.29
140nm	6400	4200	1.51	10000	7800	1.30
60nm	4100	2800	1.46	5700	5100	1.12
35nm	4000	3000	1.32	6000	5000	1.19

The reaction in bulk proceeds according to a classical step growth polymerization and the polydispersity of the resulting polymer is around 2, as may be expected. As the diameter of the pore decreases, the number of hydroxyl groups relative to the number of isocyanates increases and the reaction becomes stoichiometrically imbalanced. This imbalance leads to a lower molecular weights in the reactions conducted under nanoconfinement (see Table 6.3 and Figure 6.8), while the increase in concentration of hydroxyl groups leads to an increased rate of reaction (see Figure 6.7). With the estimated parameters a reasonable agreement between the experimental and simulated kinetics and molecular weight distribution were obtained, and the trends in the data are well described.

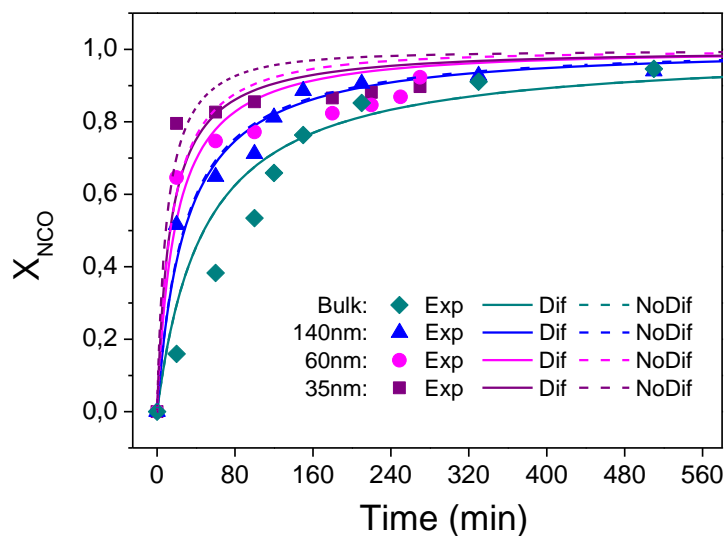


Figure 6.7. Conversion reaction versus time of polyurethanes polymerization in bulk, as well as in 35, 60 and 140nm pores at 80°C. Symbols indicate experimental data and solid lines show model predictions.

The increased rate of reaction from alumina alone is not sufficient to account for the increase in the rate of polymerization without leading to extremely low molecular weight polymers. Thus, in addition to this chemical effect on the rate of the polymerization we consider the increase in the rate of molecular collisions upon nanoconfinement, as has been shown by molecular simulation, moreover the potential catalytic effects of the presence of the acidic OH groups present on the alumina walls (observed in the chapter 4). When these factors are included a good agreement between molecular weight and rate of reaction is met.

One other interesting feature of the reactions conducted in nanoconfinement is that they lead to polymers of low dispersity (see Table 6.3). Based on the classical view of step-growth polymerization this is not expected and the polydispersity of the polymer should approach 2 at high conversion (the dotted lines in Figure 6.7 and Figure 6.8 show the results of simulations neglecting diffusion effects). Gúzman *et al.* have described the influence of diffusion limitations on step-growth polymerizations, showing that the assumption of equal reactivity of all reactive groups breaks down as the polymer becomes entangled. In this framework, the lower molecular weight oligomers are less hindered and can diffuse faster than higher molecular weight polymer. Thus the high molecular weight polymer reacts slowly and results in a decrease in the polydispersity of the polymer when

diffusion limitations arise. The simulated effect of diffusion limitations on the molecular weight distribution using the estimated parameters in the work are shown in Figure 6.8. In the graphics can be seen how the polydispersity of the polymer rapidly decreases at high conversions with decreasing pore size, as similar way happens in the experimental values.

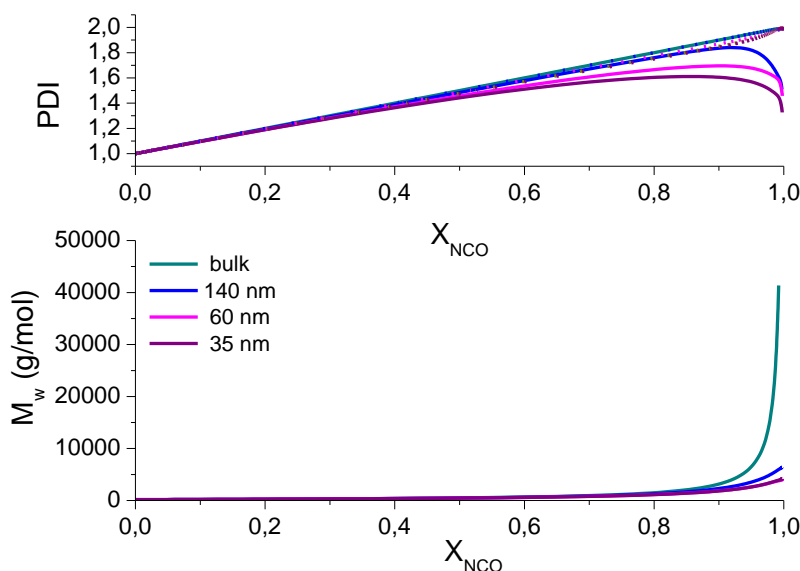


Figure 6.8. Simulated evolution of Polydispersity and Weight average molecular weight (M_w) and Number average molecular weight (M_n) with the conversion of polyurethanes polymerized in bulk and in confinement in different pore size 35, 60 and 140nm Dotted lines represent simulation with no diffusion effects data.

This mathematical model is still under study to achieve a better fit between the model and experimental data that further explains the importance of confinement and AAO templates in step-growth polymerization reactions.

6.4.3. Polymer morphology and surface properties

In order to determine the morphology of the polymer nanostructure in situ synthesized within the AAO template, scanning electron microscopy was performed. Figure 6.9 shows the polymer nanofibers synthesized inside the templates of varying diameters. It can be seen that the template was successfully replicated in all cases and densely packed nanofibers are produced by the in-situ polymerization technique. At the periphery of the template, the fibers can be seen to be slightly collapsed due to the flexible nature of the polyurethane and their relatively high length.

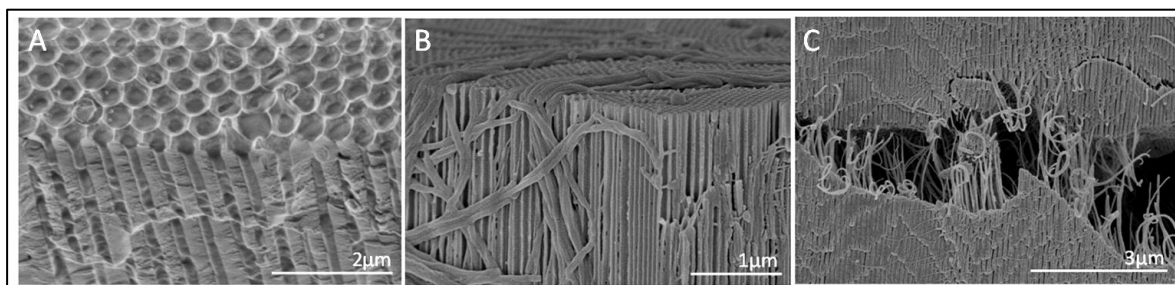


Figure 6.9. Polyurethanes fibers polymerized in situ inside of anodic alumina templates with different pore diameter. A) pore size 140nm, B) pore size 60nm and C) pore size 35nm.

The wettability of this material was studied by contact angle measurements. In order to avoid the potential collapse of the nanofibers a template with shorter pores was used. The AAO template had a pore diameter of 140 nm and a length of 1 μm . The nanostructured polymer was obtained by melt-wetting infiltration of bulk polyurethane. By SEM microscopy is observed the polyurethanes nanorods obtained in Figure 6.10.

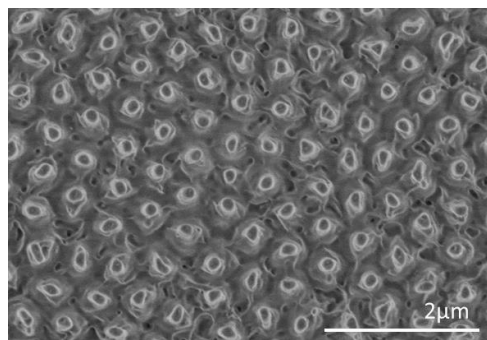


Figure 6.10. SEM image of the polyurethane nanorods obtained after polymer infiltration in AAO.

The wettability of the nanostructure and of the smooth film of polyurethane were determined by contact angle measurements. Figure 6.11 shows the images of the water contact angle of both surfaces.

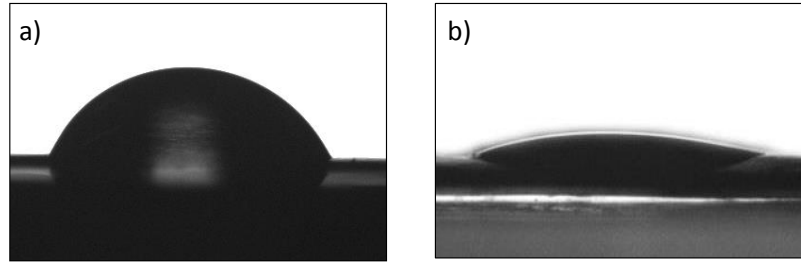


Figure 6.11. Contact angle images of a) smooth PU film and b) PU nanorods.

The ethylene glycol units and the multiple urethane groups lead to a relatively low contact angle of $67 \pm 2^\circ$ for the surface of the bulk polymer. The contact angle for the nanostructured surface decreases significantly to $15 \pm 2^\circ$ resulting in a superhydrophilic polymer. This effect of the surface roughness can be explained by Wenzel theory. According to this model, it is assumed that the space between the protrusions on the surface is filled by the liquid²⁸ (in this case water). This model predicts that hydrophilicity is reinforced by the roughness according with the equation 6.16

$$\cos\theta_w = r \cdot \cos\theta_Y \quad (6.16)$$

where θ_w is the apparent contact angle on a rough surface and θ_Y is the ideal contact angle (Young's angle) of water on the flat surface of the same polymer. The roughness factor (r) is defined as the ratio between the actual surface area to the projected surface area. In our system the roughness factor can be calculated by the following equation 6.17

$$r = \frac{\text{Actual area}}{\text{Projected area}} = \left(1 + \frac{2\pi Dh}{3\sqrt{3}L^2}\right) \quad (6.17)$$

where D is the diameter, h the length of the nanofiber and L the distance between fibers. In this case the value, 2.47, obtained with equation 6.16 agrees well with that calculated from geometric considerations, 3.11. Thus, the nanostructuration of polyurethane surface drastically changes its hydrophobicity. As can be seen in previous chapters the hydrophobicity is a function of the degree of confinement of pores geometries.

6.5. Conclusions

In the study the synthesis of nanostructured polyurethanes by step-growth polymerization of a diol and a diisocyanate within a well-defined nanoporous of AAO template the following conclusions can be drawn:

The nanoporous structure of AAO templates can be successfully replicated by infiltration of liquid monomers followed by its step-growth polymerization reaction. The effect of confinement on the rate of polymerization has been investigated using Fourier transform infrared spectroscopy, and compared with the analogous reaction in bulk. It was observed that when the polymerization was conducted inside the template, the kinetics of the reaction was faster, while the molecular weight and polydispersity were reduced.

A mathematical model was developed to explain these differences, taking into account the chemical and physical interactions encountered in the AAO template. Upon nanoconfinement, the hydroxyl groups of the alumina can react with the isocyanate groups and result in a lowering of the molecular weight. This additional reaction, coupled with the physical confinement of the chains to a small volume results in an increase in the rate of polymerization at the early stages of the reaction. At high conversions the limited diffusion of the polymer chains, which is more pronounced in the nanoconfined system, results in a slowing down of the reaction and, additionally, a polydispersity lower than that which is typically expected from a classical step-growth polymerization.

Finally, the effect of nanostructuring the polymer was observed by SEM microscopy and the hydrophobicity of the polymer determined by contact angle measurement. Nanostructuring a flat polyurethane film into a roughness surface film turns the hydrophobic material ($CA=67\pm 2^\circ$) into a superhydrophilic material ($CA=15\pm 2^\circ$). This effect of the surface roughness is in agreement with the Wenzel theory.

6.6. References

- (1). Giussi, J. M.; Blaszczyk-Lezak, I.; Cortizo, M. S.; Mijangos, C. In-situ polymerization of styrene in AAO nanocavities. *Polymer (United Kingdom)* **2013**, *54*, (26), 6886-6893.
- (2). Tarnacka, M.; Chrobok, A.; Matuszek, K.; Golba, S.; Maksym, P.; Kaminski, K.; Paluch, M. Polymerization of Monomeric Ionic Liquid Confined within Uniaxial Alumina Pores as a New Way of Obtaining Materials with Enhanced Conductivity. *ACS Applied Materials & Interfaces* **2016**.
- (3). Li, Q.; Simon, S. L. Curing of bisphenol M dicyanate ester under nanoscale constraint. *Macromolecules* **2008**, *41*, (4), 1310-1317.
- (4). Koh, Y. P.; Simon, S. L. Trimerization of monocyanate ester in nanopores. *The Journal of Physical Chemistry B* **2010**, *114*, (23), 7727-7734.
- (5). Li, P.-F.; Xie, R.; Jiang, J.-C.; Meng, T.; Yang, M.; Ju, X.-J.; Yang, L.; Chu, L.-Y. Thermo-responsive gating membranes with controllable length and density of poly (N-isopropylacrylamide) chains grafted by ATRP method. *Journal of Membrane Science* **2009**, *337*, (1), 310-317.
- (6). Amanuel, S.; Malhotra, V. M. Effects of physical confinement (< 125 nm) on the curing behavior of phenolic resin. *Journal of Applied Polymer Science* **2006**, *99*, (6), 3183-3186.
- (7). Tarnacka, M.; Dulski, M.; Starzonek, S.; Adrjanowicz, K.; Mapesa, E. U.; Kaminski, K.; Paluch, M. Following kinetics and dynamics of DGEBA-aniline polymerization in nanoporous native alumina oxide membranes - FTIR and dielectric studies. *Polymer (United Kingdom)* **2015**, *68*, 253-261.
- (8). Báez, J. E.; Ramírez, D.; Valentín, J. L.; Marcos-Fernández, A. Biodegradable poly(ester-urethane-amide)s based on poly(ϵ - caprolactone) and diamide-diol chain extenders with crystalline hard segments. Synthesis and characterization. *Macromolecules* **2012**, *45*, (17), 6966-6980.
- (9). Lyman, D. J. Polyurethanes. I. The solution polymerization of diisocyanates with ethylene glycol. *Journal of Polymer Science* **1960**, *45*, (145), 49-59.
- (10). Choi, M. K.; Yoon, H.; Lee, K.; Shin, K. Simple fabrication of asymmetric high-aspect-ratio polymer nanopillars by reusable AAO templates. *Langmuir* **2011**, *27*, (6), 2132-2137.
- (11). She, X.; Yang, D.; Jing, D.; Yuan, F.; Yang, W.; Guo, L.; Che, Y. Nitrogen-doped one-dimensional (1D) macroporous carbonaceous nanotube arrays and their application in electrocatalytic oxygen reduction reactions. *Nanoscale* **2014**, *6*, (19), 11057-11061.
- (12). Akduman, C.; Özgüney, I.; Kumbasar, E. P. A. Preparation and characterization of naproxen-loaded electrospun thermoplastic polyurethane nanofibers as a drug delivery system. *Materials Science and Engineering C* **2016**, *64*, 383-390.

- (13). Chen, R.; Huang, C.; Ke, Q.; He, C.; Wang, H.; Mo, X. Preparation and characterization of coaxial electrospun thermoplastic polyurethane/collagen compound nanofibers for tissue engineering applications. *Colloids and Surfaces B: Biointerfaces* **2010**, *79*, (2), 315-325.
- (14). Zhao, Y. J.; Zhao, Q. S.; Lu, L. J.; Ye, S. Y. Fabrication of polyurethane(PU) nanotubes with array by wetting anodic aluminium oxide template with polymer solution and melt. *Materials Research Innovations* **2015**, *19*, (5), 345-348.
- (15). Han, G.; Liu, Y.; Luo, J.; Lu, X.; Dong, Y. Preparation, characterization and formation mechanism of thermoplastic polyurethane nanostructures using solution wetting template. *Journal of Nanoscience and Nanotechnology* **2011**, *11*, (11), 10240-10246.
- (16). Qu, J. B.; She, X. L.; Yuan, F. Preparation of thermal polyurethane (TPU) nanotubes using a porous template method. *Nami Jishu yu Jingmi Gongcheng/Nanotechnology and Precision Engineering* **2007**, *5*, (4), 256-260.
- (17). Liu, J.; Ma, Y.; Wu, R.; Yu, M. Molecular simulation of diffusion-controlled kinetics in stepwise polymerization. *Polymer (United Kingdom)* **2016**, *97*, 335-345.
- (18). Li-Tang, Y. A. N.; Bao-Hua, G. U. O.; Jun, X. U.; Xu-Ming, X. I. E. Monte carlo simulation of diffusion effects on chain-extension reactions. *Journal of Polymer Science, Part B: Polymer Physics* **2006**, *44*, (19), 2902-2911.
- (19). Malvaldi, M.; Bruzzone, S.; Picchioni, F. Confinement effect in diffusion-controlled stepwise polymerization by Monte Carlo simulation. *The Journal of Physical Chemistry B* **2006**, *110*, (25), 12281-12288.
- (20). Sardon, H.; Pascual, A.; Mecerreyes, D.; Taton, D.; Cramail, H.; Hedrick, J. L. Synthesis of Polyurethanes Using Organocatalysis: A Perspective. *Macromolecules* **2015**, *48*, (10), 3153-3165.
- (21). Guzmán, J. D.; Pollard, R.; Schieber, J. D. Modeling of Diffusion Effects on Step-Growth Polymerizations. *Macromolecules* **2005**, *38*, (1), 188-195.
- (22). Fetters, L. J.; Lohse, D. J.; Colby, R. H., Chain Dimensions and Entanglement Spacings. In *Physical Properties of Polymers Handbook*, Mark, J. E., Ed. Springer New York: New York, NY, 2007; pp 447-454.
- (23). Nakhoda, H. M.; Dahman, Y. Novel biodegradable polyurethanes reinforced with green nanofibers for applications in tissue engineering. Synthesis and characterization. *Canadian Journal of Chemical Engineering* **2014**, *92*, (11), 1895-1902.
- (24). Nielsch, K.; Choi, J.; Schwirn, K.; Wehrspohn, R. B.; Gösele, U. Self-ordering Regimes of Porous Alumina: The 10 Porosity Rule. *Nano Letters* **2002**, *2*, (7), 677-680.
- (25). Li, H.; Yan, Y.; Liu, B.; Chen, W.; Chen, S. Studies of surface functional modification of nanosized α -alumina. *Powder Technology* **2007**, *178*, (3), 203-207.

- (26). Chattopadhyay, D.; Raju, K. Structural engineering of polyurethane coatings for high performance applications. *Progress in Polymer Science* **2007**, 32, (3), 352-418.
- (27). Freund, H.-J.; Roberts, M. W. Surface chemistry of carbon dioxide. *Surface Science Reports* **1996**, 25, (8), 225-273.
- (28). Wenzel, R. N. Resistance of solid surfaces to wetting by water. *Industrial & Engineering Chemistry* **1936**, 28, (8), 988-994.

Chapter 7

POLYMER INFILTRATION PROCESS. DEVELOPMENT OF NOVEL POLYMER NANOSTRUCTURES

This chapter is focused on the development of combined methods of polymer infiltration in AAO templates. It includes three sections and each section describes the fabrication of a new nanostructure, core-shell Polycaprolactone-Polystyrene (PCL-PS) nanocylinders; core-shell Nickel-Polystyrene (Ni-PS) magnetic nanowires and nano-micro Polycaprolactone-Polydimethylsiloxane (PCL-PDMS) patterning.

7.1. Core-Shell PCL-PS nanocylinders

7.1.1. Introduction

The emphasis of new technologies at nanoscale level demands a comprehensive understanding of how the physical properties of polymeric materials may change under such small environment.^{1, 2} Confined crystallization is observed in any system where the number of isolated microdomains of a crystallizable polymer is several orders of magnitude larger than the typical number of active heterogeneities in the bulk polymer. Thus, confinement has been achieved in the past through several strategies that include droplets, polymer blends, segregated block copolymers, thin films, inorganic templates and porous anodic aluminium oxide (AAO) templates. The last ones have emerged as a very effective method to produce polymeric nanostructures with confinement effects in the infiltrated polymeric chains.

As widely reported, polymer crystallization inside AAO nanocavities occurs at much larger supercoolings as compared to bulk samples. These higher supercoolings, which bring the crystallization temperature closer to the glass transition temperature, might be caused by changes in nucleation mechanisms. Thus, depending on the supercooling observed, the nucleation might go from heterogeneous, to surface induced or to homogeneous.¹ The reduction in the crystallization temperature obeys to a variation in the character of the nucleation mechanism that can change from a heterogeneous to a homogeneous (or surface) nucleation. In addition, the overall crystallization kinetics of polymers is affected by the degree of confinement inside AAO templates, as the size of the nanoporous decreases, the overall crystallization rate is slower. In general, the crystallization mechanism depends on degree of confinement and the nature of surface in contact. So by changing the nature of alumina wall, the polymer crystallization could be modulated. Then, the aim of this study is to modify the surface of the alumina nanopores with a polymer

coating (i.e., PS shell) to later investigate how is the crystallization of the semicrystalline PCL core under confinement. In fact, this method provides an easier and more versatile way to study the effect of the surface on confined polymer crystallization in comparison with other possibilities such as chemical functionalization of AAO pores. In this part is described the double nanomolding process by melt infiltration of Polystyrene and Polycaprolactone to obtain PCL- PS core-shell cylindrical nanostructures, using AAO templates with different length and pore diameters.

7.1.2. Experimental part

The AAO templates were prepared by a two-step electrochemical anodization process of aluminium foils, following the procedure described in the chapter 3.2. Four AAO templates of 350, 250, 140, and 60 nm pore diameter were synthesized. The pore lengths of the templates are 25 and 80 μm . The fabricated templates are summarized in Table 7.1.

Table 7.1. Dimensions of the fabricated AAO templates

AAO template	Pore diameter (nm)	Widening time H_3PO_4 (5wt%) (min)	Pore diameter after widening (nm)	Pore Length (μm)
AAO350/80	140	90	350	80
AAO250/80	140	60	250	80
AAO140/25	140	-	140	25
AAO60/25	35	30	60	25

The employed polymers are the polycaprolactone (PCL) ($M_w = 43\,000\text{ g mol}^{-1}$, PDI = 1.38) (Capa 6430) provided by Perstorp (Sweden) and polystyrene (PS) ($M_w = 192\,000\text{ g mol}^{-1}$, PDI = 2.04) supplied by Sigma-Aldrich (Spain). Two PCL-PS core-shell structures of different pore diameter sizes are prepared. To that purpose, AAO templates of 350 and 140 nm pore diameter are employed. The equipment to infiltrate the polymers inside the AAO is the oven reported in the chapter 4.2.

In order to achieve this particular nanostructure a novel double-infiltration approach from the melt was designed. First, a PS nanotube inside the AAO template was generated. In order to achieve this, a PS film of 0.8 mm thickness was prepared by casting a 5% PS solution in tetrahydrofuran (THF). The first melt infiltration step was done by placing the

PS film on top of the AAO templates and then heating it in the oven under nitrogen atmosphere at 200 °C for 1 h. The excess of bulk PS on the surface of the templates was removed using a sharp blade and acetone. A second infiltration step to form the PCL cores inside the PS nanotubes in both templates is performed. With that purpose, a PCL film of 0.3 mm thickness is first prepared by compression molding. Then, the infiltration procedure was similar to the one used for PS but with different conditions. The PCL film was placed on top of the previously infiltrated templates with PS nanotubes, and next, the PCL infiltration was carried out at 80 °C and for 6 h, under vacuum. The infiltration was aided by application of mechanical force. The excess of bulk PCL on the surface of the template was removed using a sharp blade and acetone. Additionally, and for comparison purposes, a single infiltration of a PCL film inside AAO templates of 250 and 60 nm pore diameter was carried out following the aforementioned procedure. The infiltration was carried at 80 °C for 2 h, under vacuum (see Table 7.2).

Table 7.2. Experimental conditions for single and double infiltrations.

Infiltrated Polymer	Pore diameter (nm)	Atmosphere in an oven	Temperature of infiltration (°C)	Infiltration time (h)	Structure
PCL	250	vacuum	80	2	nanofiber
PCL	60	vacuum	80	2	nanofiber
PS	350	nitrogen	200	1	nanotube
PS	140	nitrogen	200	1	nanotube
PCL/PS	250/350	vacuum	80	6	core-shell
PCL/PS	60/140	vacuum	80	6	core-shell

The morphology of AAO templates and infiltrated samples was observed by scanning electron microscopy (SEM) employing a Philips XL-30ESEM and FESEM Hitachi model SU8000 microscope. Moreover, in order to verify that the PCL infiltration is a continuous fiber along the PS tube, nanofibers were characterized by the TEM detector operated at 0.5-3 kV. In order to perform the analysis over the polymer samples without the AAO template the aluminium and the alumina were removed as explained in earlier chapters.

To verify the correct infiltration of the polymers, the infiltrated AAO templates were examined by Fourier transform infrared spectroscopy (FTIR) employing a PerkinElmer Spectrum One coupled with an attenuated total reflectance (ATR) accessory.

To perform differential scanning calorimetry (DSC) measurements, the infiltrated templates were encapsulated in aluminium pans and tested in a previously calibrated DSC

PerkinElmer 8500 under ultrahigh purity nitrogen atmosphere. A bulk PCL sample was also examined. The instrument was previously calibrated with an indium standard. All the samples were cool down until $-80\text{ }^{\circ}\text{C}$ at $20\text{ }^{\circ}\text{C min}^{-1}$ after 3 min melting at $85\text{ }^{\circ}\text{C}$. Then, they were heated up until $85\text{ }^{\circ}\text{C}$ at the same rate.

7.1.3. Results and discussion

The SEM images of AAO template prepared under different conditions are showed in Figure 7.1. The images confirm the dimensions of the synthesized AAO templates and the pore diameters of the templates correspond, almost perfectly, to the expected dimensions. The pore diameters of the AAO templates in Figure 7.1 a, b were $253 \pm 15\text{ nm}$ and $348 \pm 14\text{ nm}$, and in Figure 7.1 d, e, were $145 \pm 7.8\text{ nm}$ and $60 \pm 4\text{ nm}$, respectively. The lateral views of the templates of 80 and 25 μm lengths can be seen in Figure 7.1 c, f. From the images, it is clear that the AAO templates exhibited high quality order pores, regularity in the size of the pores, and invariance of the diameter through the length of template.

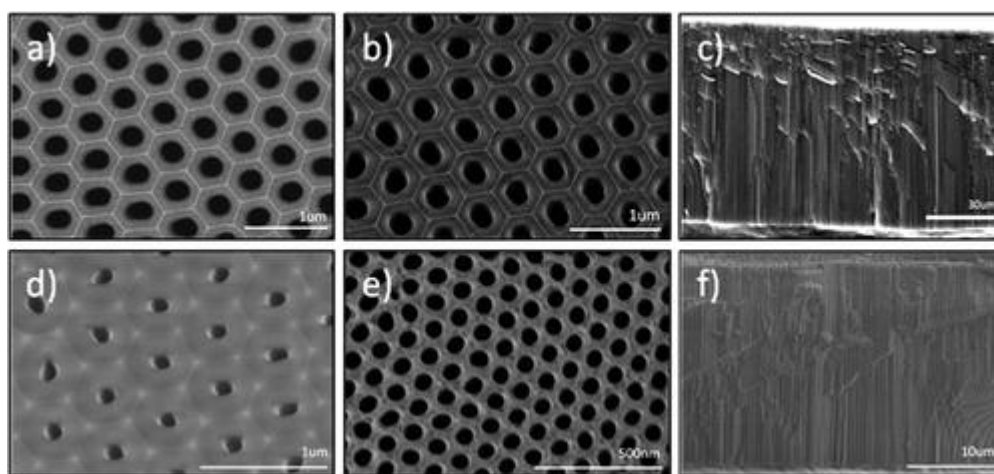


Figure 7.1. SEM images of AAO templates with different pore diameters (nm) and lengths (μm): a) 250 nm/80 μm (top view), b) 350 nm/80 μm (top view), c) 250 nm/80 μm (lateral view), d) 140 nm/25 μm (top view), e) 60 nm/25 μm (top view), and f) 140 nm/25 μm (lateral view).

From the templates shown above, those with 350 and 140 nm pore diameter were employed for the double-infiltration procedure, whereas the 250 and 60 nm pore diameter AAO templates were used for the single-infiltration of PCL. The effectiveness of the infiltration methods was verified by FTIR technique. Figure 7.2 depicts the FTIR spectra of the single infiltrated PS in a 350 nm pore diameter template, the single infiltrated PCL

in a 250 nm pore diameter template, and of the double infiltrated PS and PCL inside a 350 nm pore diameter template. The first spectrum exhibits signals at 3025 cm^{-1} (C-H stretch, aromatic), 1601 cm^{-1} (C=C stretches in the aromatic ring), 1451 cm^{-1} (CH_2 symmetric stretch), and 694 cm^{-1} (C-H bending) that correspond to PS vibrations.³ In the second spectrum, the distinctive signals belonging to PCL can be seen, located at 1720 cm^{-1} (C=O stretch), 1238 cm^{-1} (C-H bending), and 1167 cm^{-1} (C=O stretch).^{4,5} In the third spectrum, the bands of both PS and PCL appear, thus confirming the infiltration of PCL inside the PS nanotubes.

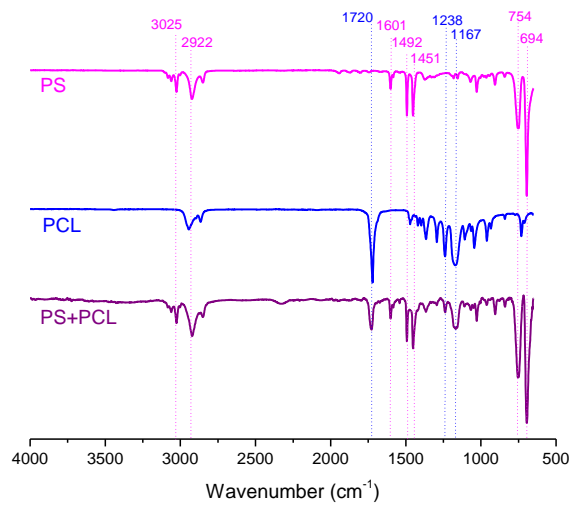


Figure 7.2. FTIR-ATR spectra of PS nanotube infiltrated in a 250 nm pore diameter template, PCL nanofiber infiltrated in a 250 nm pore diameter template, and PCL+PS double-infiltrated nanostructure inside a 350 nm pore diameter template

Assuming that all the pores have the same radius and the volume, we can estimate the theoretical percentage of each polymer infiltrated into the template. The volume of the PCL fiber with a diameter of 220nm is,

$$Volume_{PCL} = \pi r^2 h \quad (7.1)$$

and the volume occupied by the PS nanotubes whose diameter is 350nm is,

$$Volume_{PS} = \pi(R^2 - r^2)h \quad (7.2)$$

Then, the theoretical percentages of each polymer is:

$$PS\% = \frac{18252}{30625} * 100 = 60.5\% \quad PCL\% = \frac{12100}{30625} * 100 = 39.5\% \quad (7.3)$$

From the FTIR-ATR results we can quantitatively estimate the amount of every polymer. Firstly, every spectrum has to be normalized to a common peak, 840cm^{-1} , that belongs to the bending vibration of C–H. For each polymer a specific band with moderate intensity and little interfering factors must be selected. In the case of PS, the representative band is that corresponding to 1238 cm^{-1} and for the PCL is the band at 1601 cm^{-1} , as shown the Figure 7.3.

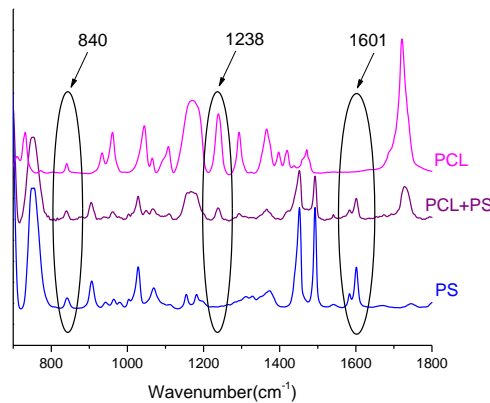


Figure 7.3. Reference signals to calculate the fraction of PCL and PS.

The fractions of PCL and PS calculated from the intensity of the bands are:

$$\text{Fraction PCL} = \frac{\text{Intensity PCL+PS}}{\text{Intensity PCL}} = \frac{1.3}{6.9} 100 = 19\% \quad (7.4)$$

$$\text{Fraction PS} = \frac{\text{Intensity PCL+PS}}{\text{Intensity PS}} = \frac{2.5}{4.7} 100 = 53\% \quad (7.5)$$

The experimental results are not very different from the theoretical ones, taking into account the experimental error.

In order to provide undeniable evidence of the nanostructures formed inside of the AAO templates, exhaustive SEM observations were carried out, as well as TEM. Figure 7.4 illustrates that PS nanotubes and PCL-PS core-shell nanocylinders were successfully achieved with the single- and double-infiltration approach, respectively.

Figure 7.4 a shows the PS nanotubes obtained employing an AAO template with 350 nm pore diameter and Figure 7.4 b and c, the PCL-PS core-shell nanocylinders achieved after the subsequent infiltration of the PCL. As can be seen from Figure 7.4 a, the thickness of

the walls of PS nanotubes was around 70 nm. Thus, the internal diameter (cavity) of PS nanotube filled with PCL was ~220 nm. A proof of the successful double infiltration and of the PCL-PS core-shell nanostructures formed is given in Figure 7.4 b, c. The nanostructures shown in Figure 7.4 b were obtained and observed after dissolving the AAO template with NaOH. One PS nanotube (circled in pink) that was not filled with PCL can be clearly seen, while all others exhibit fully infiltrated PCL cores.

To confirm the core-shell nanostructure, lateral view observations were made after a cryogenic fracture of the AAO template (see Figure 7.4 c). The SEM image shows a PCL nanofiber (smaller diameter) covered by a PS shell (larger diameter), coming out of a nanopore inside the AAO template (in Figure 7.4 d, the PS shell and the PCL core were colored in pink and blue, respectively, to guide the eye). Since the PS is fragile, the PS shell was broken, confirming that a complete PCL nanofiber constitutes the core of the nanostructure. Additionally, Figure 7.4 e, f demonstrates that PS nanotubes and PCL-PS core-shell nanocylinders of smaller dimensions can also be successfully obtained. In this case, the PS nanotube wall was approximately 40 nm and the PCL core ~60 nm. The reduction of the PS wall thicknesses in the smaller AAO templates might obey to a stronger influence of the surface tension over the PS as the size of the pore is reduced.

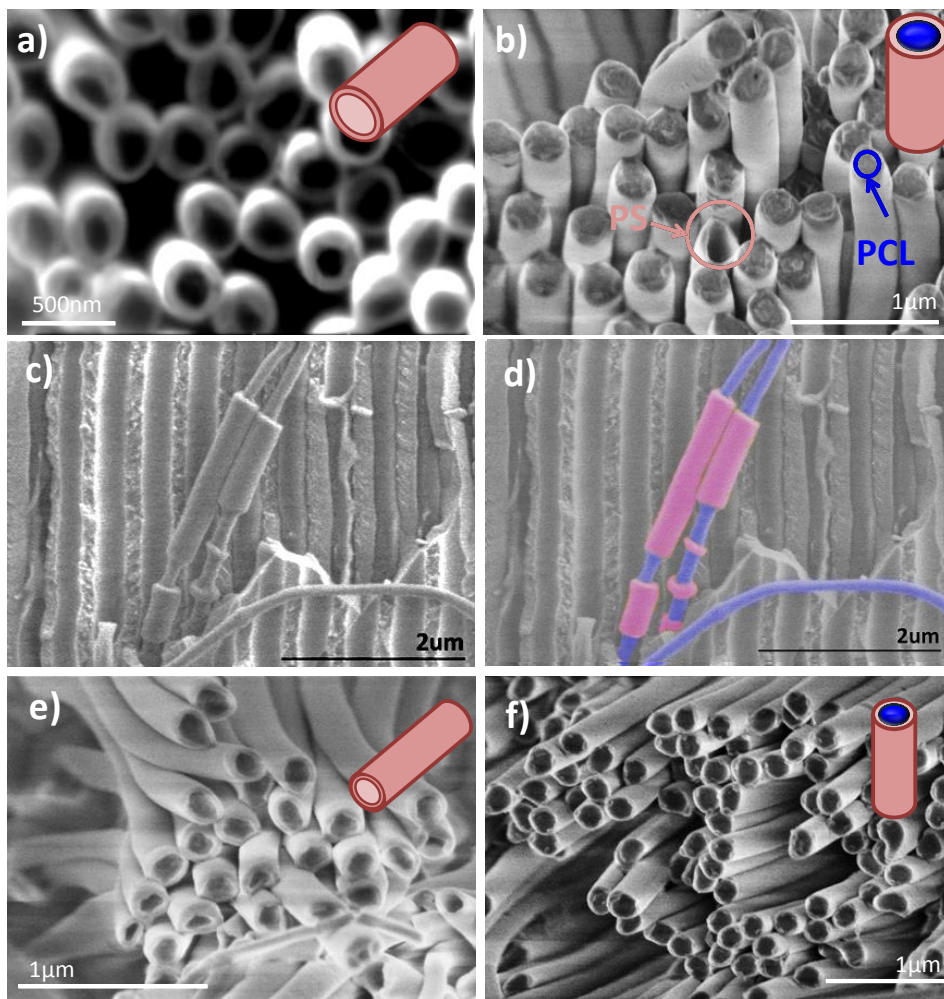


Figure 7.4. SEM images of a) PS nanotubes after infiltration inside AAO templates with nanopores of 350 nm diameter, b) PCL-PS core-shell nanostructure of 350 nm diameter (PCL core 220 nm diameter), c) PCL-PS core-shell nanostructure of 350 nm diameter (PCL core 220 nm diameter) inside the AAO template (lateral view), d) coloured figure of c) to guide the eye, blue for PCL core and pink for PS shell, e) PS nanotubes after infiltration inside AAO templates with nanopores of 140 nm diameter, and f) PCL-PS core-shell nanostructure of 140 nm diameter (PCL core 60 nm diameter).

TEM images of this sample can be observed in Figure 7.5. The darker core constitutes the PCL nanofiber inside the PS nanotube (i.e., light grey shell). Furthermore, the dimensions of the core-shell cylinders correspond exactly with the expectation for complete double infiltration.

As demonstrated in the preceding figures, PS can be successfully infiltrated into AAO template nanopores to create PS nanotubes. These nanotubes can be filled with PCL in a second infiltration step. The result of this double-infiltration technique is a core-shell nanostructure: a nanotube of PS filled with a PCL nanofiber. In other words, PCL

nanofibers are surrounded by a PS surface and not by the AAO template surface. Therefore, the nature of the surface surrounding the PCL nanofibers and its effect on the nucleation and crystallization can be potentially study.

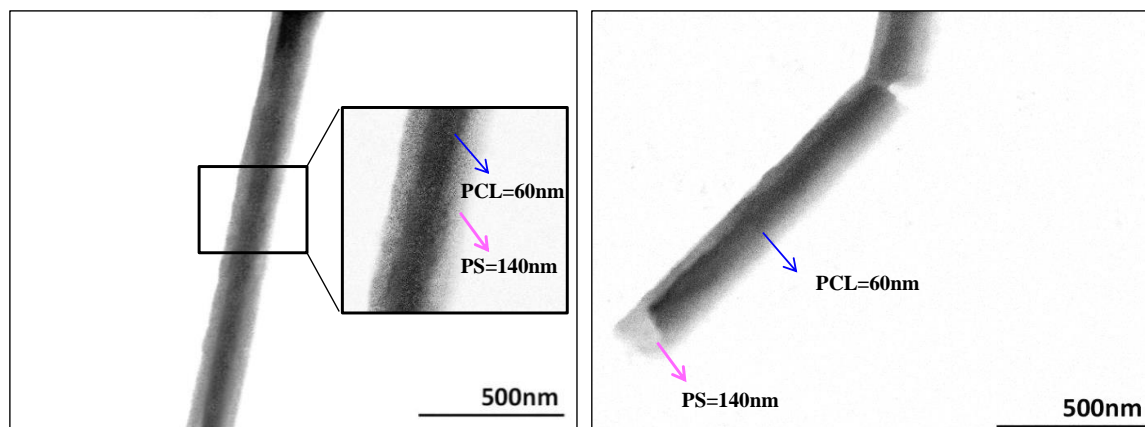


Figure 7.5. TEM images of PCL-PS core-shell nanostructure of 140 nm diameter (PCL core 60 nm diameter).

As said before, this technique is easy to implement as long as the infiltration temperatures of the core material are lower than the melting point or glass transition temperature (or more generally speaking the heat distortion temperature) of the shell material. Therefore, the major interest with this technique is to achieve very small nanodomains in which the PCL could crystallize. It is reported here that this was indeed possible in core-shell nanocylinders of very small dimensions.

Then, an exploratory DSC experiments about the study of effects of double infiltration were performed to the PCL-PS core-shell nanostructures shown in Figure 7.4 f, which is the one with the smallest dimensions (PS nanotube, ~140 nm diameter, PCL core, ~60 nm diameter). As mentioned earlier, an AAO template with ~60 nm pore diameter was infiltrated with PCL for comparison purposes. Both samples were tested inside their AAO templates. Figure 7.6 presents the cooling and second heating scan of the three samples.

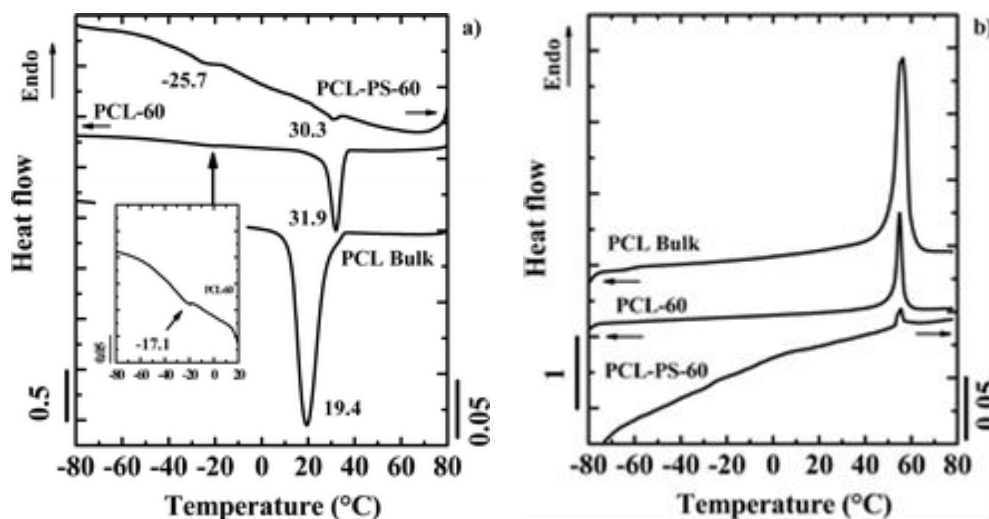


Figure 7.6. a) DSC cooling scans and b) subsequent heating scans at $20\text{ }^{\circ}\text{C min}^{-1}$.

The crystallization and melting temperatures of the bulk sample are typical for a high molecular weight PCL sample, 19.4 and $56.4\text{ }^{\circ}\text{C}$, respectively. Confinement is expected to reduce the crystallization temperature of infiltrated polymers. Nevertheless, it can be seen that the PCL infiltrated inside the AAO template (PCL-60) exhibits two crystallization peaks. The main one, located at $31.9\text{ }^{\circ}\text{C}$, and the other more weak, at $-17.1\text{ }^{\circ}\text{C}$. If the PCL is now confined inside a PS nanotube of similar dimensions within the AAO template (PCL-PS-60 core-shell nanostructure), then the low crystallization temperature peak was reduced to even lower temperatures, until $-25.7\text{ }^{\circ}\text{C}$ while the other remained almost unchanged, at $30.3\text{ }^{\circ}\text{C}$ (PCL-PS-60). Similar fractioned crystallization behavior was observed for the PCL inside the core-shell nanocylinders of larger dimensions (PS nanotube, $\sim 350\text{ nm}$ diameter, PCL core, $\sim 220\text{ nm}$ diameter), results not shown (a high temperature crystallization was observed at $31.2\text{ }^{\circ}\text{C}$ and a low one at $-18.2\text{ }^{\circ}\text{C}$). The higher crystallization peaks exhibit an increase of approximately $10\text{ }^{\circ}\text{C}$ when compared to bulk PCL. This unexpected behavior was observed regardless of the type of surface: AAO or PS, and requires further research in order to understand it. A similar observation was reported by some authors⁶ for infiltrated PCL inside AAO templates with nanopore diameters between 25 and 65 nm. However, the increment reported was only $2\text{ }^{\circ}\text{C}$.

The low temperature small peaks present a dramatic reduction of the crystallization temperature (36.5 and $45.1\text{ }^{\circ}\text{C}$, respectively) that accounts for a confinement effect over the PCL crystallization. These extreme supercoolings are probably due to a change in the

nucleation mechanism from heterogeneous to homogeneous (or surface induced nucleation). The higher crystallization peaks (31.9 and 30.3 °C) correspond to the crystallization starting from heterogeneous nuclei. But, as the volume per active heterogeneous nuclei estimation of bulk PCL is 3 to 5 orders of magnitude higher than the volume per pore, only a fraction of nanopores will contain heterogeneous nuclei^{1, 6} and the rest can be considered as heterogeneity free nanodomains, in which the crystallization takes place from homogeneous nuclei (or from surface induced nucleation). Therefore, the lower crystallization temperature peaks (-17.1 and -25.7 °C) are due to confined crystallization of clean microdomains (without heterogeneity). Suzuki et al.^{1, 6} reported a homogeneous crystallization temperature at around -20 °C for PCL infiltrated in AAO templates of 65 nm pore diameter.

The increase in the supercooling is higher for PCL in the core-shell nanocylinders as compared to the single infiltrated PCL, even though both PCL core and PCL nanofibers have similar dimensions. The nature of the surface (alumina versus PS) in contact with PCL may be the origin of this difference. This observation requires deeper examination to ascertain the exact origin of the heterogeneity free nucleation in each case (i.e., surface versus homogeneous nucleation). The in-depth study of the nucleation and crystallization of double infiltrated systems will be the subject of future investigations. However, it is important to point out that although the nature of the surface had an effect that needs to be studied further, the PS wall thickness has no influence on the crystallization behavior, since crystallization only depends on the size of the nanodomain.

7.2. Core-shell Ni-PS nanowires

7.2.1. Introduction

The electrodeposition of metallic elements and their alloys with high magnetic response into AAO templates is attracting much interest due to their low cost fabrication process and the broad spectrum of their technological applications.⁷

Most studies employing electrochemical deposition focus on template synthesis of metal nanowires, nanorods, nanotubes and nanoparticles.⁸⁻¹⁰ Up to now, the use of AAO membranes as templates has turned out to be a convenient experimental access which enables one to design and fabricate directly the metal,¹¹⁻¹⁵ the polymer nanowires or nanotubes, or even nanoparticles-filled carbon nanotubes.¹⁶

Although these one-dimensional polymer nanostructures are currently used for different confinement effects studies on polymer properties¹⁷⁻¹⁹ or technological purposes,²⁰⁻²² only few works study the combination of both materials and structures,²³⁻²⁶ but most of them are focused on nanoparticles embedded into the polymer nanorods or nanotubes.^{21, 27, 28} While core/shell nanowires can be synthesized by other techniques,^{29, 30} the use of polymer introduces some specific characteristics that enhances further applications of these composite system as for example to subsequent functionalization with organic compounds.

In this regard, we propose a new approach to synthesize ordered arrays of magnetic nanowires covered by polystyrene nanotubes by combined electrochemical and chemical routes. So, following a similar methodology to that reported in previous section on polymer infiltration methods, the fabrication of core-shell metallic-polymer nanostructures with magnetic properties, by infiltration of a polymer and posterior electrodeposition of a metallic element, is reported. PS nanotube being the shell and nickel nanofiber the core. It should be underlined that the present study faces the challenge of synthesizing the hybrid magnetic/polymeric nanowires system which can be of relevance for its applied functionalization.

7.2.2. Experimental part

The AAO template were prepared by a two-step electrochemical anodization process of aluminium, following the procedure described in the chapter 3.2 The AAO template, fabricated by phosphoric acid and after widening pore process, had 280 nm of pore diameter and 100 μm of pore length. To obtain nanopores opened by both side, the remaining aluminium was chemically removed using a mixed solution of CuCl_2 , H_2O and HCl . After that, the alumina barrier layer was removed by chemical etching, submerging the membrane into a H_3PO_4 solution (10wt%) at room temperature. The template was cleaned in the oven at 200°C in vacuum atmosphere for 2 hours.

A polymer film is prepared by pressing the polystyrene homopolymer (Aldrich Ltd., $M_w=192000$ g/mol) at 240°C to get a $80\mu\text{m}$ thin layer. To get polystyrene nanotubes, the PS film is placed on the surface of the alumina membrane and the PS is infiltrated in the oven at 200°C for 1 hour in nitrogen atmosphere³³. The residual polystyrene layer on top of the membrane was chemically etched using tetrahydrofuran (THF). In order to observe the PS nanotubes, the alumina is dissolved in 0.5wt% NaOH solution³² at room temperature.

Then, a thin Au layer was sputtered at the bottom of the membrane covering the pores and serving as an electrode for Ni nanowire electroplating. The Ni nanowires electrodeposition is carried out in a three-electrode cell using a Watts-type bath under constant potential at room temperature. The composition of the bath was 0.76 M $\text{NiSO}_4\cdot 6\text{H}_2\text{O}$, 0.17 M $\text{NiCl}_2\cdot 6\text{H}_2\text{O}$, and 0.65 M H_3BO_3 , and the potential used in the electrodeposition was a -1.0V vs Ag/AgCl reference electrode.

A scheme including the complete set of the fabrication stages is depicted in Figure 7.7 a, while a view of an individual Ni/PS hybrid nanowire is shown in Figure 7.7 b.

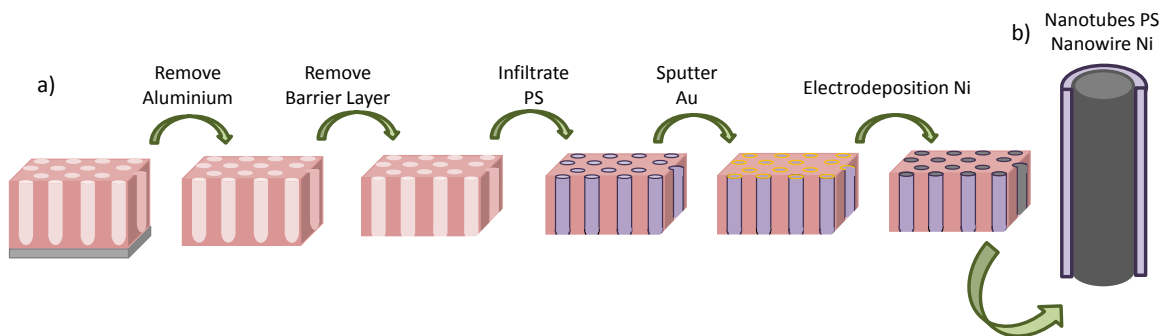


Figure 7.7. Diagram of the fabrication process (a) and final structure (b) of Ni nanowires inside PS nanotubes.

7.2.3. Results and discussion

The AAO templates and the free PS nanotubes (out of the alumina nanopores) were morphologically characterized by scanning electron microscopy (SEM) Philips XL-30 ESEM. To perform the analysis of free polymer nanostructures, the aluminium was firstly removed and then the alumina by chemical etching, as it has been mentioned above. The template has not a homogeneous pore diameter size, Figure 7.8.a the resulting average of pore diameter is $280 \pm 30\text{nm}$, the interdistance between hexagonally ordered pore is 420nm and the pore length is $100\ \mu\text{m}$. Figure 7.8.b shows the pores (darker areas in the figure) surrounded by thin polystyrene nanotubes (grey color). Figure 7.8.c shows PS nanotubes out of the AAO templates, with a wall thickness of around 70nm , in agreement with previous works.^{2, 34}

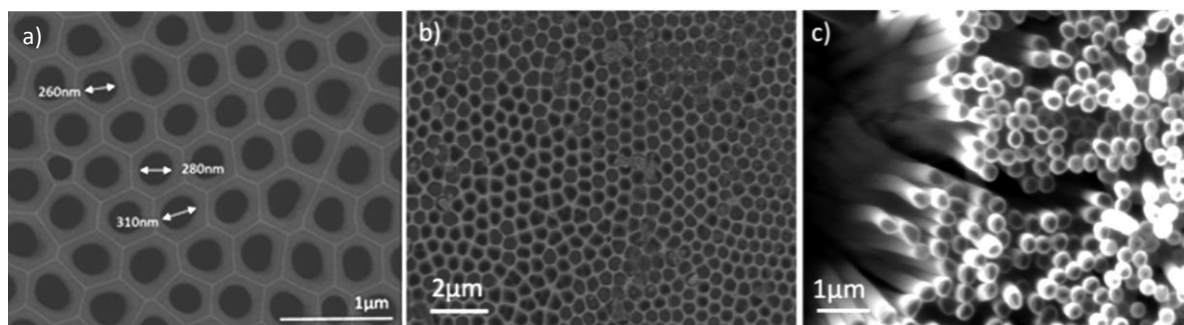


Figure 7.8. Top view SEM images of AAO membrane with average pore diameter of $280\text{ nm} \pm 30$ (a), polystyrene nanotubes embedded into AAO membrane (b), and polystyrene nanotubes out of AAO membrane (c).

The complete penetration of PS along the pore channels is shown in Figure 7.9.a. The image has a low magnification (1000 magnification) of the lateral cross-sectional view of AAO template from the top to the bottom. Polymer goes to the end of the template (bottom) while some nanotubes get out from the pores, indicating the presence of polystyrene along the pore channels. The PS tube diameter is exactly the same size of AAO pore as it can be seen in the Figure 7.9.b that there are some nanotubes slightly larger or smaller.

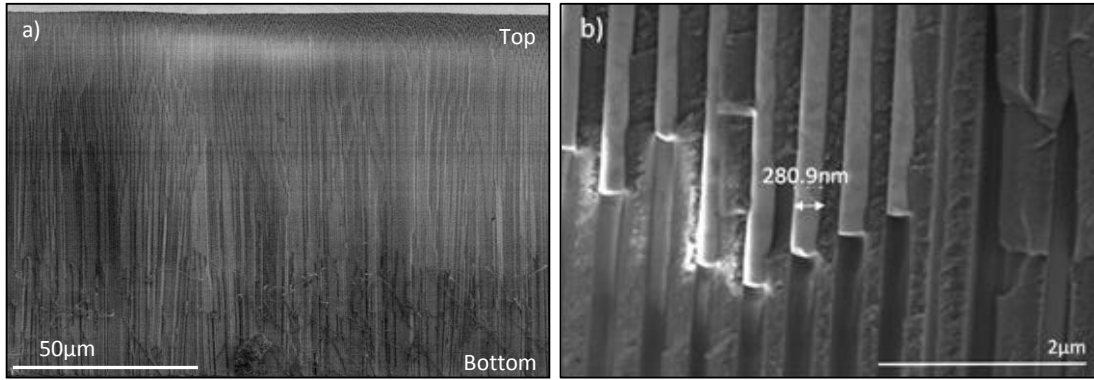


Figure 7.9. a) Low magnification image (1000 magnification) of the lateral cross-sectional view of AAO template from the top to the bottom. b) Cross-section of PS nanotubes inside pores

Figure 7.10 shows the nickel nanowires of around 140nm of diameter and 25μm length covered by the polystyrene nanotubes. The magnetic characterization of nickel nanowire arrays inside polystyrene nanotubes, both embedded into AAO membrane, is carried out in a vibrating sample magnetometer (VSM), ADE system EV7 KLA-Tencor, under a maximum magnetic field of $\pm 18\text{kOe}$, applied parallel (\parallel) and perpendicular (\perp) to the nanowires axis.

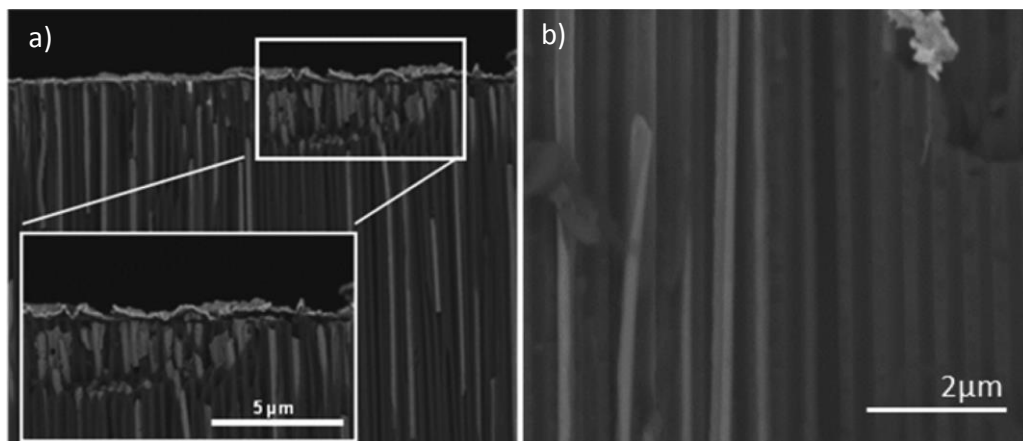


Figure 7.10. Cross section of SEM images of nickel nanowires inside polystyrene nanotubes, both embedded into the AAO membrane.

The hysteresis loops of the nanowires array are shown in Figure 7.11. Coercivity (H_c) and fractional remanence (M_r/M_s) values have been obtained for both applied magnetic field configurations. Particularly, for the parallel applied field $H_c (\parallel)$ takes a value of 187 Oe and the $M_r/M_s (\parallel)$ and is 0.80, while for the perpendicular applied field, $H_c (\perp) = 90$ Oe and $M_r/M_s (\perp) = 0.03$. Since the remnant magnetization and the coercivity take significantly

larger values for the parallel applied field configuration we can derive an effective magnetization easy axis parallel to the nanowires characterized by a longitudinal magnetic anisotropy field of around 3 kOe. The origin for that magnetic anisotropy can be ascribed mostly to the shape anisotropy of Ni nanowires as determined by their high length-to-diameter aspect ratio, as described elsewhere for Ni nanowires not embedded in polystyrene nanotubes.³⁵

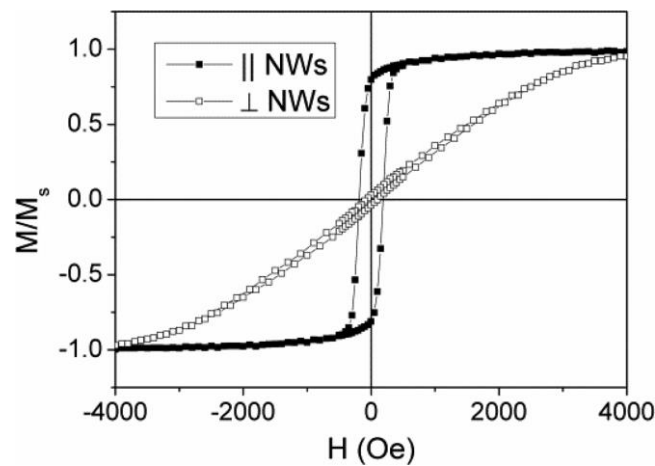


Figure 7.11. Hysteresis loops measured under applied field parallel and perpendicular to the nanowires.

Consequently, the synthetic approach shown here allows us, for the first time, to easily grow nickel nanowires covered by polymer nanotubes. In the present particular study, the nanowire-nanotube metallic-polymer magnetic composite presents an effective magnetization in the axis parallel to the nanowires, mostly ascribed to the shape anisotropy of Ni nanowires. This kind of layered metallic-polymer material in which the metallic nanowire is enveloped by a polymer could be developed for a variety of systems therefore opening new opportunities in numerous applications fields. In this work, PS has been selected as the enveloping material because its properties offer the advantage of an easy infiltration process in AAO templates. As it possesses mechanical and thermal stability and transparency, and it is isolating and inflammable. Moreover, alternative polymer precursors, such as PMMA, PLGA, PEO, PVDF, PVDF-PVtF, or PU, are envisaged as protecting envelopes because they are proven to give polymer nanotubes when infiltrated in AAO under established conditions. In the present study, nickel was selected as the metallic element for the nanowires because it is biocompatible,^{36, 37} and possess easy growing, magnetic, and electrical properties, but it also can be replaced by other metallic materials also proven to grow in AAO template. The dimensions of polymer metallic nanowires

were selected to achieve measurable magnetic response, and they can be further adjusted to fit suitable requirements. The length of nanowires can be tailored in a range of 5 and 100 μm or even longer, and the diameter could be also reduced to some tens of nanometer. In short, the suitable choice of polymer and magnetic nanowire enables in a relatively simple, reliable, and less-expensive way, the tailoring of the composite nanowire for applications such as hyperthermia, drug delivery, biodetection, removal of water contamination or magnetic biasing.

7.3. PCL-PDMS Micropatterning to mimic the frog toe pad

7.3.1. Introduction

In the last ten years, natural patterned adhesives have caught the attention of the scientific world³⁸. The particular topography is based on the specific design at micro and nanoscale. The gecko is the animal best studied in this regard. The toe pad of this reptile consists of several hundred thousand of densely packed and highly branched hairs which allow the intimate contact with different substrates and achieve a great adhesive strength, mainly relying on van der Waals forces.³⁹⁻⁴²

In contrast to geckos, the tree frog is an amphibian that can adapt to dry and wet environments and can climb on vertical or overhanging surfaces without falling.⁴³⁻⁴⁵ Their toe pad surface shows a regular hexagonal topography with epithelial cells separated by wide channels of the one micron⁴⁶. Each epithelial cell is formed by an array of densely packed nanopillars, 300-400nm in diameter, and a slightly concave top surface.⁴⁷ The principle behind the enhanced friction was clarified using frog-like polydimethyl siloxane (PDMS) micropatterns.⁴⁸ The difference between the torrent and tree frogs is an anatomical difference in the toe pad: elongated epithelial cells versus regular geometry, respectively. Iturry *et al.*⁴⁹ compared the friction properties of artificial hexagonal arrays of PDMS micropillars in the presence of water, observing that elongated pillar patterns show significantly higher friction forces than regular patterned or non-structured surfaces under wet conditions.

In the third part is reported the influence of nanostructures on adhesion/friction performances. For this purpose, the micro-nanostructure is based on the combination of top-down and bottom-up methods to mimic the hierarchical structure of the tree frog toe pad. Once the system is obtained, the friction and adhesion forces are evaluated with Particle Interaction Apparatus (PIA). The work developed in this section took place during the internship at the Max Planck Institute in Germany.

7.3.2. Experimental part

Description of the process

In order to know the stages developed in the work, Diagram 7.1 shows the steps required for the manufacture of the nano and micro structures. This diagram is divided into two parts: a) manufacturing of the nanostructure (nanopillars) and b) manufacturing of the microstructure. Then, the steps are briefly described. The fabrication of the nanopillars is made from the anodic aluminium template (1.a), where the aluminium support is removed (2.a). The polymer (PCL) is infiltrated inside the AAO template with temperature and pressure (3.a) and later the nanopillars array (NPA) are released by wet etching (4.a). The fabrication of the hexagonal microstructure is made from photoresist micropattern. Firstly, the SU-8 photoresist is deposited into the silicon wafer (1.b). For the optical lithography, a mask is added and then exposed to UV light, to create the micropattern (2.b). The mask is removed and the non-cross-linked photoresist is dissolved, obtaining the SU-8 micropattern (3.b). Through double soft-molding, the PDMS is cured over the SU-8 micropattern (4.b) and peeled away to obtain the micropattern of soft polymer, PDMS (5.b)

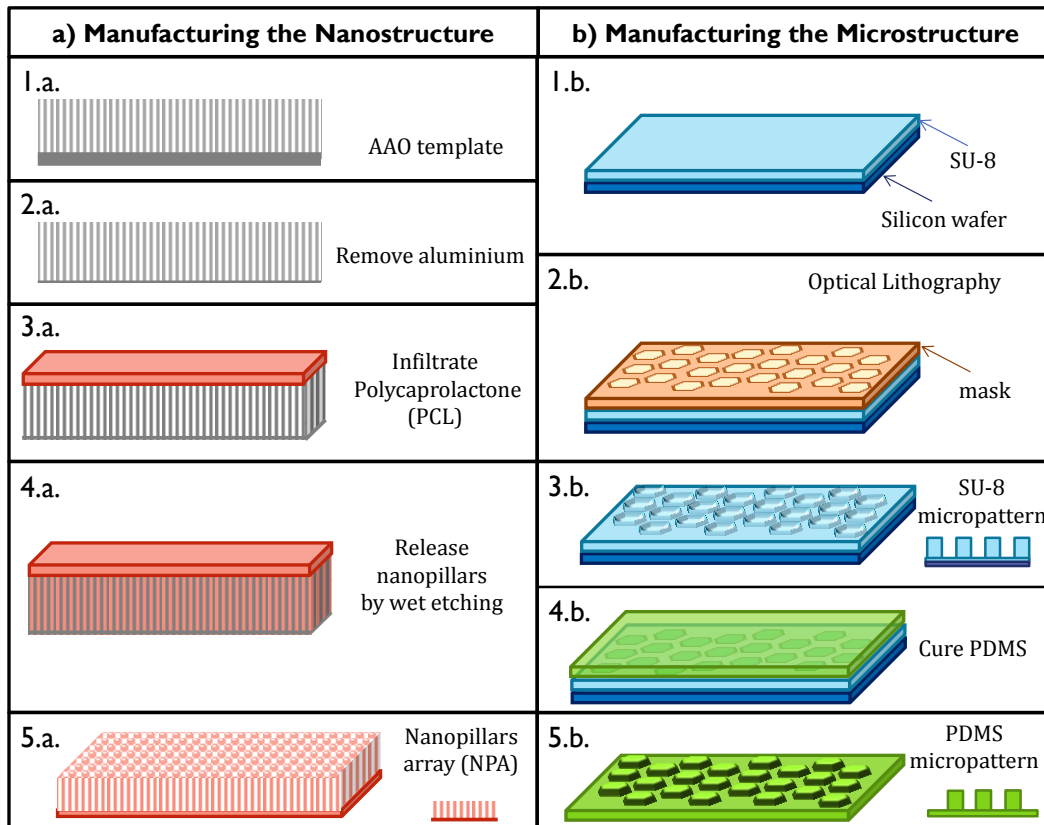


Diagram 7.1. Schematic overview of the fabrication process to obtain the nano and micropatterning.

In order to obtain a material with higher mechanical properties, the same procedure was repeated with PMMA and pACAA instead of PCL and PDMS, respectively. After obtaining the starting materials, the nanopillars array (NPA) is joined with the SU-8 micropattern (6) and the nanopillars are deformed with magnet pressure (7). The bulk support of the NPA is broken by micromanipulator (8). Then it is filled with PDMS and precursor, and cross-linked at room temperature with the soft polymer (9). The nano/micropatterning is peeled away from the SU-8 template (10). Diagram 7.2 shows all the steps, which are described in detail by section.

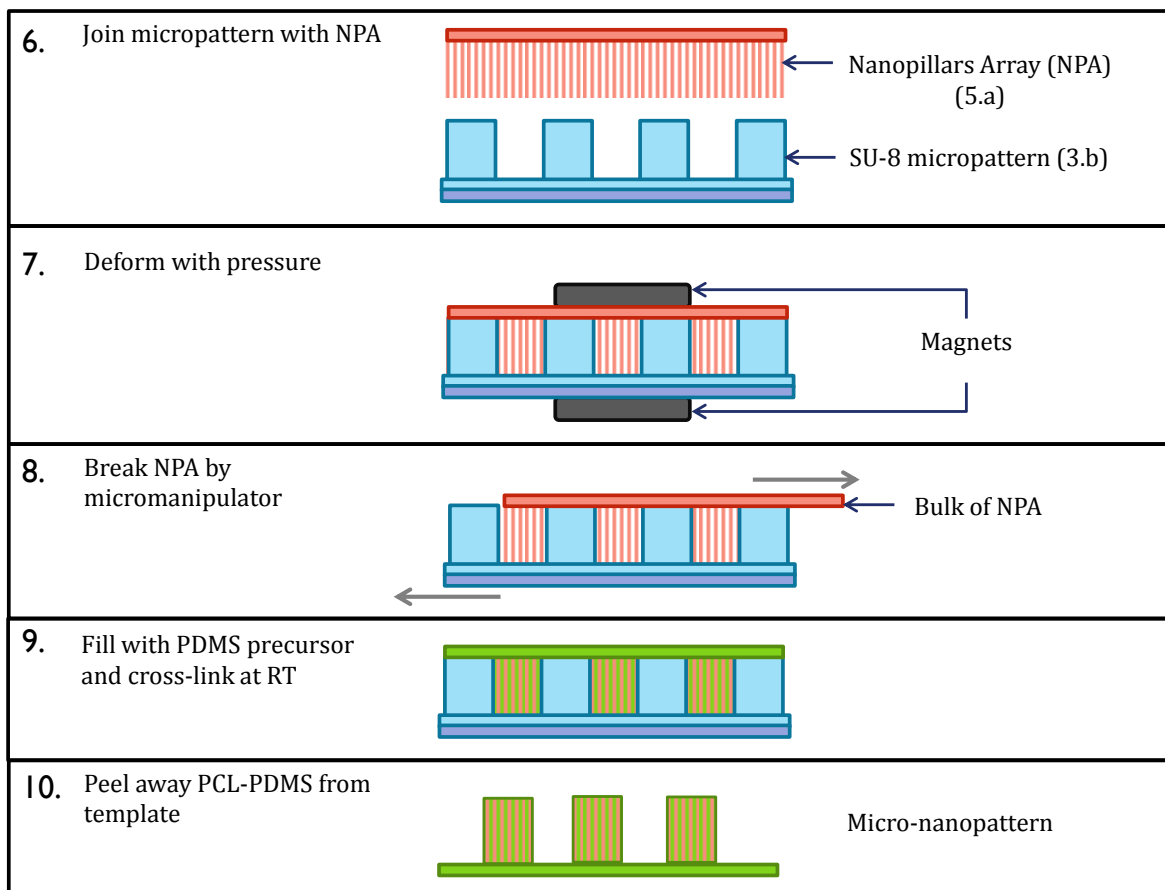


Diagram 7.2. Overview of the fabrication process to obtain the combination of nano-micropatterning.

Fabrication polymer nanopillars array (NPA) by AAO template

NPA are prepared following the steps described in the Diagram 7.1 (1.a-5.a). The anodic alumina templates are fabricated with phosphoric acid electrolyte, following the aforementioned procedure in the chapter 3.2. Three different templates of 140nm pore diameter and with 10, 12 and 14 μm length are produced in order to have the same aspect ratio (diameter/length) but with different nanopillars length dimensions. Later, the pores are widened in phosphoric acid solution 10wt% at 30°C until obtaining diameters of 330, 400 and 440nm. The aluminium support is removed by dissolving in a solution of copper chloride (II), hydrochloric acid and water. Then polymer infiltration process was carried out in a thin template. Polycaprolactone (PCL) with $M_n = 80.000$ g/mol was infiltrated in AAO templates and it was placed in an oven at 65°C, for 20 minutes, under vacuum. Polymethylmethacrylate (PMMA) with $M_w=35.000$ g/mol was infiltrated in a similar way but different conditions in the oven at 200°C, for 24 hours, under vacuum. In both cases, the alumina template was removed with a NaOH 5% solution for 2 hours at room temperature. To remove the basic solution, it was rinsed with water several times. In order to obtain freestanding nanopillars, the nanopillars in water were frozen and dried through freeze drying to avoid the collapse of nanopillars.

Fabrication of SU-8 Mold Micropatterns by Optical Lithography

Micropatterns were prepared following the steps described in the Diagram 7.1.(1.b-3.b) Silicon wafers were cleaned in a piranha solution (7:3 (v/v) 98% H_2SO_4 /30% H_2O_2) overnight and rinsed with deionized water. The wafers were rinsed with acetone and dried with nitrogen. Patterns fields (mask) of $8 \times 8 \text{ mm}^2$ with arrays of hexagonal regular micropillars in hexagonal packing were obtained. Regular hexagon has an apothem of 8.5 μm , the height of the pillars is 5 μm , and the interpillar channels were 3 μm wide (see Figure 7.12. Before SU-8 lithographic processing, the SU-8 photoresist patterned wafers were perfluorinated. Samples were treated in oxygen plasma for 10 s (power 100%, gas 100%, pressure 0.1 mbar) to activate the surface, and then placed in an evacuated desiccator for 30 min using $\approx 50 \mu\text{L}$ of 1H,1H,2H,2H-perfluorodecyltrichlorosilane for silanization. To complete the silanization process, the substrate was baked for 1 h at 90 °C in an oven, under vacuum. The obtained patterns were used as hard molds for the subsequent soft replication processes with PDMS and pACAA.

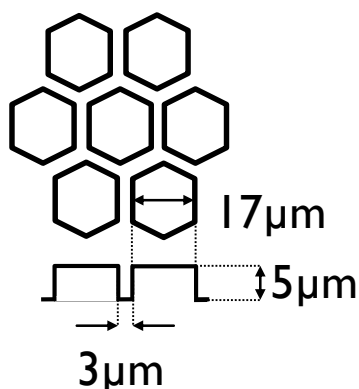


Figure 7.12. Dimensions of the fabricated microstructures by optical lithography.

Fabrication of Pillar Micropatterns by Double Soft-Molding

PDMS pillars micropatterns were prepared following the steps described in the Diagram 7.1 (4.b-5.b). PDMS precursor (ratio prepolymer to crosslinker of 10:1) was degassed and poured onto the SU-8 patterned wafer. The curing process of PDMS is different in function of the nanopillars polymer (PCL or PMMA). The cure temperature must be lower than the glass transition temperature of the polymer. In the case of PCL nanopillars, the cure must be at room temperature for 24 h. In the case of Poly(acrylamide-co-acrylic acid), pACAA, the solution was cured with 1.7% crosslinker, before being covered with acryl-silanated coverslip and cross-link at room temperature for a few minutes. Two flat surfaces of PDMS and pACAA samples are also cured under the same conditions of the patterned ones in order to be compared.

Fabrication of micro-nanopatterns

The fabrication of micro-nanopatterns in by combinations of nanopillars (NPA) with the SU-8 micropattern, see Diagram 7.2 (6-10). The nanopillars are joined with the SU-8 mask where part of the NPA remains in the hexagonal holes of the template and the rest are deformed. The pressure and force produce by two magnets are used to obtain a good contact and deformation. The most important step is the removal of the bulk part of the NPA, for that a macromanipulator is used. This gadget is a home-made device to break the nanorods, see Figure 7.13. In order to obtain the nanostructures inside the SU-8 template, two pieces of manipulator are perpendicularly arranged. Firstly, the SU-8 template was placed on the holder facing upwards. Nanopillar polymer array (NPA) was put on top of the SU-8 template in order to be in contact with each other with the aid of the pressure of

two strong magnets. The micromanipulator is a device consisting of an assembly of pieces that breaks the sample, by shearing in parallel and under cryogenic conditions. This fracture leaves nanopillars inside the SU-8 template.

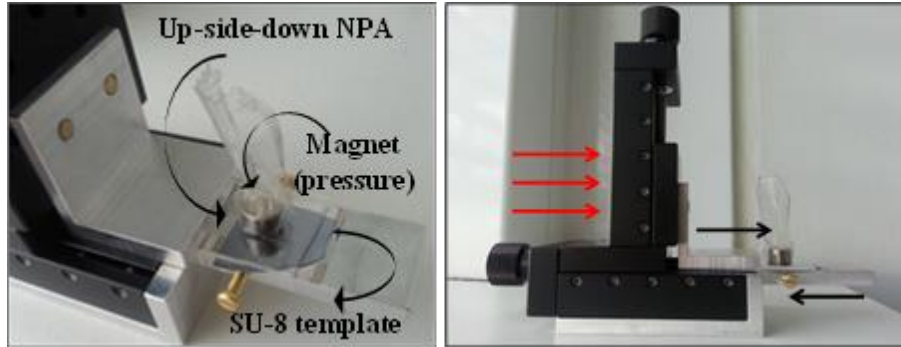


Figure 7.13. Micromanipulator for breaking the NPA inside the SU-8 template.

Characterization techniques

Microscopies: The profiles of the microstructures were measured with a Confocal Laser Scanning Microscopy (CLSM) μ Surf. Surface microstructures were characterized by scanning electron microscopy (SEM) LEO 1530VP and with the Optical microscopy, Zeiss Axiophot, which is equipped with a Leica color CCD camera in order to document the microscopy measurements.

Particle Interaction Apparatus (PIA). Friction forces measurements are carried out using custom-built equipment.^{48, 49} The samples were brought into contact with a ruby sphere probe of 5 mm diameter and mounted at the end of a cantilever with a thin film force sensor (Figure 7.14). The lateral (friction) and normal forces between the sample and the sphere were measured. A load of 1 mN was applied and kept constant during the measurement using force feedback. Before data collection, a previous test was run to set a predefined and constant normal force during the friction test. The sample was moved at 100 $\mu\text{m/s}$ over a distance of 500 μm forward and backward (trace and retrace). The measurements were performed in dry state and also in the presence of water, the latter was applied to the spherical probe using a micropipette. The laboratory temperature and humidity were recorded for each measurement and were in the range of 20-25 $^{\circ}\text{C}$ and 20%-35% humidity. During the experiment, the contact area between the spherical probe and the PDMS sample was recorded by a camera attached to an optical microscope. A

minimum of 3-5 measurements on at least three different locations were performed on each sample.

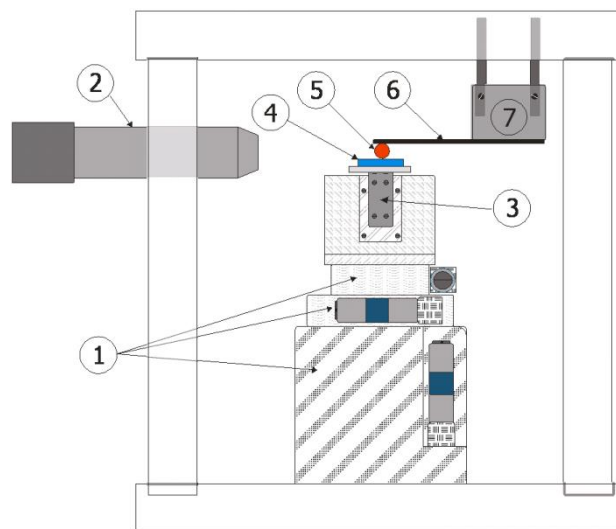


Figure 7.14. Particle Interaction Apparatus (PIA). Set-up for measuring friction/adhesion forces. (1) A motorized XYZ-stage allows coarse positioning, (2) video microscope, (3) piezo translation stages are used to move the sample and friction forces are recorded by the lateral thin film force sensor, (4) sample, (5) a ruby sphere with 4mm diameter, mounted at the end of a vertical thin film load sensor (6) acts as a force probe(7). Motion control and signal acquisition are done by a computer with an AD/DA board running a self-written LabView program.

7.3.3. Results and discussion

Polymer nanopillars array (NPA) by AAO template

One important step to obtain a free nanopillar array that stands up is the drying process after removing alumina. As described above in the experimental part, after washing to eliminate the basic solution and dissolved alumina, the water removal process was done by freeze drying. In this way, the sample is frozen with liquid nitrogen and it is dried by lyophilization to eliminate the water. Freeze drying is a process in which the nanopillars are preserved in the same state as before the frozen water is removed, therefore nanopillars are separated individually. On the contrary, if the drying step is realized with air, the nanopillars form clusters. Figure 7.15 shows the difference between PCL nanopillars obtained by (a) air-drying or (b) freeze drying.

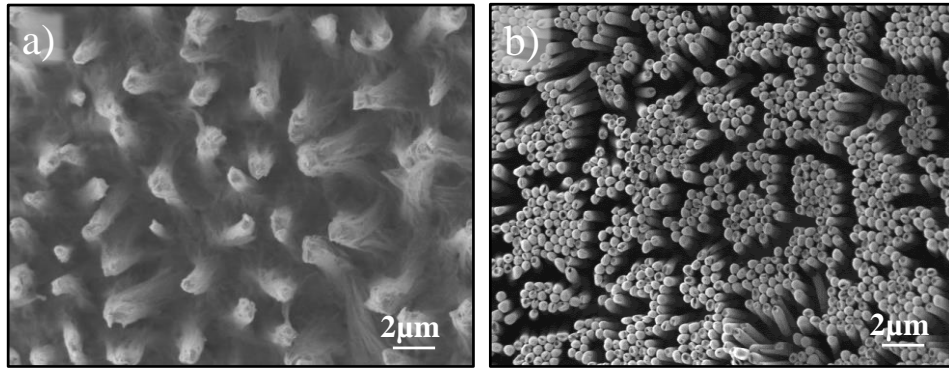


Figure 7.15. Difference of obtaining PCL nanopillars by air-drying (a) and by freeze drying (b).

The aspect ratio of obtained polycaprolactone nanofibers was studied by scanning electron microscopy. Figure 7.16 shows PCL nanopillar arrays with different dimensions of diameter/length (AR) obtained by infiltration in different AAO templates (330nm/10 μ m; 400nm/12 μ m and 440nm/14 μ m). Figure 7.16.a shows that the aspect ratio of 330nm/10 μ m presents the better and homogeneous distribution of the nanopillars standing up, without nanofibers bunching together neither without big holes or areas without nanopillars. Figure 7.16.b presents bunched nanopillars and Figure 7.16.c presents areas with gaps. Therefore, the aspect ratio of nanopillars to continue the work is 330nm of diameter by 10 μ m of length.

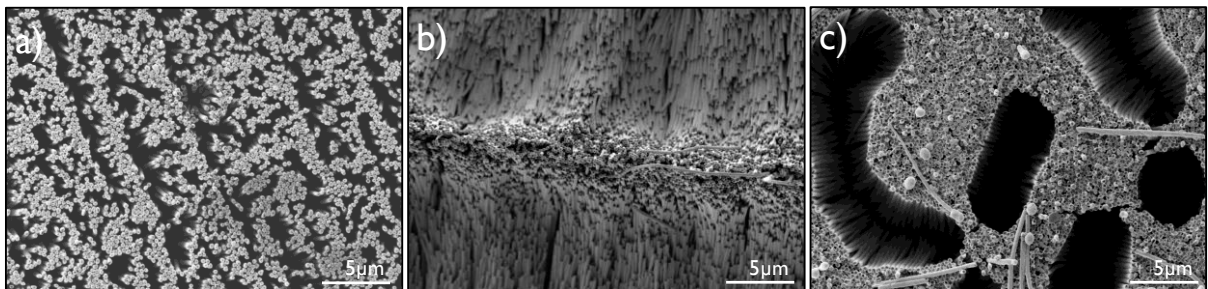


Figure 7.16. Polycaprolactone Nanopillar Array (NPA) with different dimensions diameter/length: a) 330nm/10 μ m b) 400nm/12 μ m a) 440nm/14 μ m.

Another experiment was carried out to prepare PMMA nanopillars. Observing that the AAO template of 330 nm of diameter by 10 μ m in length keeps the better aspect ratio, PMMA was infiltrated in the template of 330nm by 10 μ m, and the nanopillars were characterized by scanning electron microscopy. Figure 7.17 shows PMMA nanopillars array after removing the alumina template. As observed in the image the nanofibers are clearly stand-up and homogeneously distributed.

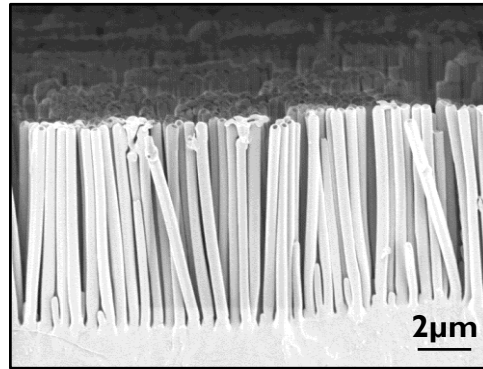


Figure 7.17. PMMA nanopillar array of 10 μm length and 330nm of diameter.

SU-8 Mold Micropatterns and soft pillar Micropatterns by Double Soft-Molding

The SU-8 mold micropatterns (Diagram 1 step 3.b), obtained by optical lithography, were characterized by the confocal laser scanning microscopy to determine the reproducibility and regularity of the mask. Figure 7.18.a represents the optical image of the hexagonal mask made of SU-8. Once the SU-8 mask is created, the soft micropatterns are replicated (Diagram 1 step 5.b). The microstructure of SU-8 soft polymer, without nanopillars inside, was obtained by cross-linking at room temperature. Figure 7.18.b and c show the optical images of the hexagonal micropatterns of PDMS and pACAA, respectively.

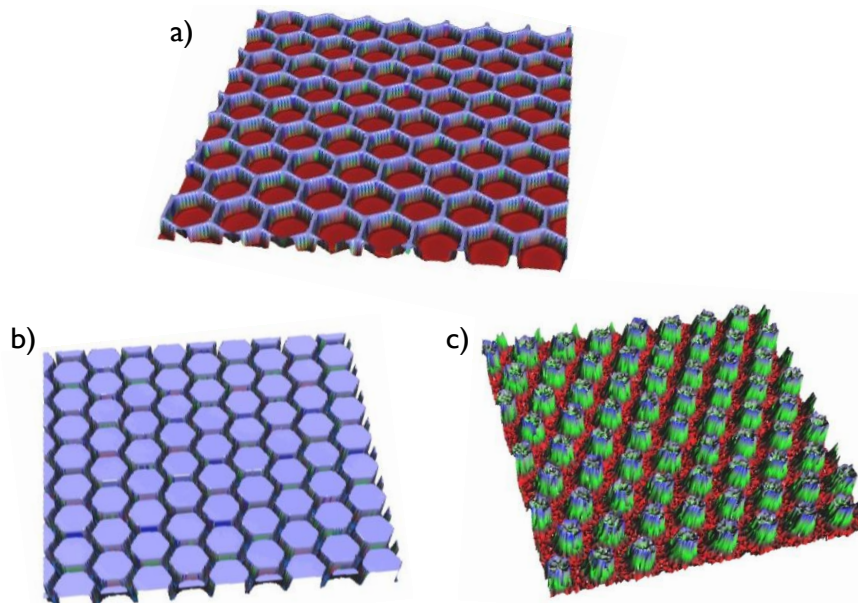


Figure 7.18. a) Optical image of SU-8 mold micropatterns produced by optical lithography. Optical image of soft pillar micropatterns by double soft-molding of PDMS (b) and pACAA (c).

As observed, high reproducibility of the hexagonal micropattern of PDMS has been obtained from the SU-8 mask, with a hexagonal dimension of $5\mu\text{m}$ of height and $17\mu\text{m}$ of diameter. However, in the case of pACAA it is different. The measurement had been realized in dry and wet state, since the pACAA is a hydrogel that with water the micropatterns increase the volume. For this reason, this sample was measured by the optical microscope both state.

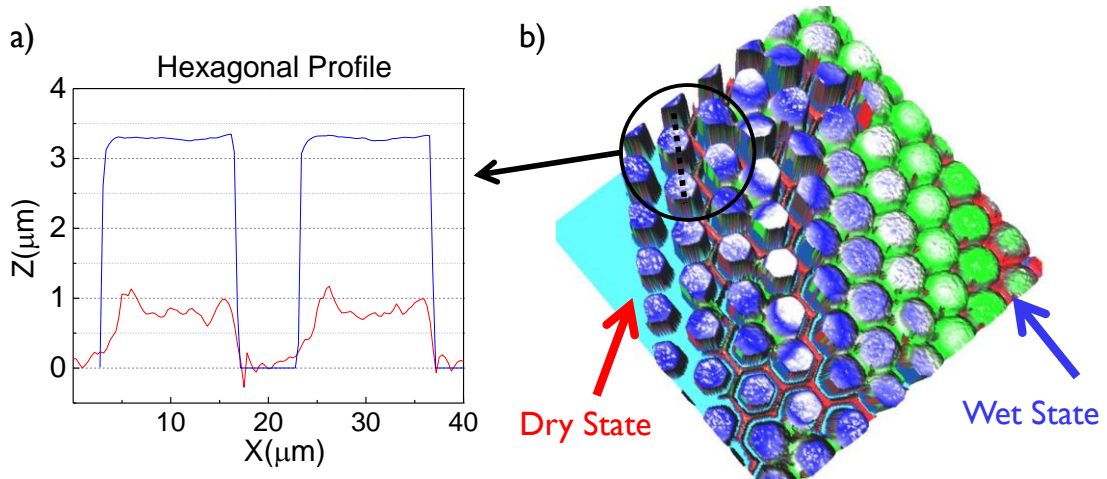


Figure 7.19. Evolution of the pACAA micropatterns profile from the dry to wet state. a) Graphic of micropatterns in dry (red) and wet (blue) state. b) Optical 3D imagen.

Figure 7.19 a) depicts a graphic of the profile of micropatterns in the dry state (red) and wet state (blue) this graphic is obtained by the measurement of the optical image in 3D. The increase of the patterns is bigger in height ratio than in width ratio. The swelling ratio can be determined by the dimensions of hexagonal profile, in the dry and wet state, shown in Table 7.3. The swelling ratio is 5 in the height ratio.

Table 7.3. The height and width dimension of the pACAA micropatterns in dry and wet state

Hexagonal	Dry	Wet
Height (μm)	0.64 ± 0.05	3.28 ± 0.02
Width (μm)	11.7 ± 2.11	14.47 ± 0.28

The friction and adhesion experiments were measured by the Particle Interaction Apparatus (PIA). The flat surface and a patterned surface with regular hexagons were analyzed for PDMS and pACAA materials. Figure 7.20 shows the representative friction a) and adhesion b) curves measured on PDMS arrays.

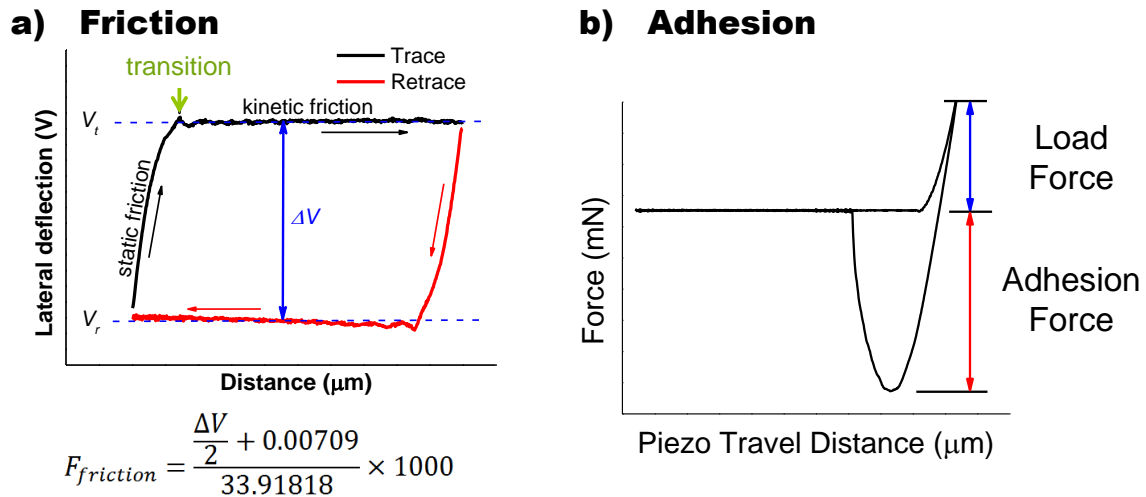


Figure 7.20. Friction and Adhesion curves measured on PDMS arrays by PIA equipment.

The PIA has been used for obtaining the friction and adhesion curves measured on the patterned surfaces through a ruby spherical probe. The lateral deflection signal of the force sensor represents the lateral displacement of the sample in two opposite directions (trace and retrace). The friction curves measured in the two orientations were inversely identical and showed two different regions. Initially, the friction force rapidly increased with increasing lateral displacement, but no sliding occurred (static friction). At a certain displacement, a transition (green arrow in Figure 7.20.a takes place and the probe started to slide at a constant friction value (kinetic friction). The half-distance between dynamic friction plateaus ($\Delta V/2$) corresponds to the dynamic sliding friction force. The friction force is calculated with dynamic sliding multiplied by a correction factor, as can be seen in Figure 7.20.a.

For adhesion force, the sample was periodically moved up to down at a constant speed by a piezo translator while recording the force. The adhesion force is the force required to pull the sphere from the sample surface. From the registered curve in the graphic, force vs piezo position is calculated for the adhesion force for every load force (from 1-10 mN).

The approach and retract speed could be adjusted to $100 \mu\text{m s}^{-1}$. The contact time and delay time between single force curves could be set independently.

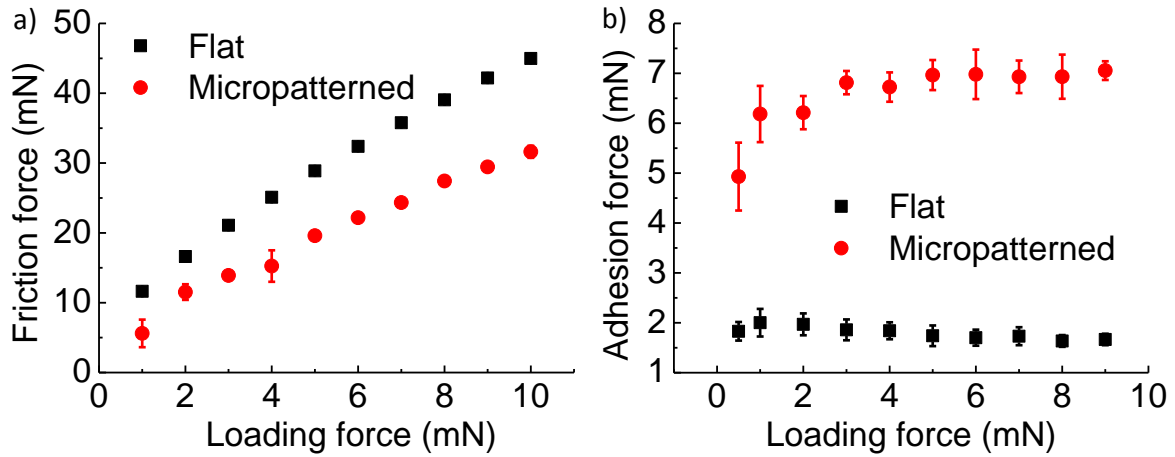


Figure 7.21. Load dependence of friction force (a) and of adhesion force (b) for the flat and micropatterned PDMS surfaces.

The friction force on the arrays of regular hexagonal pillars (height = $5 \mu\text{m}$) and on the flat film sample were also tested. Measurements were performed in the absence of water and after three days of curing at room temperature. Figure 7.21 depicts the difference between flat and micropatterned PDMS. The friction force (Figure 7.21.a) on the flat surface had slightly higher slope values than the micropatterned surface because of the larger contact area and a higher stiffness. Similar results are found in the referenced literature⁴⁹. The adhesion force (Figure 7.21.b) in the micropatterned surface is higher and increasing compared to the flat one, which is constant between 1-2 mN. This is because the splitting contact causes larger adhesion force of a patterned surface compared to a flat surface.

In the case of pACAA hydrogel, the friction force of the micropatterned and flat surfaces were checked. Measurements were carried out in the presence and the absence of water. Firstly, the adhesion force was studied in order to know what the maximum load force that can be applied is without destroying the micropatterns. Different loading forces between 8, 6 and 5 mN were tested.

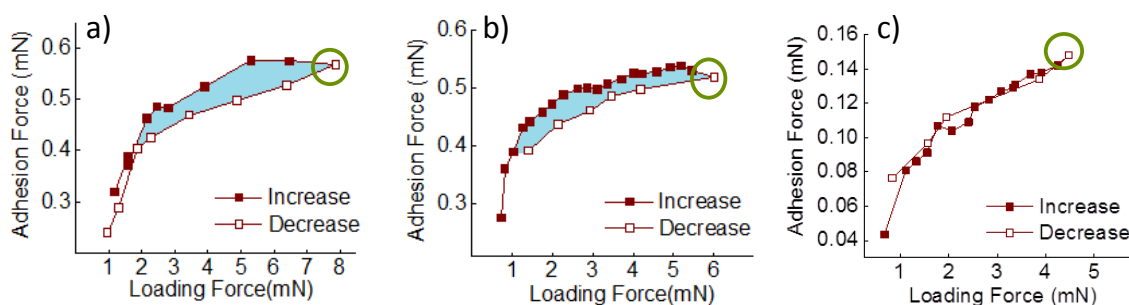


Figure 7.22. Friction force of microstructures hydrogel until different maximum loading force 8mN (a), 6mN(b) and 5mN(c).

The reduced adhesion force in the cycle of decreasing loading force indicates deformation or destroying of the hydrogel microstructures. If the adhesion force is higher relative to the increase cycle compared to the decrease cycle. This can be explained because the micropatterns have been destroyed. Figure 7.22 shows that an increment in the loading force to 8 and 6 mN produces a deformation of the micropatterns, whilst when the loading force does not exceed 5mN, the microstructure of hydrogel remains unaltered. Thus the friction force has been studied with a maximum loading force of 5mN. Figure 7.23 depicts the load dependence of the friction force for the flat and micropatterned pACAA surface in the wet and dry state.

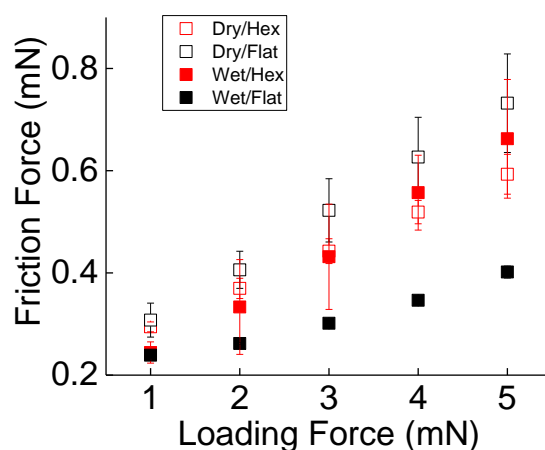


Figure 7.23. Load dependence of friction force for the flat (black) and micropatterned (red) pACAA surface in wet (fill symbol) and dry (empty symbol) state.

As observed in the Figure 7.23 micropatterned hydrogels have slightly bigger friction force in wet state than in dry state, a part of at a loading force of 4 and 5mN. A flat surface has

larger friction force in dry state than in wet state. Figure 7.24 shows the images obtained with the optical microscopy of hydrogel micropatterns in the dry and wet state. In wet state, microstructures swell and touch each other so the friction on them behaves similar to on a flat surface. These measurements were performed to be compared later with the sample obtained by combination of nano and micropatterns.

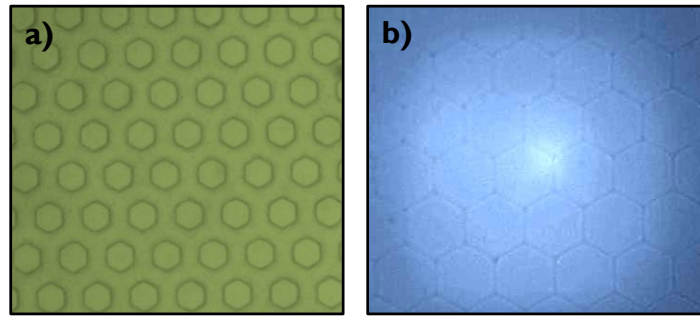


Figure 7.24. pACAA hydrogel micropatterns in dry (a) and in wet (b) state.

After the micro and nano structures were created separately, the challenge was to combine the two structures together. The break step with the help of the macromanipulator was the most difficult stage, with failed results. Several attempts were performed with the following results shown by SEM images (Figure 7.25)

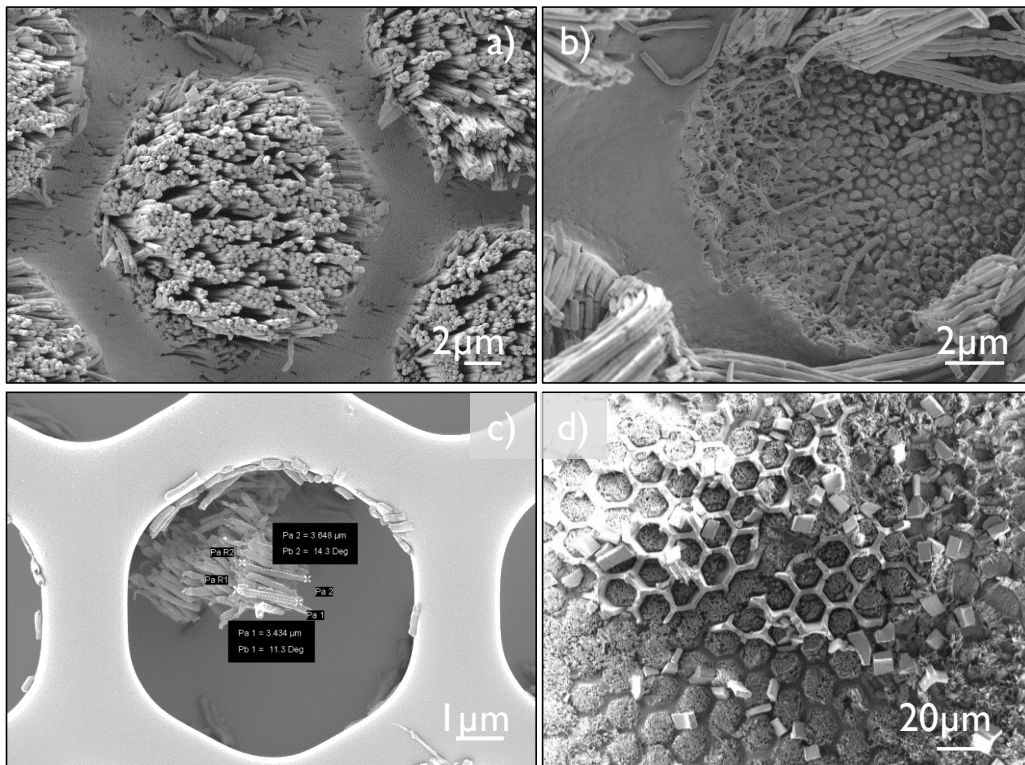


Figure 7.25. Results of the breaking step. a) Deformed Micropatterns (NPA), b) broken nanopillars in NPA, c) nanopillars in the SU-8 mask, d) part of the SU-8 mask in the NPA.

The results were not as expected. This happened because the two parameters failed. The first one was the chosen polymer. The breaking step is carried out in cryogenic temperatures (under liquid nitrogen): at this condition the polymer must break in a brittle way, that is, the polymer has to be under its glass transition temperature. In the case of the PCL, the glass transition is -60°C , and the polymer can be easily deformed but the break is not the desired. Micropatterns of PCL are easily deformed (Figure 7.25.a) but not uniformly broken from the nanopillar array polymer (NPA), Figure 7.25 b and c. The PMMA nanopillar array had the problem that the film was so brittle, resulting in difficult manipulation in the breaking process. The second one, the material of the lithography mask (SU-8 resin) is not hard enough for the breaking process. Figure 7.25.d shows how part of the mask remains in the NPA instead of staying on the wafer silicon. To better understand the result obtained, Figure 7.26 shows a diagram of the expected situation and the actual situation between steps 8-9, shown in previous SEM images.

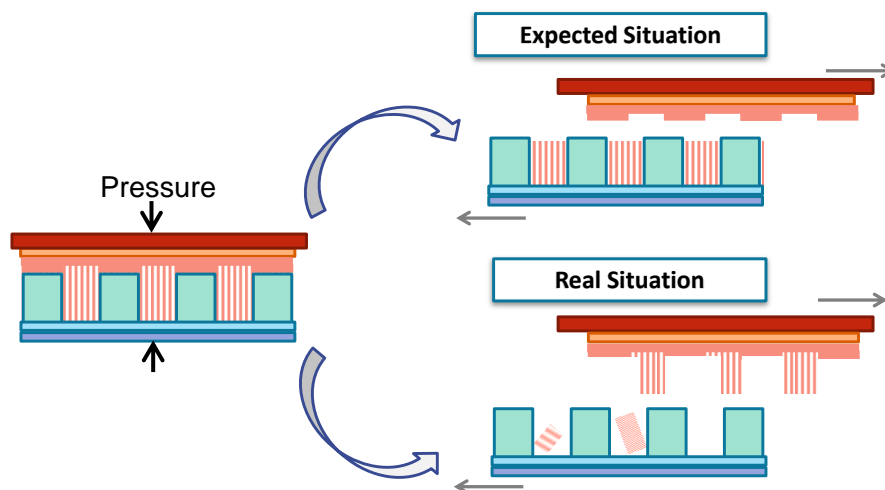


Figure 7.26. Scheme of the expected and the actual situation between steps 8-9.

This experiment was attempted with PMMA but the sample was too brittle, therefore the result was worse than with PCL. The work developed in this section, realized during the internship at the Max Planck Institute in Germany, has been continued there. The following advances were introduced: a matrix polystyrene nanopillars instead of polycaprolactone; posterior functionalization of PS nanostructures surface with vinyltriethoxysilane; and use of a nickel mask instead of SU-8. In this case successfully results were obtained.

7.4. Conclusions

The main conclusions drawn from three combined polymer infiltration processes to obtain core-shell Polycaprolactone-Polystyrene (PCL-PS) nanocylinders; core-shell Nickel-Polystyrene (Ni-PS) magnetic nanowires and nano-micro Polycaprolactone-Polydimethylsiloxane (PCL-PDMS) patterning, can be summarized in:

- The double infiltration technique proposed here has successfully produced PCL-PS core-shell nanocylinders, in which the PCL core can crystallize under confined conditions. The proposed methodology is easy to carry out and allows obtaining polymer nanostructures through nano-molding using AAO templates of different pore diameters. SEM observations clearly show PS nanotubes, and PCL-PS nanocylinders composed of a PCL core surrounded by a PS shell. The double infiltration was also verified by FTIR measurements. DSC experiments proved that the infiltrated PCL undergoes fractionated crystallization with two crystallization steps, one attributed to the crystallization from heterogeneity containing domains and a second to homogeneous nucleation. The low crystallization temperature characteristic of clean PCL nanocylinders depends on the nature of the surface that surrounds them (i.e., alumina or PS).
- Ordered arrays of nickel nanowires covered by polystyrene nanotubes have been synthesized for the first time by combined electrochemical and chemical routes from anodic alumina templates. The achieved long-range hexagonal ordering of nanowire-nanotube composite mimics that of the precursor anodic alumina oxide template. The resulting cylindrical composite, 25 μm in length, consists of a polymer nanotube shell of 280 nm outer diameter filled with a metallic magnetic nanowire core of 140 nm diameter. The magnetic characterization of the nanowire-nanotube composite array indicates the presence of an effective magnetization in the axis parallel to the nanowires, ascribed mostly to the shape anisotropy of Ni nanowires.
- With the objective to mimic the toe pad of the tree frog, preliminary studies have been performed to obtain structures based on the natural patterned adhesives. In

order to replicate the structures, two polymer patterns have been done at different scales, nano and micro. The nanostructure of the hard material part has been made of nanopillars of the PCL and PMMA, which have been obtained by polymer infiltration inside the AAO template. The microstructure of soft material part has been achieved by micropatterns of PDMS and pACAA, from a double soft-molding. The resulting soft polymer microstructure has been studied by adhesion and friction forces, observing differences in the flat and micropatterned surfaces, although not successfully results were obtained. To overcome these disadvantages, other materials were selected. The continuation of the work, carried out in the Max Planck laboratory, by changing the materials to polystyrene nanopillars (instead of PLC) and to nickel mask (instead of SU-8) at the microscopic scale, allowed to achieve important advances in obtaining the desired structure and properties.

7.5. References

- (1). Michell, R. M.; Müller, A. J. Confined crystallization of polymeric materials. *Progress in Polymer Science* **2016**, *54-55*, 183-213.
- (2). Martín, J.; Hernández, R.; Mijangos, C. A review on the progress of polymer nanostructures with modulated morphologies and properties, using nanoporous AAO templates. *Prog. Polym. Sci* **2015**, *30*, 148-182.
- (3). Liang, C. Y.; Krimm, S. Infrared Spectra of High Polymers. 6. Polystyrene. *J. Polym. Sci.* **1958**, *27*, 241-254.
- (4). Bassi, A. K.; Gough, J. E.; Zakikhani, M.; Downes, S. The Chemical and Physical Properties of Poly(ϵ -Caprolactone) Scaffolds Functionalised with Poly(Vinyl Phosphonic Acid-co-Acrylic Acid). *J. Tissue Eng.* **2011**, *2*, 615328.
- (5). Elzein, T.; Nasser-Eddine, M.; Delaite, C.; Bistac, S.; Dumas, P. FTIR study of polycaprolactone chain organization at interfaces. *Journal of Colloid and Interface Science* **2004**, *273*, (2), 381-387.
- (6). Suzuki, Y.; Duran, H.; Akram, W.; Steinhart, M.; Floudas, G.; Butt, H. J. Multiple nucleation events and local dynamics of poly(ϵ -caprolactone) (PCL) confined to nanoporous alumina. *Soft Matter* **2013**, *9*, (38), 9189-9198.
- (7). Sousa, C. T.; Leitao, D. C.; Proenca, M. P.; Ventura, J.; Pereira, A. M.; Araujo, J. P. Nanoporous alumina as templates for multifunctional applications. *Applied Physics Reviews* **2014**, *1*, (3).
- (8). Thompson, G. E.; Furneaux, R. C.; Wood, G. C.; Richardson, J. A.; Goode, J. S. Nucleation and growth of porous anodic films on aluminium. *Nature* **1978**, *272*, (5652), 433-435.
- (9). Fan, H. J.; Werner, P.; Zacharias, M. Semiconductor nanowires: From self-organization to patterned growth. *Small* **2006**, *2*, (6), 700-717.
- (10). Martin, C. R. Nanomaterials: A membrane-based synthetic approach. *Science* **1994**, *266*, (5193), 1961-1966.
- (11). Pan, H.; Liu, B.; Yi, J.; Poh, C.; Lim, S.; Ding, J.; Feng, Y.; Huan, C. H. A.; Lin, J. Growth of single-crystalline Ni and Co nanowires via electrochemical deposition and their magnetic properties. *Journal of Physical Chemistry B* **2005**, *109*, (8), 3094-3098.
- (12). Ovejero, J. G.; Bran, C.; Vilanova, E.; Kosel, J.; Morales, M. P.; Vazquez, M. Electrochemical synthesis of core-shell magnetic nanowires. *Journal of Magnetism and Magnetic Materials* **2015**, *389*, 144-147.
- (13). García, J.; Prida, V. M.; Vivas, L. G.; Hernando, B.; Barriga-Castro, E. D.; Mendoza-Reséndez, R.; Luna, C.; Escrig, J.; Vázquez, M. Magnetization reversal dependence on effective magnetic anisotropy in electroplated Co-Cu nanowire arrays. *Journal of Materials Chemistry C* **2015**, *3*, (18), 4688-4697.
- (14). Nguyen, T. H. L.; Laffont, L.; Capsal, J. F.; Cottinet, P. J.; Lonjon, A.; Dantras, E.; Lacabanne, C. Magnetolectric properties of nickel nanowires-P(VDF-TrFE) composites. *Materials Chemistry and Physics* **2015**, *153*, 195-201.
- (15). Lonjon, A.; Demont, P.; Dantras, E.; Lacabanne, C. Mechanical improvement of P(VDF-TrFE)/nickel nanowires conductive nanocomposites: Influence of particles aspect ratio. *Journal of Non-Crystalline Solids* **2012**, *358*, (2), 236-240.
- (16). Stojak Repa, K.; Israel, D.; Alonso, J.; Phan, M. H.; Palmero, E. M.; Vazquez, M.; Srikanth, H. Superparamagnetic properties of carbon nanotubes filled with NiFe₂O₄ nanoparticles. *Journal of Applied Physics* **2015**, *117*, (17).

- (17). Martín, J.; Krutyeva, M.; Monkenbusch, M.; Arbe, A.; Allgaier, J.; Radulescu, A.; Falus, P.; Maiz, J.; Mijangos, C.; Colmenero, J.; Richter, D. Direct observation of confined single chain dynamics by neutron scattering. *Physical Review Letters* **2010**, *104*, (19).
- (18). Blaszczyk-Lezak, I.; Hernández, M.; Mijangos, C. One dimensional PMMA nanofibers from AAO templates. evidence of confinement effects by dielectric and raman analysis. *Macromolecules* **2013**, *46*, (12), 4995-5002.
- (19). Li, L.; Zhou, D.; Huang, D.; Xue, G. Double glass transition temperatures of poly(methyl methacrylate) confined in alumina nanotube templates. *Macromolecules* **2014**, *47*, (1), 297-303.
- (20). Wu, Y.; Gu, Q.; Ding, G.; Tong, F.; Hu, Z.; Jonas, A. M. Confinement induced preferential orientation of crystals and enhancement of properties in ferroelectric polymer nanowires. *ACS Macro Letters* **2013**, *2*, (6), 535-538.
- (21). Han, X.; Maiz, J.; Mijangos, C.; Zaldo, C. Nanopatterned PMMA-Yb:Er/Tm:Lu₂O₃ composites with visible upconversion emissions. *Nanotechnology* **2014**, *25*, (20).
- (22). Grimm, S.; Martín, J.; Rodriguez, G.; Fernández-Gutierrez, M.; Mathwig, K.; Wehrspohn, R. B.; Gösele, U.; San Roman, J.; Mijangos, C.; Steinhart, M. Cellular interactions of biodegradable nanorod arrays prepared by nondestructive extraction from nanoporous alumina. *Journal of Materials Chemistry* **2010**, *20*, (16), 3171-3177.
- (23). Lahav, M.; Weiss, E. A.; Xu, Q.; Whitesides, G. M. Core-shell and segmented polymer-metal composite nanostructures. *Nano Letters* **2006**, *6*, (9), 2166-2171.
- (24). Nielsch, K.; Castaño, F. J.; Matthias, S.; Lee, W.; Ross, C. A. Synthesis of cobalt/polymer multilayer nanotubes. *Advanced Engineering Materials* **2005**, *7*, (4), 217-221.
- (25). Nielsch, K.; Castaño, F. J.; Ross, C. A.; Krishnan, R. Magnetic properties of template-synthesized cobalt/polymer composite nanotubes. *Journal of Applied Physics* **2005**, *98*, (3).
- (26). Kelly, D. N.; Wakabayashi, R. H.; Stacy, A. M. A modified sol-gel technique for pore size control in porous aluminum oxide nanowire templates. *ACS Applied Materials and Interfaces* **2014**, *6*, (22), 20122-20129.
- (27). Martín, J.; Maiz, J.; Sacristan, J.; Mijangos, C. Tailored polymer-based nanorods and nanotubes by "template synthesis": From preparation to applications. *Polymer* **2012**, *53*, (6), 1149-1166.
- (28). Martín, J.; Vázquez, M.; Hernández-Vélez, M.; Mijangos, C. Ordered arrays of magnetic polymer-based nanorods by template synthesis. *Journal of Nanoscience and Nanotechnology* **2009**, *9*, (10), 5898-5902.
- (29). Zierold, R.; Wu, Z.; Biskupek, J.; Kaiser, U.; Bachmann, J.; Krill Iii, C. E.; Nielsch, K. Magnetic, multilayered nanotubes of low aspect ratios for liquid suspensions. *Advanced Functional Materials* **2011**, *21*, (2), 226-232.
- (30). Vega, V.; Böhnert, T.; Martens, S.; Waleczek, M.; Montero-Moreno, J. M.; Görlitz, D.; Prida, V. M.; Nielsch, K. Tuning the magnetic anisotropy of CoNi nanowires: Comparison between single nanowires and nanowire arrays in hard-anodic aluminum oxide membranes. *Nanotechnology* **2012**, *23*, (46).
- (31). Masuda, H.; Fukuda, K. Ordered metal nanohole arrays made by a two-step replication of honeycomb structures of anodic alumina. *Science* **1995**, *268*, (5216), 1466-1468.
- (32). Masuda, H.; Yada, K.; Osaka, A. Self-ordering of cell configuration of anodic porous alumina with large-size pores in phosphoric acid solution. *Japanese Journal of Applied Physics, Part 2: Letters* **1998**, *37*, (11 PART A), L1340-L1342.
- (33). Sun, C.; Luo, J.; Wu, L.; Zhang, J. Self-ordered anodic alumina with continuously tunable pore intervals from 410 to 530 nm. *ACS Applied Materials and Interfaces* **2010**, *2*, (5), 1299-1302.

- (34). Song, G.; She, X.; Fu, Z.; Li, J. Preparation of good mechanical property polystyrene nanotubes with array structure in anodic aluminum oxide template using simple physical techniques. *Journal of Materials Research* **2004**, *19*, (11), 3324-3328.
- (35). Sharma, M.; Kuanr, B. K.; Veerakumar, V.; Basu, A.; Celinski, Z. J. Magnetization dynamics and reversal mechanisms in Ni nanowire and nanotube arrays. *IEEE Transactions on Magnetics* **2014**, *50*, (11).
- (36). Byrne, F.; Prina-Mello, A.; Whelan, A.; Mohamed, B. M.; Davies, A.; Gun'ko, Y. K.; Coey, J. M. D.; Volkov, Y. High content analysis of the biocompatibility of nickel nanowires. *Journal of Magnetism and Magnetic Materials* **2009**, *321*, (10), 1341-1345.
- (37). Gao, N.; Wang, H.; Yang, E. H. An experimental study on ferromagnetic nickel nanowires functionalized with antibodies for cell separation. *Nanotechnology* **2010**, *21*, (10).
- (38). Boesel, L. F.; Cremer, C.; Arzt, E.; Campo, A. D. Gecko-inspired surfaces: A path to strong and reversible dry adhesives. *Advanced Materials* **2010**, *22*, (19), 2125-2137.
- (39). Autumn, K.; Sitti, M.; Liang, Y. A.; Peattie, A. M.; Hansen, W. R.; Sponberg, S.; Kenny, T. W.; Fearing, R.; Israelachvili, J. N.; Full, R. J. Evidence for van der Waals adhesion in gecko setae. *Proceedings of the National Academy of Sciences of the United States of America* **2002**, *99*, (19), 12252-12256.
- (40). Arzt, E.; Gorb, S.; Spolenak, R. From micro to nano contacts in biological attachment devices. *Proceedings of the National Academy of Sciences of the United States of America* **2003**, *100*, (19), 10603-10606.
- (41). Del Campo, A.; Greiner, C.; Álvarez, I.; Arzt, E. Patterned surfaces with pillars with controlled 3D tip geometry mimicking bioattachment devices. *Advanced Materials* **2007**, *19*, (15), 1973-1977.
- (42). Del Campo, A.; Greiner, C.; Arzt, E. Contact shape controls adhesion of bioinspired fibrillar surfaces. *Langmuir* **2007**, *23*, (20), 10235-10243.
- (43). Barnes, W. J. P.; Oines, C.; Smith, J. M. Whole animal measurements of shear and adhesive forces in adult tree frogs: Insights into underlying mechanisms of adhesion obtained from studying the effects of size and scale. *Journal of Comparative Physiology A: Neuroethology, Sensory, Neural, and Behavioral Physiology* **2006**, *192*, (11), 1179-1191.
- (44). Federle, W.; Barnes, W. J. P.; Baumgartner, W.; Drechsler, P.; Smith, J. M. Wet but not slippery: Boundary friction in tree frog adhesive toe pads. *Journal of the Royal Society Interface* **2006**, *3*, (10), 689-697.
- (45). Hanna, G.; Barnes, W. J. P. Adhesion and detachment of the toe pads of tree frogs. *Journal of Experimental Biology* **1991**, *155*, 103-125.
- (46). Mizuhira, V. The digital pads of rhacophorid tree-frogs. *Journal of Electron Microscopy* **2004**, *53*, (1), 63-78.
- (47). Drotlef, D. M.; Appel, E.; Peisker, H.; Dening, K.; Del Campo, A.; Gorb, S. N.; Barnes, W. Morphological studies of the toe pads of the rock frog, *Stauroids parvus* (family: Ranidae) and their relevance to the development of new biomimetically inspired reversible adhesives. *Interface Focus* **2015**, *5*, 20140036.
- (48). Drotlef, D. M.; Stepien, L.; Kappl, M.; Barnes, W. J. P.; Butt, H. J.; Del Campo, A. Insights into the adhesive mechanisms of tree frogs using artificial mimics. *Advanced Functional Materials* **2013**, *23*, (9), 1137-1146.
- (49). Iturri, J.; Xue, L.; Kappl, M.; García-Fernández, L.; Barnes, W. J. P.; Butt, H. J.; Campo, A. D. Torrent frog-inspired adhesives: Attachment to flooded surfaces. *Advanced Functional Materials* **2015**, *25*, (10), 1499-1505.

Chapter 8

CONCLUSIONS AND PERSPECTIVES

In the present work, we have studied the in-situ polymerization processes, as an alternative to polymer infiltration method, to obtain polymer nanostructures and developed combined polymer infiltration processes, from laboratory-made anodic aluminium oxide (AAO) templates used as “nanoreactors” and “nanomolds”, respectively. With the aid of mathematical models, the differences between polymerization in bulk and in confinement have been interpreted on the basis of confinement effects. In all cases, the polymer nanostructures have been morphological, thermal and chemical characterized and at least a “specific” property determined.

The experimental results obtained allow us to conclude the following:

- a) Ordered AAO templates have been successfully fabricated by a two-step anodization process. AAO nanocavities are achieved with a homogeneous, suitable and uniform pore size distribution. Choosing the appropriate anodization conditions, the concentration of the electrolyte, voltage, temperature and time, ordered AAO templates have been obtained with adjusted dimensions, the diameter ranging from 15 up to 400 nanometers and the length from a few to 100 microns. The preparation process is highly reproducible, therefore, obtained templates are suitable to be used as “nanomold” and “nanoreactor”
- b) The most relevant features in the study of three in-situ polymerization processes, the free radical polymerization of MMA and of FA monomers and the step-growth polymerization of a diol and a diisocyanate, carried out in confinement in AAO nanoreactors can be summarized by the following conclusions:
 - The free radical polymerization kinetic of methyl methacrylate inside the pores of an anodic alumina template can be easily studied by monitoring the progress of the reaction by DSC or Raman Microscopy techniques. When the reaction is conducted inside the AAO templates the polymerization rate is significantly higher and the polymer molecular weight is reduced, as compared to the reaction in bulk. Moreover, a conversion close to 90% is obtained in one hour.

A mathematical model has been implemented to describe the differences between polymerization in bulk and in AAO nanocavities, based on confinement effects. Firstly, as the dimensions of the template are reduced, in the early stages of polymerization, an increasing catalytic effect is observed (due to the AAO surface walls) in the initiator decomposition and thus leading to a faster polymerization rate. Secondly, when the reaction is carried out in confinement in the AAO nanocavities, the rate of termination increases in

the latter stages of the reaction. The two confinement effects combine to lead to lower molecular weight polymers and reduced polydispersity in comparison to the reaction conducted in bulk.

- The free radical polymerization of a fluorinated acrylic monomer can be also satisfactorily studied in confinement in an AAO nanoreactor by Raman spectroscopy. The polymerization conversion in two hours is of 90%, so in-situ polymerization is a faster process than polymer infiltration. A simpler mathematical model than the previous one is implemented to describe the differences between polymerization in bulk and in AAO nanocavities. In this case, the decrease in polymerization rate is directly related to the increase in the termination step, due to a lower effective volume experienced by the radicals when confined to a cylindrical volume.

Furthermore, when PFA is infiltrated into AAO nanocavities of 200nm of pore diameter and 1 μ m of pore length, a superhydrophobic surface is achieved, deduced from a water contact angle of 159°, being much higher than its analogous non-nanostructured PFA, 114°. The “lotus effect” is observed in the superhydrophobic surface, since the low sliding angle is of 8°.

- The step growth polymerization kinetic of a diol and diisocyanate inside the pores of an anodic alumina template has been easily studied by monitoring the progress of the reaction by FT-IR microscopy. A mathematical model was developed to study confinement effects on the rate of polymerization. It is proposed that an additional reaction takes place between the isocyanate groups and the hydroxyl groups of the alumina wall. This additional reaction joined with the physical confinement of the chains to a small volume results in an increase in the rate of polymerization at the early stages of the reaction. At high conversions the limited diffusion of the polymer chains, results in a slowing down of the reaction. The reaction time is 240 minutes to reach conversion close to 90% in the case of polymerization in confinement. Consequently, the molecular weight and the dispersity were reduced.

c) In the preparation of novel polymer nanostructures by combination of polymer infiltration process within AAO nanomolds, we can conclude the following:

- The nanostructure of PCL-PS core-shell nanocylinders has been successfully produced. The method followed is a two- step infiltration process of two different polymer melts.

The first lead to PS nanotubes (shell) and the second is PCL nanofibers (core). The double infiltration is verified by FT-IR and SEM, TEM images, where is observed that the nanocylinders composed of a PCL core is quantitatively surrounded by a PS shell.

The effect of confinement on PCL was proved by DSC experiments. It was observed that infiltrated PCL suffers a fractionated double crystallization, one at higher temperatures that can be attributed to the crystallization from heterogeneity containing domains and the other one to the crystallization from clean PCL homogeneous nucleation. The low crystallization temperature depends on the nature of the surface that surrounds the core (i.e. alumina or polystyrene).

- Nickel nanowires covered by polystyrene nanotubes have been synthesized by combination of infiltration of polystyrene in side alumina template and electrochemical synthesis of nickel. The magnetic characterization of the Ni nanowire-PS nanotubes composite array indicates the presence of an effective magnetization in the axis parallel to the nanowires, attributed mainly to the anisotropy form of Ni nanowires. From them, individual composite could be chemically released from the template in which individual composite nanowires would benefit from their polymer functionalization while could be simultaneously oriented/displaced under a suitable magnetic field.
- Preliminary studies have been carried out to obtain “patterned” nano-micro structures, based on the natural patterned adhesives, to mimic the toe pad of the tree frog. Two patterns have been developed on two scales, nano and micro. The nanostructure part is made of nanopillars of PCL or PMMA (hard material), obtained by infiltration within the AAO template. While the microstructure part is made of PDMS or pACAA micropatterns (soft material) obtained by double soft- molding process. The properties of soft polymers have been studied by forces of adhesion and friction, observing differences in flat and micropattern surfaces. Although the double structure was not successfully obtained because of the selection of the polymers, the continuation of the work carried out in the Max Planck laboratory, by changing the materials to polystyrene nanopillars (instead of PLC) and to nickel mask (instead of SU-8) at the microscopic scale, allowed to achieve important advances in obtaining the desired structure and properties.

In resume, advances addressed to the in-situ polymerization process in AAO nanocavities allowed the straightforward preparation of polymer nanostructures from monomers, by radical and step polymerization reactions, and developments in polymer infiltration process

by combining two different processes allowed to obtain core-shell nanostructures and patterned nano-micro structures. Following both strategies, we have produced a portfolio of nanostructured polymers that combine functionality and size. The list includes not only homopolymer nanostructures, segregated hard and soft polymer nanostructures, core-shell nanostructures, electrical conducting composite polymer nanostructures, flexible magnetic nanostructures but superhydrophobic and biomimetic nanostructured surfaces, among others.

Furthermore, the results of the present work have opened news challenges that will continue in our group with other PhD and Master projects. In-situ polymerization process now continues with the study of co-polymerization of vinyl monomers and of ring-opening polymerizations also under confinement in AAO templates. Moreover, the same methodology of polymer infiltration methods developed in this work to study the influence of the nature of surface walls (i.e. metal or polymer) is now being employed in the study of dielectric properties and crystallization of different core-shell polymer nanocylindres.

Annex

PNIPAM NANOPILLARS OBTAINED BY ATRP POLYMERIZATION IN AAO TEMPLATE

This annex describes the synthesis of PNIPAm-AAm gel nanopillars by the atom transfer radical polymerization, carried out in the porous surface of the AAO template.

A.1 Introduction

Hydrogels based on PNIPAm are thermo-responsive materials that show adaptive changes in mechanical properties.¹ The main change in the mechanical properties of the PNIPAm is the transition temperature, which is related to the quantity of water expelled or absorbed from the hydrogel network. One way to control the mechanical properties of the gel is through the crosslinking of PNIPAm with other monomers.² For example, Forney *et al.*³ observed that the incorporation of the cross-linked poly (dimethylsiloxane) (PDMS) in a PNIPAm gel causes an increase in the mechanical toughness. Janovak *et al.*⁴ reported, contrary to expectations, that the presence of copolymerized acrylamide (AAm) in a macrogel of PNIPAM produced an improvement in the mechanical properties. This behavior was observed through the rheology characterization due to the strong union of water molecules to the AAm monomers, resulting in a stronger gel structure.

As known, Atom Transfer Radical Polymerization (ATRP) allows the synthesis of polymers with well-controlled molecular weight, narrow molecular weight distribution, and defined topology.⁵ The possibility of combining AAO templates with atom transfer radical polymerization (ATRP) technique leads to a more controlled and friendly polymerization systems.^{6, 7} Cui *et al.* have prepared PNIPAm nanotubes by ATRP polymerization using AAO as a template. The diameter of the nanotubes was controlled and these nanostructures showed a high flexibility.⁸

As a part of this PhD work we have collaborated with Dr. J. Giussi of the Universidad de la Plata in Argentina, and carried out an exploratory work for the preparation and characterization of nanopillars based on PNIPAm microgels with tunable LCST through surface initiated-atom transfer radical polymerization (SI-ATRP). To meet these goals, we combine AAO template synthesis with SI-ATRP of NIPAm and Acrylamide (AAm) monomers in order to attain low aspect ratio unidimensional nanopillars. Infrared and Raman spectroscopy are used to determine the chemical composition of the polymers and Scanning Electron Microscopy to confirm the nanostructures obtained.

A.2 Experimental part

Materials and AAO templates

N-Isopropylacrylamide (NIPAM, 97%); Acrylamide, 98% by Fluka; N,N'-methylenebisacrylamide (BIS, 99%); 3-aminopropyltrimethoxysilane (APTMS); N,N,N',N',N''-pentamethyldiethylenetriamine (PMDETA, 99%) and 2-bromoisobutryl bromide (BIBB, 97%) were supplied by Aldrich and used as received. AAO templates used in this study were prepared by two-step anodizations in phosphoric acid and followed by a pore widening process as described in the chapter 3. The pore diameter obtained is 200 nm and the pore length is around 700 nm.

Synthesis of PNIPAM nanopillar

Previous to the ATRP polymerization, the abundant hydroxyls groups on the AAO membrane surface and the pore surface need to be modified. PNIPAM-AAm nanopillars are achieved by grafting linear PNIPAm chains onto the pore surfaces of porous AAO template by ATRP polymerization method. The synthesis is initiated from the nanoreactor walls and it requires a number of steps, shown in Figure A.1.

Firstly the ATRP initiator must be immobilized onto the AAO substrate membrane following two steps: silanization and acrylation. In the first step, the hydroxyl groups of the AAO wall were activated by APTMS, for that the alumina template was immersed in a mixture of 0.5 ml of APTMS in ethanol for one hour according to previous reports.^{8,9} The template was cured for one hour in an oven at 150°C (*step1*).

In the second step the amino groups on the wall react with the ATRP initiator (BIBB). The template with -NH₂ groups was immersed into 97 ml of dry dichloromethane containing dry triethylamine (2 vol%). Afterwards, 1 ml of BIBB was added dropwise into the solvent for 10 min with an ice bath. The template was treated in an ultrasonic bath for 30 s to make sure that the -NH₂ groups in the membrane pores can contact the BIBB solution sufficiently. The reaction was carried out for 4 h at room temperature. The resultant AAO template with -Br groups was then washed with ethanol for 24 h and dried at 50 °C for 8 h (*step2*).

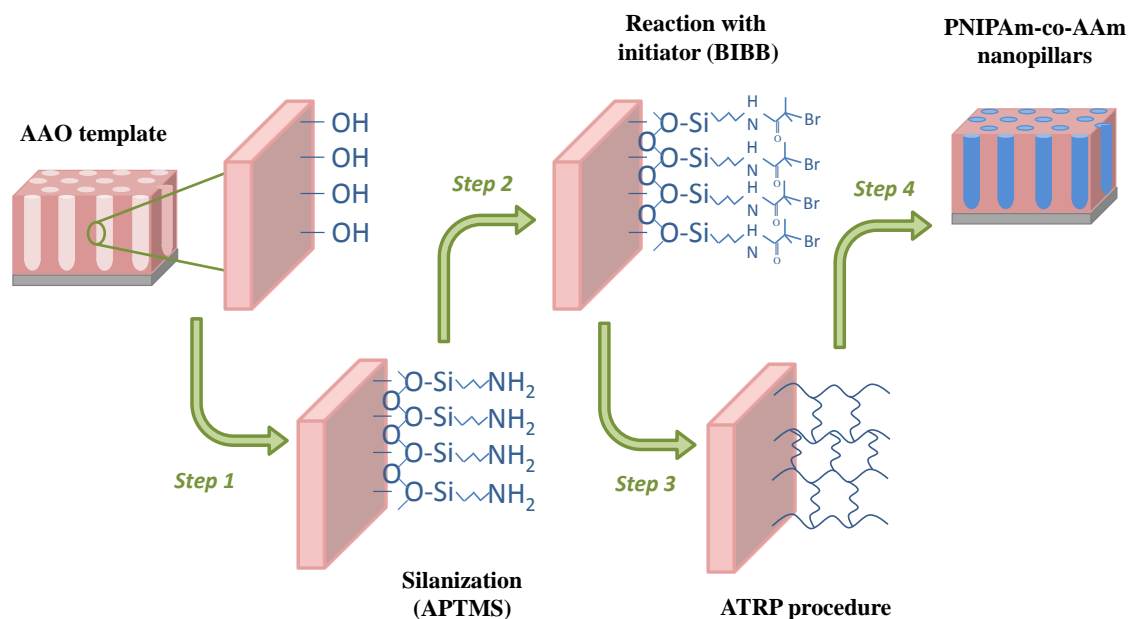


Figure A.1. Steps synthesis of PNIPAm-co-AAm nanopillars.

The aminopropylsilane grafted AAO nanoreactor previously in vacuum 30 min was immersed in an exhaustively degassed solution which contained 4.70 mmol of Amide (NIPAm and AAm) and 0.11 mmol of BIS in a mixture of 2 mL of H_2O and 2 mL of MeOH containing 0.105 mmol of CuCl (this compound was added last, after purging with nitrogen, to prevent its oxidation) and 0.502 mmol of PMDETA for 48 hours, at room temperature (*step3*). After this time the AAO nanoreactor with the nanopillars inside was retired from the reaction medium and intensively washed with water. The samples were stored immersed in degassed water in closed containers before specific treatment for each study (*step4*).

In order to tune the LCST to higher values, homo and copolymers of NIPAm and AAm were prepared with different chemical composition (100:0, 90:10, 80:20), following the general procedure described above.

Characterization methods

IR and Raman Spectroscopy. The obtained nanopillars were chemically characterized by Infrared and Raman Spectroscopy, FT-IR Varian 660 and by Renishaw InVia Raman Microscope. FT-IR experiments were performed during the step modification of the alumina membrane before and after the ATRP polymerization.

Scanning Electron Microscopy. The nanopillars obtained were morphologically characterized by scanning electron microscopy (SEM) (Philips XL30). In order to perform the analysis of free nanopillars, the aluminum substrate was treated with a mixture of HCl, CuCl₂, and H₂O and the alumina was dissolved in 10 % wt H₃PO₄. Previously, in order to support the free nanostructures, a coating was placed over the template. The samples were lyophilized before the study in order to preserve the morphology.

A.3 Results and Discussion

Sample Preparation and Characterization

Thermo-responsive poly(N-isopropylacrylamide)-based nanopillares were synthesized by SI-ATRP on functionalized AAO nanoreactors. In order to tune LCST, different compositions of NIPAm and AAm were polymerized. For this purpose, PNIPAM-AAm copolymers with different ratios of NIPAm and AAm were fed: 100:0 NIPAm:AAm (PNIPAm₁₀₀), 90:10 NIPAm:AAm (P(NIPAm₉₀-co-AAm₁₀), and 80:20 NIPAm:AAm (P(NIPAm₈₀-co-AAm₂₀). In the first place, FT-IR spectra were employed at different synthesis steps to monitor the grafting of ATRP initiator in the AAO nanoreactor. The ATRP process to obtain nanopillars was also monitored by FT-IR. Figure A.2 shows FT-IR spectra for AAO nanoreactor, AAO nanoreactor after silanization procedure and AAO nanoreactor with ATRP initiator (2-bromoisobutyryl bromide) and detail FT-IR spectra for PNIPAm₁₀₀ close to 2500 and 3200 cm⁻¹.

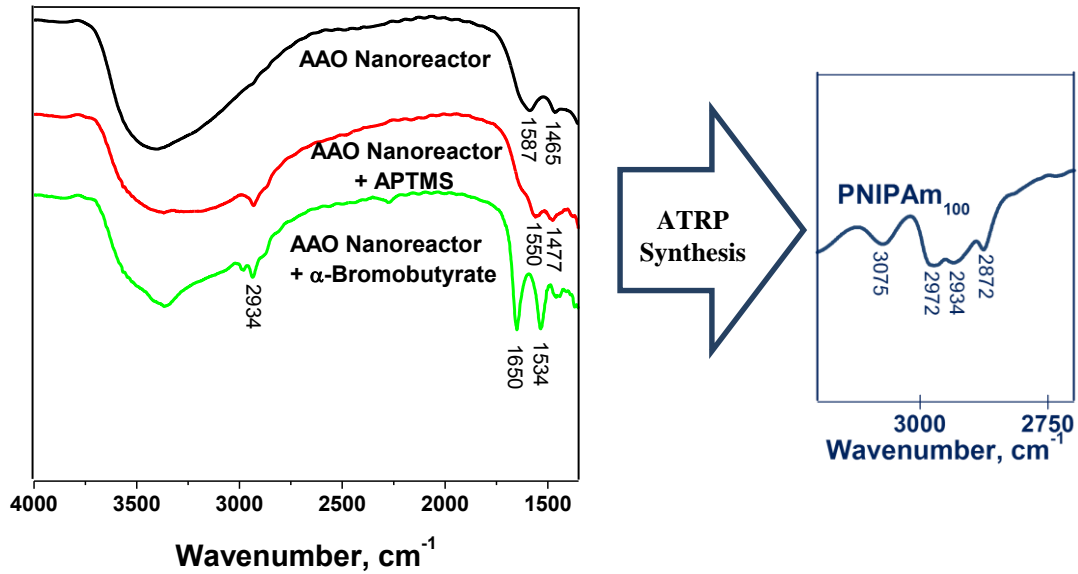


Figure A.2. The FT-IR spectra of AAO membrane (black line), AAO membrane with APTMS (red line) and AAO membrane with α -bromoisobutyrate (green line). On the right side, a magnification of PNIPAm₁₀₀ spectra is represented.

FTIR spectroscopy was used to characterize the chemical composition of the template along grafting of ATRP initiator procedure. After the silanization, in the FTIR spectrum of the simple AAO template (black), an additional peak of methylene group ($-\text{CH}_2$) appears at 2934 cm^{-1} in the spectrum of membrane with APTMS (red). In spectrum of AAO template with α -bromoisobutyrate, the peak of carbonyl group ($\text{C}=\text{O}$) at 1650 cm^{-1} is associated to the characteristic peak of 2-bromoisobutyryl bromide. After ATRP procedure, the apparitions of characteristics peaks of PNIPAm, specially newly emerged methyne ($-\text{CH}-$) and methyl group ($-\text{CH}_3$) at 2972 and 3075 cm^{-1} indicate that the PNIPAm has been successfully fabricated in AAO nanoreactor by the ATRP method. From the comparison of spectra black and green from FT-IR is observed that the $-\text{Br}$ groups have been successfully introduced onto the AAO nanoreactor by silanization and acylation.

Raman spectroscopy was employed to characterize the chemical composition of nanopillars within AAO nanoreactors as previously reported for a similar system.¹⁰ To analyze the presence of AAm monomer in the PNIPAm nanostructures inside pore nanocavities, confocal methodology was conducted. Figure A.3 illustrates the normalized Raman spectra of PNIPAm₁₀₀, P(NIPAm₉₀-co-AAm₁₀) and P(NIPAm₈₀-co-AAm₂₀). The signal at 1650 cm^{-1} corresponds to the carbonyl group present in both monomers and the signal at 2920 cm^{-1} corresponds to the methyl group presents only in NIPAm¹¹ monomer. The rapport between the two bands allows qualitative examination of the change in the nanopillar composition. $I_{\text{CH}_3}/I_{\text{C}=\text{O}}$

ratio was 1.78 for PNIPAM₁₀₀, 1.50 for P(NIPAm₉₀-co-AAm₁₀) and 1.37 for P(NIPAm₈₀-co-AAm₂₀). This decrease in the value indicates an increment of AAm monomer in the copolymer network.

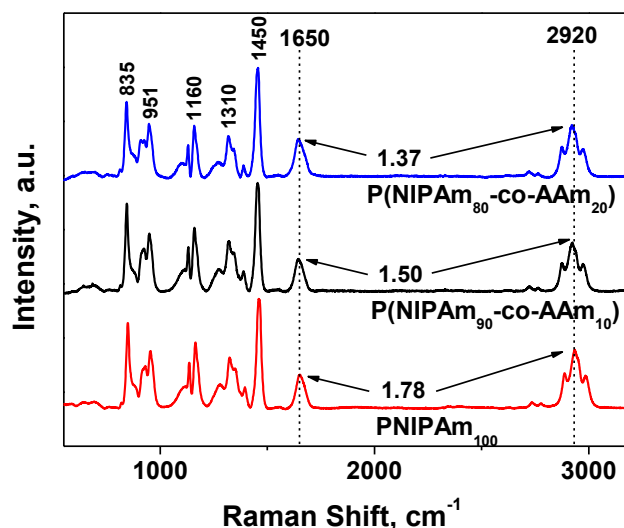


Figure A.3. Raman spectra of PNIPAM₁₀₀, P(NIPAm₉₀-co-AAm₁₀) and P(NIPAm₈₀-co-AAm₂₀) and relationship between the carbonyl group signal at 1650 cm⁻¹ present in both monomers, and the methyl signal at 2920 cm⁻¹ corresponding to the Raman shift of the methyl group present only in NIPAm monomer.

Unlike the compositional study inside the nanocavities via the confocal approach using Raman spectroscopy, SEM microscopy permitted to characterize the morphology of the obtained nanostructures. To this end, the samples were lyophilized before the study in order to preserve morphologies. Figure A.4 provides details of SEM images for PNIPAm₁₀₀, P(NIPAm₉₀-co-AAm₁₀) and P(NIPAm₈₀-co-AAm₂₀).

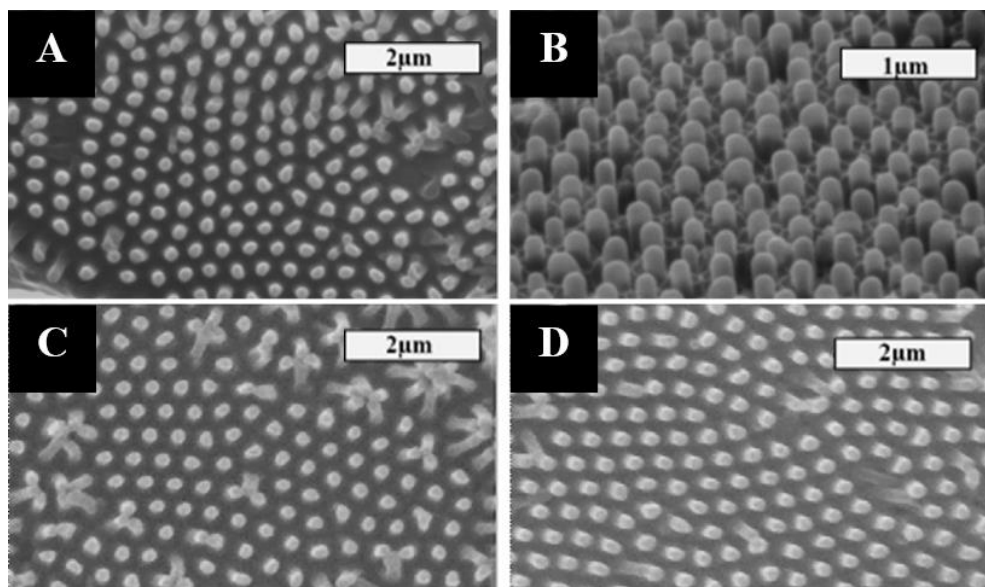


Figure A.4. SEM images of PNIPAm₁₀₀ nanopillars (A) top view, (B) side view; (C) P(NIPAm₉₀-co-AAm₁₀) and; (D) P(NIPAm₈₀-co-AAm₂₀).

Figure A.4 confirms that nanopillars were formed through SI-ATRP in AAO template. Images also evidences that the nanopillar sizes are comparable to the size of AAO nanoreactor.

The continuity of this work has been realized in the Institute of Physical and Theoretical Investigations Theoretical and Applied (INIFTA), Argentina. The characteristics like behavior and the topology were studied by atomic force microscopy, molecular dynamics simulations and water contact angle measurements.

A.4 Conclusion

A useful nanomaterial based on Poly N-Isopropylacrylamide nanopillars with thermally-induced softening was synthesized by initiation atom transfer radicals polymerization (ATRP) started on the surface of alumina wall. FTIR spectroscopy was used to follow the ATRP polymerization. The compositional study inside the nanocavities by the confocal approach using Raman spectroscopy and SEM microscopy permitted to evaluate the morphology of the nanostructures obtained.

A.5 References

- (1). Kaholek, M.; Lee, W.-K.; Feng, J.; LaMattina, B.; Dyer, D. J.; Zauscher, S. Weak polyelectrolyte brush arrays fabricated by combining electron-beam lithography with surface-initiated photopolymerization. *Chemistry of materials* **2006**, *18*, (16), 3660-3664.
- (2). Fernandes, P. A.; Schmidt, S.; Zeiser, M.; Fery, A.; Hellweg, T. Swelling and mechanical properties of polymer gels with cross-linking gradient. *Soft Matter* **2010**, *6*, (15), 3455-3458.
- (3). Forney, B. S.; Baguenard, C.; Guymon, C. A. Improved stimuli-response and mechanical properties of nanostructured poly (N-isopropylacrylamide-co-dimethylsiloxane) hydrogels generated through photopolymerization in lyotropic liquid crystal templates. *Soft Matter* **2013**, *9*, (31), 7458-7467.
- (4). Janovák, L.; Varga, J.; Kemény, L.; Dékány, I. Investigation of the structure and swelling of poly (N-isopropyl-acrylamide-acrylamide) and poly (N-isopropyl-acrylamide-acrylic acid) based copolymer and composite hydrogels. *Colloid and Polymer Science* **2008**, *286*, (14-15), 1575-1585.
- (5). Patten, T. E.; Matyjaszewski, K. Atom transfer radical polymerization and the synthesis of polymeric materials. *Advanced Materials* **1998**, *10*, (12), 901-915.
- (6). Wang, H.-J.; Zhou, W.-H.; Yin, X.-F.; Zhuang, Z.-X.; Yang, H.-H.; Wang, X.-R. Template synthesized molecularly imprinted polymer nanotube membranes for chemical separations. *Journal of the American Chemical Society* **2006**, *128*, (50), 15954-15955.
- (7). Md Jani, A. M.; Losic, D.; Voelcker, N. H. Nanoporous anodic aluminium oxide: Advances in surface engineering and emerging applications. *Progress in Materials Science* **2013**, *58*, (5), 636-704.
- (8). Cui, Y.; Tao, C.; Zheng, S.; He, Q.; Ai, S.; Li, J. Synthesis of Thermosensitive PNIPAM-co-MBAA Nanotubes by Atom Transfer Radical Polymerization within a Porous Membrane. *Macromolecular Rapid Communications* **2005**, *26*, (19), 1552-1556.
- (9). Li, P.-F.; Xie, R.; Jiang, J.-C.; Meng, T.; Yang, M.; Ju, X.-J.; Yang, L.; Chu, L.-Y. Thermo-responsive gating membranes with controllable length and density of poly (N-isopropylacrylamide) chains grafted by ATRP method. *Journal of Membrane Science* **2009**, *337*, (1), 310-317.
- (10). Giussi, J. M.; Blaszczyk-Lezak, I.; Cortizo, M. S.; Mijangos, C. In-situ polymerization of styrene in AAO nanocavities. *Polymer (United Kingdom)* **2013**, *54*, (26), 6886-6893.
- (11). Sousa, R. G.; Freitas, R. F.; Magalhães, W. F. Structural characterization of poly (N-isopropylacrylamide) gels and some of their copolymers with acrylamide through positron annihilation lifetime spectroscopy. *Polymer* **1998**, *39*, (16), 3815-3819.

ABBREVIATIONS

1D	One dimensional
2D	Two dimensional
AAO	Anodic Aluminium Oxide
AIBN	2,2'-azo-bis-isobutyronitrile
Al	Aluminium
ATR-FTIR	Attenuated Total Reflectance Fourier Transform Infrared Spectroscopy
ATRP	Atom Transfer Radical Polymerization
CA	Water contact angle
CPG	Control Pore Glasses
CRM	Confocal Raman Microscopy
DMF	Dimethylformamide
DSC	Differential Scanning Calorimetry
<i>f</i>	Initiator efficiency
F8BT	Poly(9,9-di- <i>n</i> -octylfluorene- <i>alt</i> -benzothiadiazole)
<i>f_{res}</i>	Residual termination constant
Ha	Hatta number
Hc	Coercivity
HDI	hexamethylenediisocyanate
HPLC	High Performance Liquid Chromatography
K₃	Rate constant
<i>k_d</i>	Initiator decomposition constant
<i>k_p</i>	Propagation constant
<i>k_t</i>	Termination constant
LPP	Liquid Phase Polymerization
MCM-41	Mobil Composition of Matter n°41
MMA	Methyl methacrylate
Mn	Number Average Molecular Weight
MOF	Metal Organic Framework
Mw	Weight Average Molecular Weight
<i>N_a</i>	Avogadro's number
Ni	Nickel
NMR	Nuclear Magnetic Resonance
NPA	Nanopillars array
P3HT	Poly (3-hexylthiophene)
PA6	Polyamide 6

pACAA	Poly(acrylamide-co-acrylic acid)
PANI	Polyaniline
PBLG	Polybenzyl glutamate
PCL	Polycaprolactone
PCP	Porous Coordination Polymer
PDMS	Polydimethylsiloxane
PE	Polyethylene
PEDOT	Poly(3,4-ethylenedioxythiophene)
PEEK	Poly(ether-ether-ketone)
PFA	Poly (1H,1H,2H,2H-perfluorodecyl acrylate)
PFO	Poly (9, 9-dioctylfluorene)
PIA	Particle Interaction Apparatus
PLLA	Poly (l-lactic acid)
PMMA	Poly(methylmethacrylate)
PNIPAM	Poly(<i>N</i> -isopropylacrylamide)
PP	Polypropylene
PPy	Polypyrrole
PS	Polystyrene
PS-b-P2VP	Polystyrene-block-poly-2-vinylpyridine
PS-b-P4VP_Au	Polystyrene-block-poly-4-vinylpyridine with gold
PTFE	Polytetrafluoroethylene
PU	Polyurethane
PVC	Poly(vinyl chloride)
PVDF	Poly(vinylidene fluoride)
RAFT	Reversible Addition-Fragmentation Chain Transfer Polymerization
S	Spreading coefficient
SAINT	Solvent Anneling Induced Nanowetting in Templates
SBA-15	Santa Barbara Amorphous n°15
SEC	Size Exclusion Chromatography
SEM	Scanning Electron Microscopy
SU-8	Epoxy based negative photoresist
T_c	Crystallization temperature
TEG	Triethylene glycol
TEM	Transmission Electron Microscopy
T_g	Glass transition temperature

T_m	Melting temperature
TGA	Thermogravimetric analysis
THF	Tetrahydrofuran
TPU	Thermoplastic polyurethanes
V_f	Free volume
ΔH_T	Total heat of reaction
θ_Y	Young contact angle
F_C	Capillary force
F_V	Counter force

LIST OF PUBLICATIONS

1. **Belén Sanz**, Nicholas Ballard, Jose María Asua, Carmen Mijangos. “Effect of confinement on the synthesis of PMMA in AAO templates and modelling of free radical polymerization”. *Macromolecules*, 50, **2017**, pp 811-821
2. **Belén Sanz**, Iwona Blaszczyk-Lezak, Carmen Mijangos, Jordana K. Palacios, Alejandro J. Müller, “New Double-Infiltration Methodology to Prepare PCL-PS Core-Shell Nanocylinders Inside Anodic Aluminium Oxide Templates”. *Langmuir* 32 (31), **2016**, pp. 7860-7865
3. **Belén Sanz**, Esther M. Palmero, Rafael P. Del Real, Manuel Vázquez, Carmen Mijangos, “Arrays of Magnetic Ni Nanowires Grown Inside Polystyrene Nanotubes”. *Industrial and Engineering Chemistry Research*, 54 (51), **2015**, pp. 13005-13008
4. Maitane Salsamendi, Nicholas Ballard, **Belén Sanz**, Jose María Asua, Carmen Mijangos, “Polymerization kinetics of a fluorinated monomer under confinement in AAO nanocavities”. *RSC Advances* 5 (25), **2015**, pp. 19220-19228
5. Juan M. Giussi, Iwona Blaszczyk-Lezak, **Belén Sanz**, Patricia Allegretti, Carmen Mijangos, Susana Cortizo "Tautomeric acetoacetate monomers as building units of functional copolymers", *European Polymer Journal* 59, **2014**, pp. 84-93
6. **Belén Sanz**, Catalina von Bilderling, Jimena Tuninetti, Lía Pietrasanta, Carmen Mijangos, Gabriel S. Longo, Omar Azzaroni, Juan M. Giussi “*Thermally-Induced Softening of PNIPAM-Based Nanopillar Arrays*”. Soft matter DOI: 10.1039/c7sm00206h *Accepted*
7. **Belén Sanz**, Nicholas Ballard, Jose María Asua, Carmen Mijangos “Step-growth polymerization in confinement within AAO templates”. *Macromolecules* (ID: ma-2017-004903). *Sent*
8. Longjian Xue, **Belén Sanz**, Michael Kappl, Rui Zhang, Hang Du, Martin Steinhart, Markus Guttman, Aránzazu del Campo “Hybrid adhesive designs mimicking frog toe pad hierarchical structure”. *To be submitted*